University of Massachusetts Amherst
ScholarWorks@UMass Amherst

Doctoral Dissertations 1896 - February 2014

1-1-1984

Processing-morphology-property relationships of polyurethanes/

An-Lou Chang
University of Massachusetts Amherst

Follow this and additional works at: https://scholarworks.umass.edu/dissertations_1

Recommended Citation

Chang, An-Lou, "Processing-morphology-property relationships of polyurethanes/" (1984). *Doctoral Dissertations 1896 - February 2014*. 682.
https://doi.org/10.7275/gty7-jk76 https://scholarworks.umass.edu/dissertations_1/682

This Open Access Dissertation is brought to you for free and open access by ScholarWorks@UMass Amherst. It has been accepted for inclusion in Doctoral Dissertations 1896 - February 2014 by an authorized administrator of ScholarWorks@UMass Amherst. For more information, please contact scholarworks@library.umass.edu.

UMASS/AMHERST

312066 0024 2841 1

PROCESSING-MORPHOLOGY-PROPERTY RELATIONSHIPS OF POLYURETHANES

A Dissertation Presented

By

AN-LOU CHANG

Submitted to the Graduate School of the
University of Massachusetts in partial fulfillment
of the requirements for the degree of

DOCTOR OF PHILOSOPHY

February 1984

Polymer Science and Engineering

© An-Lou Chang

All Rights Reserved

PROCESSING-MORPHOLOGY-PROPERTY RELATIONSHIPS OF POLYURETHANES

A Dissertation Presented

By

AN-LOU CHANG

Approved As To Style And Content By:

Edwin L. Thomas, Chairperson of Committee

Richard S. Stein, Member

Horst H. Winter, Member

William J. MacKnight, Department Head
Polymer Science and Engineering

Dedicated to my wife

Yi-Hsiang

for her support, understanding and love

throughout the course of this work

ACKNOWLEDGMENTS

I would like to express my sincerest appreciation to my thesis advisor Dr. Edwin L. Thomas, for his guidance, patience and stimulating discussions throughout the course of this work. It has been the most challenging and rewarding experience to work in the field of polymer morphology.

I am also grateful to the members of my thesis committee, Dr. Richard S. Stein and Dr. Henning H. Winter, for their invaluable advice and discussions.

A special thanks is extended to Dr. Christopher W. Macosko whose ideas and suggestions were of great help in this work.

I am deeply indebted to Drs. R. J. Zdrahala and F. E. Critchfield of Union Carbide for providing all the polyurethane samples studied in this work, and for their support and cooperation throughout the course of this work.

The assistance of Drs. R. E. Camargo, R. Briber and P. Young is greatly appreciated.

The support of a grant-in-aid from the Union Carbide Corporation is also greately acknowledged.

Lastly, I am indebted to my parents for their endless support and for putting up with me all these years.

ABSTRACT

Processing-Morphology-Property Relationships
of Polyurethane
(February 1984)
An-Lou Chang, B.S., Tunghai University,
M.S., University of Minnesota,
M.S., Ph.D., University of Massachusetts
Directed by: Professor Edwin L. Thomas

The unique high plateau modulus properties of polyurethanes over wide temperature range are believed to arise from their small scale phase separation (hard segment microdomains formation) characteristics. In order to explicitly characterize detailed sample morphology and domain structure, we have systematically studied PPO-EO/MDI/BDO, PPO-EO/MDI/BEDO and PCP/MDI/BDO based polyurethanes made by simple well-mixed and isothermal batch reaction. DSC, WAXS, SAXS, Instron, optical and electron microscopy were employed to characterize these polyurethane samples.

We have found that polyurethane random block copolymers can have many possible structures depending on chemical composition, formulation and thermal history.

These structures include hard segment-rich globules (HSG),fibrils (HSF), two types of spherulite (α, β-HSS), hard segment-rich matrix (HSM), micro paracrystallite hard segment domains (MPC), and soft segment-rich matrix (SSM). In addition, the sample can have a pronounced skin/core morphology at high hard segment concentration due to the high exothermic heat of polymerization.

The universal findings of globules and skin/core morphology in virtually all the sample types examined lead us to conclude what is usually thought to be homogeneous and isothermal batch reaction is really nonhomogeneous and nonisothermal reaction. The former is caused by poor mixing or incompatibility of the reacting components, plus further phase separation during the polymerization and solidification (molecular weight, hydrogen-bonding or crystallization effect). The latter is due to the high exothermic heat of polymerization of polyurethane and poor heat conductivity of polymer. The complex, simultaneously occurring (macro)phase separation-polymerization-(micro) phase separation-crystallization processes will vary according to sample composition, position in the mold and the detailed temperature history.

Since the mechanical properties are a composite average of the whole sample, the interpretation of the

relationship between mechanical properties and microstructure is greatly complicated by the influence of the variations and heterogeneties present in the morphology.

TABLE OF CONTENTS

ACKNOWLEDGMENTS v

ABSTRACT vi

LIST OF TABLES xi

LIST OF FIGURES xii

Chapter

I. INTRODUCTION 1

1.1 General Perspectives 1
1.2 The Thesis Problem 4

II. REVIEW OF POLYURETHANE MORPHOLOGICAL STUDIES . . 7

2.1 Types of Polyurethane Previously Investigated 7
2.2 Proposed Structural Models 9
2.3 Segment Crystallinity 14
2.4 Block Length Distribution 19
2.5 Domains and Spherulites 22

III. EXPERIMENTAL 27

3.1 Experimental Materials 27
3.2 Experimental Techniques 30
A. Differential Scanning Calorimetry (DSC). 31
B. Polarized Light Microscopy 31
C. Electron Microscopy. 32
D. Cryo Ultramicrotomy. 34
E. OsO_4 Staining. 35
F. Hot-pressing 35
G. Wide-angle X-ray Scattering 36
H. Small-angle X-ray Scattering 37

IV. RESULTS FOR 100°C CURE PPO-EO/MDI/BDO SERIES . . 39

4.1 Differential Scanning Calorimetry Results 41
4.2 Optical Microscopy Results 43
4.3 Transmission Electron Microscopy Results . 55
4.4 Mechanical Properties 74
4.5 Scanning Electron Microscopy Results . . . 77
4.6 Adiabatic Temperature Rise Results 77

Chapter

4.7 Wide-angle X-ray Scattering Results. . . . 81
4.8 Small-angle X-ray Scattering Results . . . 83
4.9 Annealing Study of Sample A-V 89
4.10 Discussion and Conclusions 92

V. RESULTS FOR 175°C CURE PPO-EO/MDI/BDO SERIES . . 100

5.1 Differential Scanning Calorimetry Results. 100
5.2 Optical Microscopy Results 105
5.3 Transmission Electron Microscopy Results . 110
5.4 Wide-angle X-ray Scattering Results. . . . 120
5.5 Mechanical Properties 120
5.6 Discussion and Conclusions 124

VI. POLYURETHANES WITH BUTENE DIOL-AN APPROACH TO STAINING OF THE HARD SEGMENT DOMAINS 127

6.1 Differential Scanning Calorimetry Results 128
6.2 Optical Microscopy Results 132
6.3 Transmission Electron Microscopy Results 137
6.4 Wide-angle X-ray Scattering Results . . . 146
6.5 Small-angle X-ray Scattering Results . . . 148
6.6 Domain Structure Characterization-TEM Results and Discussion of Cryomicrotomed Sections of OsO_4 Stained Bulk PPO-EO/MDI/BEDO Samples . . . 151
6.7 Discussion and Conclusions 165

VII. RESULTS FOR 145°C CURE PCP/MDI/BDO SERIES . . . 168

7.1 Differential Scanning Calorimetry Results. 168
7.2 Optical Microscopy Results 170
7.3 Transmission Electron Microscopy Results . 186
7.4 Wide-angle X-ray Scattering Results . . . 205
7.5 Small-angle X-ray Scattering Results . . . 208
7.6 Discussion and Conclusions 212

VIII. SUMMARY AND CONCLUSIONS/POSSIBLE FUTURE WORK . . 215

8.1 Summary and Conclusions 215
8.2 Possible Future Work 220

REFERENCES 223

APPENDIX 232

LIST OF TABLES

Table

1. Summary of Structural Studies of Polyurethane Systems 8
2. Compositions of the Polyurethanes Studied 28
3. Hot-pressing Temperatures for 100°C Cure PPO-EO/MDI/BDO Samples 36
4. Summary of Composition and Heats of Fusion for 100°C Cure PPO-EO/MDI/BDO Samples 44
5. Summary of DSC Results of Skin and Core Regions of Samples A-VI and A-VII 44
6. Mechanical Properties of 100°C Cure PPO-EO/MDI/BDO Samples 76
7. Small-angle X-ray Spacing for As-reacted Series A Samples 87
8. Small-angle X-ray Spacing for Hot-pressed Series A Samples 87
9. Summary of Composition and Heats of Fusion for 175°C Cure PPO-EO/MDI/BDO Samples 103
10. Summary of DSC Results of Skin and Core Regions of Samples B-V and B-VI 103
11. Mechanical Properties of 175°C Cure PPO-EO/MDI/BDO Samples 123
12. Mechanical Properties of 100°C Cure PPO-EO/MDI/BDO Samples 123
13. Summary of Composition and Heats of Fusion for As-reacted and Annealed PPO-EO/MDI/BEDO Samples 131
14. Wide-angle X-ray Diffraction Data of PPO-EO/MDI/BEDO Samples 148
15. Summary of Heats of Fusion of the Hard Segment for As-reacted PCP/MDI/BDO Samples 171
16. Wide-angle X-ray Diffraction Data of PCP/MDI/BDO Samples 207
17. Wide-angle X-ray Diffraction Data of MDI/BDO Copolymer and Poly-ε-Caprolactone Homopolymer 207
18. Small-angle X-ray Bragg Spacing for As-reacted PCP/MDI/BDO Samples 208

LIST OF FIGURES

Figure

1. Suggested organization of crystalline hard segment strands. 10
2. (a) Schematic drawing of the structure in a polyurethane block polymer stretched approx. 200 percent; (b) Schematic drawing of the structure in material stretched approx. 500 percent and subsequently fixed in water at 80°C. 11
3. Model of highly oriented segmented polyurethane 12
4. Two proposed models to account for the spherulitic structure present in segmented polyurethanes. 12
5. Schematic representation of proposed two-phase model domain structure 13
6. (a) Physical structure of crosslinking in purely two-dimensional hard segment aggregates; (b) Diagrammatical representation of the three-dimensional crosslinking structure. 15
7. Proposed structure of MDI/BDO copolymer: ac projection 17
8. Proposed MDI/BDO crystal structure and interurethane hydrogen bonding viewed along the a axis of the unit cell. 18
9. Crystal structure of MeMMe modification II: projection along c axis. 20
10. First run DSC scans of samples A-I to A-VII over the temperature range 330-550°K 42
11. First run DSC scans of skin and core regions of samples A-VII (78 percent hard segment) and sample A-VI (66 percent). 45
12. Micrographs of the globular morphology of sample A-I (10 percent hard segment), (a) optical micrograph; (b) and (c) TEM micrographs. 47
13. Low magnification optical micrographs (crossed polarizers): (a) sample A-IV (43 percent hard segment); (b) sample A-V (55 percent); (c) sample A-VI (66 percent) and (d) sample A-VII (78 percent). 50
14. Optical micrograph (crossed polarizers) of sample A-IV (43 percent hard segment) . . . 52
15. Optical micrograph (crossed polarizers) of sample A-V (55 percent hard segment). . . . 52

Figure

16. Optical micrograph (crossed polarizers) of skin regions of sample A-VI (66 percent hard segment). 54
17. Optical micrograph (crossed polarizers) of skin regions of sample A-VII (78 percent hard segment). 54
18. (a) and (b) TEM micrographs of sample A-II (21 percent hard segment) 57
19. (a) and (b) TEM micrographs of sample A-III (32 percent hard segment). 59
20. (a) and (b) TEM micrographs of sample A-IV (43 percent hard segment) 61
21. (a) and (b) TEM micrographs of sample A-V (55 percent hard segment). 64
22. (a) and (b) TEM micrographs of the skin regions of sample A-VI (66 percent hard segment) 66
(c) and (d) TEM micrographs of the core regions of sample A-VI (66 percent hard segment) 68
23. (a) and (b) TEM micrographs of the skin regions of sample A-VII (78 percent hard segment) 70
(c) TEM micrograph of the core regions of sample A-VII (78 percent hard segment) 72
(d) High magnification TEM micrograph of ultrathin sections of the core regions of sample A-VII (78 percent hard segment) 72
24. Load versus strain curves for samples A-I to A-VII 75
25. SEM micrographs of sample A-VII: (a) before tensile deformation; (b) after tensile deformation. 79
26. Calculated and experimental adiabatic temperature rise versus hard segment content. 80
27. Wide-angle X-ray scans of samples A-I to A-VII 82
28. Pinhole SAXS scattering patterns of as-reacted bulk samples A-I to A-VII 84
29. Pinhole SAXS scattering patterns of hot-pressed samples A'-I to A'-VII 85
30. Pinhole SAXS scattering patterns of skin and core regions of as-reacted bulk sample A-VII 86

Figure

31. (a) TEM micrograph of sample A-V (55 percent hard segment) before annealing . . 91
(b) TEM micrograph of annealed sample A-V 91
32. Possible temperature versus time pathways for different compositions: (A) high hard segment content; (B) intermediate hard segment content; (C) low hard segment content 97
33. First run DSC scans of samples B-I to B-VII over the temperature range 330-550°K 101
34. First run DSC scans of skin and core regions of samples B-V (55 percent hard segment) and B-VI (66 percent hard segment) 104
35. Low magnification optical micrographs (crossed polarizers) of samples B-IV(a), B-V(b) and B-VI(c). 107
36. High magnification optical micrographs (crossed polarizers) of samples B-IV(a), B-V(b) and B-VI(c). 109
37. TEM micrograph of the globular morphology of sample B-I (10 percent hard segment). . . . 112
38. TEM micrograph of the globular morphology of sample B-II (21 percent hard segment) . . . 112
39. TEM micrograph of the globular morphology of sample B-III (32 percent hard segment) 114
40. TEM micrograph of sample B-IV (43 percent hard segment). 114
41. TEM micrographs of sample B-V (55 percent hard segment): (a) skin regions; (b) core regions 117
42. TEM micrographs of sample B-VI (66 percent hard segment): (a) skin regions; (b) core regions 119
43. Wide-angle X-ray scans of samples B-I to B-VI. 121
44. Load versus strain curves for samples B-I to B-VI. 122
45. First run DSC scans of samples BEDO-I to BEDO-III (I and I' are two different sampling regions for sample BEDO-I). 129
46. DSC scans of both the as-reacted (II) and annealed (II') sample BEDO-II. 130
47. Optical micrograph (crossed polarizers) of sample BEDO-I (10 percent hard segment) . . 134

Figure

48. Optical micrograph (crossed polarizers) of sample BEDO-II (43 percent hard segment) 134
49. Optical micrographs (crossed polarizers) of sample BEDO-III (78 percent hard segment) 136
50. TEM micrograph of sample BEDO-I (10 percent hard segment). 139
51. TEM micrograph of sample BEDO-II (43 percent hard segment). 139
52. TEM micrograph of as-reacted sample BEDO-II (43 percent hard segment) 142
53. TEM micrograph of annealed sample BEDO-II (43 percent hard segment). 142
54. TEM micrograph of the skin regions of sample BEDO-III (78 percent hard segment) 144
55. TEM micrograph of the core regions of sample BEDO-III (78 percent hard segment) 144
56. Wide-angle X-ray scans of samples BEDO-I to BEDO-III and pure hard segment copolymer (MDI/BEDO) 147
57. Pinhole SAXS scattering patterns of samples BEDO-I to BEDO-III 149
58. High magnification TEM micrographs of OsO_4 stained and microtomed thin sections of sample BEDO-I (10 percent hard segment), taken at (a) near focus ($\Delta f \simeq 0$), (b) underfocus ($\Delta f = -3.4$ μm) and (c) overfocus ($\Delta f = +3.4$ μm) respectively 154
59. (a), (b) and (c) High magnification TEM micrographs of OsO_4 stained and microtomed thin sections of sample BEDO-II' (43 percent hard segment, annealed sample), taken at (a) near focus ($\Delta f \simeq 0$), (b) underfocus ($\Delta f = -3.4$ μm) and (c) overfocus ($\Delta f = +3.4$ μm) respectively. . . 157
(d) and (e) High magnification TEM micrographs of OsO_4 stained and microtomed thin sections of sample BEDO-II' (43 percent hard segment, annealed sample), taken at (d) underfocus ($\Delta f = -6.8$ μm) and (e) overfocus ($\Delta f = +6.8$ μm) respectively 159

Figure

60. (a) High magnification TEM micrograph of OsO_4 stained and microtomed thin sections of sample BEDO-III (78 percent hard segment), taken at near focus ($\Delta f \simeq 0$) 162
60. (b) to (e) High mangification TEM micrographs of OsO_4 stained and microtomed thin sections of sample BEDO-III (78 percent hard segment), taken at (b) underfocus ($\Delta f = -3.4$ μm), (c) overfocus ($\Delta f = +3.4$ μm), (d) underfocus ($\Delta f = -6.8$ μm) and (e) overfocus ($\Delta f = +6.8$ μm) respectively . . 164
61. DSC scans of the as-reacted PCP/MDI/BDO samples over the 320-520°K temperature range . 169
62. DSC scans of as-reacted (I) and annealed (II) PCL-165 samples 172
63. Optical micrographs of sample PCL-121 (13 percent hard segment): (a) uncrossed polarizers; (b) crossed polarizers 175
64. Optical micrographs of sample PCL-132 (23 percent hard segment): (a) uncrossed polarizers; (b) crossed polarizers 177
65. Optical micrographs of sample PCL-143 (31 percent hard segment): (a) uncrossed polarizers; (b) crossed polarizers 179
66. Optical micrographs of sample PCL-154 (38 percent hard segment): (a) uncrossed polarizers; (b) crossed polarizers 181
67. Optical micrographs of sample PCL-165 (43 percent hard segment): (a) uncrossed polarizers; (b) crossed polarizers 183
68. Optical micrographs of annealed sample PCL-165 (43 percent hard segment): (a) uncrossed polarizers; (b) crossed polarizers 185
69. (a) and (b) TEM micrographs of sample PCL-121 (13 percent hard segment) 188
(c) and (d) TEM micrographs of sample PCL-121 (13 percent hard segment) 190
70. (a) and (b) TEM micrographs of sample PCL-132 (23 percent hard segment) 193
71. (a) and (b) TEM micrographs of sample PCL-143 (31 percent hard segment) 196

Figure

72. (a) and (b) TEM micrographs of sample PCL-154 (38 percent hard segment) 198
73. (a) and (b) TEM micrographs of sample PCL-165 (43 percent hard segment) 201
74. (a) and (b) TEM micrographs of annealed sample PCL-165 (43 percent hard segment) 203
75. Wide-angle X-ray scans of the as-reacted PCP/MDI/BDO samples 206
76. Pinhole SAXS scattering patterns of as-reacted bulk samples of PCP/MDI/BDO series 209
77. Schematic representations of the various structures with different dimensions present in the 100°C cure PPO-EO/MDI/BDO based polyurethane samples 219

C H A P T E R I

INTRODUCTION

1.1 General Perspectives

The interesting elastomeric properties of polyurethanes are currently atrributed to the formation of microdomains[1-4]. Thermoplastic polyurethane elastomers are linear multiblock copolymers of the $+AB+_n$ type consisting of short, immobile, polyurethane sequences ("hard" segments) connected via long and flexible chains ("soft" segments). A variety of aliphatic and aromatic diisocyanates with low molecular weight diol or diamine chain extenders of about two to twelve carbon atoms have been used for the hard segment with typically 1,000-3,000 molecular weight polyether, polyester or polybutadiene polyols for the soft segment. Due to the polar nature of the urethane group in the hard segments and their ability to form hydrogen bonds, the strong molecular association within the hard segments makes it possible for the hard segments to undergo phase separation into regions termed domains. The unique elastomeric properties of the polyurethanes are currently attributed to the formation of microdomains in these systems, which act as pseudo-crosslinks for the flexible soft segment phase and

give thermoplastic urethane elastomers high plateau modulus properties over wide temperature range. Mechanical properties can then be conveniently tailored by varying the ratio of hard to soft phase.

Previous work has shown that stereoregularity[5] and block length[6] as well as thermal history[7,8] during and after polymerization all play important roles in determining the degree of phase separation as well as the degree of order of the soft and hard segment domains. Better phase separation is favored for nonpolar soft segment systems[9] and with longer sequence-lengths of the respective hard/soft segments.

Compatibility is greater for (di)block than for a blend of the homopolymers and is greater still for multiblock copolymers, particularly with short block lengths. Of course, in the limiting case of regular alternating noncrystallizable copolymer $\text{-}(AB)\text{-}_n$, a single homogeneous phase is obtained. The length scale of the inhomogeneities of incompatible (phase separated) systems depends on both the length of the individual blocks of the copolymer and the degree of thermodynamic equilibrium attained. Although it is usual to speak in terms of an average block size and average domain size, random copolymerized segmented polyurethanes are multiple block copolymers, containing a distribution of block lengths[10,11,12]. Such a distribution will tend to increase phase compatibility -

e.g., more diffuse phase boundaries, appreciable mixing of hard and soft sequences within the respective domains and a distribution of domain sizes.

The substantial work on polystyrene/polybutadiene and polystyrene/polyisoprene blends and diblock and triblock copolymer systems[13,14,15] has led to a general understanding of the nature of phase separation in regular block copolymer systems. The additional complexities of multiblocks with variable block length as well as possible hard and/or soft phase crystallinity makes the morphological characterization of polyurethane systems a challenge.

Reaction Injection Molding (RIM) is a relatively new polymer processing method which forms molded parts directly from monomers and oligomers by fast, in situ polymerization. The low viscosity reactants are easily mixed by impingement and require low pressure to fill the mold. This reduces capital equipment costs especially for large parts. Because of the low temperature and pressure requirements, the energy cost of a RIM part can be considerably lower than for a typical thermoplastic, vulcanized rubber or metal part. Newly improved automated RIM equipment, like closed-loop process control automation which is simple to operate and highly productive, has attracted more interest in RIM process polymer production.

Although most RIM processes are currently applied to polyurethane production[17], new reinforced RIM systems and alternative RIM materials such as epoxies, silicones, polyesters and nylons have been suggested as reaction injection moldable polymers. It is predicted that more than 20 percent of the annual production of all plastics will be processed by RIM in the next five years[18].

Although the RIM process itself has been extensively studied[16,19-22], there is still little known about how the RIM process influences the structure and properties of the polymer formed. While all polyurethane samples investigated in this thesis are made by one step batch polymerization process, certain features are relevent to RIM, indeed, industry screens candidate RIM formulations by first examining batch processed hand cast plaques.

1.2 Thesis Problem

In order to better understand the processing-structure-properties of polyurethanes, it is essential that detailed sample morphology and domain structure be explicitly characterized. We have systematically characterized the morphology of PPO-EO/MDI/BDO, PPO-EO/MDI/BEDO and PCP/MDI/BDO based polyurethanes made by simple, well-mixed and isothermal batch reaction. DSC, WAXS. SAXS, Instron, optical and electron microscopy were employed to

characterize these samples.

Our main interest is thus to provide a mapping of the size and shape of the domains (and any superstructure such as spherulites) and the degree of order (i.e. crystallinity or orientation) as a function of the fraction of the hard segment phase and as a function of the processing conditions used to form the polymer. To achieve this goal, SAXS and TEM (direct observation of cryomicrotomed ultra-thin sections of the polymer at high magnification of bright field (B.F.) or dark field (D.F.) image were employed.

Because of the intrinsic low image contrast of polymers under TEM observation, it is extremely difficult to visualize any small scale (circa 100 Å) domain structure. There are four kinds of image-contrast in the polymer:

1. electron density variations due to composition and density differences of the phases,

2. thickness variations due to film preparation (undesirable) and electron beam etching (desirable if selective and understood),

3. phase contrast due to differences in optical path through the polymer phases and the microscope optics,

4. diffraction contrast due to coherent scattering from local ordered regions (e.g., crystalline MDI/BDO hard segment domain).

Unless the hard segment or soft segment is highly crystalline and the microtomed section is "super" thin, (i.e., less than say 400Å which is normally, also, not the case), the image contrast is insufficient to determine the small scall domain structure. Therefore, we attempted to enhance the contrast via "extrinsic" OsO_4 staining of a double bond containing hard segment. The polymer used for this special study employed butene diol as the chain extender.

C H A P T E R II

REVIEW OF POLYURETHANE MORPHOLOGICAL STUDIES

A large number of microstructural studies have been previously conducted on polyurethanes. Three excellent review articles on polyurethanes have been reported by Aggarwal[13], Allport[14] and Noshay[15]. The majority of morphological data for these systems is based on differential scanning calorimetry[2,8,23-31] (DSC), wide-angle X-ray scattering[2,9,23,32-39] (WAXS), small-angle X-ray scattering[2,7,23,36-42] (SAXS), small-angle light scattering[9,37,38,43] (SALS), infra-red[24,25,38,44-46] (IR) and Fourier transform infra-red[47] (FTIR), nuclear magnetic resonance[26,48] (NMR), and optical microscopy techniques[2,37-39] with relatively few systematic observations of super and microstructure via scanning and transmision electron microscopy[1,2,36,37,39,49-51] (SEM, TEM). As well, near all TEM studies were done on solution cast films, only two were done on microtomed as-reacted samples[2,68].

2.1 Types of Polyurethane Previously Investigated

A summary of polyurethane systems which have been structurally investigated is shown in Table 1. We will

TABLE 1

SUMMARY OF STRUCTURAL STUDIES OF POLYURETHANE SYSTEMS

	SYSTEM	INVESTIGATOR
1.	PCP/MDI/BDO	Present study, Seefried et al[52-59]
2.	PTMA/MDI/BDO	C. Wilkes[23], G. Wilkes[7,8,27], Koutsky[1]
3.	PTMO/MDI/BDO	G. Wilkes[7,13], Koutsky[1], Clough[9], Cooper[4]
4.	PPO-EO/MDI/BDO	Schnieder[2], Present study
5.	PPO-EO/MDI/BEDO	Present Study
6.	PO/MDI/EO	Aggarwal[13]
7.	PBA/MDI/BDO	Clough[9,37], Cooper[3,4,24,44], Miller[28]
8.	PEA/HBI, MDI, TDI, NDI	Onder[5]
9.	PEA/MDI/BDO	Miller[60], Bonart[32-35]
10.	PTMO, PBA/TDI/BDO	Schnieder[25]
11.	PTMO/MDI/EDA, PDA, HH, DAM	Bonart[32-34], Kimura[35,50,51]
12.	PB/TDI/HDO, HPA	Lagasse[36,39]
13.	PTMO/ 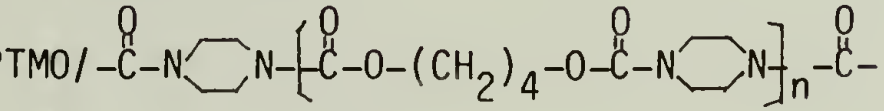	Harrell[6], G. Wilkes[37,43,49]
14.	PTMO, PCP/TODI/BDO	Lagasse[39]

Key: PCP = polycaprolactonediol; PTMA = poly (tetramethylene adipate); PEA = poly (ethylene adipate); PTMO = PTMG = (polytetramethylene oxide); PPO-EO = propylene oxide-ethylene oxide; BEDO = butene diol; PBA = poly (1.4-butylene adipate); HDI = hexamethylene diisocyanate; TDI = toluene diisocyanate; NDI = naphthalene diisocyanate; EDA = ethylene diamine; PDA = propylene diamine; HH = hydrazine; DAM = diamino diphenyl methane; PB = polybutadiene; HDO = hexanediol; HPA = hydroxy propyl aniline; TODI = bitolylene diisocyanate.

concentrate our attention on the polycaprolactone-diol polyester/4,4'-diphenylmethane diisocyanate/1,4-butane diol (PCP/MDI/BDO) system and on polyether (oxypropylene-oxyethylene diol) systems containing MDI/BDO or MDI/BEDO (butene diol) hard segment.

2.2 Proposed Structural Models

The morphology of polyurethane is complex--both soft and hard segment domains in polyurethanes can be amorphous or partially crystalline, depending on the particular systems. Models have been proposed by Schneider[2], (see Figure 1), Bonart[32] (see Figure 2), C. Wilkes[23] (see Figure 3) and S. Samuels[49] (see Figure 4). The occurrence of a spherulitic superstructure has also been observed by S. Samuels[43,49] (also see Figure 4). Although the block length and volume fraction of each type of segment will influence the overall domain morphology, both bicontinuous and discrete-isolated domain morphologies have been proposed[44,61] (Figure 5).

Of all these various models, there is still no good agreement on which model(s) represent the actural structural arrangement of the soft and hard segments in a given polyurethane system.

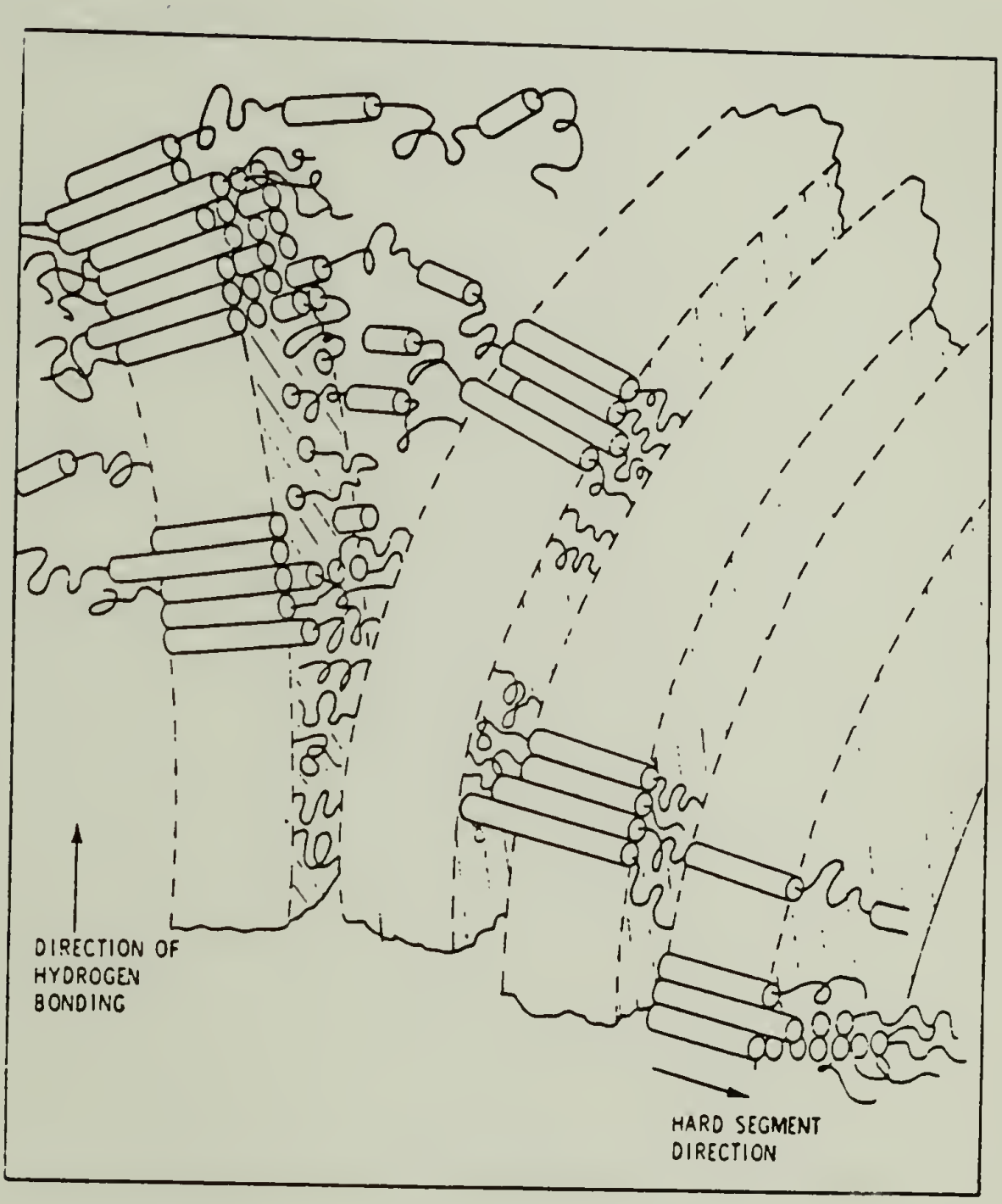

Figure 1. Suggested organization of crystalline hard segment strands. The average orientation of the strands is in the radial direction (N. Schneider[2]).

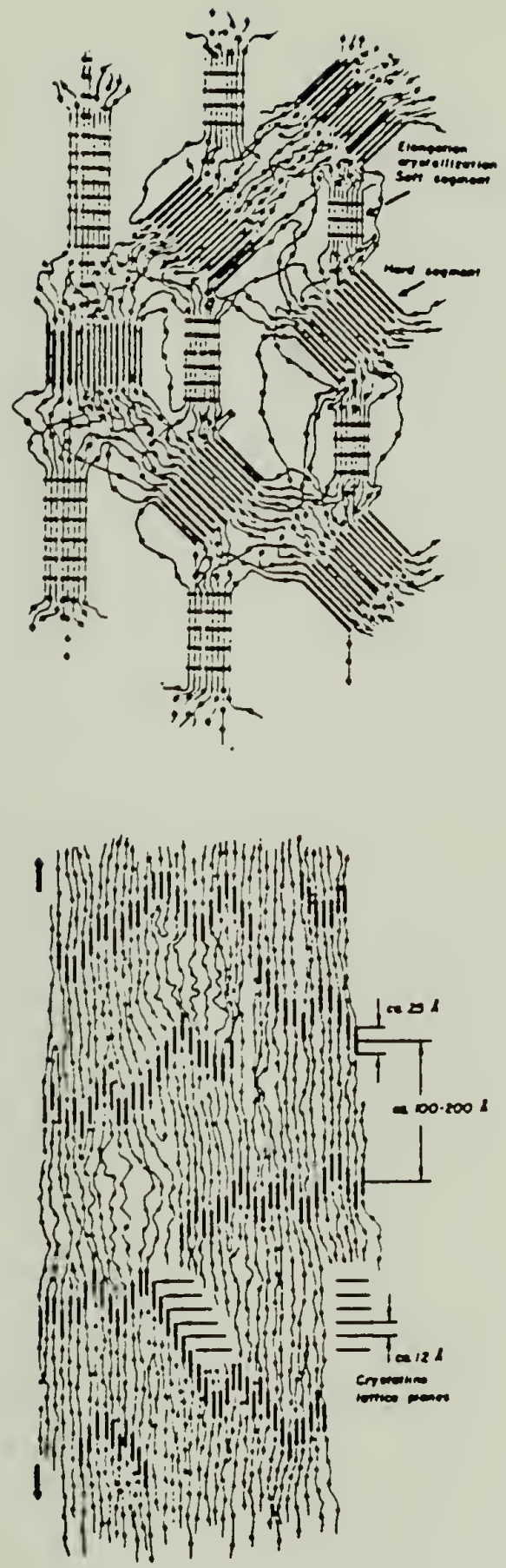

Figure 2. (a) Schematic drawing of the structure in a polyurethane block polymer stretched approx. 200 percent. The thick strokes represent hard segments and the thin strokes soft segments; (b) Schematic drawing of the structure in material stretched approx. 500 percent and subsequently fixed in water at 80°C (R. Bonart[32]).

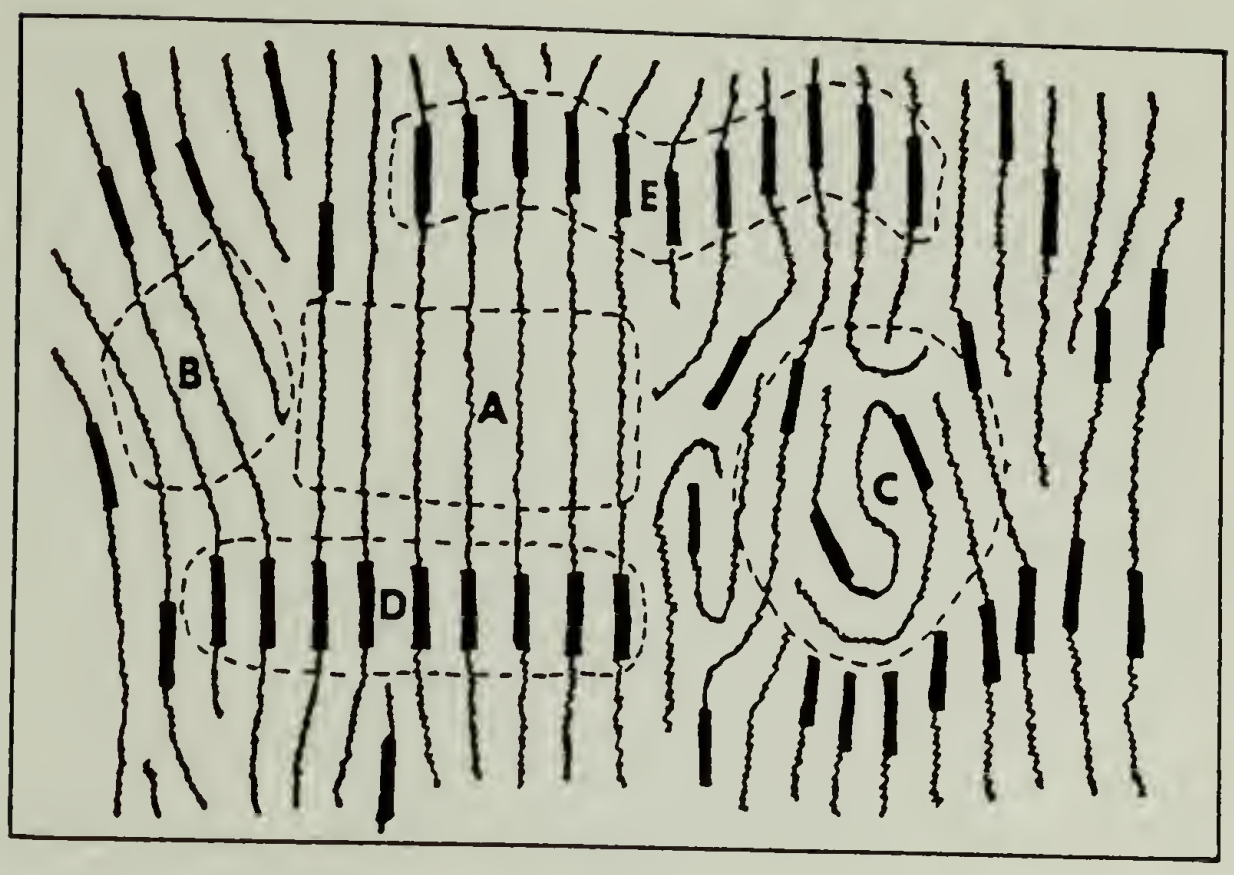

Figure 3. Model of highly oriented segmented polyurethane: (A) stress-crystallized polyester or polyether; (B) ordered but noncrystalline polyester or polyether; (C) amorphous "solution" of hard and soft segments; (D) crystalline hard-segment (urethane) domains; (E) ordered but noncrystalline hard-segment domains. Black bars represent hard segments consisting of the products from the reaction of the diisocyanate and a low molecular weight glycol (C. Wilkes[23]).

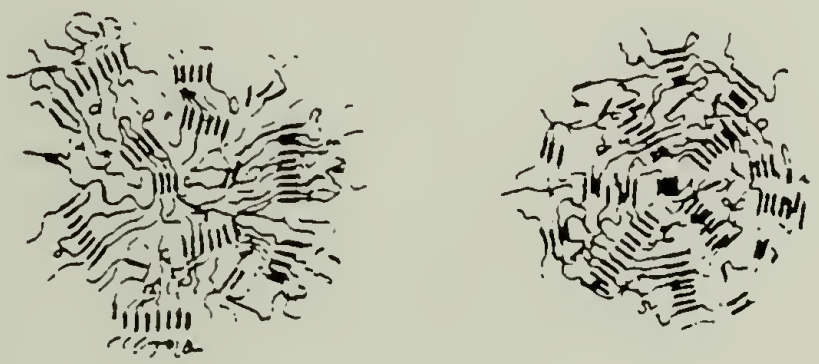

Figure 4. Two proposed models to account for the spherulitic structure present in segmented polyurethanes: (a) chain orientation tangential as hard segments crystallize radially; (b) chain orientation radial as hard segments crystallize tangentially (G. Wilkes[49]).

Figure 5. Schematic representation of proposed two-phase model domain structure (S. Cooper[61]).

2.3 Segment Crystallinity

Providing a block is stereoregular, block length is important in determining crystallinity. The occurrence of MDI/BDO hard segment crystallinity in various polyurethane systems has been reported[2,4,5,23,25,39]. Hard segment crystallization can occur even for quite short block lengths.

Harrell[6] prepared a systematic series of polymers with monodisperse hard segment sizes and showed that crystallization occurred even for chains containing only a single hard segment repeat unit (it should be noted that Harrell's polymers had no hydrogen bonding, see Table 1). Interestingly, he reported that increasing the hard segment block length did not appreciably affect the degree of order within the hard domains, though the melting point of the hard segment phase was raised. Wilkes[37,43,49] and coworkers have characterized the morphology of these specially prepared polymers and have found both spherulitic superstructure and domain structures. Domain size apparently increased with increasing hard segment content as evidenced by sharpening of the wide-angle X-ray (WAXS) reflections[37].

Bonart has proposed two-dimensional and three-dimensional models of MDI/BDO hard segment (para) crystals[33,34,62] (see Figure 6). Arrangements were

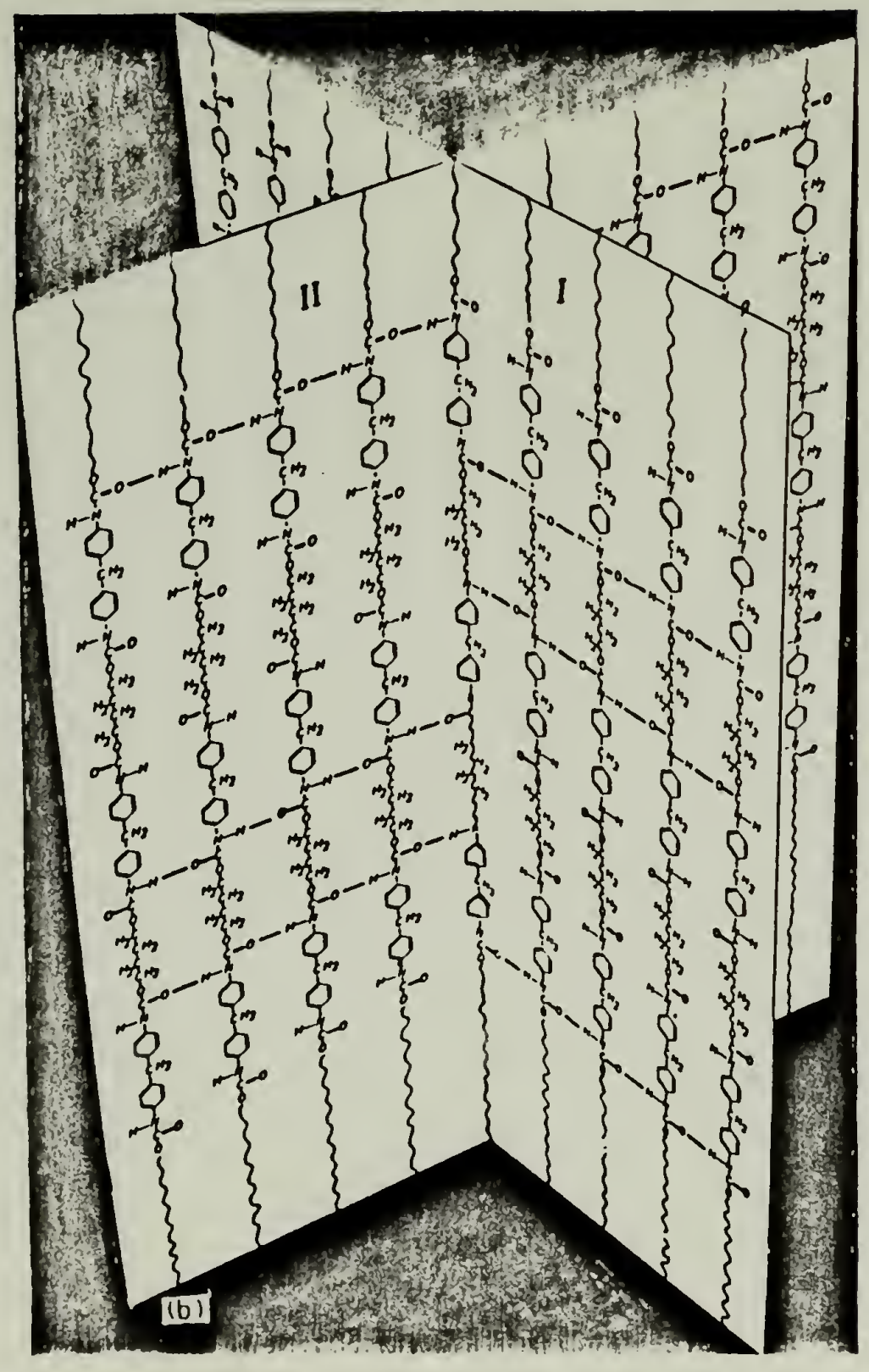

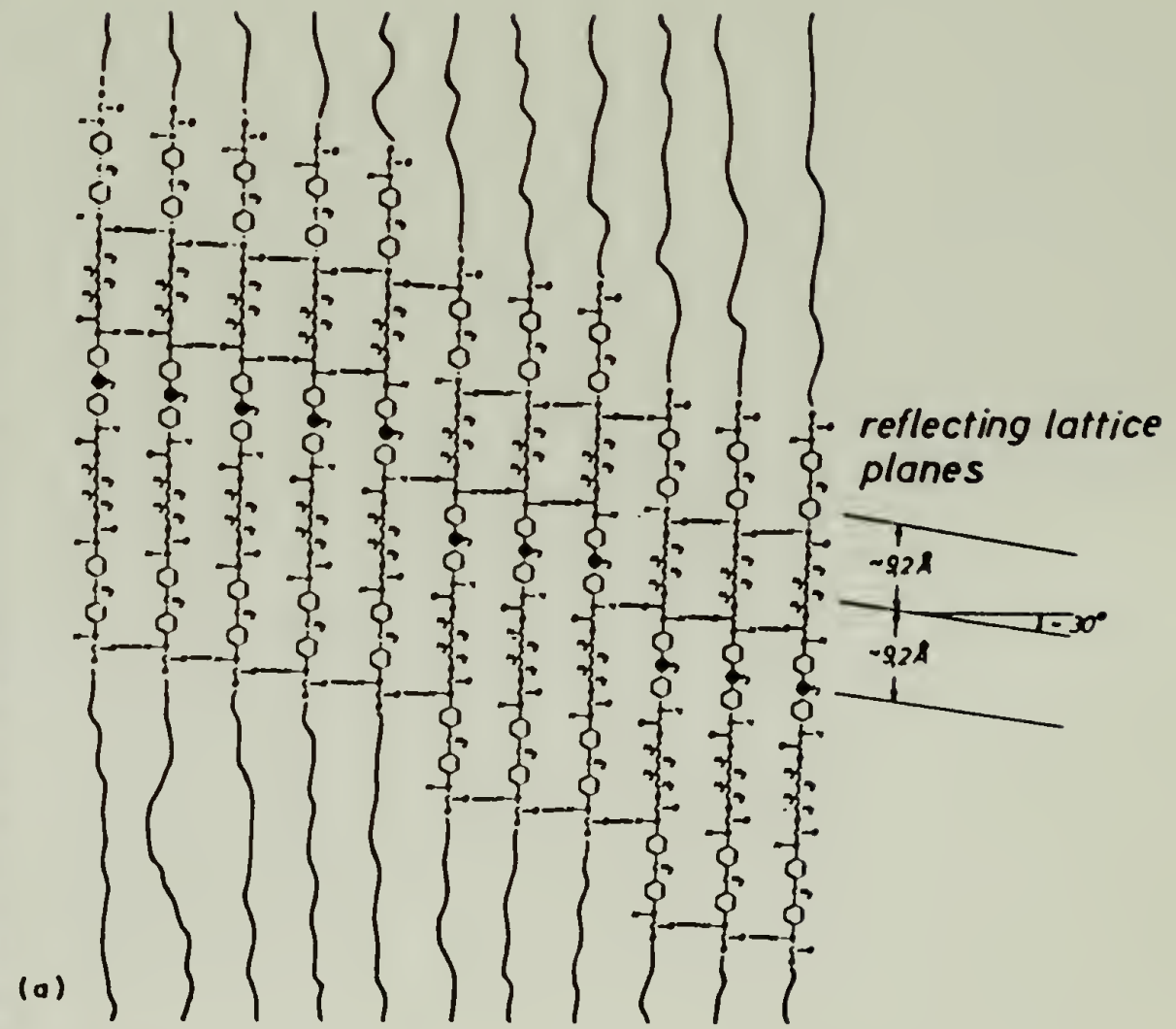

Figure 6. (a) Physical structure of crosslinking in purely two-dimensional hard segment aggregates; (b) diagrammatical representation of the three-dimensional crosslinking structure (extended with butane diol (R. Bonart[33]).

constructed which provide optimum hydrogen bonding. The ~7.9 Å paracrystalline hard segment reflection was thought to arise from the hydrogen bond containing planes inclined 30° to the chain axis. Quite high temeperatures and long annealing times (190°C, 12 hours) were reportedly required for significant hard segment (MDI/BDO) crystallinity[4]. For the MDI/BDO copolymer T_g is between 109°C[29] and 125°C[54] and T_m is between 225°C to 235°C[29]. Three incomplete X-ray studies of the MDI/BDO hard segment[2,4,23] have been previously reported. Recent studies by Blackwell et al.[63-65], and Hocker and Born[66] (Bayer A.G. Group) have provided much more valuable information in understanding its crystal structure.

Blackwell and Gardner[65] have determined the structure of a model compound, methanol-capped MDI (MeMMe) using single crystal X-ray method. Assuming that the MeMMe conformation is retained in the polymer, and that the butanediol section is a planar zigzag, they were able to predict the structure of the hard segment, as shown in Figure 7. The predicted unit cell is triclinic with dimensions a=5.2 Å, b=4.8 Å, c=35.0 Å, α=115°, β=121°, and γ=85°, and space group P1. Figure 8 shows the packing of the chains and interurethane hydrogen bonding viewed along the a axis of the unit cell.

Hocker and Born[66] reported that MeMMe can also occur in a second form of crystal structure (Modification II)

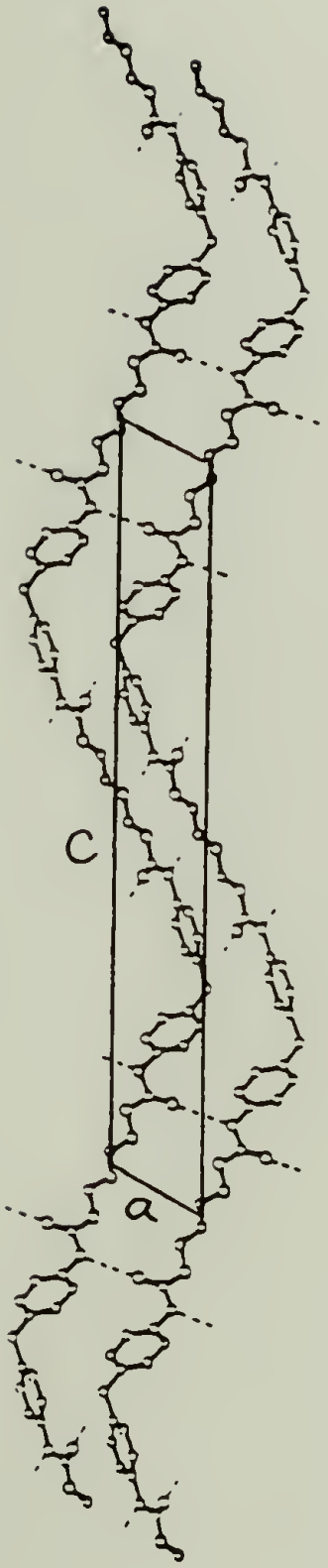

Figure 7. Proposed structure of MDI/BDO copolymer: ac projection (J. Blackwell and K. Gardner[65]).

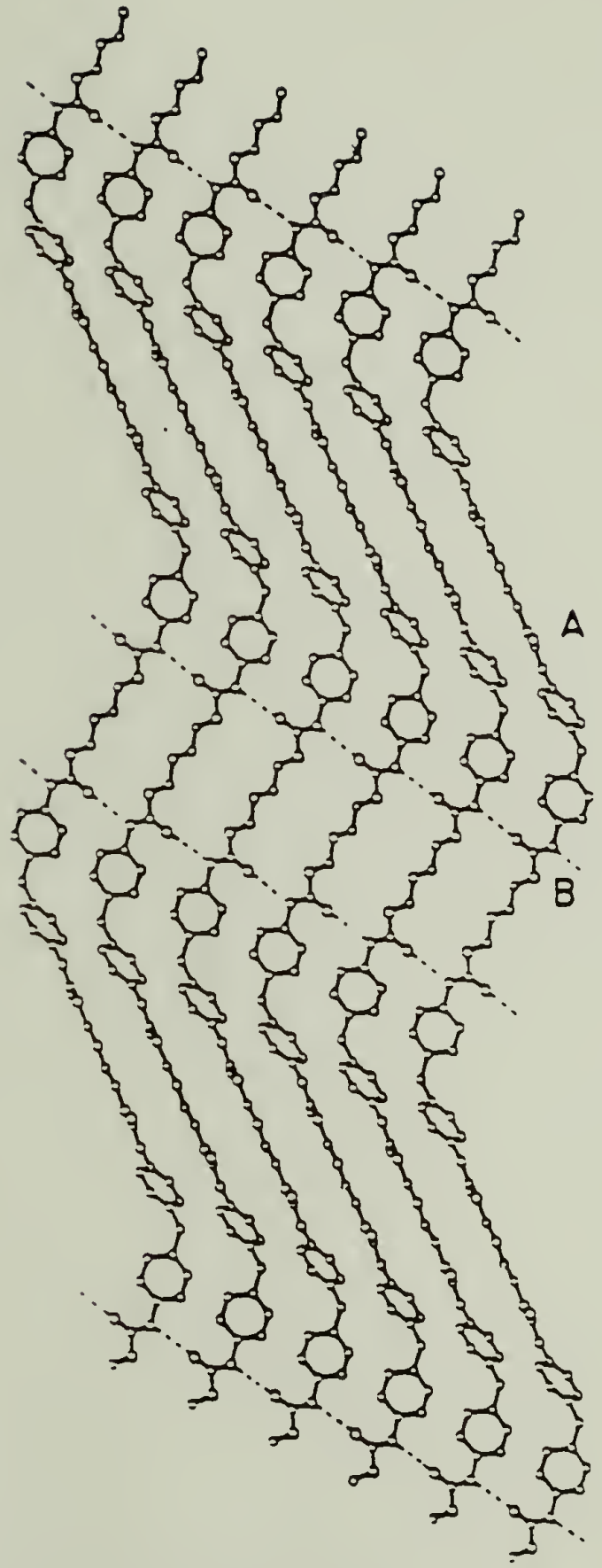

Figure 8. Proposed MDI/BDO crystal structure and interurethane hydrogen bonding viewed along the a axis of the unit cell (J. Blackwell and K. Gardner[65]).

which differs by the type of the hydrogen bridge linkage. They found that modification II has an orthorhombic unit cell with the dimensions a=8.167 Å, b=16.536 Å, and c=11.563 Å. The space group is Aba2 and the unit cell contains four molecules. Figure 9 shows an ab projection of modification II. Above the molecular layer shown in Figure 9, there is a second layer of identical structure. However, this layer is shifted in b direction by half the lattice dimension with respect to the layer lying underneath. The distance between the layers equals half the c dimension. No hydrogen bridge linkages exist between the two layers.

The soft segment of PPO-EO/MDI is thought to be noncrystalline but that of PCP/MDI is crystalline[52]. The PPO-EO/MDI/BDO and PCP/MDI/BDO series have been previously studied by means of DSC and mechanical testing by Zdrahala[30], Critchfield[55] and Chang and Thomas[67].

2.4 Block Length Distribution

Normally polyurethanes are assumed to have a random block size distribution. The distribution will have significant effect on both crystallinity and phase separation of the polymer. If some minimum hard segment length is required for either phase separation and/or crystallization, knowledge of the type of hard segment

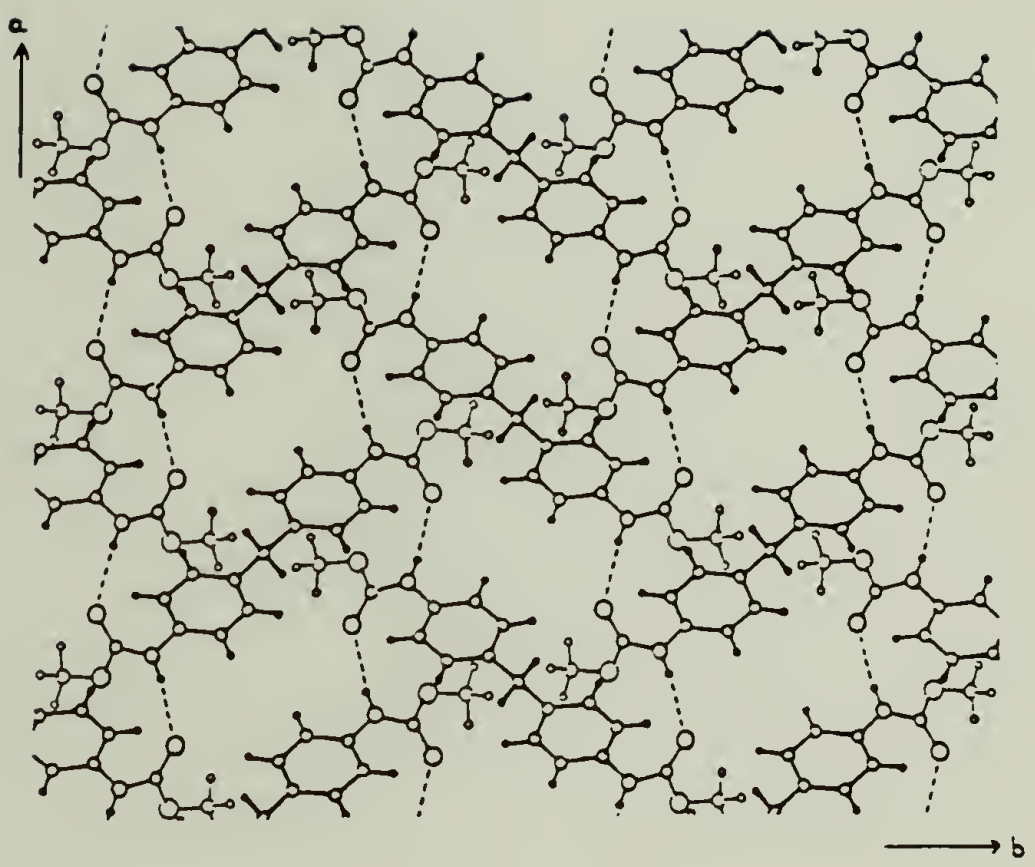

Figure 9. Crystal structure of MeMMe modification II: projection along c axis. The bonding lines are thicker in those areas where the molecule rises above the plane of observation. Hydrogen bridge linkages are indicated by hatched lines (J. Hocker[66]).

block length distribution will give an indication of the weight and volume fraction and the size of hard segment domains expected in the polymer. It is therefore of importance to understand the block distribution in such systems.

The block length distribution in multiblock copolymers has been investigated theoretically by Frensdorff[10] and Peebles[11]. Frensdorff's study was directed at determining the amount of polymer which can undergo phase separation (and hence provide mechanical reinforcement) by calculating the weight fraction of chains containing blocks greater than some minimum block size. Cella[12] employed Frensdorff's method to calculate both the integral and differential hard segment block length distribution for segmented polyester thermoplastic elastomers.

Peebles[11] has developed the weight fraction distribution for polyurethanes as a function of the length of the hard segment sequence for a variety of polymerization conditions. As the hard segment content increases (increasing concentration of diisocyanate and diol), the number of long hard segment blocks slowly increases, but the distribution is very broad--suggesting that if phase separation occurs by the association of hard segments of approximately the same size, a large variation in domain size may be expected.

2.5 Domains and Spherulites

Direct TEM studies of domain structures in polyurethanes have been limited to solution cast thin films[1,36,39,51]. Although solution cast thin films provide an easy way to examine the sample under TEM observation, they cannot represent the original structure of the sample. No distinct micelle-lamellae platelets as suggested by the schematic models in Figures 1 to 5, have yet been observed in the urethane systems thus studied. Instead, the domain structures which have been observed generally appear as isolated equiaxed grains 30-500Å in diameter[1,36,39,51]. Randomly oriented fibrils with lateral dimensions of 300-600Å have been observed in a polyether/MDI/BDO system[2,13]. It remains to be seen what relation the equiaxed grains (domains) and the fibrils observed by transmission electron microscopy have with the micelle-lamellae structures inferred from WAXS and SAXS[23,37].

Several SAXS studies on MDI/BDO based polyurethanes have shown a discrete small angle maximum in the 200Å range[2,23,37,40]. This maximum has been attributed to the average center-to-center spacing of the hard segment domains. One would expect a systematic variation in the position of this maximum with composition but this has not always been observed[2,23]. The influence of soft segment

hydrogen bond ability and hard segment block size on the phase separation have been clearly shown in SAXS studies. For the same molecular weight polyol ($\overline{M}n$=1,000), the 1/2/1 polyester/MDI/BDO system was single phased (i.e., compatible) whereas the 1/2/1 polyether/MDI/BDO system was phase separated[40].

In addition to microphase structures, several polyurethane systems[1,7,9,10,11] (see Table 1) have exhibited spherulitic superstructure. These spherulitic superstructures were investigated by polarized light microscopy[2,37-39], SALS[37,38,43,49], SEM[37,43,49], and TEM[2,49,68]. It is clear that some polyurethane systems have the ability to form spherulitic superstructures depending on composition and method of preparation.

In summary, although polyurethanes are thought to be phase separated into domain structures, most experimental "proof" is based on the existence of a SAXS peak and on TEM observation of granularity in solution cast thin films. Because of complexity of random block copolymers, one can usually assume a random two phase model and calculate the correlation length and infer a domain size. However, there is very likely a broad distribution of domain size and interfacial mixing region can exist. Therefore, the value calculated from SAXS is only a comparative, average value.

TEM provides a good experimental technique to observe

the domain structure directly. All previous reports of TEM studies on domain structure of polyurethane were based on observation of stained or unstained solution cast thin films. Thomas and Roche[69,70] have pointed out that the imaging of fine scale polymer microstructure is greatly influenced by the microscope transfer function. To decide whether the observed image features are related to real domains in the object or are simply due to the microscope spatial frequency filtering of a homogeneous random array of scatters is quite problematic since images of completely different object models are qualitatively indistinguishable[70]. Irregular domain structures, such as a random array of hard segment domains, it is not possible to reliably reconstruct the projected potential variations of the object. Even if the imaging system were perfect, it would be difficult, unless the domain size is of the order of the film thickness, to determine the true object structure from the recorded image since the image is a two Previous bright field images of "supposed" domain structures in unstained polymer films are suggested to be essentially filtered noise. The actual polymer specimen may indeed possess a distinct domain micromorphology but the bright field electron micrographs thus published are totally misleading and contain no reliable information on the actual micromorphology. For this reason, it is better if possible to employ scattering contrast to image small

scale domain structures. For polymer systems containing ordered domains this would indicate dark field imaging and for microphase separated multicomponent polymer systems, heavy atom staining. The PPO-EO/MDI/BEDO urethane system has recently been successfully investigated in this laboratory with the latter technique[68] (solution cast thin film stained with OsO_4). It would be quite useful to unambiguously image hard segment domains in the as-reacted polymer by a direct observation of a heavy atomic number stained, microtomed ultra-thin film. For domains on the order of 100 Å in size, thin section of less than 500 Å thick is needed. This is an extremely difficult experiment to do, but image interpretation should be reliable.

Spherulitic superstructure is only present in segmented polyurethanes which have crystalline hard segments. Two models have been proposed by Samuels[49] to account for spherulitic structure formation. They only differ by the chain orientation: tangential or radial ashard segments crystallize radially or tangentially (as seen in Figure 4).

One other unusual and interesting feature is the occurrence of the globular structure in some polyurethane systems, which were recently reported in a RIM urethane study from this laboratory[68]. These globules are presently explained only as glassy hard segment-rich

regions. It will be shown in the subsequent chapters that this kind of globular structure is very commonly seen in both the PCP/MDI/BDO and PPO-EO/MDI/BDO systems. The detailed characterization and interpretation of this globular structure will be given in the text.

C H A P T E R III

EXPERIMENTAL

In this chapter we describe the composition and molecular structure of the materials. Specimen preparation and various experimental techniques are also discussed.

3.1 Experimental Materials

There are three main series of segmented polyurethane samples used in this study. They are based on PPO-EO/MDI/BDO, PPO-EO/MDI/BEDO and PCP/MDI/BDO. Also included for comparison are MDI/BEDO, MDI/BDO and PPO-EO/MDI regular alternating copolymers. All samples were made available by the Union Carbide Company. The soft segments are based on polyether diol (PPO-EO of $\overline{M}n$=2,000, which contains 30.4 wt. percent oxyethylene as an end block on polyoxypropylene with 83 percent primary hydroxyls and a functionality of 1.964) or polyester diol (PCP of $\overline{M}n$=2,000). The elastomers represent a series in which hardness (modulus) is increased by fixing the molecular weight of the soft segment (polyether or polyester) and adding more MDI and BDO/or BEDO. Table 2 shows the chemical compositions of the polyurethanes studied. The preparation and physical properties of PPO-EO/MDI/BDO series has been published by

TABLE 2

COMPOSITIONS OF THE POLYURETHANES STUDIED

SERIES 1*

SAMPLE DESIGNATION	PPO-EO/MDI/BDO MOLE RATIO	WT. FRACTION HARD SEGMENT**
A/B-I	1/1.7/0.7	10
A/B-II	1/2.8/1.8	21
A/B-III	1/4.2/3.2	33
A/B-IV	1/6.1/5.1	44
A/B-V	1/9.1/8.1	55
A/B-VI	1/14.0/13.0	66
A/B-VII	1/23.8/22.8	78

SERIES 2

SAMPLE DESIGNATION	PPO-EO/MDI/BEDO MOLE RATIO	WT. FRACTION HARD SEGMENT**
BEDO-I	1/1.74/0.74	10
BEDO-II	1/6.18/5.18	44
BEDO-III	1/23.9/22.9	78

SERIES 3

SAMPLE DESIGNATION	PCP/MDI/BDO MOLE RATIO	WT. FRACTION HARD SEGMENT**
PCL-121	1/2/1	13
PCL-132	1/3/2	23
PCL-143	1/4/3	31
PCL-154	1/5/4	38
PCL-165	1/6/5	43

*SERIES 1 CONSISTS OF 100°C (A SERIES) AND 175°C (B SERIES) CURE SAMPLES

**CALCULATION OF WEIGHT FRACTION HARD SEGMENT BASED ON 1/L/M (MOLE RATIO PPO-EO/MDI/BDO) IS
M(250+90)/(2000+L(250)+M(90))

Zdrahala et al.[30] and that of PCP/MDI/BDO series by Seefried et al.[54]

The soft segment based on polyether polyol (PPO-EO) has the structure of:

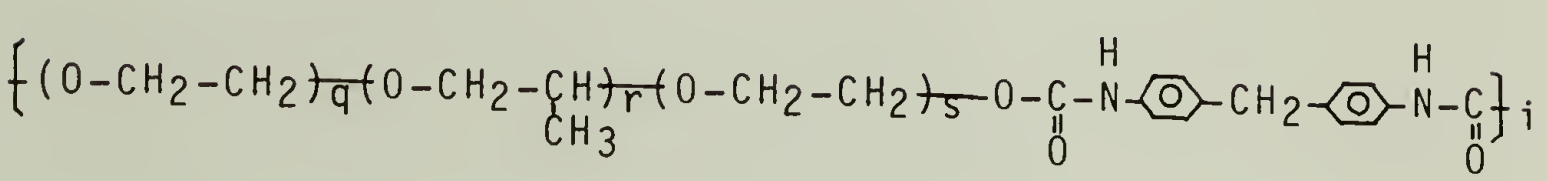

~200Å

where q+s≈14, r≈24 and that based on polyester polyol has the structure of:

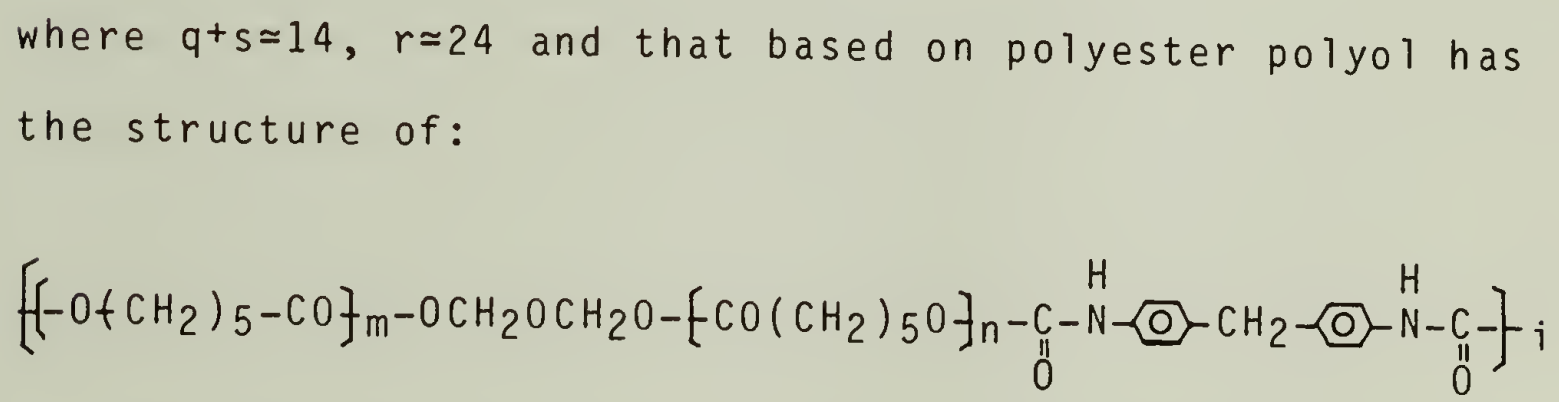

~180Å

where m+n≈17.

The hard segment sequences $(MDI/BEDO)_j$;or $(MDI/BDO)_j$, have the following structure:

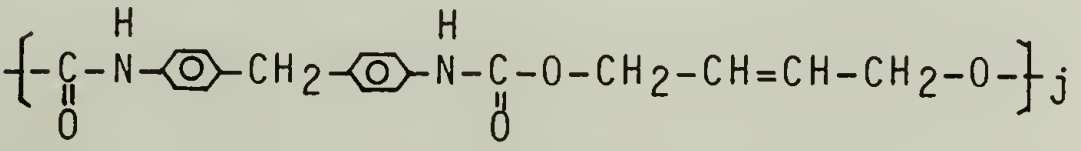

~20.5Å

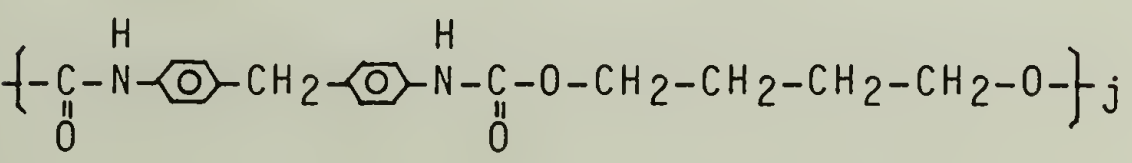

All polyurethane samples were batch* polymerized in sheet form (3 mm thick). MDI/BEDO and MDI/BDO copolymers were supplied in chunk and fibrous form respectively, from solution polymerization. The PPO-EO/MDI/BDO system was prepared with both 100°C and 175°C mold temperatures. The PPO-EO/MDI/BEDO and PCP/MDI/BDO systems were prepared at 100°C and 145°C respectively.

3.2 Experimental Techniques

Differential scanning calorimetry was used to detect transition temperatures, as well as the heat of fusion of the polymers. Wide-angle X-ray scattering and electron diffraction were used to study the crystal structure and crystallinity of the polymers. Small-angle X-ray scattering provided evidence of phase separation and average center-to-center spacing of the hard segment domains. Polarized light microscopy was used to determine the birefringence and existence of spherulitic superstructure. Transmission electron and scanning transmission electron microscopy were used to characterized superstructure (spherulite, ~μm size) and microstructure (domain, ~100 Å size).

---

*Details of the batch polymerization of the urethane elastomer are given in the Appendix.

In order to examine the as-processed samples, the only method is to microtome the samples and observe them directly in the microscope. Other methods such as solution cast thin films and hot-pressed films do not preserve the original morphology although they offer a much easier way to prepare thin films. The most important job is to get good microscopy specimens--ultra-thin and uniform. One must devote much time to master this art!

A. Differential scanning calorimetry (DSC). A Perkin-Elmer DSC II was used to characterize the thermal properties of polyurethane elastomers. The temperature scale and the energy input of the DSC were calibrated with the melting transition and heat of fusion of an Indium standard. DSC scans of all samples were carried out starting from ambient temperature at heating rate of 20°C/min in the range of 5 mcal/sec. Sample size was approximately 10 to 20 mg. The areas under the endothermic peaks were measured by area weighting method. The glass transition temperature was defined as the temperature at which the specific heat reached a value midway between the specific heats corresponding to those of the glass and liquid.

B. Polarized light microscopy. Microtomed sections of ~5 μm thick were observed directly on the glass slide

using a Leitz polarized light optical microscope. Photomicrographs were taken with and without crossed polarizers. Birefringence of the polymer was easily checked by crossed polarizer method. We also used 1/4 λ plate method (Carl Zeiss optical microscope) to determine the sign of birefringence (+ or -) of the shperulites (if any) present. A Mettler hot-stage was used to check the melt transition temperature and to follow annealing and recrystallization kinetics.

C. Electron Microscopy. A JEOL 100 CX electron microscope was used to conduct TEM, STEM and electron diffraction experiments. This electron microscope is equipped with a double tilt ± 60° side entry goniometer stage and has high resolution (3.4 Å in the TEM mode and 15 Å in the STEM mode). A clean high vacuum of about 10^{-6} torr is obtained in the specimen chamber with the contamination rate below 1 Å/min obtainable with a liquid N_2 anticontamination trap.

i. Transmission electron microscopy (TEM). TEM was done at 100 Kv with magnifications of 250x to 30,000x. Specimens were directly observed on a copper grid of 200 or 300 mesh. In order to get better contrast in the bright field images, 40 μm and 60 μm diameter objective apertures were used. To observe large spherulitic superstructure, low magnifications of 250x - 750x were

necessary and were used with no objective aperture but with selected area diffraction apertures 80μm or 20μm diameter to enhance contrast.

ii. Scanning transmission electron microscopy (STEM). A scanning electron microscope image formed with the transmitted electrons as the signal (called the STEM image) has been suggested to have an advantage over conventional transmission electron microscopy (CTEM) for two principal reasons: 1) the collection efficiency of scattered electrons is higher for STEM than for CTEM (which results in high S/N ratios in the image for a given incident electron dose -- or equivalently a reduced specimen dose is possible for the same quality image) and 2) microarea diffraction patterns may be obtained without cumulative radiation damage to adjacent areas.

iii. Electron diffraction. Selected area diffraction (SAD) was used to obtain electron diffraction patterns. Because the polymer samples were extremely sensitive to radiation damage, we used condenser lens spot size (No. 3) to obtain minimum dose electron diffraction patterns.

iv. Radiation damage problem. Electron beam damage occurs in crystalline polymers by ionization of main chain atoms and subsequent crosslinking of chains or chain scission. These effects alter the crystal lattice and the morphology of the specimen. The radiation damage can be

reduced by cooling the specimen and working with low electron dose rates. No low temperature stage was available for our study. Fresh (previously unirradiated) areas were always employed for diffraction work after electron optical adjustments were made on a given (beam damaged) area.

D. Cryo ultramicrotomy. A Sorvall MT2-B Porter-Blum ultramicrotome with frozen thin sectioning attachment was used. The cryo sectioning attachment has the feature of insulated knife stage with position controls, liquid nitrogen reservoir, sample holder, temperature sensor and control unit. A Du Pont diamond knife (with fixed boat) was used. Polymers were embedded in cylindrical epoxy with a 2-3 mm protruding length. Such samples can be microtomed at low temperature. All microtoming was done in the temperature range of -60°C to -70°C. Both dry knife and wet knife (for which the trough is filled with propyl alcohol for floating sections) techniques were applied. Thicker sections (~5 μm) were picked up on glass slides for optical microscopy observation. Thinner sections (less than 1,000 Å thick) were picked by 300 or 400 mesh copper grids, and used for E.M. study.

Because of intrinsic difficulty of obtaining very thin microtomed sections of these elastomers, every specimen has to be checked under TEM observation to know if the

section is thin enough for TEM study.

E. OsO_4 staining. Double bond containing bulk samples (BEDO-I, BEDO-II, BEDO-II'(annealed) and BEDO-III) embedded in epoxy as described earlier were exposed to OsO_4 aqueous solution (2 percent by wt.) vapors for 6-8 hours inside a desiccator. The samples appeared darker after exposure to the OsO_4 solution vapor. Samples BEDO-I, BEDO-II and BEDO-II' were darkened completely inside and out, while sample BEDO-III was darkened in the outer layer only. These embedded, stained samples were then cryo ultramicrotomed under conditions mentioned previously.

F. Hot-pressing. Series A 100°C cure PPO-EO/MDI/BDO polyurethane samples were hot-pressed in a mold at 15,000 psi at pre-set temperatures for 15 minutes and cooled slowly in the press under pressure. It took about 5 to 6 hours for samples to cool to room temperature. The dimension of the mold used was 1 mm thick with 1 cm in width and 3 cm in length. In order to prevent degradationdue to heat induced oxidation, the mold was made by cutting 1 cm x 3 cm hole in the middle of 15 cm x 15 cm copper plate (1 mm thick) and then sandwiched between two steel plates. And the heating temperatures were so chosen that they corresponded to lower melting

peaks in the DSC experiment. Table 3 gives the hot-pressing temperatures for each sample.

TABLE 3

HOT-PRESSING TEMPERATURES FOR 100°C CURE

PPO-EO/MDI/BDO SAMPLES

Sample Designation	Hot Pressing Temperature °C
A-I	153
A-II	156
A-III	192
A-IV	195
A-V	200
A-VI	195
A-VIII	195

G. Wide-angle X-ray scattering (WAXS). Wide-angle x-ray scattering studies were done on the Siemens diffractometer of Chemical Engineering Department of the University of Minnesota. A Siemens X-ray tube operated at 40 KV and 30 mA provided CuKα radiation at λ=1.542 Å. Divergence slits were set at 0.3°, and the receiving and monochromater slit at 0.15°. The signal was recorded vs. diffraction angle at the rate of 1°/min. WAXS patterns were obtained to determine relative crystallinity of the samples as a

function of hard segment content and processing/annealing conditions.

H. Small-angle X-ray scattering (SAXS). Small-angle X-ray scattering experiment on all samples was done at the National Center for Small-Angle Scattering Research (NCSASR), located at the Oak Ridge National Laboratory, using the 10-meter small-angle X-ray scattering camera.

The NCSASR 10-meter X-ray facility utilizes a rotating anode X-ray source, crystal monochromator, pinhole collimation, a two-dimensional position-sensitive detector, and computer controlled data acquisition. Using the computer programs available at the NCSASR facility, two-dimensional contour plots of scattered intensity were obtained, and radial average intensity vs. scattering angle data, $I(2\theta)$, were determined.

If we assume a system comprised of evenly distributed electron densities (ρ_S and ρ_H) in two phases separated by sharp boundaries, the mean squared electron density fluctuation $\overline{\Delta\eta^2}$ can be written

$$\overline{\Delta\eta^2} = \overline{(\rho-\bar{\rho})^2} = \phi_S\,(\rho_S-\bar{\rho})^2 + \phi_H\,(\rho_H-\bar{\rho})^2$$

where $\bar{\rho} = \phi_S\rho_S + \phi_H\rho_H$, $\phi_S + \phi_H = 1.0$, and ϕ_S, ϕ_H are the volume fractions of material in each of the phases. Combining the above three equations and

rearranging leads to the well known relation

$$\overline{\Delta\eta}^2 = \phi_S\phi_H\,(\rho_S-\rho_H)^2 \qquad (*)$$

If ρ_S and ρ_H are known (e.g., if the phases were pure soft segment and pure hard segment) then the experimentally measured $\overline{\Delta\eta^2}$ can be used to determine the volume fraction of each phase. If however, some mixing occurs, then ρ_S and ρ_H are not known and one cannot extract the volume fraction of the phases.

If Porod's law[71] is obeyed by the two phase system so that the invariant $\overline{(\Delta\eta)^2}$ can be properly evaluated by equation (*) then following the treatment of Debye[72], Porod[71] and Kratky[73] one can calculate the so-called correlation distance l_c. The transversal and inhomogeneity lengths l_s and l_H which are measures of the size of the domains are given by $l_s = l_c/\phi_H$ and $l_H = l_c/\phi_s$.

C H A P T E R IV

RESULTS FOR 100°C CURE PPO-EO/MDI/BDO SERIES

Most previous work[4,14,15,36,74-76] on microstructure-property relations for polyurethanes has concentrated on the nature of hard segment and soft segment microphase separation. While spherulitic superstructure has been occasionally observed for crystalline hard segment materials[2,22,37,38,49,77], most authors have sought to interpret physical property data in terms of microdomains. In particular the extension of the plateau shear modulus to higher temperatures is thought to arise from the physical crosslinking effect of the hard segment domains. In a previous paper the existence of several scales of heterogenities as well as significant skin/core regions occurring in a reaction injection molded (RIM) polyurethane were noted[22]. Because of the fast exothermic urethane reaction, large temperature gradients occur across the mold, resulting in distinctly different skin region/core region microstructures. Two scales of structural organization were observed: (i) on the order of tens of microns, corresponding to hard segment-rich globules (HSG) and hard segment-rich spherulites (HSS) and (ii) on the order of one hundred angstroms, associated with hard segment-rich fibrils (HSF). The globules, a new

morphological feature in polyurethanes were preferrably present near the mold surface and were proposed to be pockets of glassy hard segment-rich material which was unable to crystallize due to low temperature. As part of an effort to better understand RIM polyurethanes, a series of polypropylene oxide endcapped with polyethylene oxide polyol/4,4'-diphenylmethane diisocyanate/1,4-butanediol (PPO-EO/MDI/BDO) polyurethanes (ranging from 10-78 percent by weight hard segment) were prepared by a hand cast procedure. An initial study[30] of tensile and dynamic mechanical properties of this system indicated a change from a soft elastomer (continuous soft phase) to a higher modulus plastic (continuous hard phase) at about 55 percent hard segment content.

Since the catalyst levels used were lower than in RIM, the sample is cured in the mold at 100°C for 16 hours. The PPO-EO soft segment was employed in order to eliminate complications of soft segment crystallinity. To the unaided eye samples up to 55 percent hard segment appeared spatially uniform while samples of 66 percent and 78 percent hard segment had a distinct cross-sectional variation. Detailed optical and electron microscopy studies revealed that all the samples were micro-heterogeneous, consisting of a variety of structures depending on hard segment content and cross-sectional location. The present chapter describes these structures

and suggests possible reasons for their development. The influence of these large scale structures on the mechanical properties of polyurethanes is illustrated.

4.1 Differential Scanning Calorimetry Results

Figure 10 shows DSC scans of the samples in the temperature range from 330°K to 550°K. Sample A-I does not exhibit much evidence of hard segment crystallinity, only a very small exothermic region probably due to induced crystallization during the DSC run followed by a very small endothermic area. Sample A-II shows several melting transitions beginning at about 420°K followed by a small endotherm and re-melting around 495°K. Samples A-III and A-IV have similar transitions to sample A-II though shifted to higher temperatures. For samples A-II to A-IV, increasing the hard segment concentration causes a corresponding increase in the transition peak temperature and crystallinity (heat of fusion). Sample A-V has the highest transition temperature range and heat of fusion. Samples A-VI and A-VII are similar to one another, both having a very pronounced lower temperature transition peak centered at 465°K and a second higher temperature doublet at 490°K and 500°K. The 465°K peak is present only in samples A-VI and A-VII. In general, the transition peaks shift to higher temperatures with

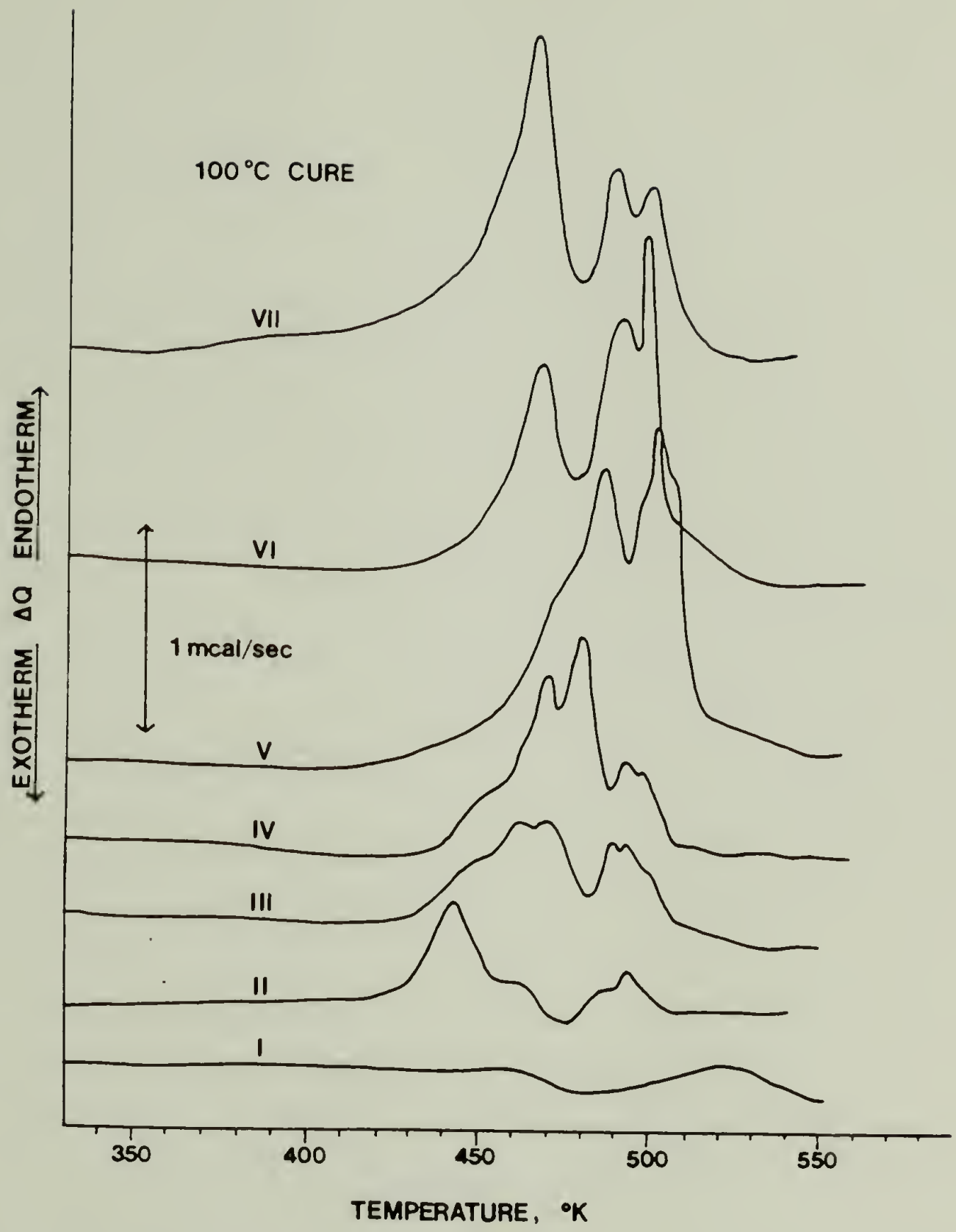

Figure 10. First run DSC scans of samples A-I to A-VII over the temperature range 330-550°K.

increasing hard segment content, reach a maximum at sample A-V and remain about the same for samples A-VI and A-VII. The total heat of fusion and heat of fusion normalized to sample hard segment content are given in Table 4. The heat of fusion per gram polymer and per gram hard segment reach a maximum at sample A-V and then decrease with further increase in hard segment content. Figure 11 shows DSC scans of the skin and core regions of sample A-VI and A-VII. Interestingly, both core portions of the two samples show a prominent low temperature transition peak (centered at ~465°K) while skin portions show prominent high temperature transition peaks (centered at ~490 and ~500°K). DSC results of the skin and core regions of sample A-VI and A-VII are summarized in Table 5. It is noted that the core regions are more crystalline than the skin regions in sample A-VII.

4.2 Optical Microscopy Results

Sample A-I is found to be isotropic with no birefringent regions or spherulites present in crossed polarized light. In partial crossed polarized light approximately 10 micron diameter globules are observed (see Figure 12a). Microtome knife marks can be seen traversing the globules indicating that the globules have a higher modulus than the surrounding soft segment

TABLE 4

SUMMARY OF COMPOSITION AND HEATS OF FUSION
FOR 100°C CURE PPO-EO/MDI/BDO SAMPLES

SAMPLE DESIGNATION	PPO-EO/MDI/BDO MOLE RATIO	VOL. FRACTION INITIAL MIX PPO-EO/MDI/BDO	WT. FRACTION HARD SEGMENT*	DSC (cal/g) POLYMER	DSC (cal/g) HARD SEGMENT*
A-1	1/1.7/0.7	0.80/0.17/0.03	10	~0	~0
A-II	1/2.8/1.8	0.70/0.24/0.06	21	2.4	11.3
A-III	1/4.2/3.2	0.60/0.31/0.09	32	3.8	11.7
A-IV	1/6.1/5.1	0.50/0.38/0.12	43	6.0	13.7
A-V	1/9.1/8.1	0.40/0.45/0.15	55	10.2	18.5
A-VI	1/14.0/13.0	0.30/0.52/0.18	66	9.4	14.2
A-VII	1/23.8/22.8	0.20/0.59/0.21	78	8.8	11.4

TABLE 5

SUMMARY OF DSC RESULTS OF SKIN AND CORE REGIONS
OF SAMPLES A-VI AND A-VII

SAMPLE DESIGNATION		DSC (cal/g) POLYMER	DSC (cal/g) HARD SEGMENT*
A-VI	Skin	10.0	15.1
	Core	9.2	13.9
A-VII	Skin	6.9	8.9
	Core	10.0	12.9

*CALCULATION OF WEIGHT FRACTION HARD SEGMENT BASED ON 1/L/M (MOLE RATIO PPO-EO/MDI/BDO) is M(250+90) / 2000+L(250)+M(90)

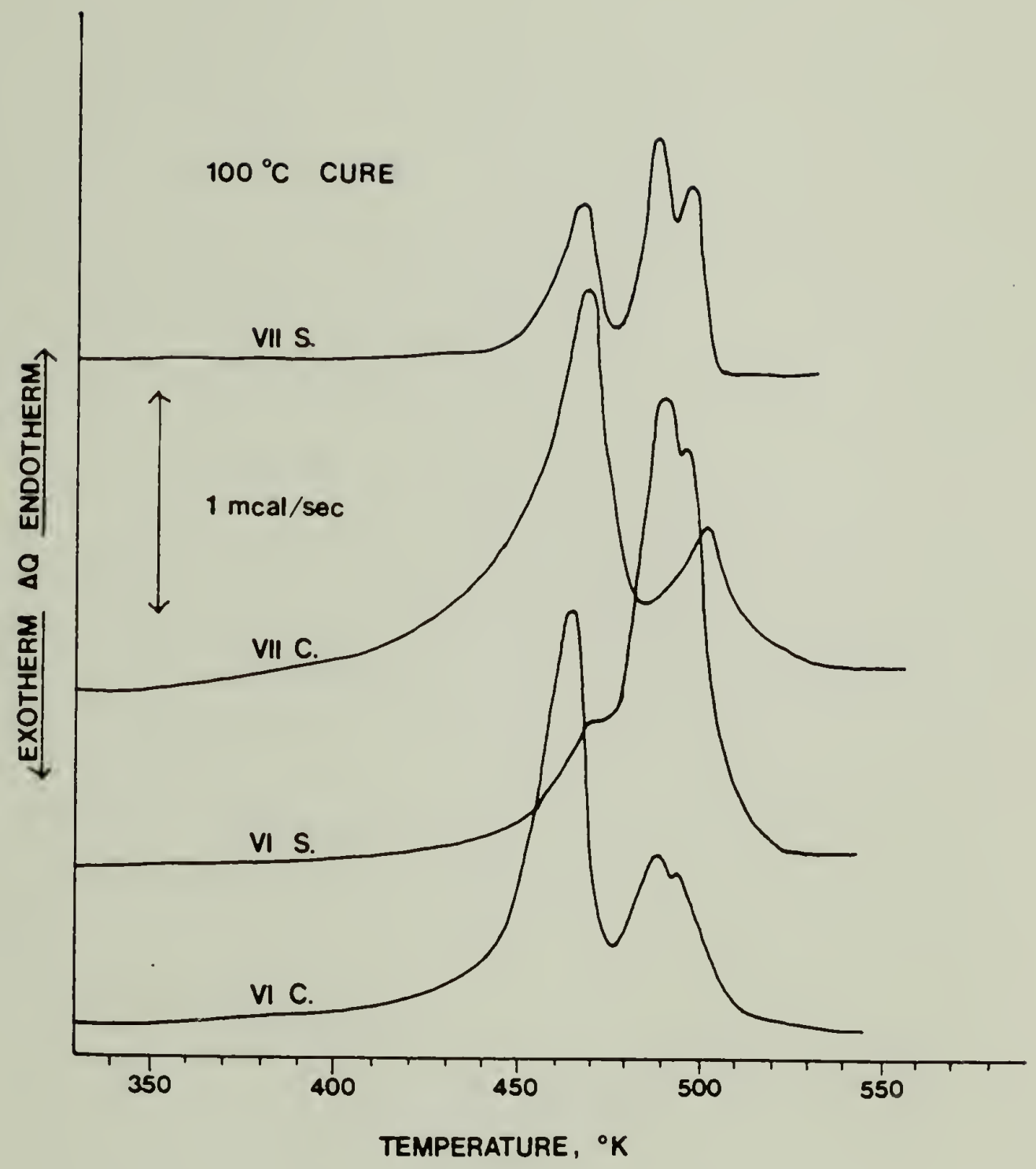

Figure 11. First run DSC scans of skin and core regions of sample A-VII (78 percent hard segment) and sample A-VI (66 percent). Note the prominent lower temperature peak appearing in the core regions.

Figure 12. Micrographs of the globular morphology of sample A-I (10 percent hard segment, same magnification for micrographs a and b): (a) optical micrograph (uncrossed polarizers); (b) and (c) TEM micrographs

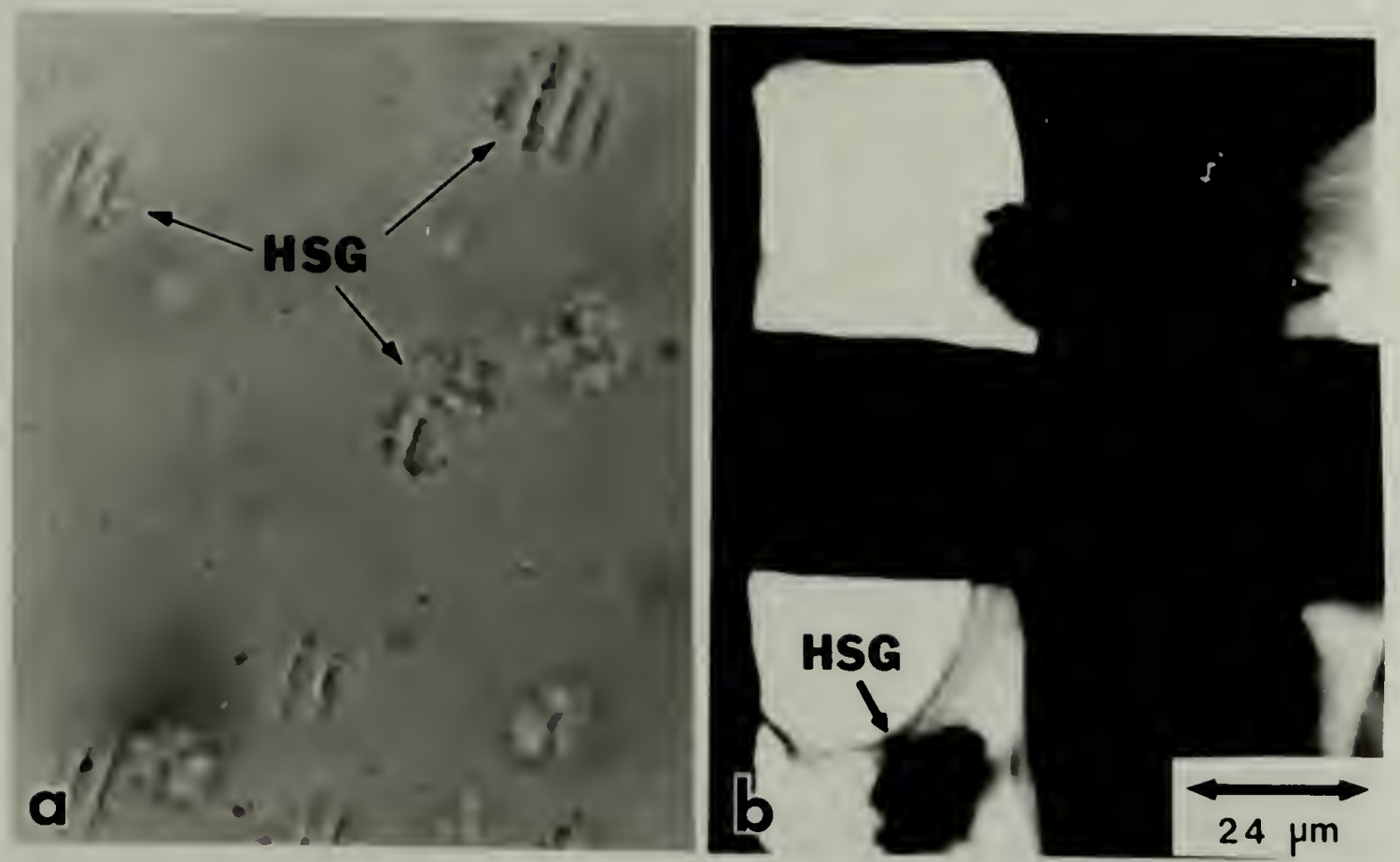

Figure 12

matrix. Sample A-II shows more globules than sample A-I along with very faint areas of birefringence probably corresponding to very small, poorly formed spherulites. Sample A-III is similar to sample A-IV although there are fewer and smaller spherulites. In sample A-IV the spherulites are uniformly distributed across the mold although not volume filling (see Figures 13a and 14). In sample A-V (55 percent hard segment) the spherulites are volume filling across the entire mold (see Figures 13b and 15). There is a slight skin/core variation in sample A-V with the core appearing less birefringent than the skin. This could be due to a higher concentration of globules at the core or incomplete impingement of the spherulites. Samples of hard segment content up to 55 percent are uniform in appearance across the mold to the naked eye. The two highest hard segment urethanes, samples A-VII and A-VI exhibit a positionally dependent morphology. Examination of sample A-VI shows spherulites mainly at the surface with some spherulites present into the core, although they are small and scattered (see Figures 13c and 16). In sample A-VII there are approximately 40 micron diameter spherulites at the surface while the core region appears homogeneous (see Figures 13d and 17). The spherulite size decreases rapidly at about 0.4 mm from the surface.

Figure 13. Low magnification optical micrographs (crossed polarizers), all micrographs are the same magnification: (a) Sample A-IV (43 percent hard segment); (b) Sample A-V (55 percent); (c) Sample A-VI (66 percent); (d) Sample A-VII (78 percent); note prominent skin/core morphology for (c) and (d); spherulite size increases with increasing hard segment.

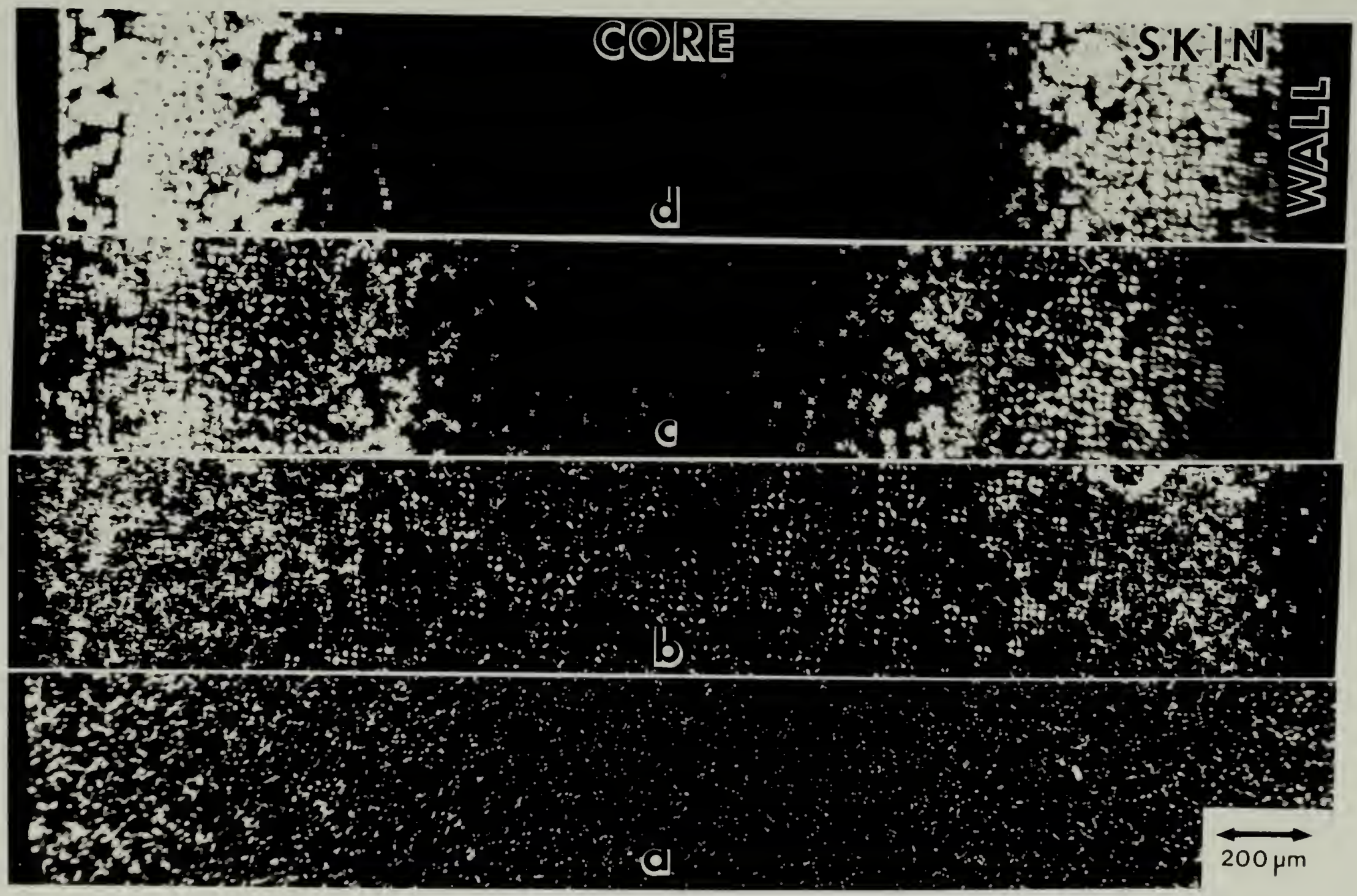

Figure 13

Figure 14. Optical micrograph (crossed polarizers) of sample A-IV (43 percent hard segment).

Figure 15. Optical micrograph (crossed polarizers) of sample A-V (55 percent hard segment) showing β spherulites and spherical non-birefringent regions.

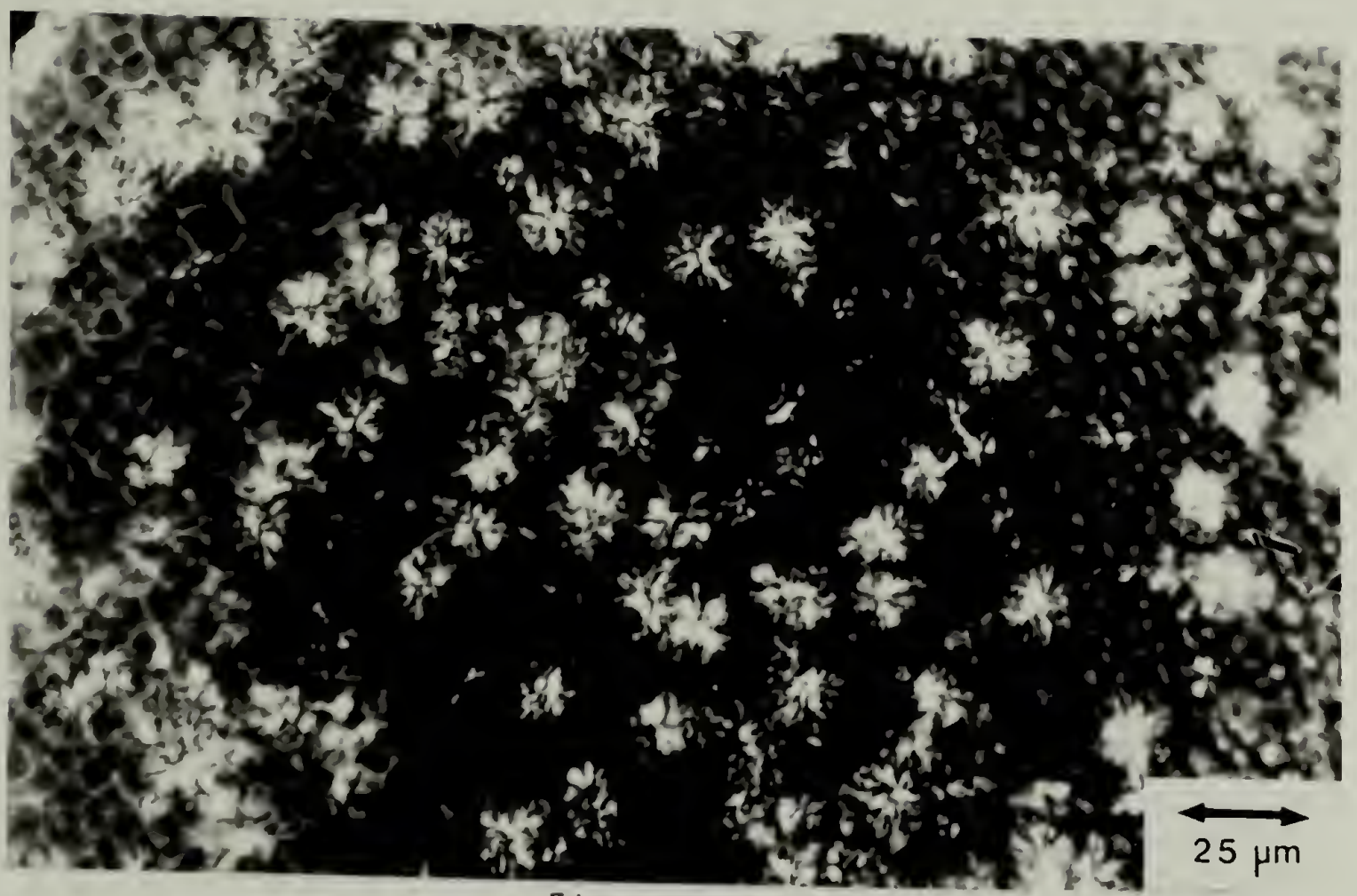

Figure 14

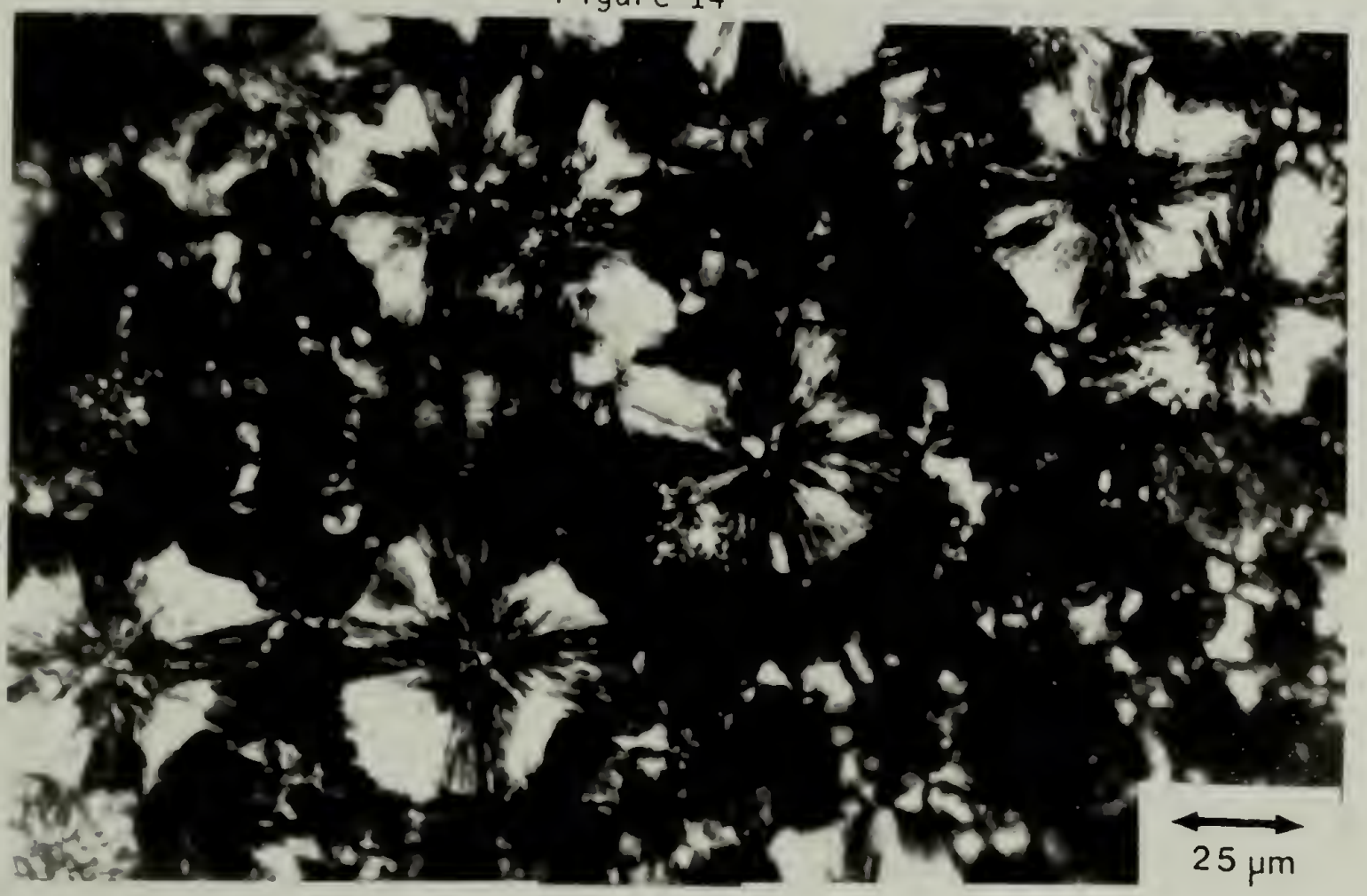

Figure 15

Figure 16. Optical micrograph (crossed polarizers) of skin regions of sample A-VI (66 percent hard segment) showing β spherulites and non-birefringent regions.

Figure 17. Optical micrograph (crossed polarizers) of skin regions of sample A-VII (78 percent hard segment) showing β spherulites and hard segment rich matrix.

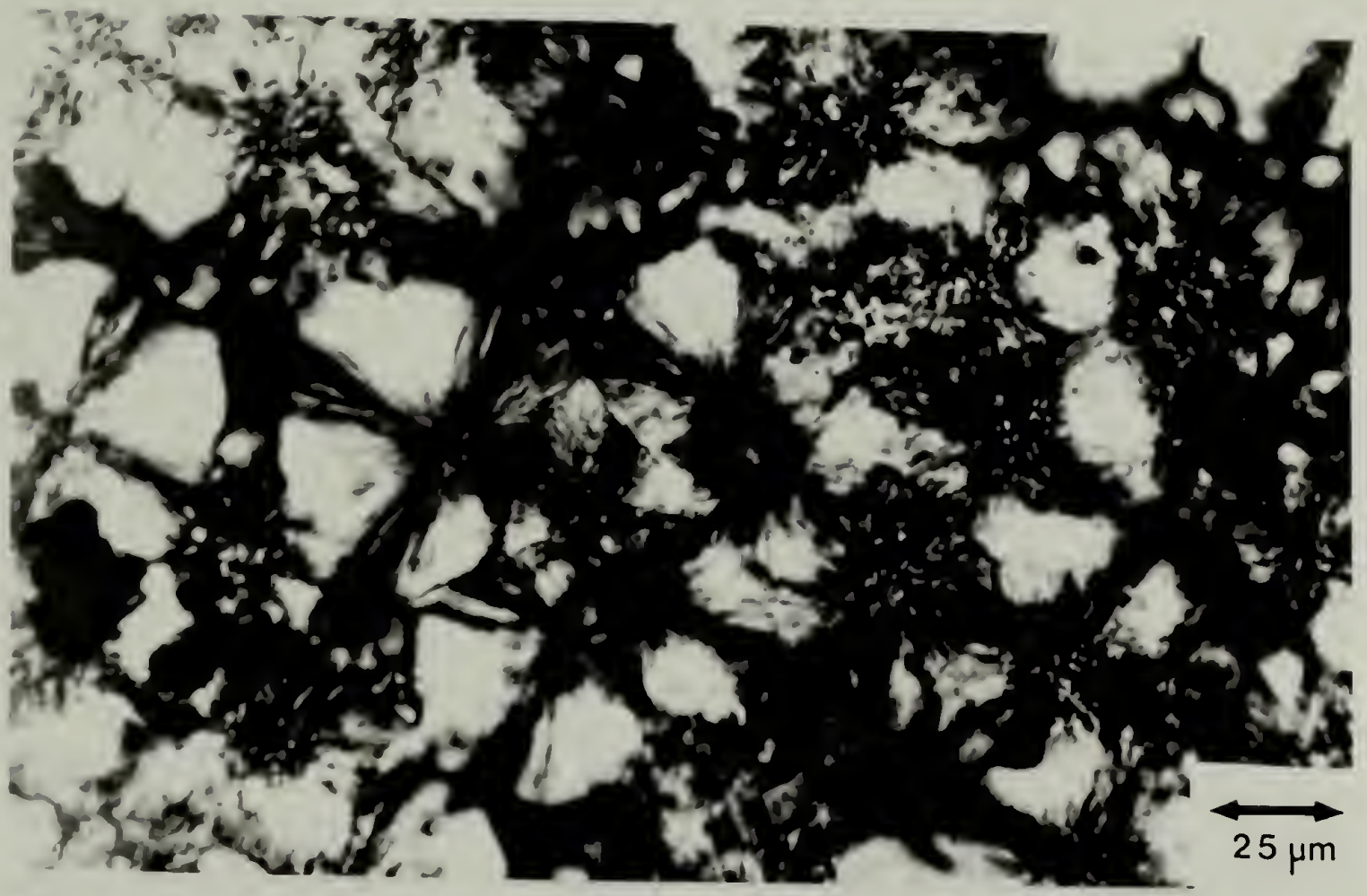

Figure 16

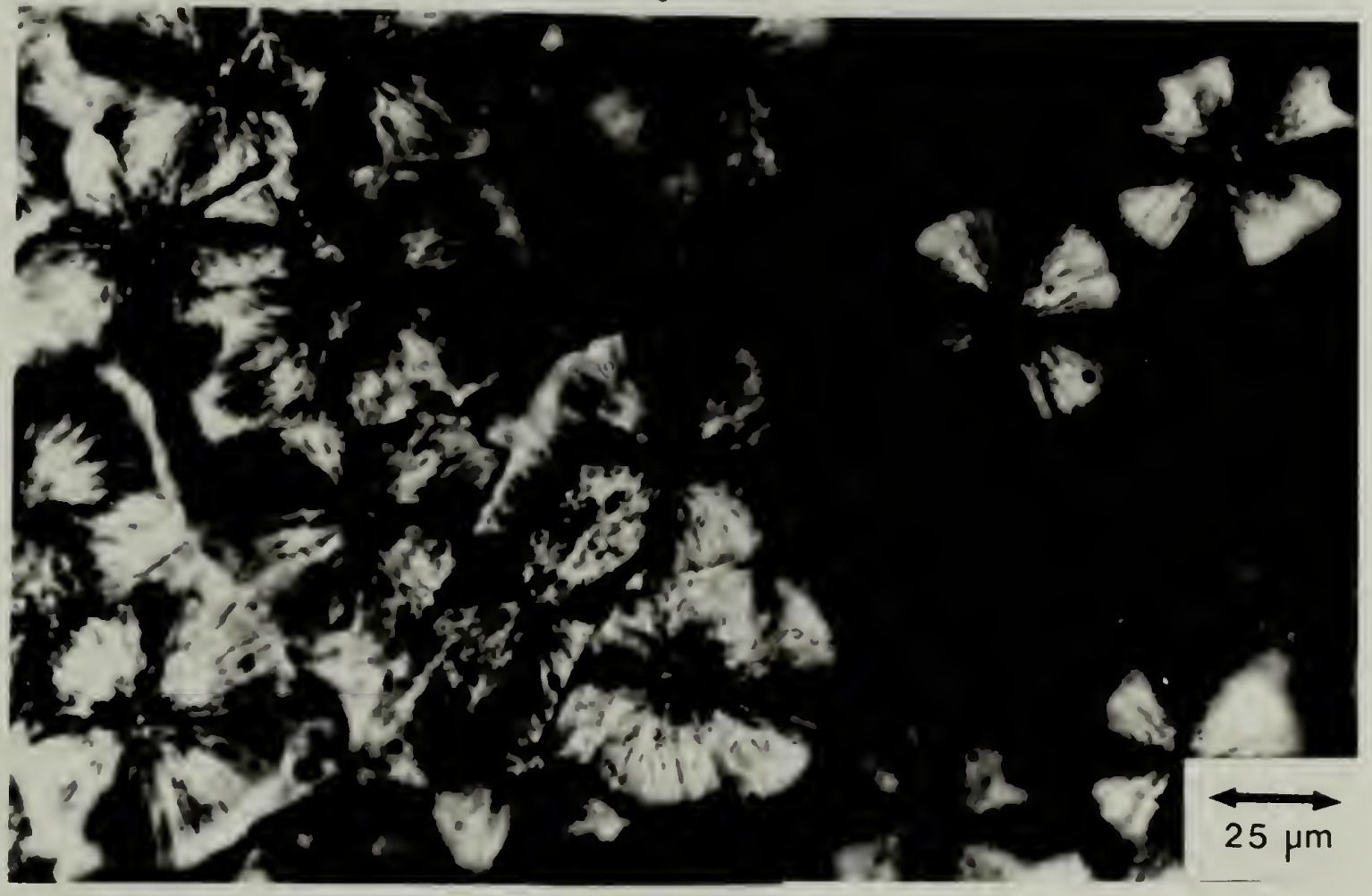

Figure 17

4.3 Transmission Electron Microscopy Results

Of all the experimental tools presently employed, electron microscopy of microtomed sections is the most localized probe of sample microstructure. TEM shows all samples to be heterogeneous at the micron scale and below. Sample A-I of only 10 percent hard segment content displays a few widely separated 10 micron diameter dark spherical regions, resembling previously observed hard segment globules (HSG) (see Figure 12b)[22]. At higher magnification (see Figure 12c), the hard segment globule seems to be composed of several smaller, irregular shape electron dense dark regions. In general, these hard segment globules are featureless and not spherulitic in nature, and are proposed to be glassy hard segment rich regions. Sample A-II has similar globules though they are larger and more numerous (see Figures 18a and 18b). The globules are embedded in a featureless, predominantly soft segment-rich matrix (SSM). Samples A-III and A-IV show an increasing volume fraction of similar globules as well as dark, radial, fibrillar hard segment-rich spherulites (HSS) in a lighter, featureless soft segment-rich matrix (see Figures 19a, 19b and 20a, 20b respectively). Note that many spherulites nucleated from the edge of hard segment globules as indicated by arrows in the figures.

Figures 18a and 18b. TEM micrographs of sample A-II (21 percent hard segment) showing the presence of hard segment-rich globules (HSG) and soft segment-rich matrix (SSM).

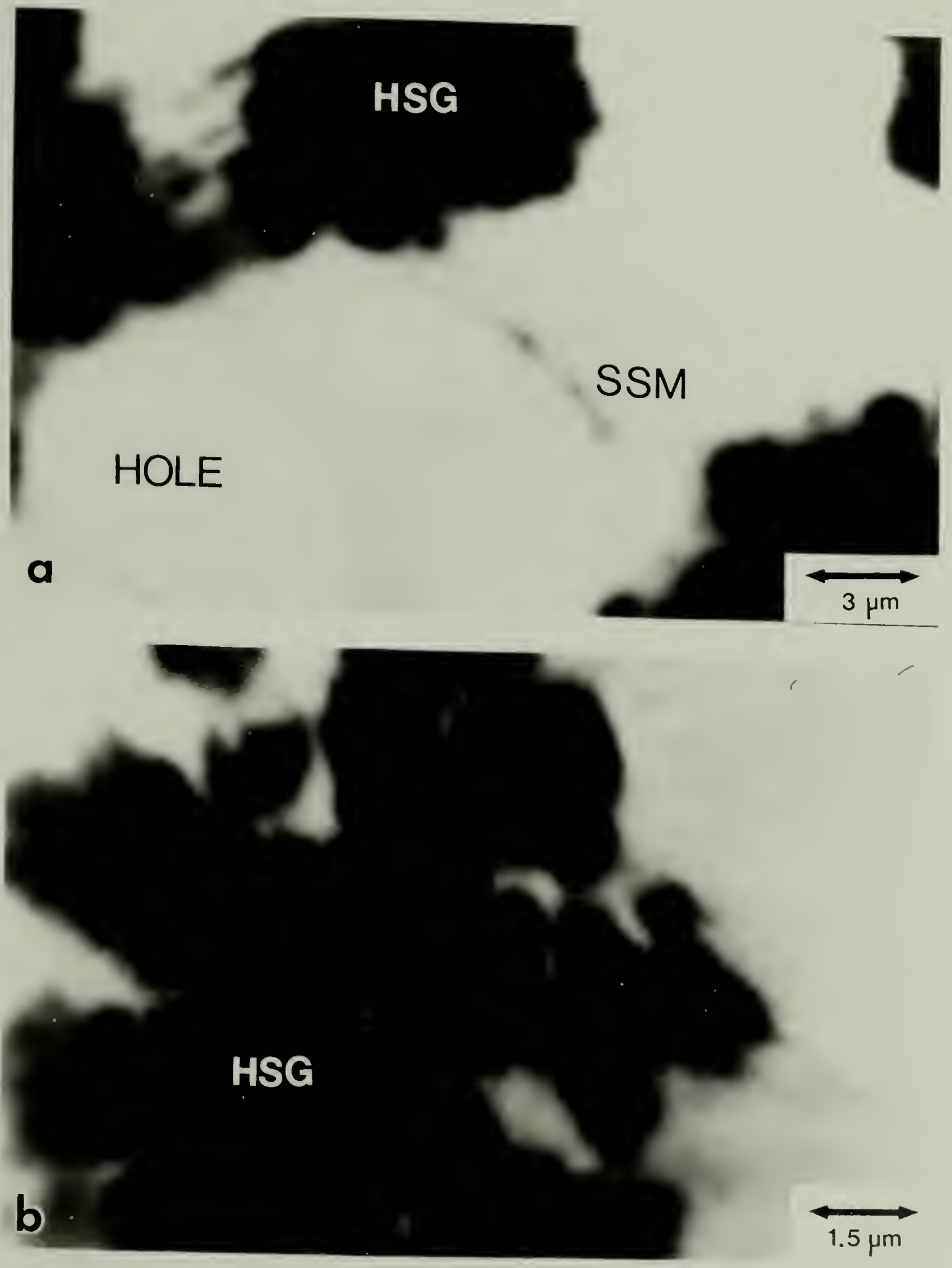

Figure 18

Figures 19a and 19b. TEM micrographs of sample A-III (32 percent hard segment). The presence of hard segment-rich spherulites (HSS, poorly formed) is first cited. Note spherulites nucleated from the edge of hard segment rich globules as indicated by arrows.

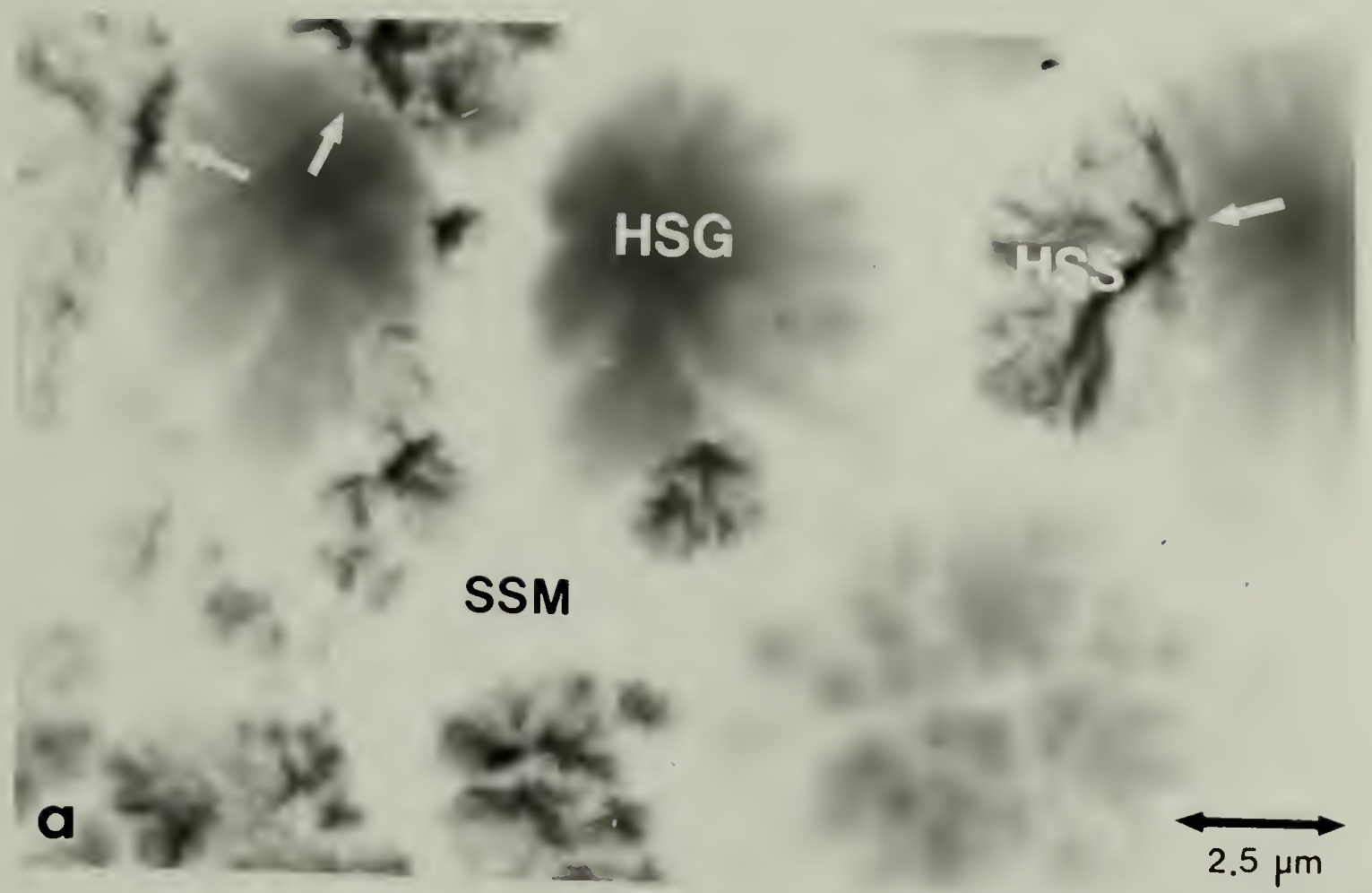

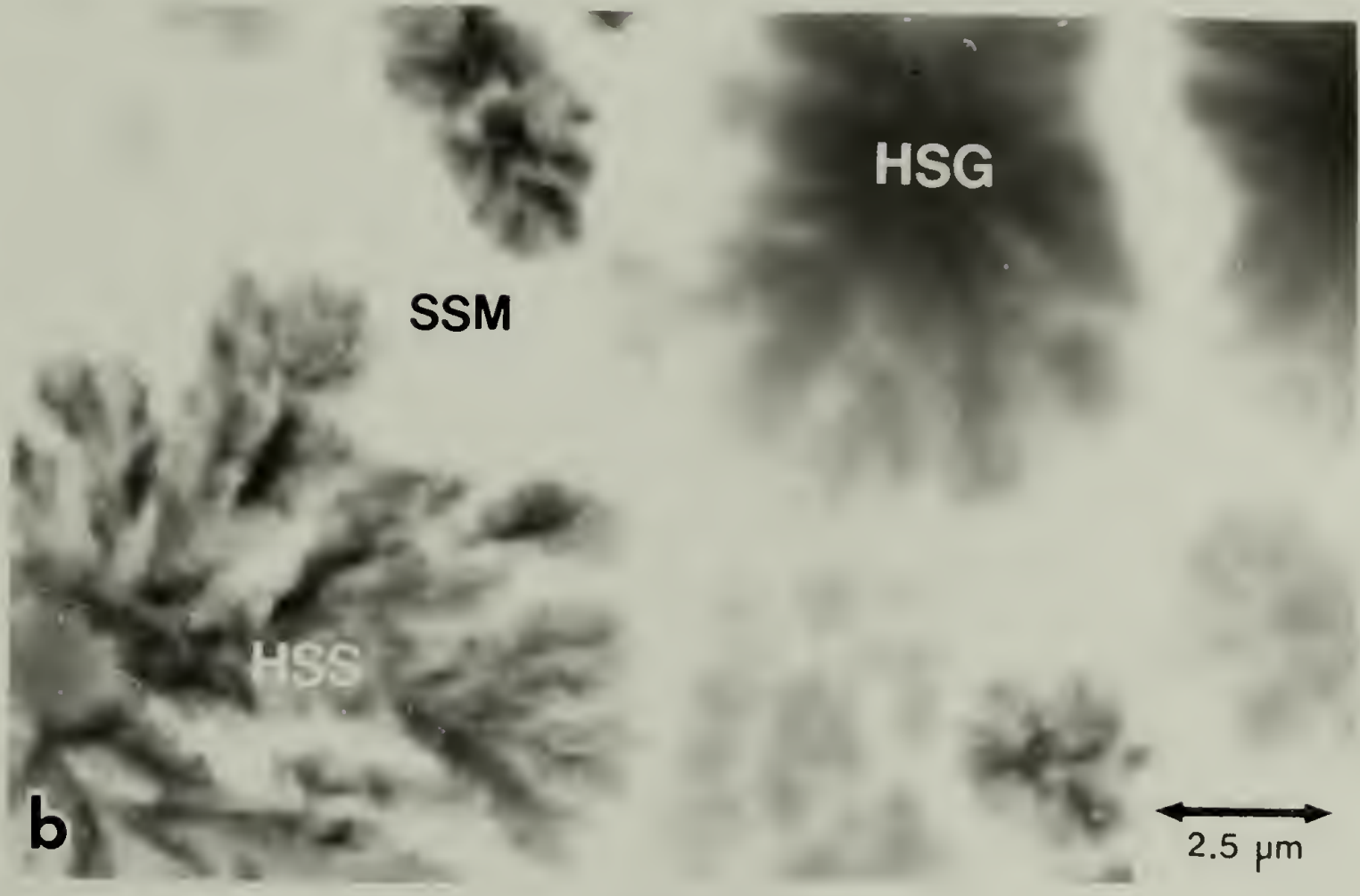

Figure 19

Figures 20a and 20b. TEM micrographs of sample A-IV (43 percent hard segment) showing the presence of hard segment-rich globules (HSG), fibrils (HSF), spherulites (HSS) and soft segment-rich matrix(SSM).

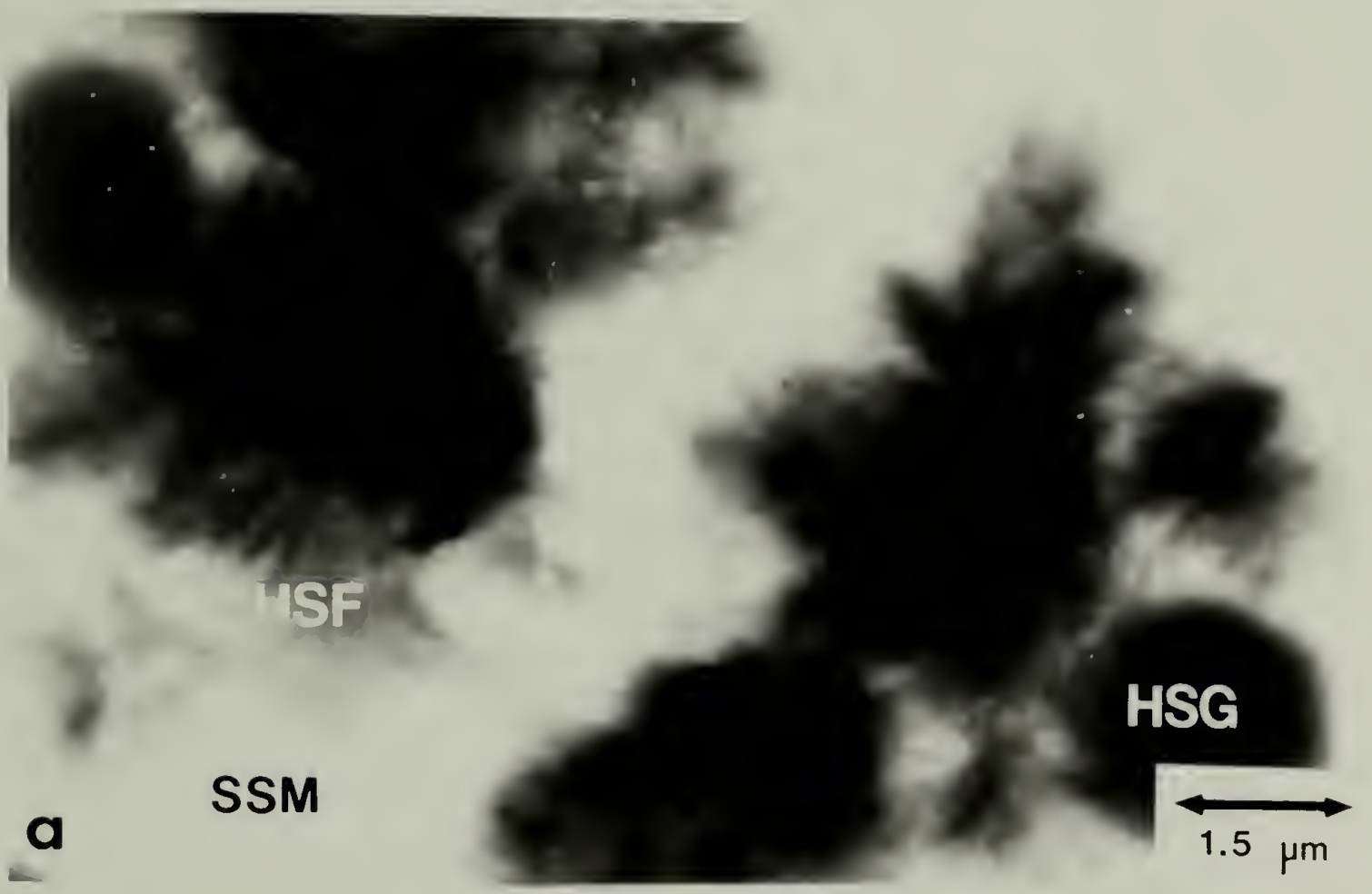

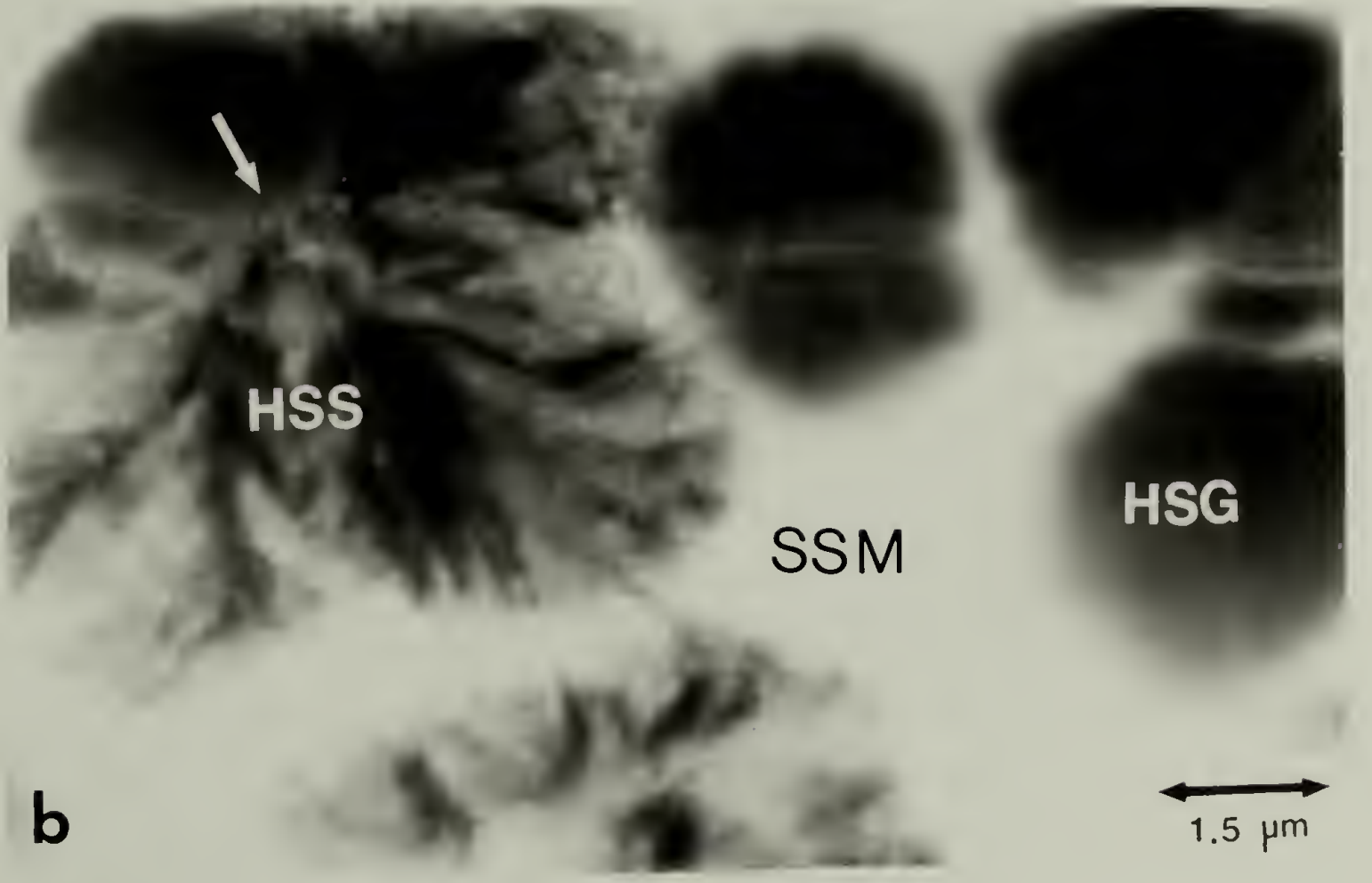

Figure 20

Sample A-V (55 percent hard segment) consists of hard segment-rich spherulites and globules with almost no soft segment matrix (see Figures 21a and 21b). Obviously, the soft segment-rich molecules must be trapped between lamellar fibrillar structure within the spherulite. It is also noted that lamellar fibrillar structure can grow both radially and tangentially as shown in Figure 21b. AS mentioned earlier, DSC and optical microscopy indicated a distinct skin/core morphology for samples A-VI and A-VII. Besides the presence of hard segment globules, the surface regions of samples A-V, A-VI, and A-VII display 2 types of volume filling spherulites. Type α are smaller, internally diffuse spherulites while type β spherulites appear larger, with a prominent radial, fibrillar structure (see Figures 21b, 22a, 22b and 23a, 23b). There is good correlation of optical and electron microscopy with samples A-IV to A-VII (see Figures 14 to 23). Still, it is difficult to distinguish between hard segment rich globules and type α spherulites with electron microscopy and polarized light microscopy due to the diffuse internal nature of type α spherulites. Figure 12b (sample A-I) clearly shows globules and Figure 22a (sample A-VI) shows α spherulites. At other hard segment concentrations the distinction is not as clear. Undoubtedly, there is a relationship between globules and α spherulites that is not well understood at present. The core regions

Figures 21a and 21b. TEM micrographs of sample A-V (55 percent hard segment) showing hard segment-rich globules, α and β spherulites. Note β spherulites nucleated from the edge of globules, arrows indicate nucleation centers. Globules and α spherulites correspond to the spherical non-birefringence regions in Figure 15.

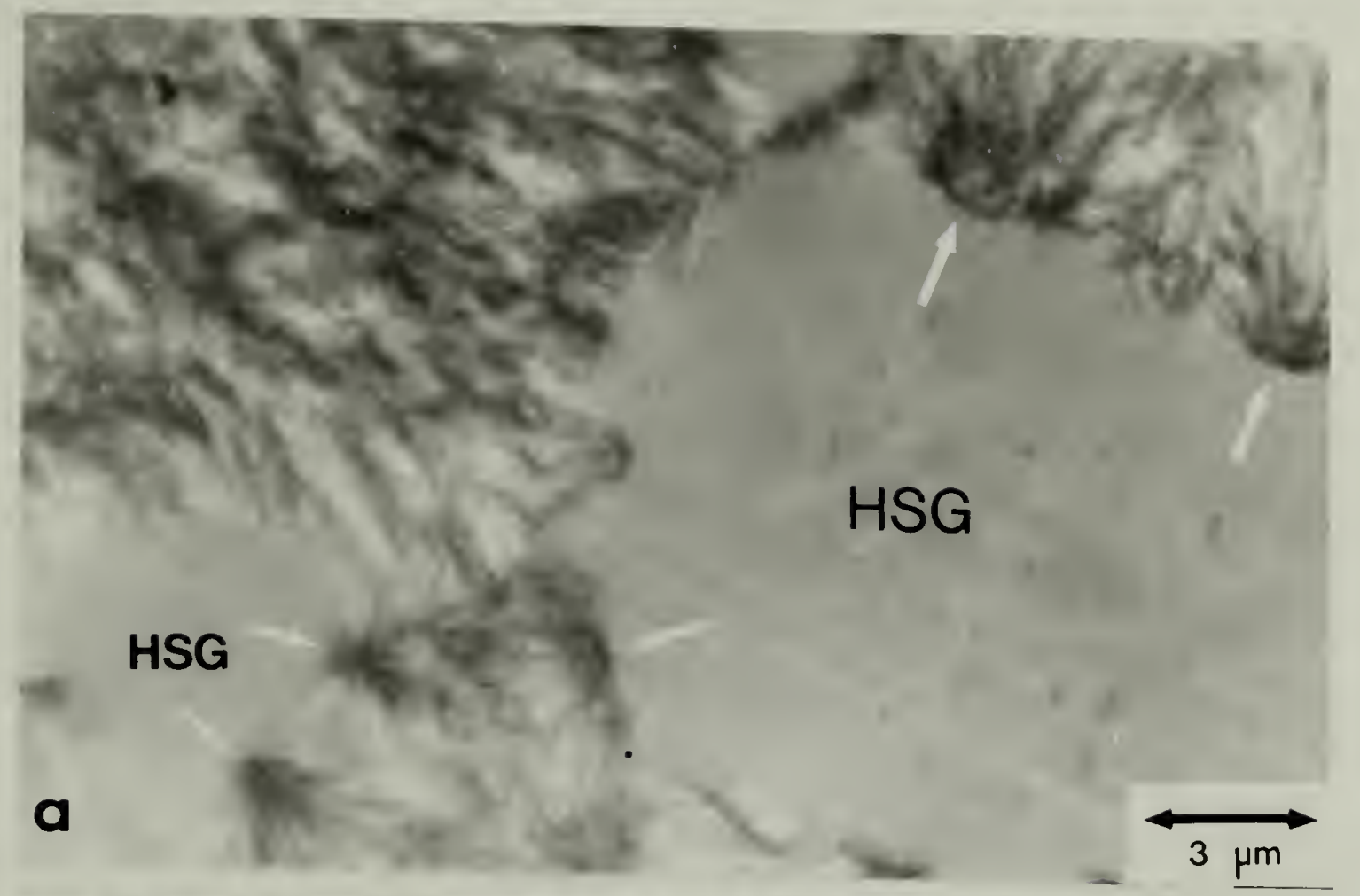

Figure 21

Figures 22a and 22b. TEM micrographs of the skin regions of sample A-VI (66 percent hard segment). Note the presence of α and β spherulites.

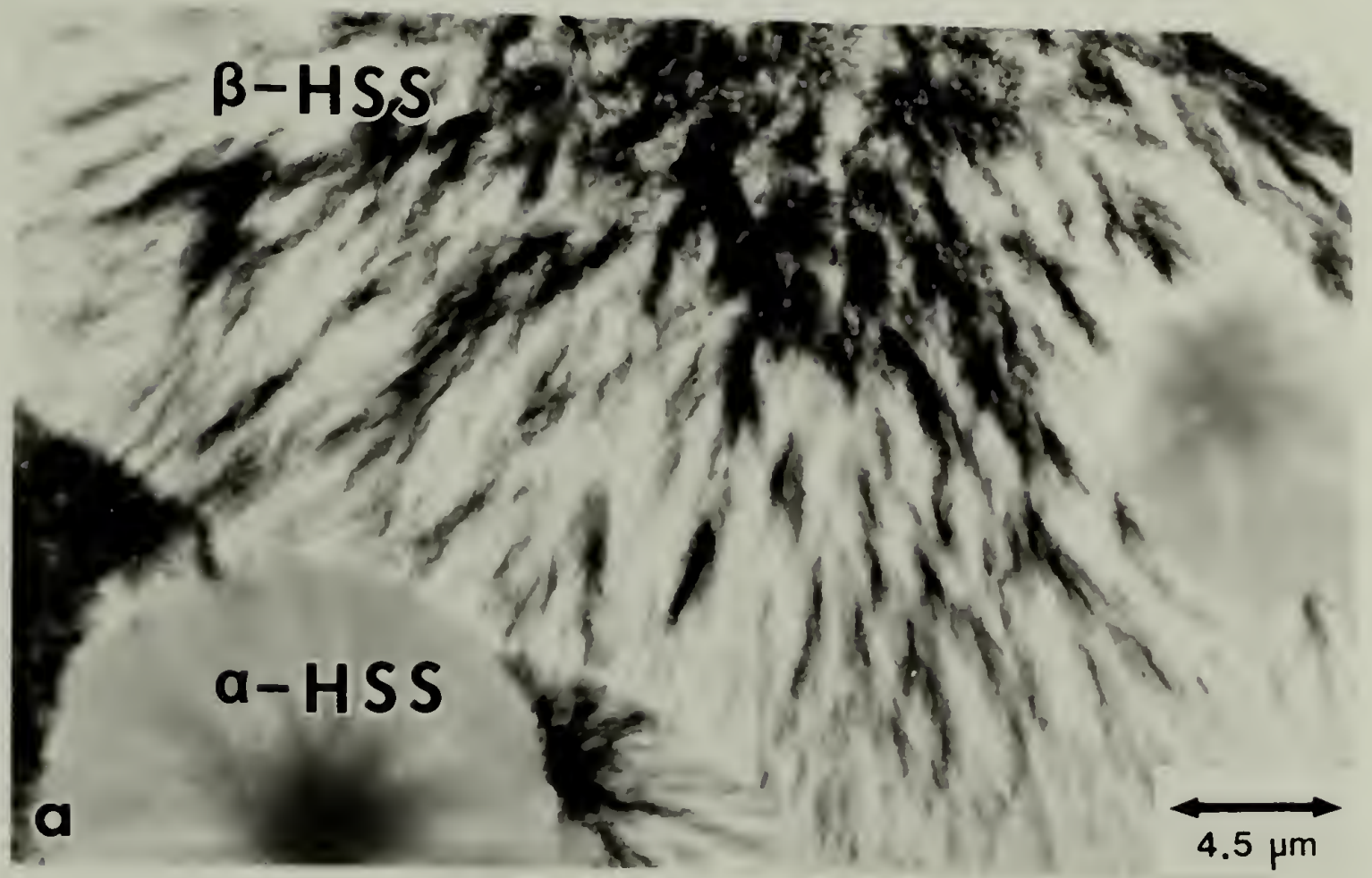

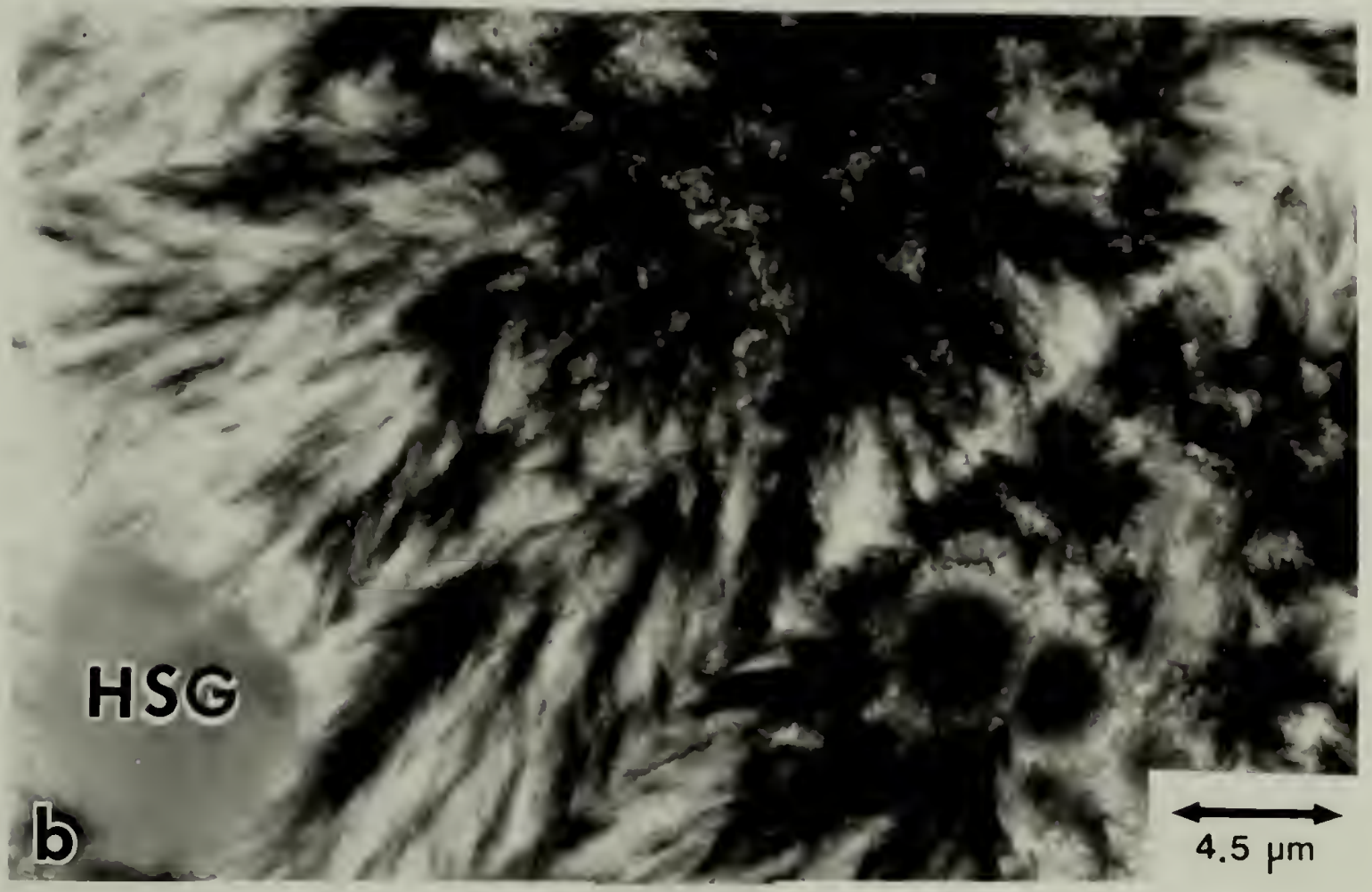

Figure 22

Figures 22c and 22d. TEM micrographas of the core regions of sample A-VI (66 percent hard segment) showing the presence of β spherulites surrounded by hard segment-rich matrix (HSM).

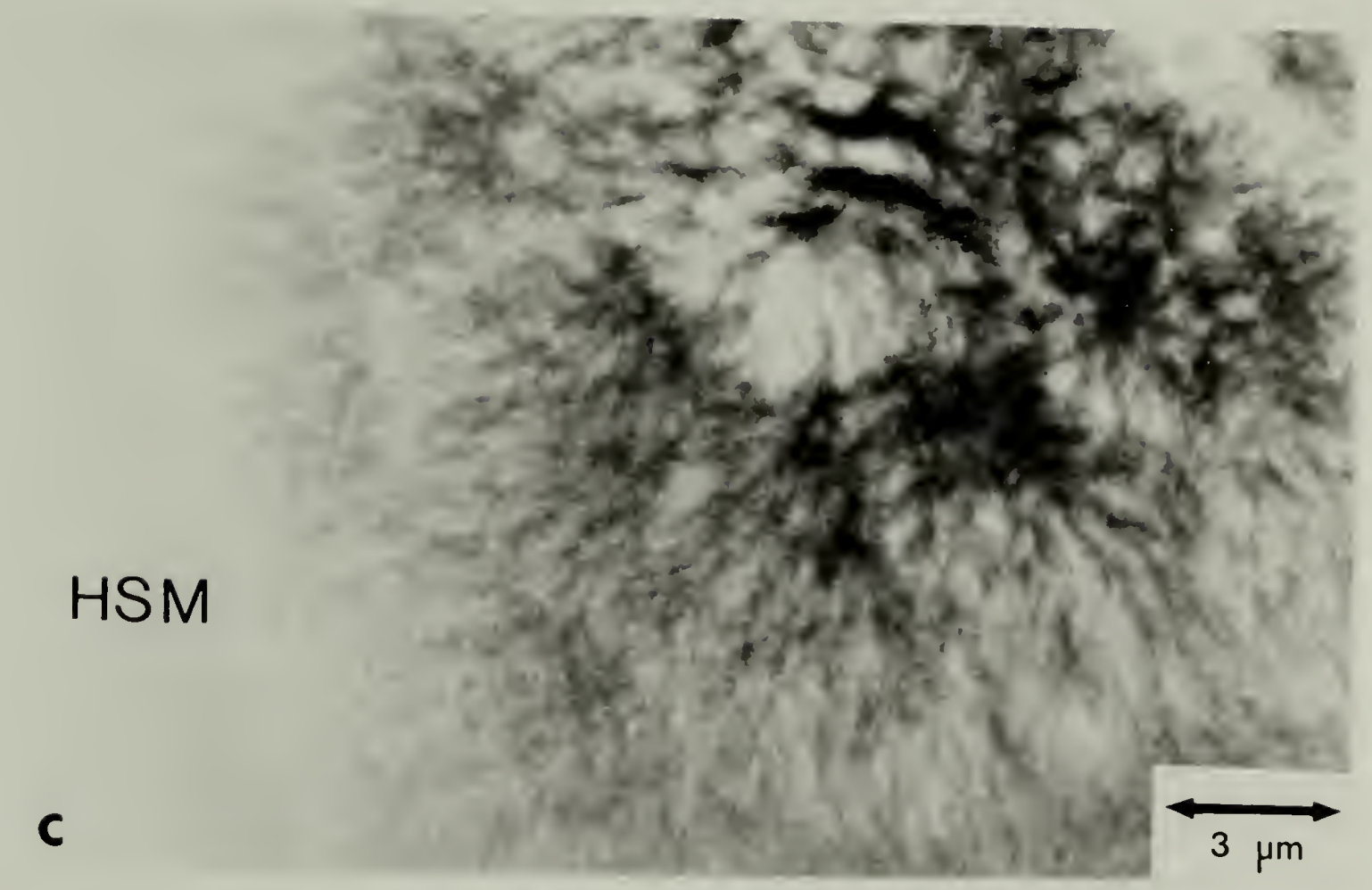

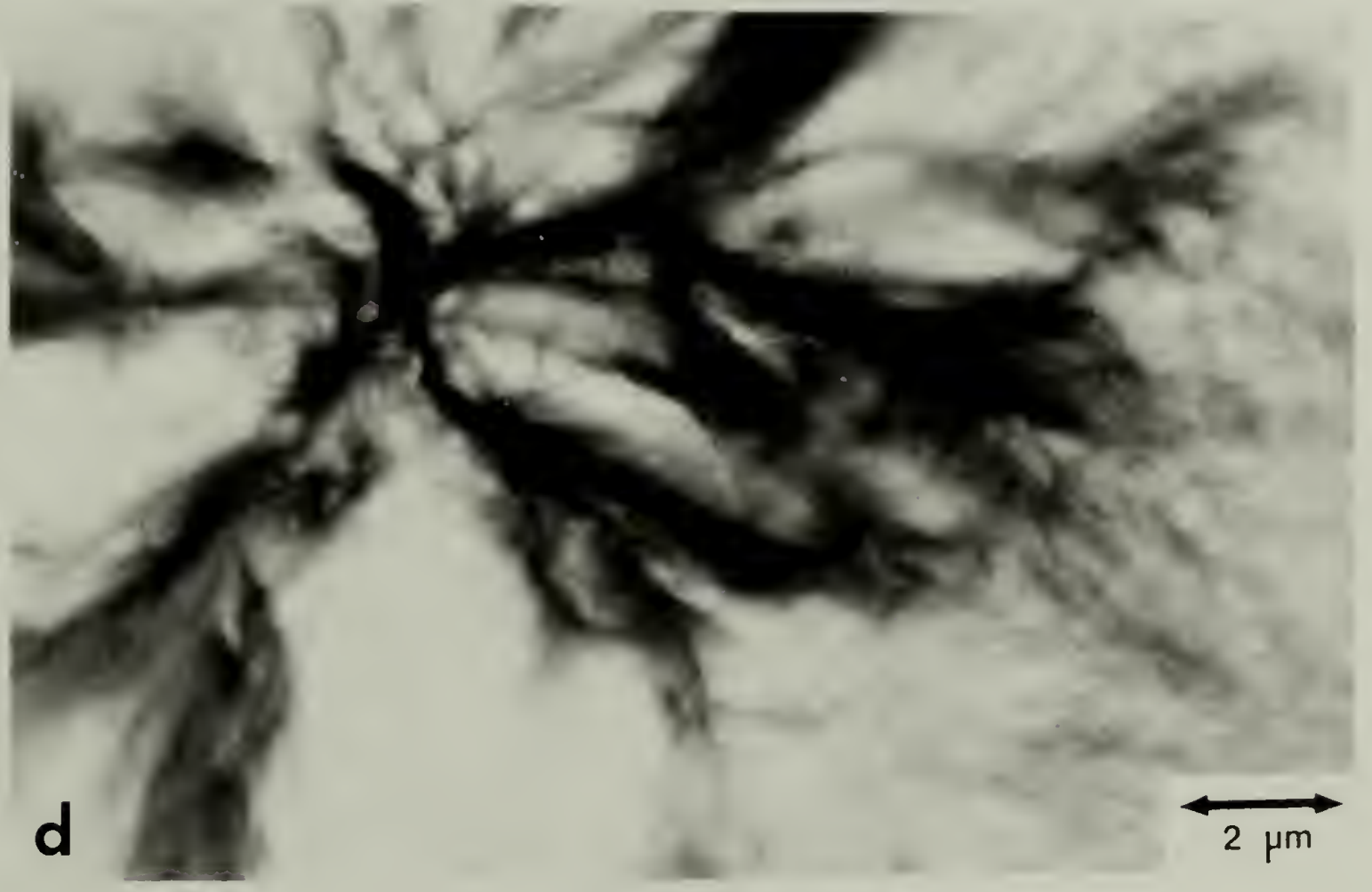

Figure 22

Figures 23a and 23b. TEM micrographs of the skin regions of sample A-VII (78 percent hard segment) showing β spherulites and globules.

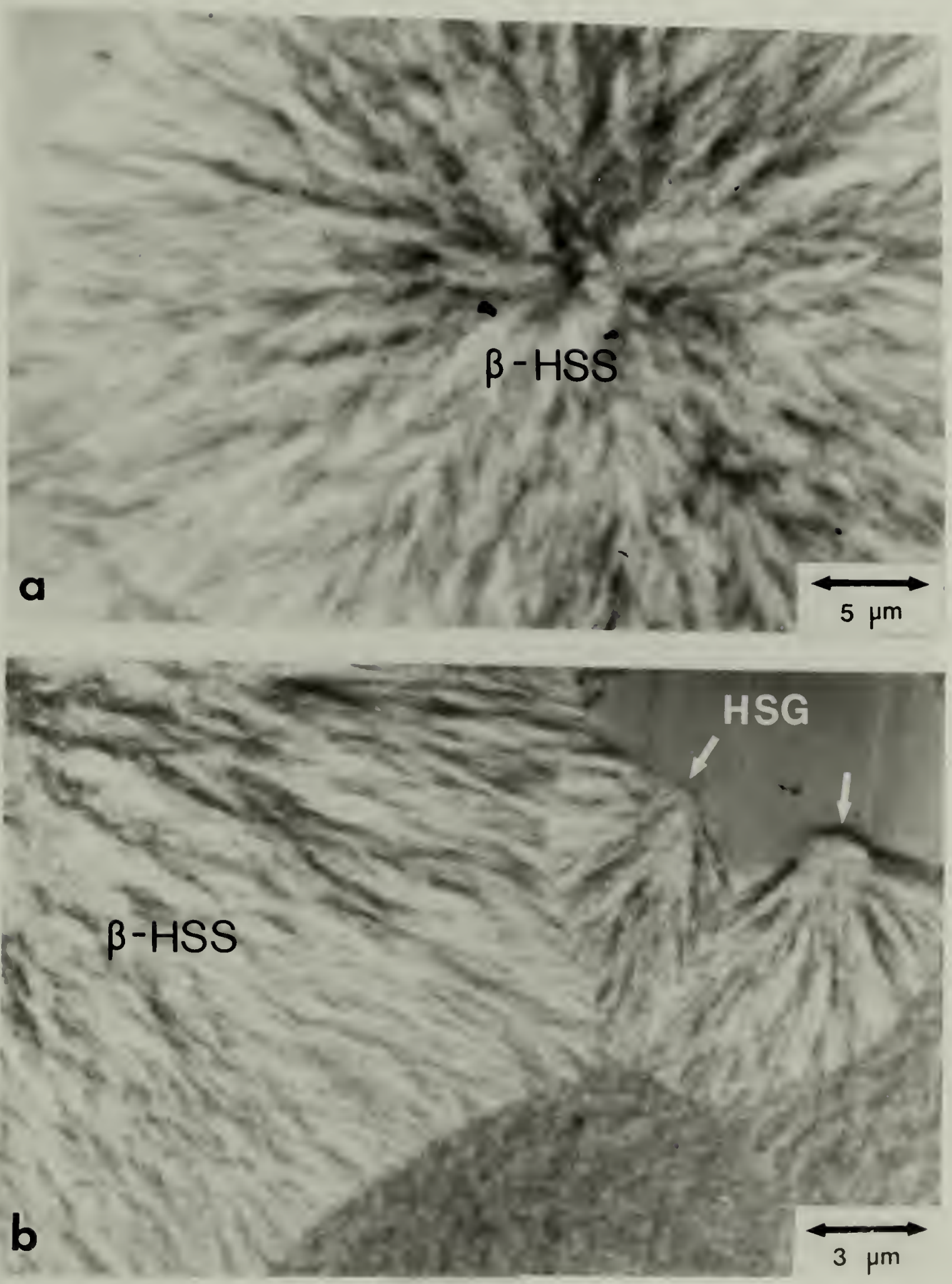

Figure 23

Figure 23c. TEM micrograph of the core regions of sample A-VII (78 percent hard segment) showing homogeneous hard segment-rich matrix at low magnification. The upper part of the microtomed section has another section on top of it.

Figure 23d. High magnification TEM micrograph of ultrathin sections of the core regions of sample A-VII (78 percent hard segment). It shows crystallite domain structure ranging from 30 to 50 Å in size with paracrystalline ordering (Original magnification 33,000X, total magnification 100,000X).

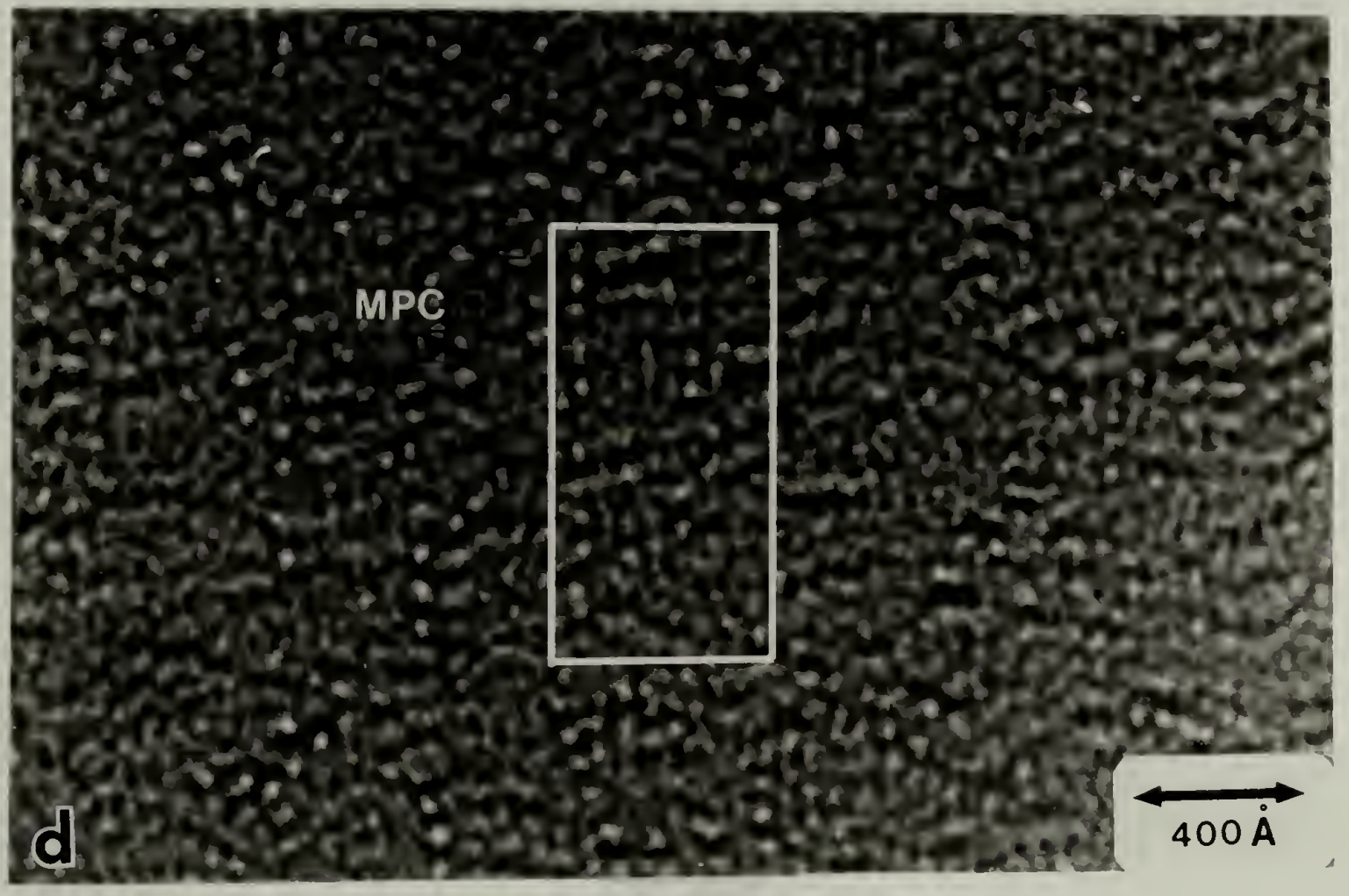

Figure 23

of samples A-VI and A-VII are quite different from the surface regions. The core of sample A-VI exhibits a few type β spherulites immersed in a featureless hard segment-rich matrix (HSM) (see Figures 22c and 22d). The core of sample A-VII is continuous hard segment-rich matrix with no spherulites (see Figure 23c). Although no superstructure was found by optical or electron microscopy, DSC results indicate the presence of comparatively high crystallinity in the core regions of sample A-VII. The presence of small crystallites is thus implied. In order to visualize these crystallite domains via TEM, it is essential to obtain thin cryomicrotomed sections (thickness comparable to the size of crystallites). Much effort, skill and time have produced convincing evidence for the existence of this crystallite domain structure. The observed size ranges from 30-50 Å accompanied with some limited ordering of crystallites into paracrystalline arrays (micro paracrystallite, MPC) in the core regions of sample A-VII (see Figure 23d). We believe this is the first imaging of the crystallite domain structure ever reported for as-reacted polyurethanes.

4.4 Mechanical Properties

Mechanical properties as determined by stress-strain analysis show a wide range of behavior, from a soft rubber at low hard segment content through a very tough, high elongation, elastomer at intermediate hard segment to a higher modulus thermoplastic at high hard segment content (see Figure 24). The elongation to break and toughness (measured as the area under the stress-strain curve) show a maximum at intermediate hard segment concentrations (see Table 6). Zdrahala et al.[30] noted an inflection in the tensile strength versus hard segment concentration curve for these samples which they interpreted as phase inversion from a soft segment-rich matrix to a hard segment-rich matrix occurring at about 55 percent hard segment content (sample A-V). Indeed our optical and electron microscopy results show that samples A-I to A-IV possess a soft segment-rich matrix while samples A-VI and A-VII possess a hard segment-rich matrix. Sample A-V has a volume filling spherulite morphology with a corresponding drop of nearly 50 percent in ultimate elongation. It appears that in order for a sample to have both high elongation and good toughness, it is necessary to have non-volume filling spherulite morphology, i.e. to have hard segment-rich spherulites in soft segment-rich matrix (see Figures 19 and 20).

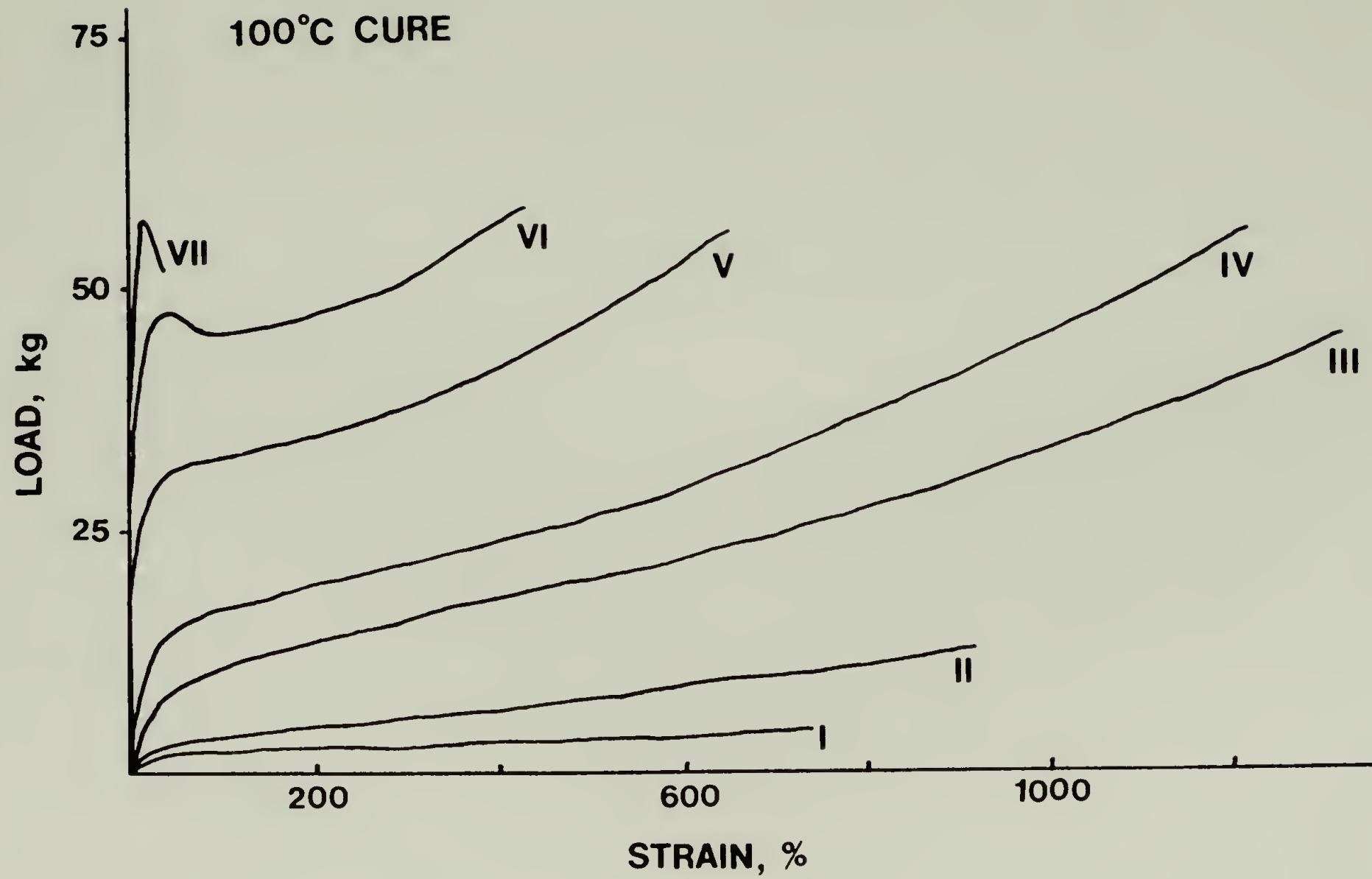

Figure 24. Load versus strain curves for samples A-I to A-VII.

TABLE 6

MECHANICAL PROPERTIES OF 100°C CURE PPO-EO/MDI/BDO SAMPLES

SAMPLE DESIGNATION	INITIAL MODULUS (MPa)	YIELD STRESS (MPa)	ULTIMATE ELONGATION (percent)	FRACTURE STRESS (MPa)	TOUGHNESS (Joules/m^3)
A-I	1.37	-----	700	1.7	8.3×10^7
A-II	5.5	-----	800	7.8	3.3×10^8
A-III	34.4	-----	1400	22	2.1×10^9
A-IV	130	-----	1200	33	2.6×10^9
A-V	260	-----	700	31	1.7×10^9
A-VI	520	30	400	33	1.2×10^9
A-VII	1400	44	40	38	1.6×10^8

4.5 Scanning Electron Microscopy Results

Figures 25a and 25b are SEM micrographs of the surface of sample A-VII before and after tensile deformation. The spherulites can be seen in the undeformed material as polyhedral, dimpled surface irregularities. The deformed sample has surface cracks running normal to the applied stress, due to the spherulitic skin breaking up along spherulite boundaries during deformation while the underlying core material (regions labeled CR) has undergone ductile deformation. It is evident that the skin/core morphology has a profound effect on the mechanical properties of the material.

4.6 Adiabatic Temperature Rise Results

Figure 26 is a plot of the maximum temperature attained under adiabatic conditions versus hard segment content. The solid line is the calculated temperature rise based on equation 1:

$$* \quad T_{max} = \frac{\Delta Hc}{\rho C_p} + T_{mix} \qquad (1)$$

where ΔH = 20,000 cal/mole OH groups
ρ = 1.14 g/cm^3
C_p = 0.45 cal/g K
T_{mix} = mix temperature of reactants
c = concentration in moles of OH groups/cm^3

---

* Values adopted from reference 79.

Figures 25a and 25b. SEM micrographs of sample A-VII: (a) before tensile deformation, the spherulites at the skin are visible as polyhedral, dimpled irregularities on the surface; (b) after tensile deformation, surface cracks appear at spherulite boundaries. The core regions (labelled CR) underwent ductile deformation. Deformation direction indicated by the arrow.

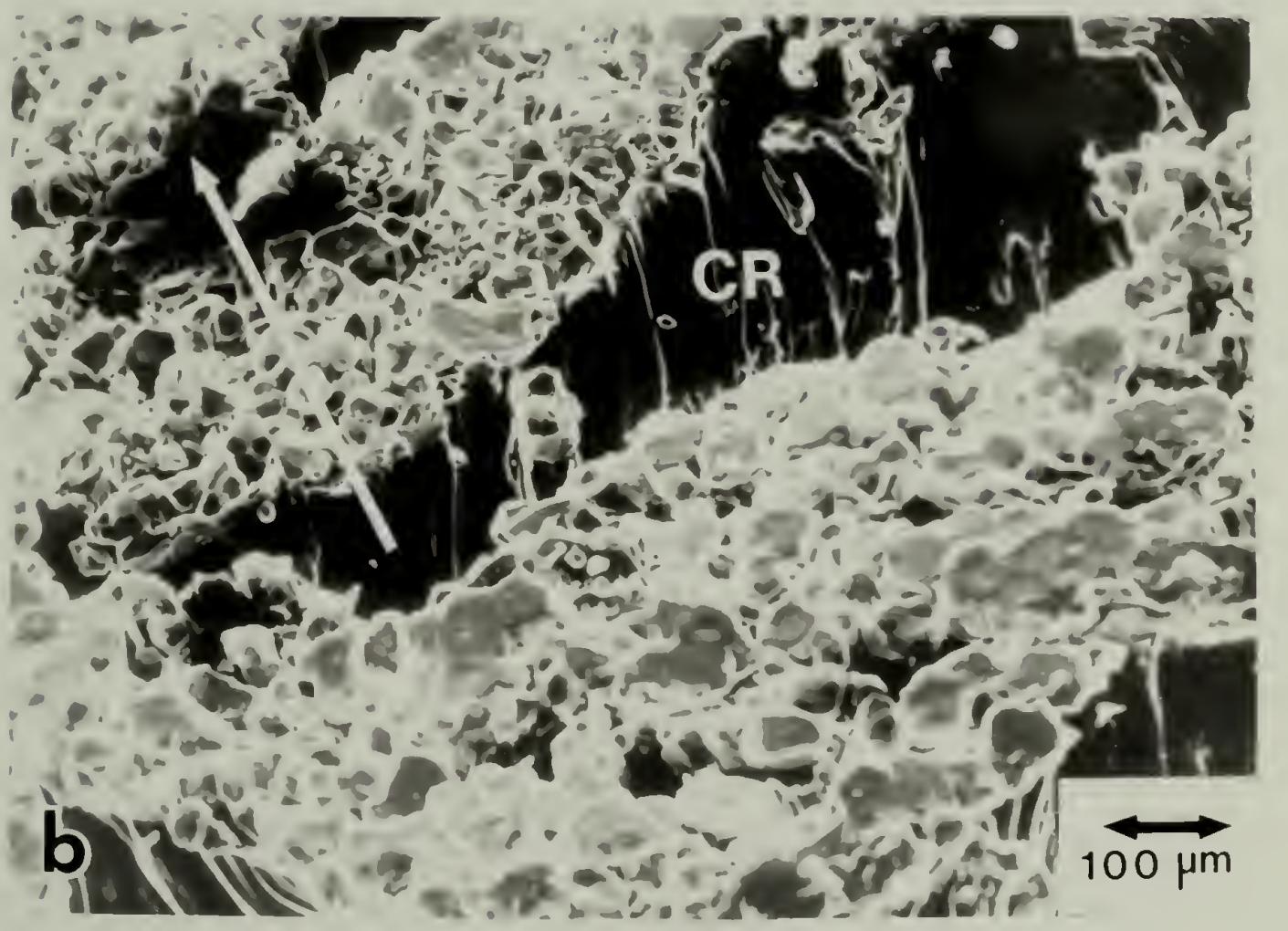

Figure 25

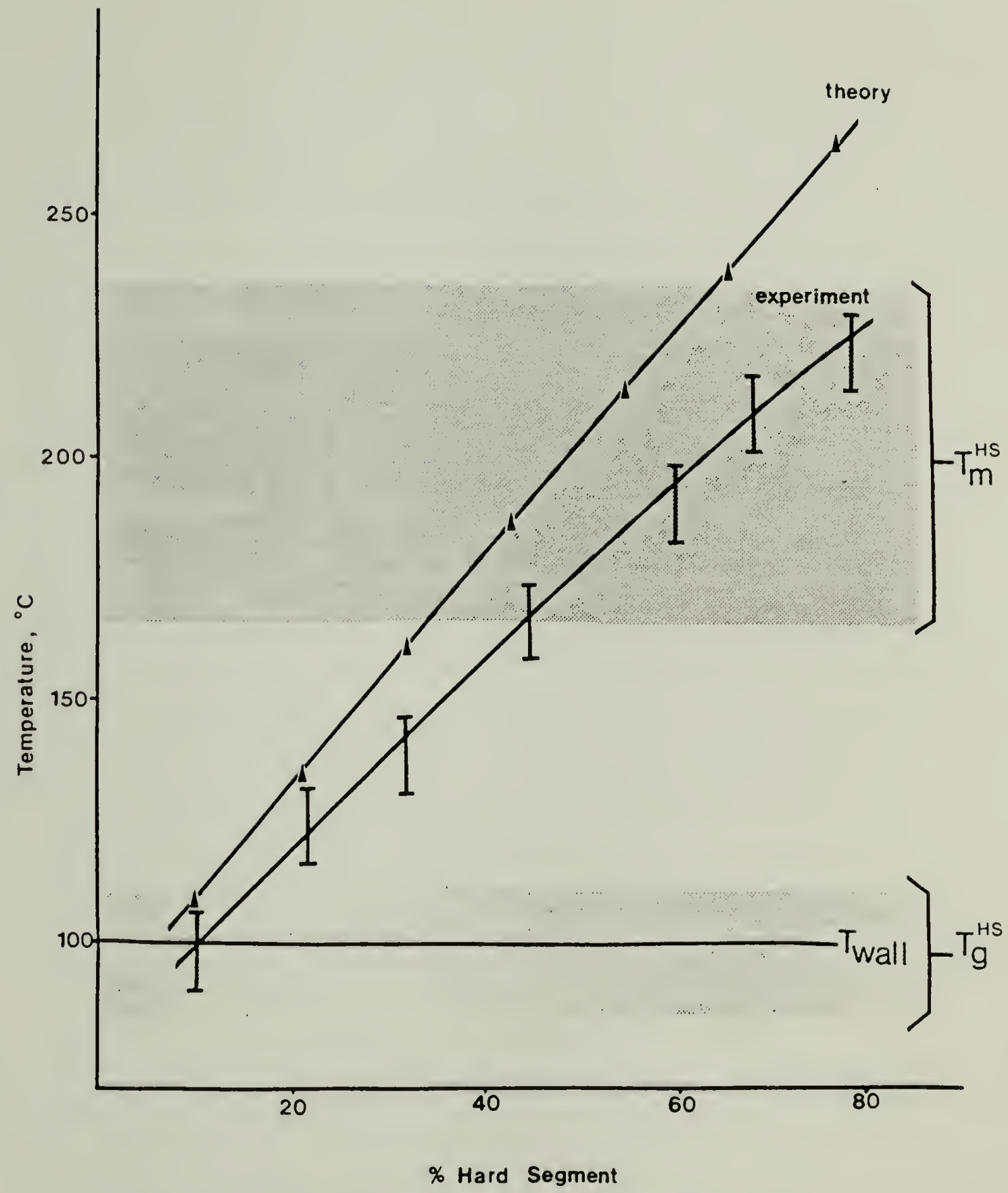

Figure 26. Calculated and experimental adiabatic temperature rise versus hard segment content.

As expected, the experimental temperature rise values are consistently less than the calculated values due to factors such as incomplete mixing and heat transfer which limit the maximum temperature attainable. It is noteworthy that for samples A-VI and A-VII the maximum temperature rise is well into the melting range of the crystalline hard segment as measured by DSC.

4.7 Wide-angle X-ray Scattering Results

Wide-angle X-ray scans of as-reacted samples are shown in Figure 27. It is evident from the traces that the highest hard segment content (78 percent) is not the best organized. The prominent reflections at 4.56 Å and 3.79 Å are sharpest for sample A-VI.

Interpretation of the WAXS results must be done carefully for samples A-VI and A-VII due to the inhomogeneous structures and positionally dependent morphologies. Calculation of the depth at which the scattered intensity falls to 1/e of the incident intensity indicates that most of the scattering occurs in the top 100 μm of the sample (i.e., in the skin regions). The sample which has the highest organization to the depth sampled by WAXS is sample A-VI.

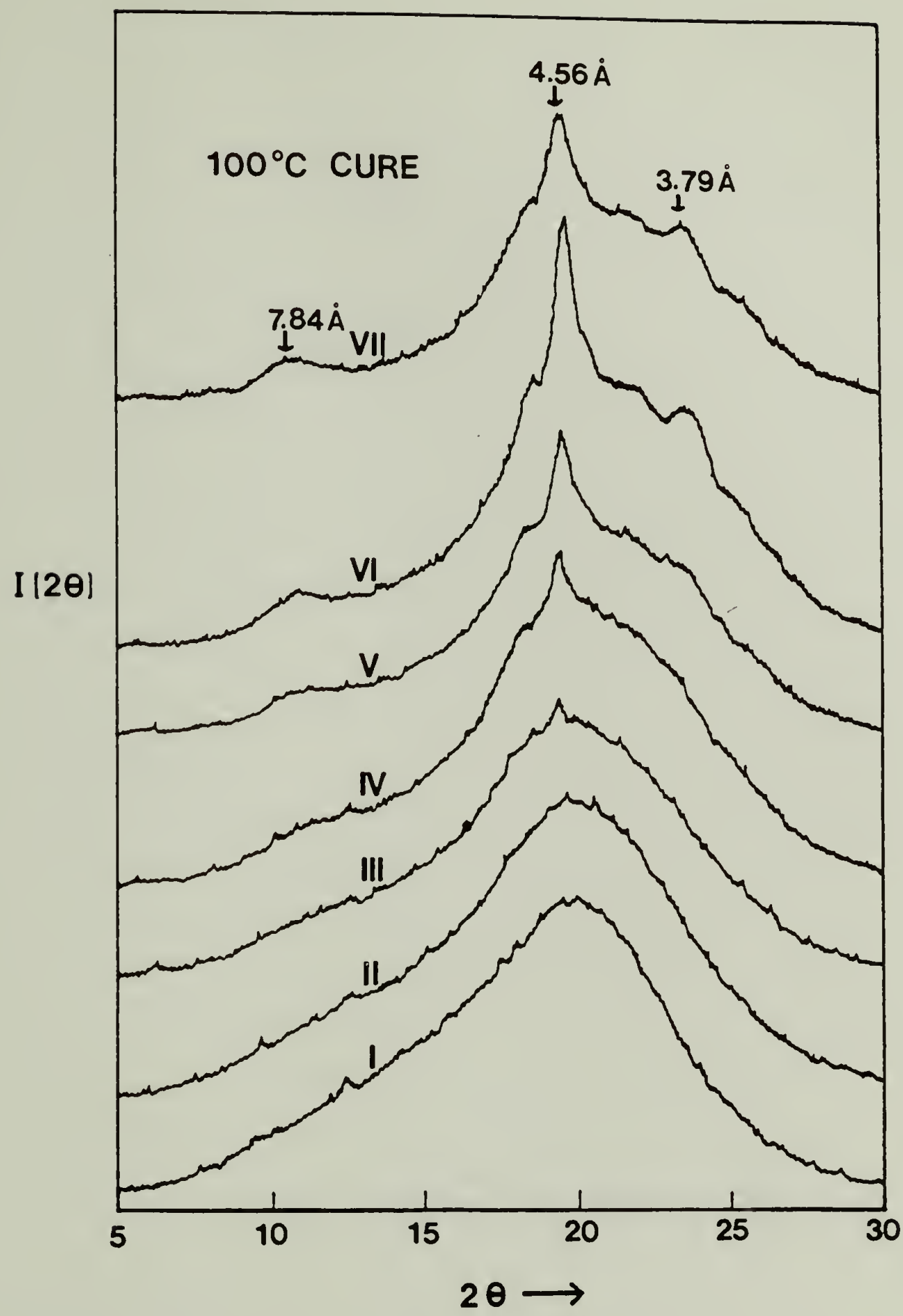

Figure 27. Wide-angle X-ray scans of samples A-I to A-VII; sample A-VI shows the sharpest reflections.

4.8 Small-angle X-ray Scattering Results

The small-angle X-ray scattering patterns (without Lorentz corrections applied) of the as-reacted (A-1 to A-VII) and hot-pressed (A'-I to A'-VII) samples are shown in Figures 28 and 29 respectively. The skin and core regions of the sample A-VII were run separately to check the skin/core difference in SAXS patterns (see Figure 30). The Bragg spacings corresponding to SAXS maximum of as-reacted and hot-pressed samples are summarized in Tables 7 and 8 respectively.

Samples A-I and A'-I with only 10 percent hard segment show no SAXS maximum regardless of thermal history (i.e., as-reacted or hot-pressed). Their scattered intensity drops off very quickly from the main beam showing little evidence of phase separation. Yet previous TEM results showed the presence of ~10 μm size globules morphology in sample A-I (see Figure 12). Since the characteristic dimension SAXS can detect is on the order of tens to thousands of angstrom units, the scale of globules is apparently too large for SAXS to detect. In addition, there seems to be little density fluctuations within the globules so that no structure (~100s Å size) can be seen by SAXS. The as-reacted bulk samples A-II to A-VII show small-angle Bragg spacings in the range 130-190 Å without any apparent correlation with hard segment content.

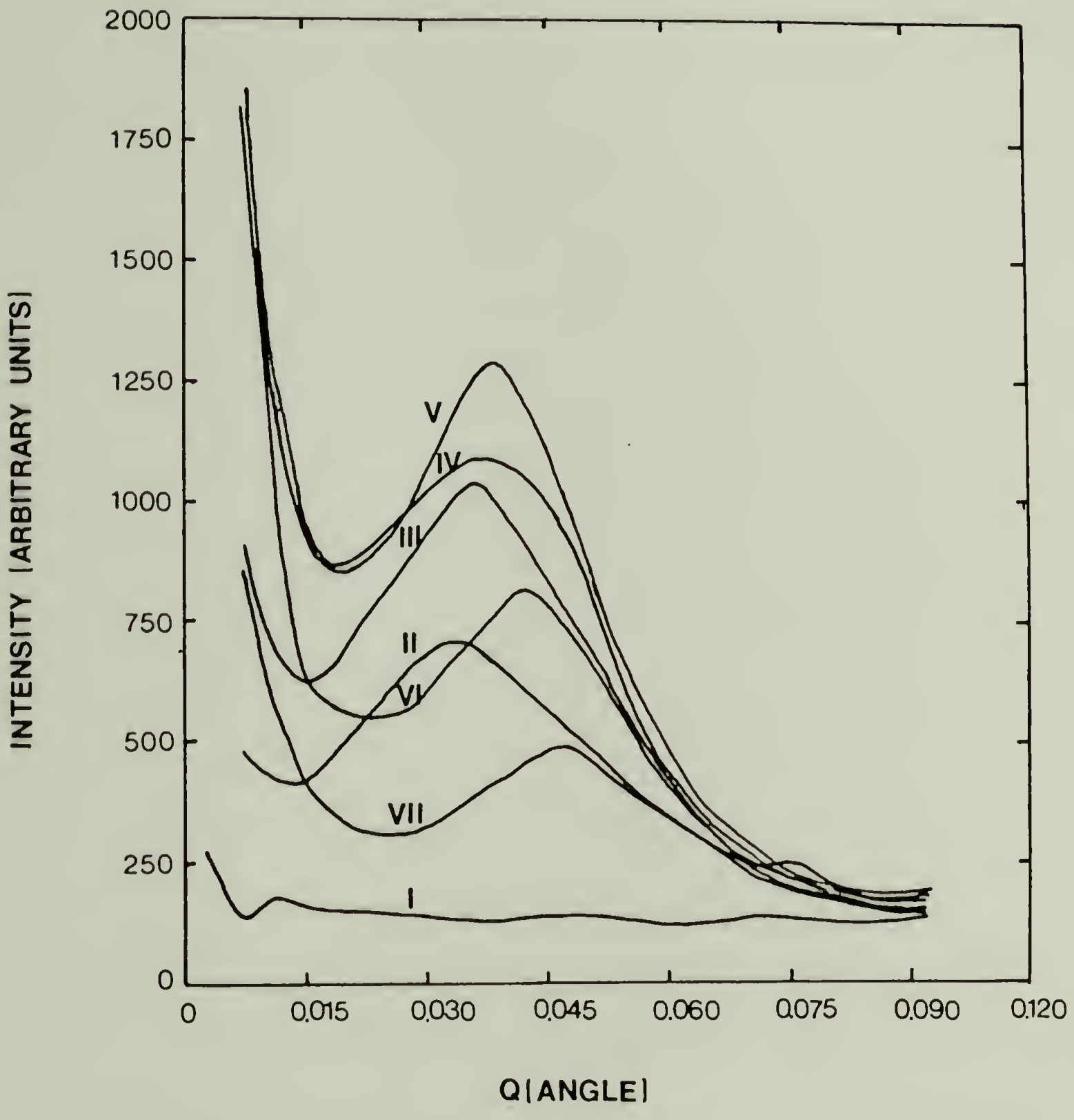

Figure 28. Pinhole SAXS scattering patterns of as-reacted bulk samples A-I to A-VII.

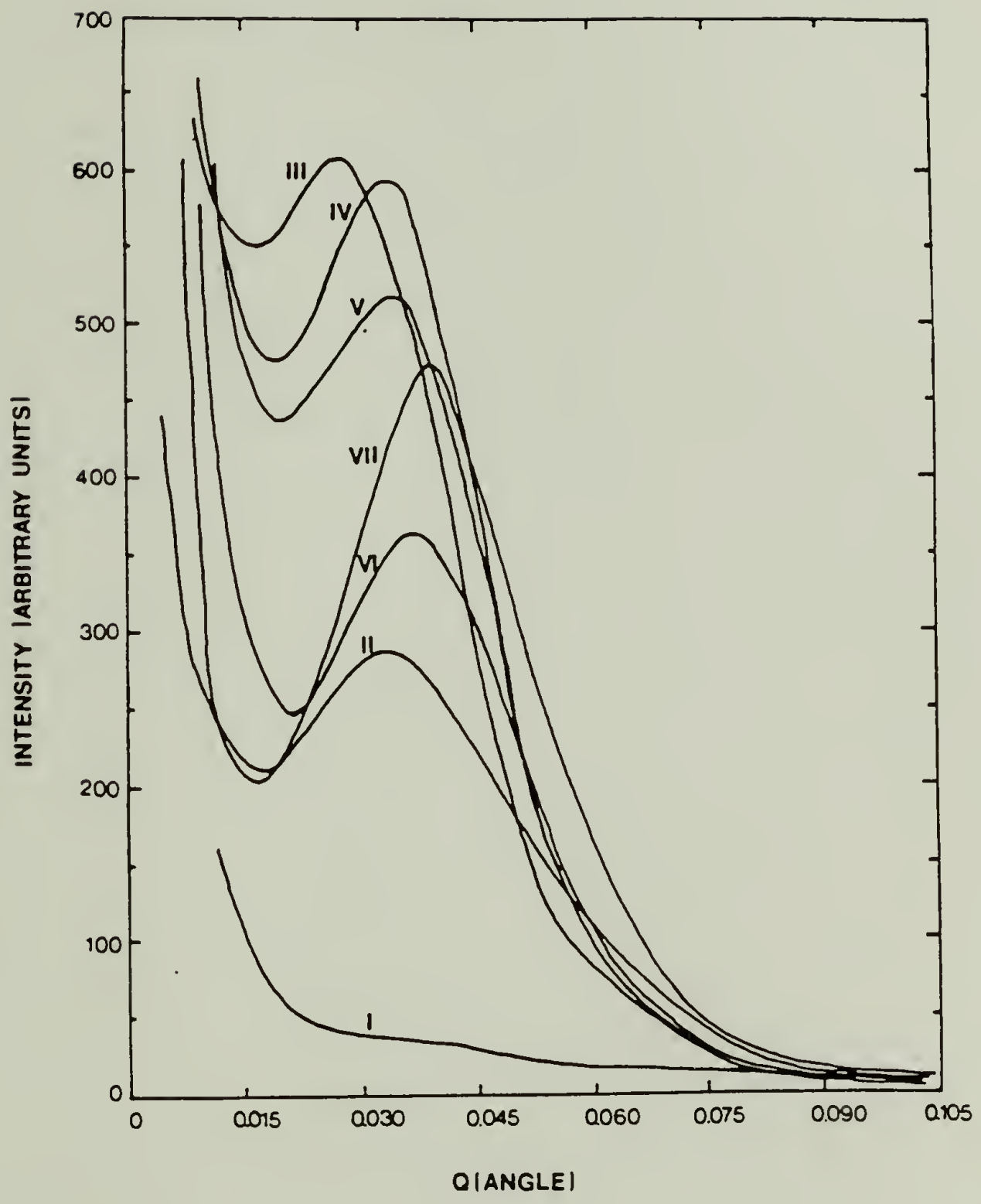

Figure 29. Pinhole SAXS scattering patterns of hot-pressed samples A'-I to A'-VII.

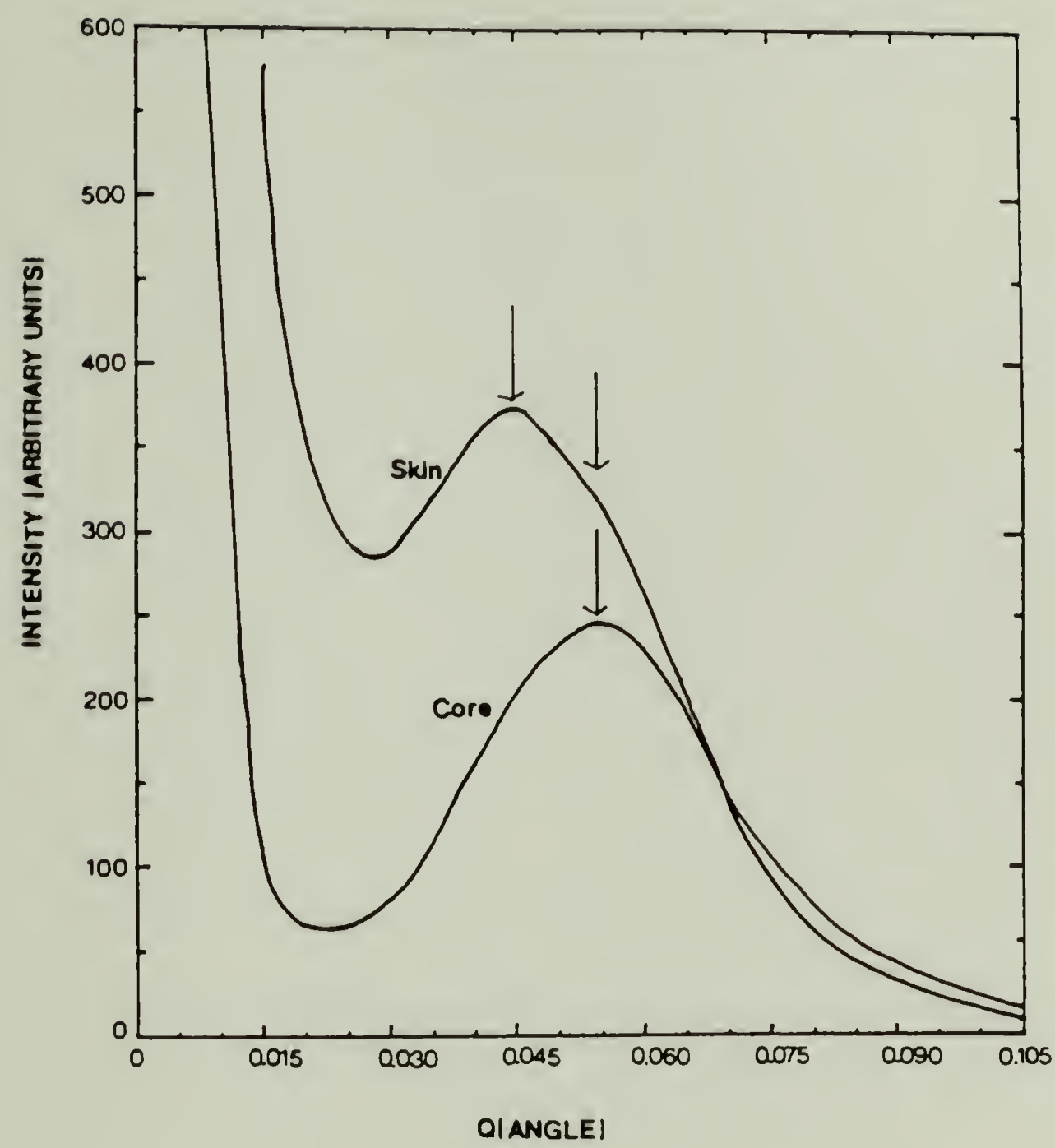

Figure 30. Pinhole SAXS scattering patterns of skin and core regions of as-reacted bulk sample A-VII.

TABLE 7

SMALL-ANGLE X-RAY SPACING FOR AS-REACTED SERIES A SAMPLES

Sample	Small-angle Bragg's Spacing, Å
A-I	none
A-II	150
A-III	180
A-IV	170
A-V	160
A-VI	190
A-VII (bulk)	130
A-VII (skin)	140
A-VIII (core)	110

TABLE 8

SMALL-ANGLE X-RAY SPACING FOR HOT-PRESSED SERIES A SAMPLES

Sample	Small-angle Bragg's Spacing, Å
A'-I	none
A'-II	170
A'-III	210
A'-IV	190
A'-V	170
A'-VI	170
A'-VII	160

The same result is found for the hot-pressed samples, except their SAXS maxima are consistently shifted to lower angle, i.e., larger Bragg spacings (ranging from 160-210 Å). The insensitivity of the measured peak spacing to the increasing hard segment content (as well as hard segment length) by SAXS may be due to the fact that these SAXS maxima are mainly attributed to the lamellar fibrillar structure within the samples (see TEM section).

Note the difference in the Bragg spacing between skin and core regions and the average bulk value of sample A-VII (see Table 7). Since the bulk sample is composed of skin and core regions, its measured value (130 Å) lies between those of the skin (140 Å) and the core (110 Å). Previous TEM study showed that skin regions (Figure 23a and 23b) are mainly composed of spherulitic superstructure while the core regions (Figure 23d) are composed of micro paracrystallites (MPC). Therefore the SAXS peak of the skin regions may arise from lamellar fibrillar structure (LFS) within spherulites and that of the core regions from MPC structure. Although skin regions may still contain a small portion of core regions due to specimen preparation method (by cutting the surface layer with razor blade), the SAXS pattern shows only trace evidence of core regions (see Figure 30). Therefore it will be misleading trying to interpret SAXS results on a bulk sample which is composed of heterogeneous structures. One should always

check the structural homogeneity of the sample, e.g., by TEM, before any meaningful SAXS analysis can be made.

4.9 Annealing Study of Sample A-V

It is of great interest to study how the morphology is changed after the sample is subjected to thermal treatment (annealing). Sample A-V was chosen for this study because it has the highest crystallinity and volume filling α, β spherulites and globules. Sample A-V was heated in DSC at 20°C/min from room temperature to 475°K, held for 4 hours and then cooled slowly at 2.5°C/min back to room temperature. The annealed sample was then cryomicrotomed and observed in TEM. Previous studies[78] on pure MDI/BDO, PCP/MDI and PPO-EO/MDI copolymers indicate the hard segment is relatively radiation resistant while the soft segment degrades. Figures 31a and 31b show TEM micrographs of sample A-V before and after annealing respectively. The annealing process has promoted better phase separation as evidenced by the thickening of lamellae structure (as well as perfection of crystal), and the appearance of many amorphous soft segment-rich pocket regions (SSP, as indicated by arrows in Figure 31b) which were easily etched away by electron beam during TEM observation. It is also a direct proof that uncrystal-lizable segments or molecules are trapped within the

Figure 31a. TEM micrograph of sample A-V (55 percent hard segment) before annealing.

Figure 31b. TEM micrograph of annealed sample A-V (55 percent hard segment) showing the thickening of lamellae structure and amorphous soft segment-rich pocket regions (SSP, indicated by arrows).

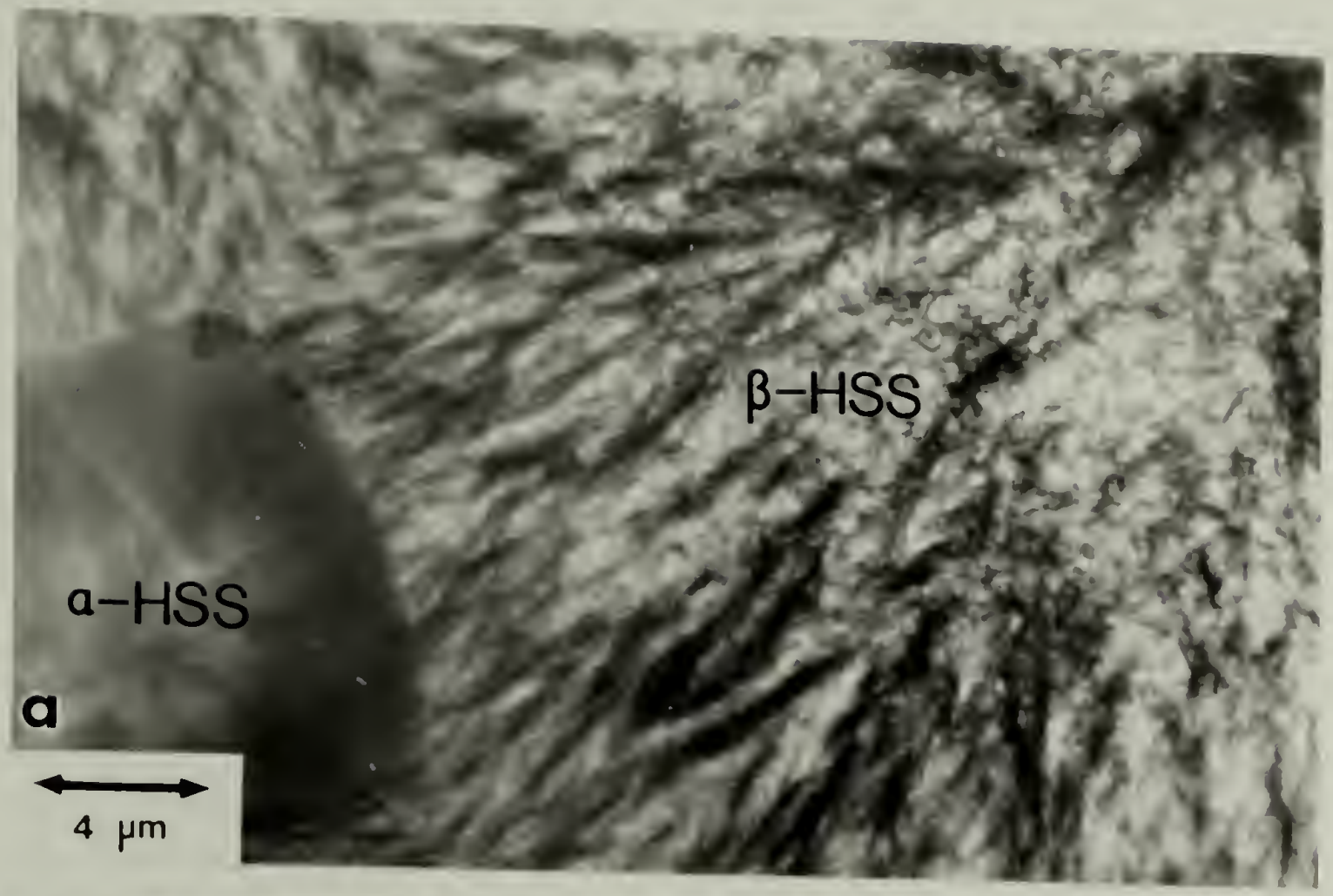

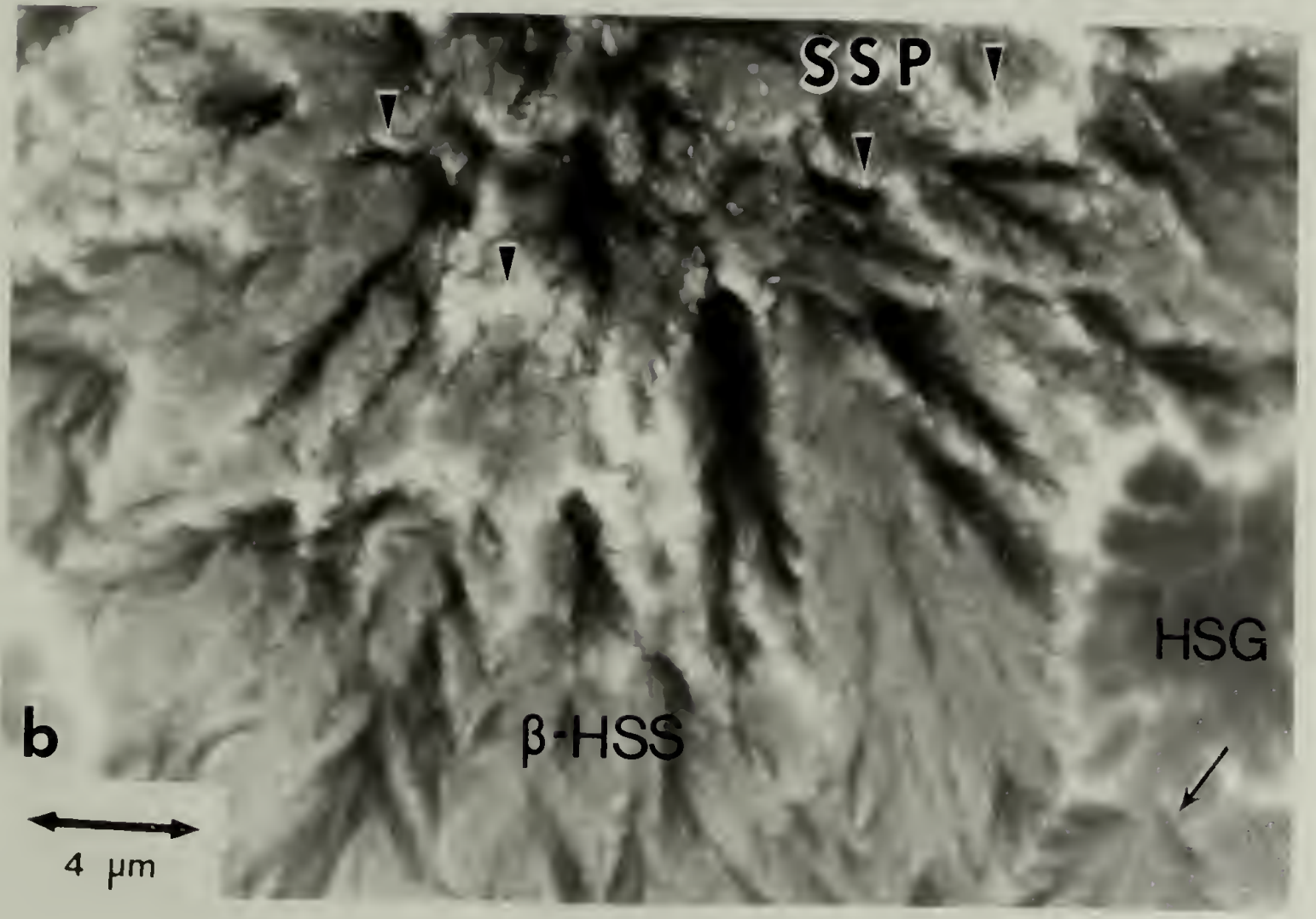

Figure 31

spherulites. The boundaries between globules and spherulites are readily etched by the electron beam, which also indicates better phase separation after annealing.

Since hot-press is also an annealing process, it is instructive to make a correlation between TEM and SAXS results of sample A-V after annealing. The SAXS Bragg spacing of the hot-pressed sample shows only a ~10 Å increase than that of the as-reacted sample (170 vs. 160 Å). The change is too small in this case to account for the lamellae thickening and better phase separation phenomena observed in TEM micrograph (see Figure 31b). Other hot-pressed samples show an increase in Bragg spacing ranging from 20-30 Å with the exception that sample A'-VI shows a decrease of 20 Å (see Tables 6 and 7). Apparently, the effect of sample heat treatment on measured SAXS Bragg spacing is still unclear at this point.

4.10 Discussion and Conclusions

The present study was undertaken to learn more about the origin and nature of the larger scale microtructures previously observed in a RIM polyurethane based on polycaprolactone/MDI/BDO of 43 weight percent hard segment[22] and their influence on mechanical properties. The use of a relatively low catalyst concentration was expected to yield a systematic series of homogeneous

urethanes polymerized isothermally at 100°C. Although skin/core differences in samples A-VI and A-VII were found with virtually every characterization method, the techniques do not sample identical regions of the specimen. Moreover, the morphology variation is continuous and the division of the sample into skin and core regions is an over simplification. Nevertheless, the dramatic skin/core morphology variations found in samples A-VI and A-VII and the hard segment-rich globules found even in the lowest hard segment content sample, indicate the notion of isothermal polymerization from well-mixed components needs closer scrutiny. Any morphological variations found must be determined within the early stages of polymerization for after this initial period the temperature histories of the samples are essentially the same. The 10 micron scale heterogeneous globule morphology of sample A-1 suggests that the assumption of an initially homogeneous system which undergoes phase separation during polymerization [20,78-83] does not hold for this system. In the following discussion, rather than attempting to account in detail for each of the complex sample microstructures, we concentrate on understanding the underlying principles leading to the general types of microstructures observed.

Globules. First, it is important to note that the MDI monomer quickly phase separates from the diol/polyol mixture at 55°C, the approximate mix temperature of the reactants. Therefore the mixing may produce only a partially dispersed system with small, molten MDI-rich droplets in a predominantly polyol/diol-rich matrix at low hard segment concentrations or small polyol/diol-rich droplets in an MDI-rich matrix at high hard segment concentrations (Table 4 shows the starting volume fraction of each monomer in the mixture). Secondly, since large round thickness variations over a scale of 1 to 10 microns within a microtomed section are extremely unlikely, the strong contrast seen in bright field TEM must be due to electron density variations caused by compositional changes. The dark, electron dense, globules observed at low hard segment concentrations are therefore MDI-rich regions. To form such globules in the low MDI content samples through phase separation and coalescing of hard segments from an initially homogeneous system, diffusion would have to occur over many tens of microns in a matter of minutes which is hardly feasible for high molecular weight polymers.

The appearance of globules is also dependent on sample composition. The volume fraction of globules increases with hard segment (MDI/BDO) content up to sample A-V, then sharply decreases with a concomitant increase in the two

types of hard segment-rich spherulites. Such a morphology could arise from MDI becoming the continuous phase in combination with the high temperatures and high mobility during the polymerization caused by the large exotherm. These conditions would disperse any PPO-EO droplets formed initially, and promote hard segment crystallization.

This type of morphology is probably characteristic of reaction-molded systems with incompatible components. The two phase "nodular" or "microgel" morphology seen in many epoxy systems could be due to a similar mechanism[84-87].

Spherulites. The two types of hard segment spherulites have different nucleation and growth characteristics. Type α spherulites appear to nucleate first but then grow slowly. At sufficient undercooling type β spherulites nucleate, often at the growth front of type α spherulites or globules (see arrows in Figure 21 and 23), and have a much faster growth rate reaching a larger average size and volume fraction.

The adiabatic temperature rise results show that the exothermic heat of reaction causes a substantial temperature rise in the (adiabatic) core. The results are probably a good estimate of the reaction conditions found at the core of the mold. As the urethane reaction proceeds, the sample temperature rises mainly due to the heat of reaction and somewhat due to heat input from the

100°C mold wall. Once the skin region is above 100°C the mold wall will conduct heat away from the surface of the sample reducing the temperature rise in the skin region. Time-temperature plots as a function of mold position have been calculated by Macosko and coworkers for bulk polyurethane reactions[79,84]. Generally they take the shape as in Figure 32 with a steep, rapid rise from the reactant mix temperature to a maximum followed by a slow decay to the mold temperature. The large amount of heat liberated with the 66 percent and 77 percent hard segment samples brings the temperature at the core within the melting range of the hard segment and into the relatively slow, nucleation controlled crystallization regime (see Figure 32A). The crystallization in the core region of samples A-VI and A-VII probably resembles conventional crystallization after cooling from the melt. In the skin of samples A-VI and A-VII heat conduction to the wall limits the temperature rise and the crystallization kinetics are faster promoting the development of well-formed β spherulites (see Figure 32B). At intermediate hard segment concentrations (samples A-IV and A-V) the temperature rise is less and the sample morphology becomes more uniform with well-formed β spherulites throughout the specimen (see Figure 32B). This also explains the variation of crystallinity with hard segment concentration seen by DSC and WAXS. With sample A-V, a balance is

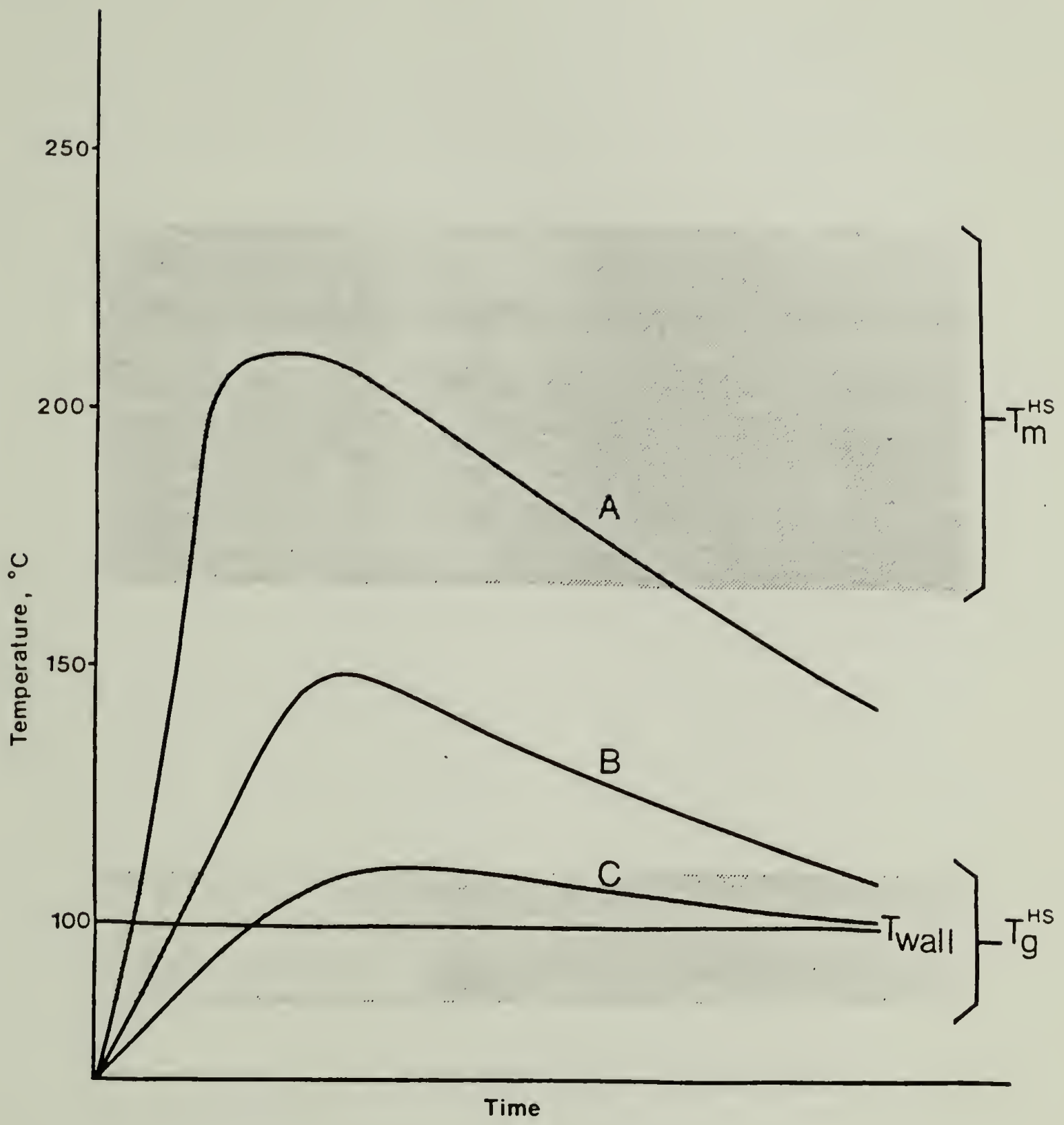

Figure 32. Possible temperature versus time pathways for different compositions: (A) high hard segment content; (B) intermediate hard segment content; (C) low hard segment content.

struck between mobility, molecular weight and crystallization kinetics yielding the highest crystallinity (total area of all DSC peaks). At lower hard segment concentrations, the size and number of spherulites decrease due to the lower temperature rise and the crystallization kinetics becoming diffusion controlled (see Figure 32C). In addition, there is less hard segment of sufficient sequence length to crystallize.

As mentioned previously both toughness and ultimate elongation reach a maximum at intermediate hard segment concentrations where there is a corresponding maximum in the product of the volume fractions of the two phases. The mechanical properties are a composite average of the influence of hard segment globules, spherulites and soft or hard segment matrix material and although informative, certainly do not represent the full potential possible for urethanes over this composition range.

In summary, the morphology of a particular polyurethane sample system will depend on composition, mixing, mobility of components and temperature history. Moreover, the detailed sample temperature history depends on position in the mold due to the large exothermic heat of reaction and heat transfer with the mold walls. For low hard segment content materials, the mold temperature gradient will be small, whereas for high hard segment content, temperature gradients of 100°C or more can

occur. The important part of the reaction, where the micron and the hundred angstrom scale morphology is determined, is the first few minutes (seconds for RIM formulations) before solidification of the mixture. The complex, simultaneously occuring (macro)phase separation--polymerization-(micro)phase separation-crystallization processes will vary according to sample composition, position in the mold and the detailed temperature history. While a phase inversion from a soft segment-rich matrix to a hard segment-rich matrix does occur between samples A-IV and A-V, interpreting the relationship between mechanical properties and microstructure is greatly complicated by the influence of the variations and heterogeneities present in the morphology.

C H A P T E R V

RESULTS FOR 175°C CURE PPO-EO/MDI/BDO SERIES

This series of polyurethanes, consisting of polypropylene oxide endcapped with polyethylene oxide polyol (PPO-EO), 4,4'-diphenylmethane diisocyanate (MDI) and 1,4- butanediol (BDO), ranges from 10-66 percent hard segment by weight. The difference between this system and the one studied earlier (chapter IV), is that the present one was cured at 175°C as opposed to the later at 100°C. In the earlier work, large differences were found in both mechanical properties and morphology across the plaque. These were thought to arise from temperature gradients between the relatively cool mold wall and the hot, adiabatic core. The idea in preparing the 175°C series was that the higher temperature cure would eliminate or at least decrease the skin/core differences in morphology and mechanical properties.

5.1 Differential Scanning Calorimetry Results

Figure 33 shows DSC scans of as-reacted PPO-EO/MDI/BDO polyurethanes which were oven cured at 175°C for 16 hours after the hand cast procedure. Sample B-I, which is only 10 percent by weight hard segment, shows only a trace of

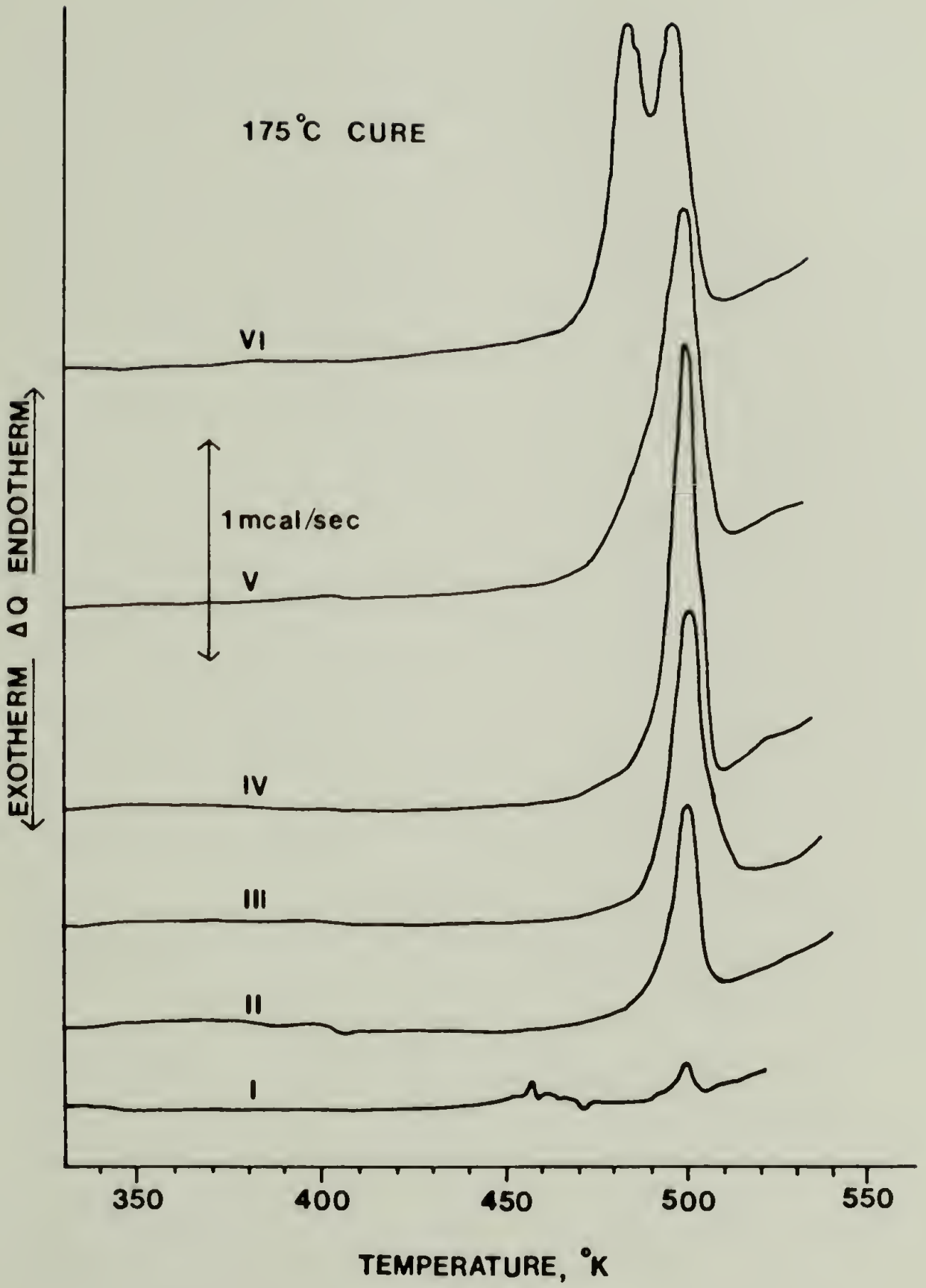

Figure 33. First run DSC scans of samples B-I to B-VII over the temperature range 330 - 550°K.

hard segment crystallinity as evidenced by very small endotherm and exotherm regions. All the melting transition peaks of sampels B-II to B-V bear remarkable resemblance to one another. Interestingly, the melting temperatures of these samples stays relatively constant at ~500°K despite the hard segment content. The heat of fusion (see Table 9) increases only slightly with increasing hard segment content. Sample B-VI displays double melting peaks centered at ~484 and ~497°K respectively. Both the melting temperature and heat of fusion (after correcting for sample hard segment content) decrease in this sample although it has the highest hard segment content in this series.

Figure 34 shows the DSC scans of skin and core regions of samples B-V and B-VI. The skin and core regions of samples B-V and B-VI do not show much differences by DSC. The core regions have a slightly higher melting transition temperature and heat of fusion than the skin regions as shown in Table 10. From the DSC measurements alone, the skin/core morphology difference in these two samples is not as pronounced as samples A-VI and A-VII in the 100°C series (also see optical micrographs).

TABLE 9

SUMMARY OF COMPOSITION AND HEAT OF FUSION FOR 175°C CURE
PPO-EO/MDI/BDO SAMPLES

SAMPLE DESIGNATION	PPO-EO/MDI/BDO MOLE RATIO	WT. FRACTION HARD SEGMENT*	DSC (cal/g)	
			POLYMER	HARD SEGMENT*
B-1	1/1.7/0.7	10.00	0.2	2.0
B-II	1/2.8/1.8	21.25	2.5	11.8
B-III	1/4.2/3.2	32.50	4.6	14.2
B-IV	1/6.1/5.1	43.75	6.4	14.6
B-V	1/9.1/8.1	55.00	8.0	14.6
B-VI	1/14.0/13.0	66.25	8.5	12.8

*CALCULATION OF WEIGHT FRACTION HARD SEGMENT BASED ON 1/L/M (MOLE RATIO PPO-EO/MDI/BDO) IS M(250+90) / 2000+L(250)+M(90)

TABLE 10

SUMMARY OF DSC RESULTS OF SKIN AND CORE REGIONS
OF SAMPLES B-V AND B-VI

SAMPLE DESIGNATION		DSC (cal/g)	
		POLYMER	HARD SEGMENT*
B-V	Skin	7.9	14.4
	Core	8.4	15.3
B-VI	Skin	8.0	12.1
	Core	9.0	13.6

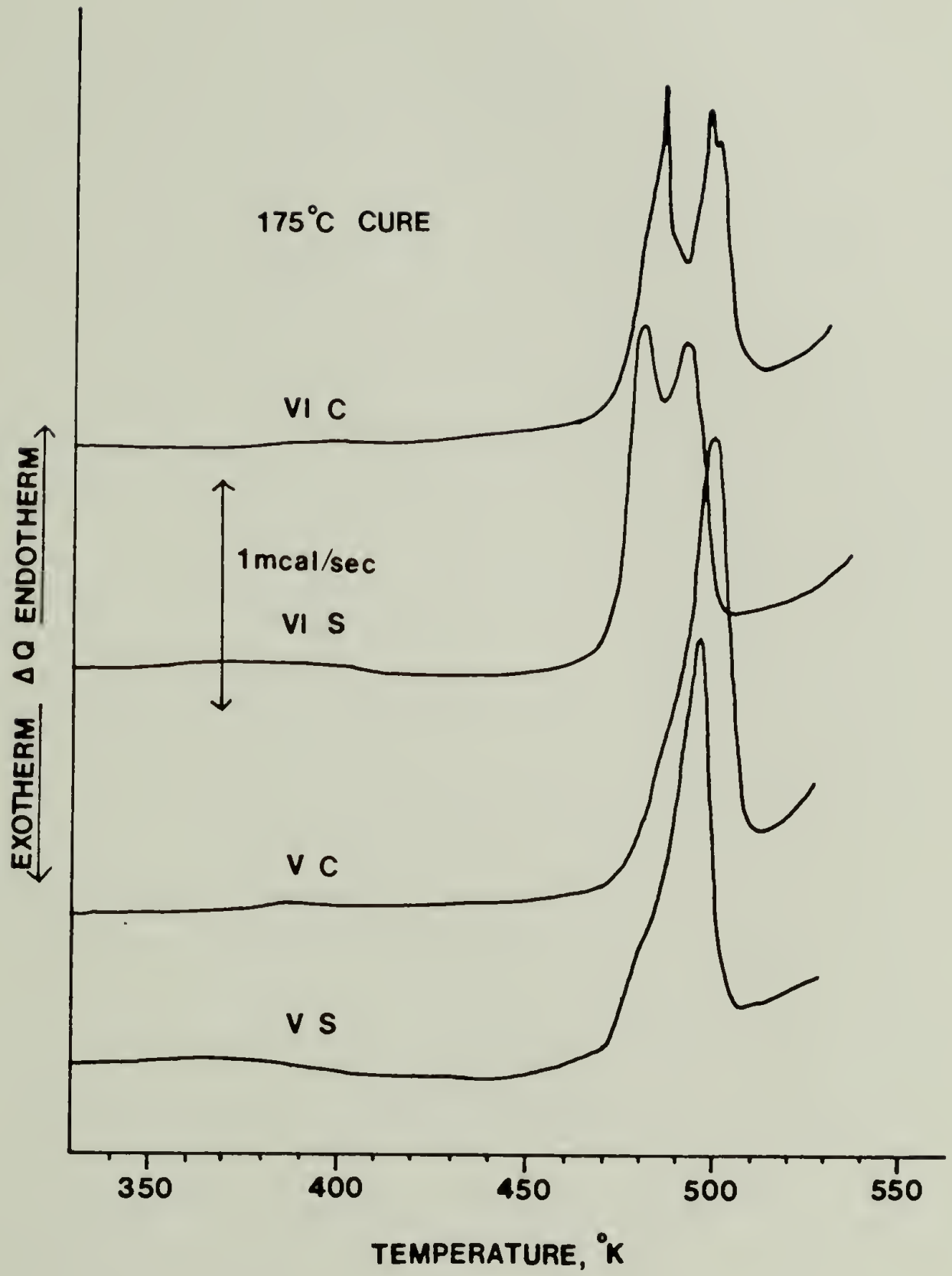

Figure 34. First run DSC scans of skin and core regions of samples B-V (55 percent hard segment) and B-VI (66 percent hard segment).

5.2 Optical Microscopy Results

The microstructures of samples B-I to B-IV appear uniform to the naked eye, whereas samples B-V and B-VI exhibit a detectable difference between the mold wall regions (skin) and the core regions. Figures 35a-c show the skin/core regions in samples B-IV, B-V and B-VI. Sample B-IV has a nearly uniform distribution of circular, optically birefringent regions across the mold. Figure 36a, at higher magnification, shows these regions to be spherulites. Samples B-V and B-VI have a decidedly non-uniform distribution of spherulites. For sample B-V the skin and much of the interior regions are optically isotropic with no spherulites visible until very near the sample center line. Sample B-VI, however, has small spherulites at the mold surface and at the centerline with a clear, optically isotropic region between them.

Detailed inspection of the optical micrographs of sample B-IV (see Figure 36a) reveals three main features: (i) large, well-defined spherulites, (ii) small, ill-defined regions of birefringence and (iii) many, isotropic dark regions, most of which appear to be circular in cross-section. Similar features are also seen in the core regions of samples B-V and B-VI (see Figures 36b and 36c). The hard segment-rich spherulites are smaller but better organized, displaying distinct Maltese cross patterns.

Figure 35. Low magnification optical micrographs (crossed polarizers) of samples B-IV(a), B-V(b) and B-VI(c).

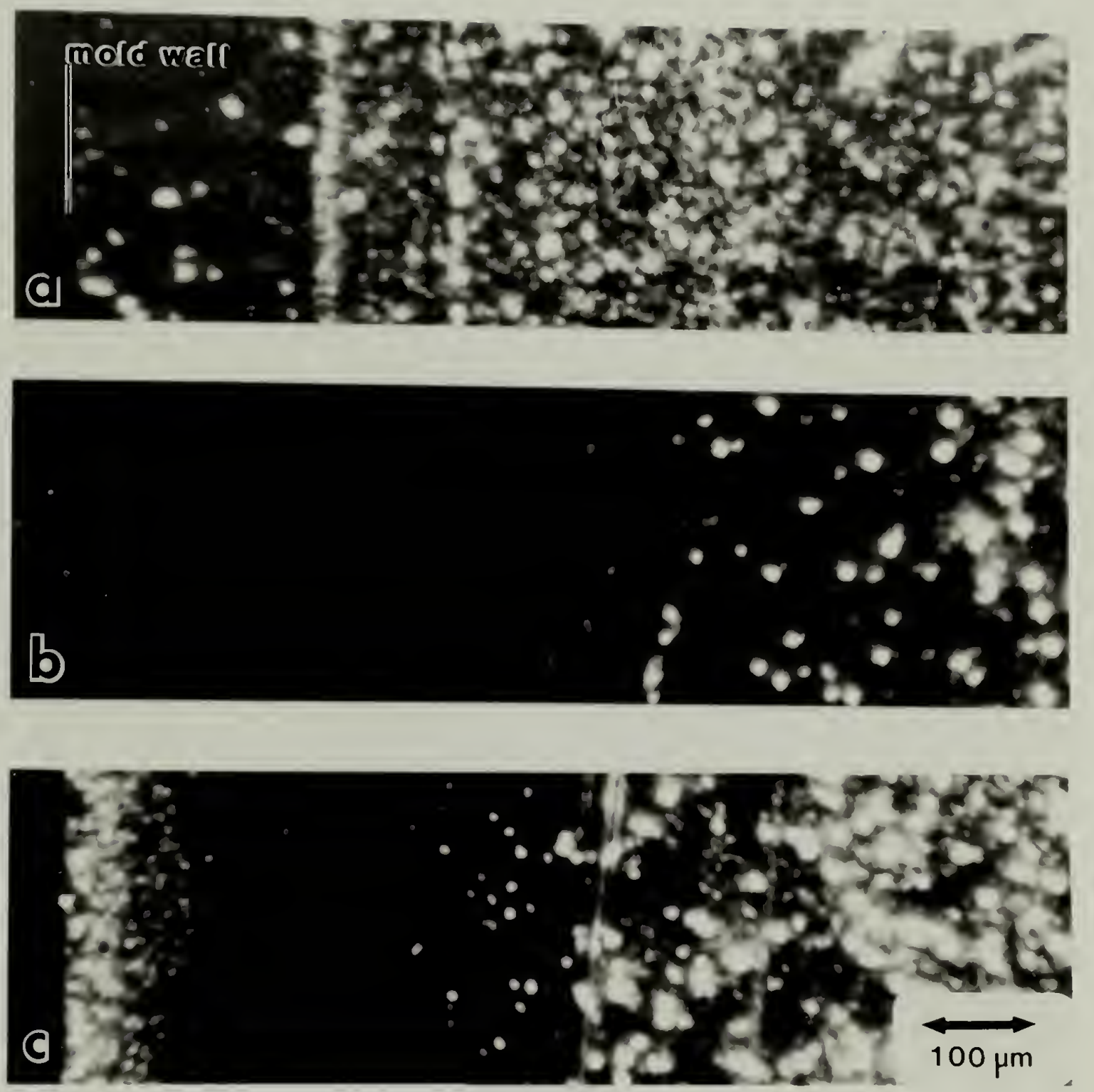

Figure 35

Figure 36. High magnification optical micrographs (crossed polarizers) of samples B-IV(a), B-V(b) and B-VI(c).

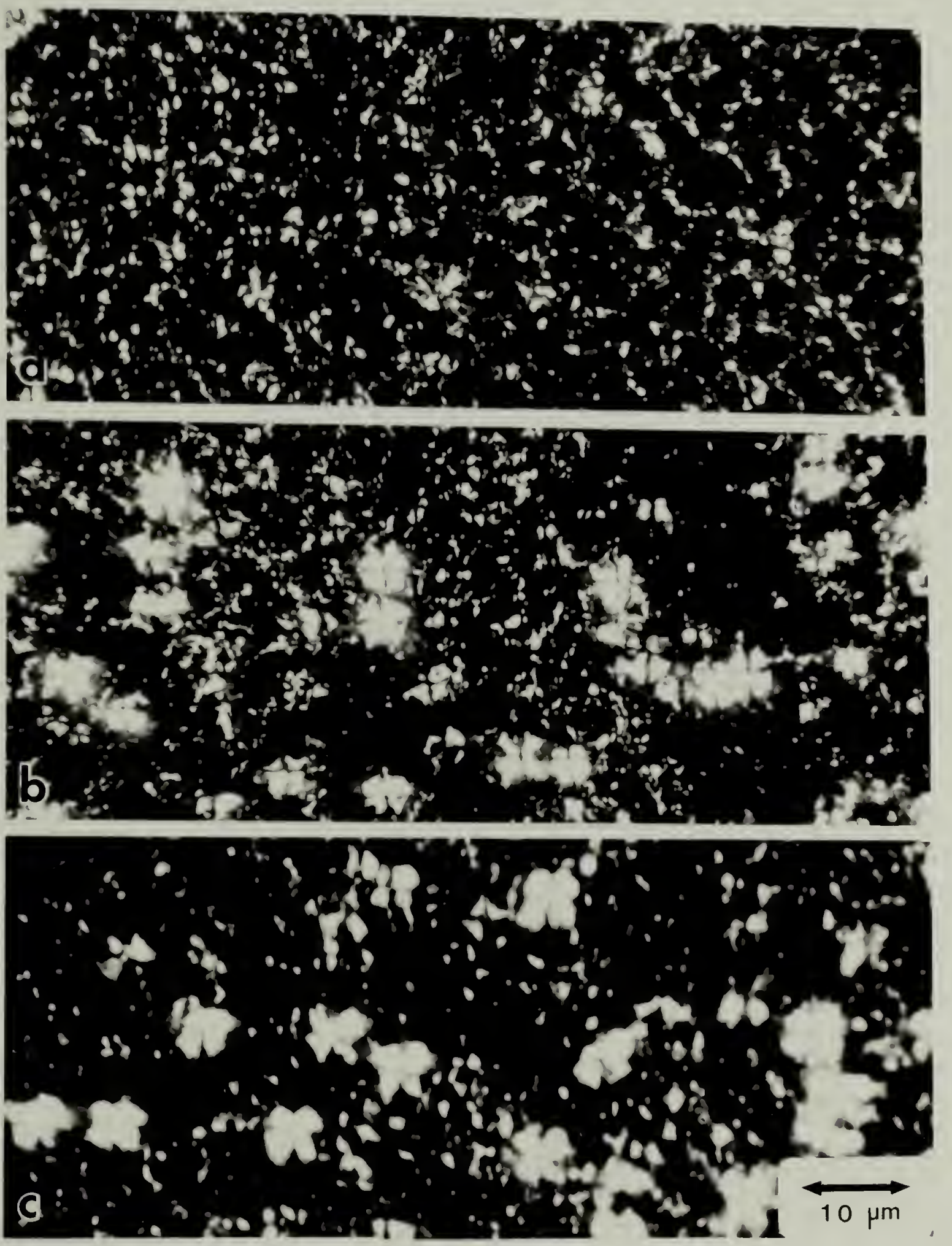

Figure 36

5.3 Transmission Electron Microscopy Results

Transmission electron micrographs of sample B-I of only 10 percent hard segment content show the presence of many diffuse blobs of approximately 3 μm size with much smaller dark regions ranging from 0.4 μm to .06 μm in size dispersed in the soft segment-rich matrix (see Figure 37). From the electron density contrast, the darker areas represent high concentrations of the hard segment.

Sample B-II (see Figure 38) also has many dark contrast globules (2-5 μm diameter) as well as the smaller dark regions scattered in the lighter contrast, soft segment-rich matrix. The globules tend to aggregate into groups. Figure 39 shows the structure of sample B-III, which is similar to that of sample B-II but with a larger volume fraction of globules (about 60 percent). There is a new feature present: many fibrillar structures connecting neighboring globules. These interconnecting fibrils range up to several microns in length. Figure 40 is a TEM micrograph of sample B-IV. The isotropic, black regions visible under polarized light appear as light contrast, somewhat spherulite-like (upper right corner) or globule-like (left center) regions in TEM. In the periphery of these regions, there is another layer of similar structure but of darker contrast. Smaller

Figure 37. TEM micrograph of the globular morphology of sample B-I (10 percent hard segment).

Figure 38. TEM micrograph of the globular morphology of sample B-II (21 percent hard segment).

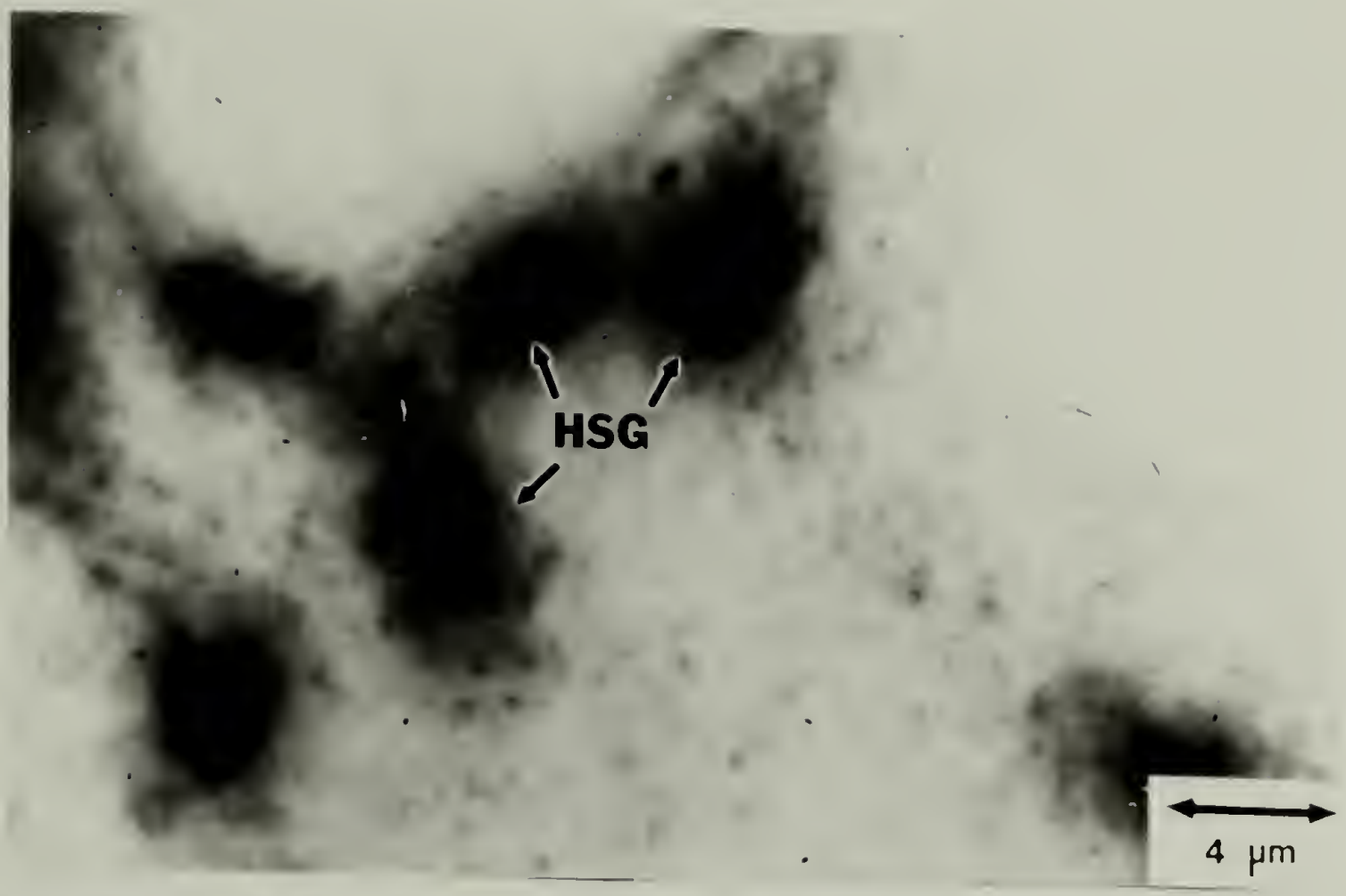

Figure 37

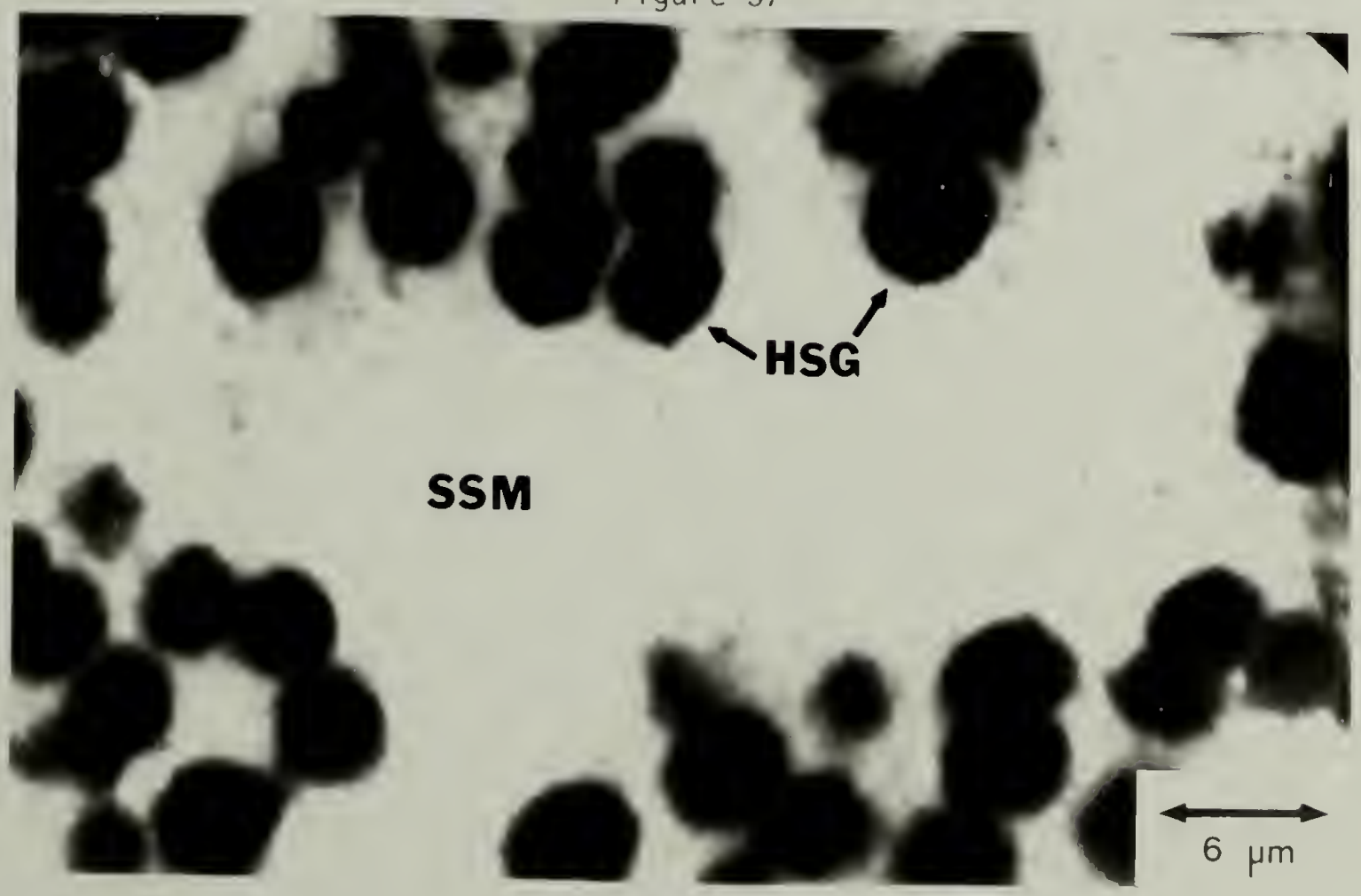

Figure 38

Figure 39. TEM micrograph of the globular morphology of sample B-III (32 percent hard segment).

Figure 40. TEM micrograph of sample B-IV (43 percent hard segment).

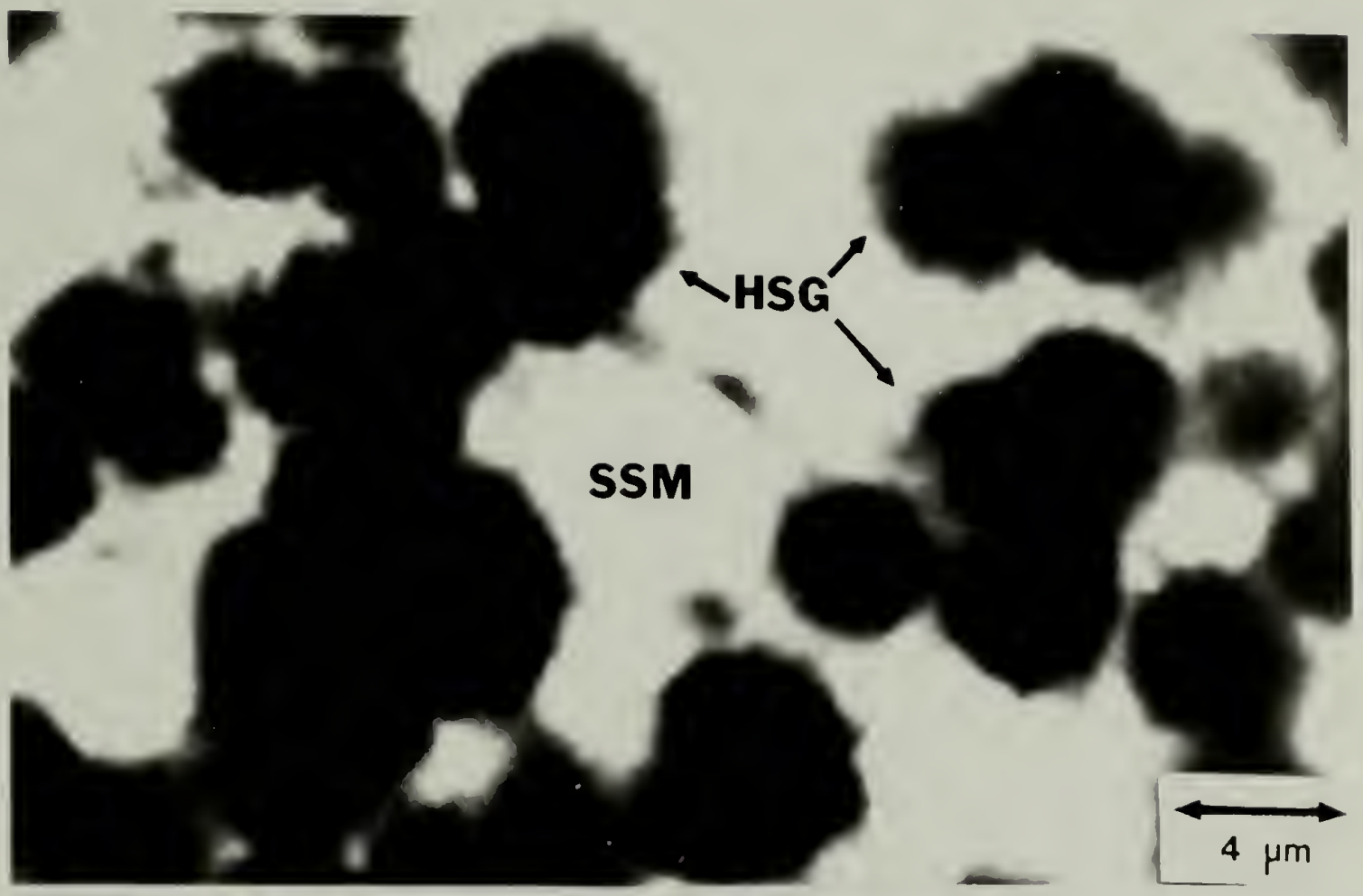

Figure 39

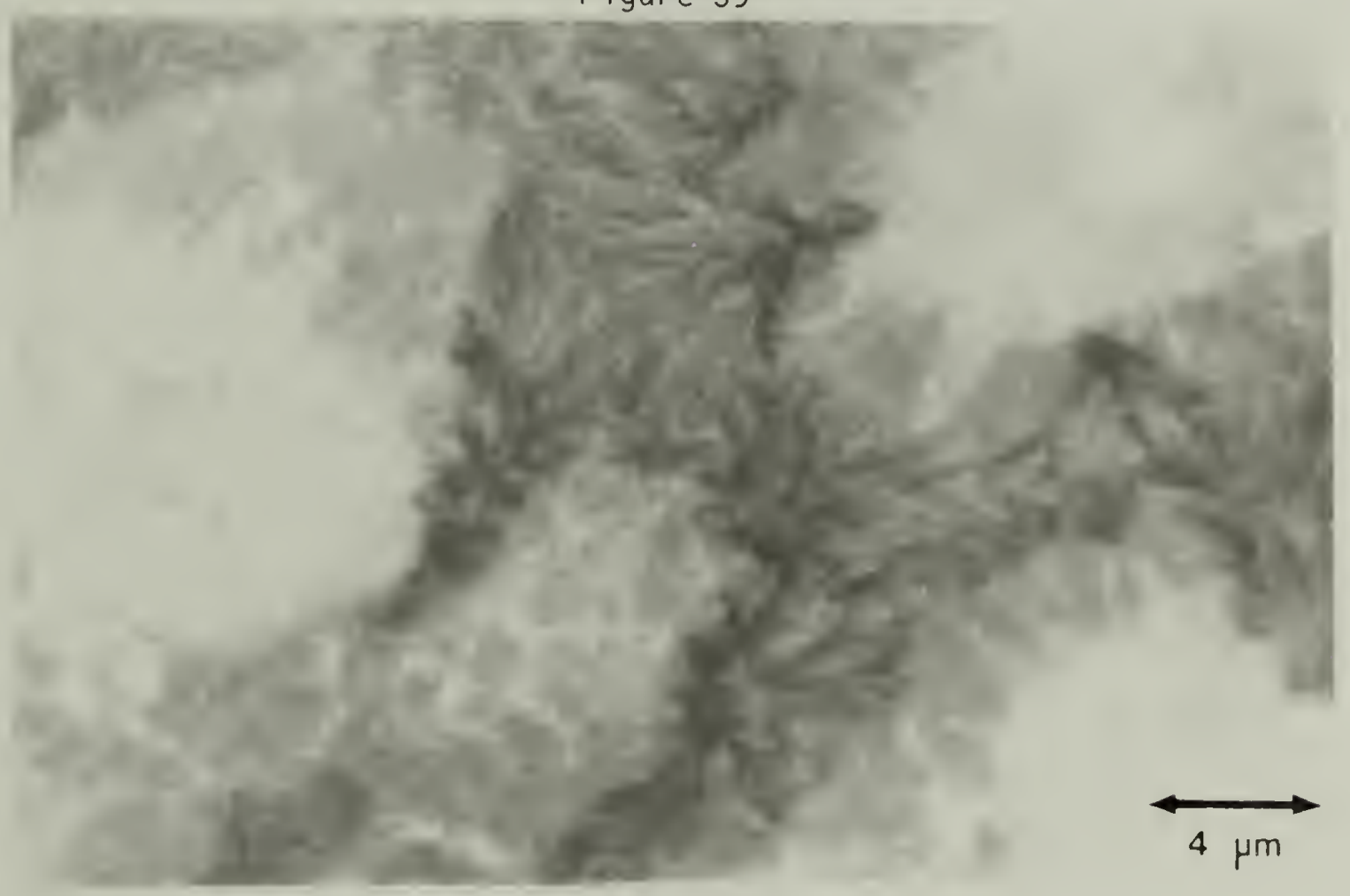

Figure 40

spherulites (darkest, textured regions) nucleate from the boundaries of these intermediate spherulite-like and globule-like entities. TEM micrographs of sample B-V are shown in Figures 41a and 41b, and reveal a very unusual morphology. Figure 41a shows the morphology near the transition zone between skin and core regions. Many "cauliflower-like" globules (5-20 μm diameter) and a few small spherulites (~1 μm diameter) are present. Figure 41b shows this same morphology in the core regions with the presence of large, well-defined spherulites (~20 μm diameter). The "cauliflower-like" entities seem to be aggregates of smaller clusters with concentrations of soft segment-rich molecules (lighter contrast areas) running between them like fingers. The reason for the formation of this unusual "cauliflower" structure is as yet unknown.

Sample B-VI has the most complex skin/core structure studied to date. The outmost skin layer and core regions show the presence of spherulitic superstructure, yet the region between appears isotropic (see Figure 35c).

The skin regions (see Figure 42a) show lots of the unusual cauliflower structures of about 5 μm size with small hard segment-rich spherulites filling in between them. However, no "cauliflower" structures are visible in the core regions (see Figure 42b), instead, very well-defined, large spherulites (~20 μm in diameter) and the

Figure 41. TEM micrographs of sample B-V (55 percent hard segment): (a) skin regions; (b) core regions.

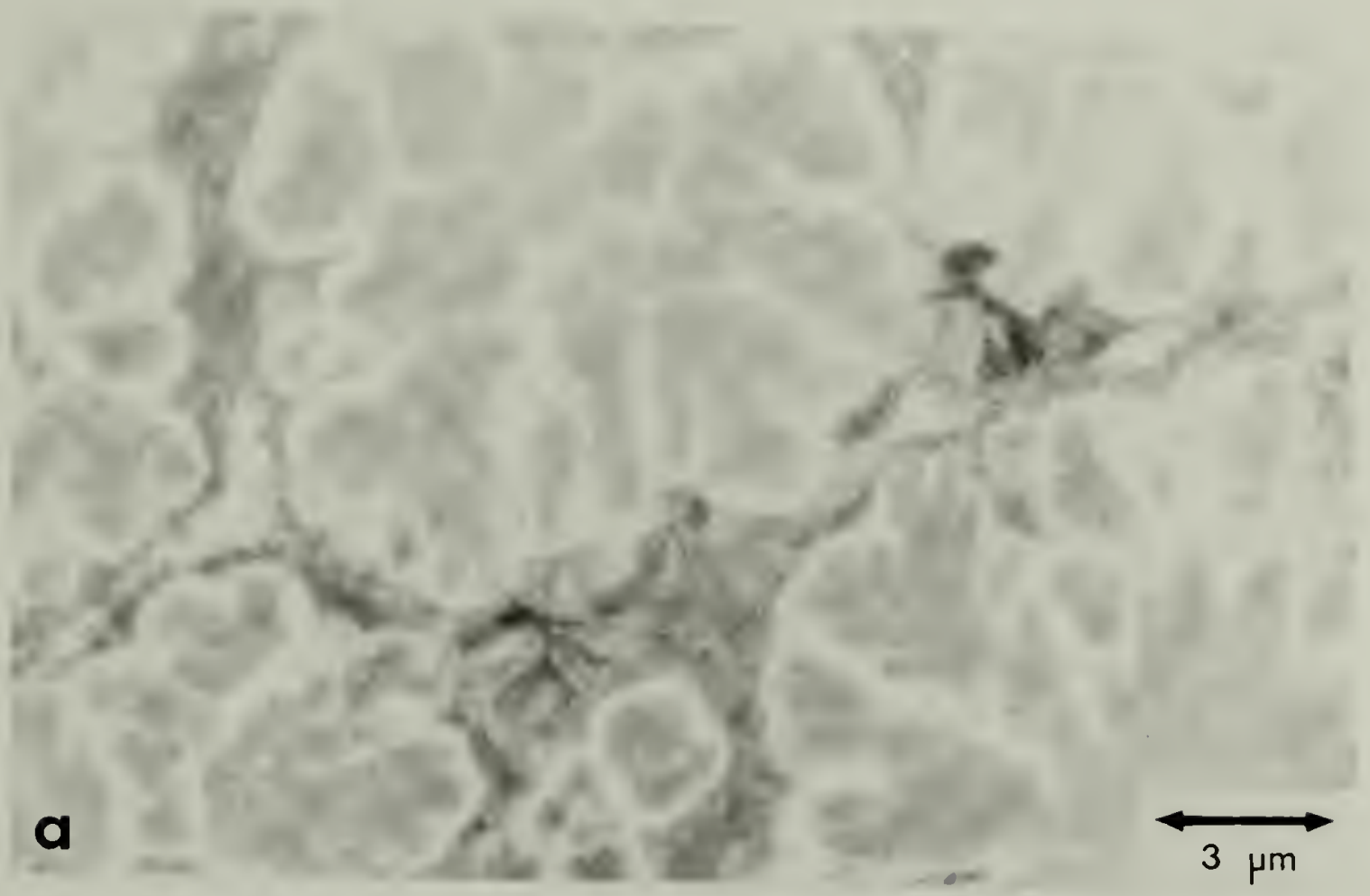

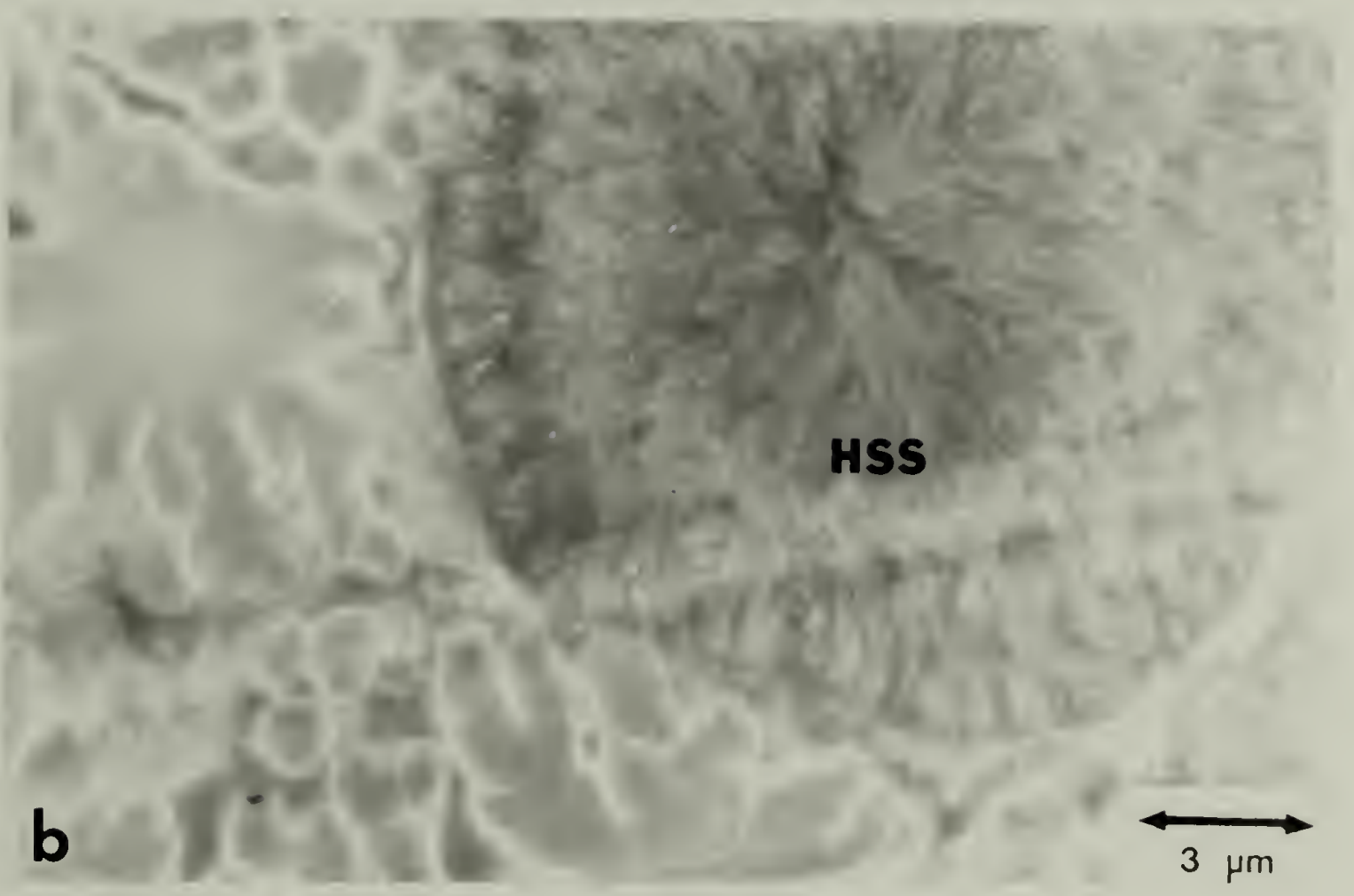

Figure 41

Figure 42. TEM micrographs of sample B-VI (66 percent hard segment): (a) skin regions; (b) core regions.

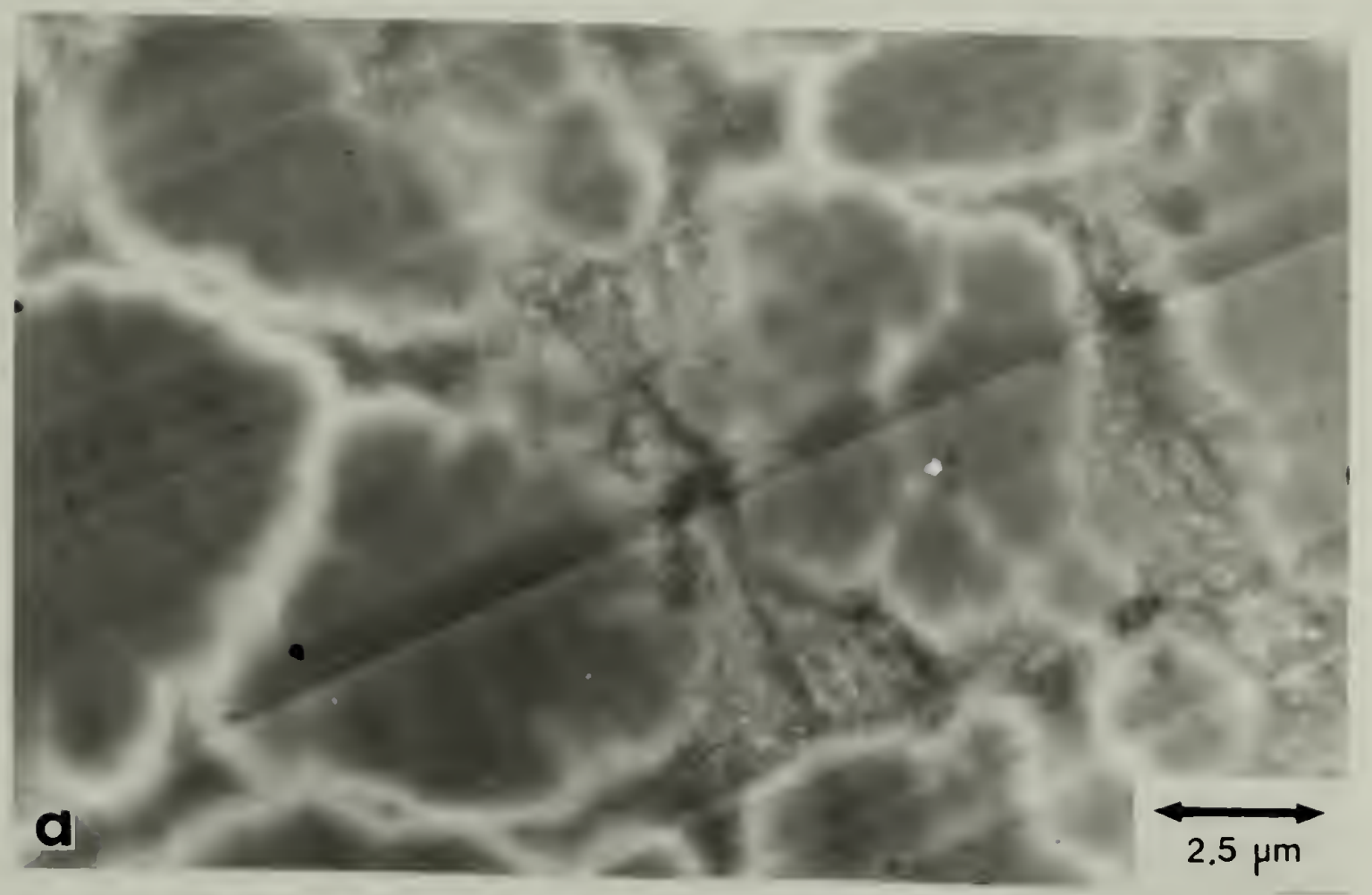

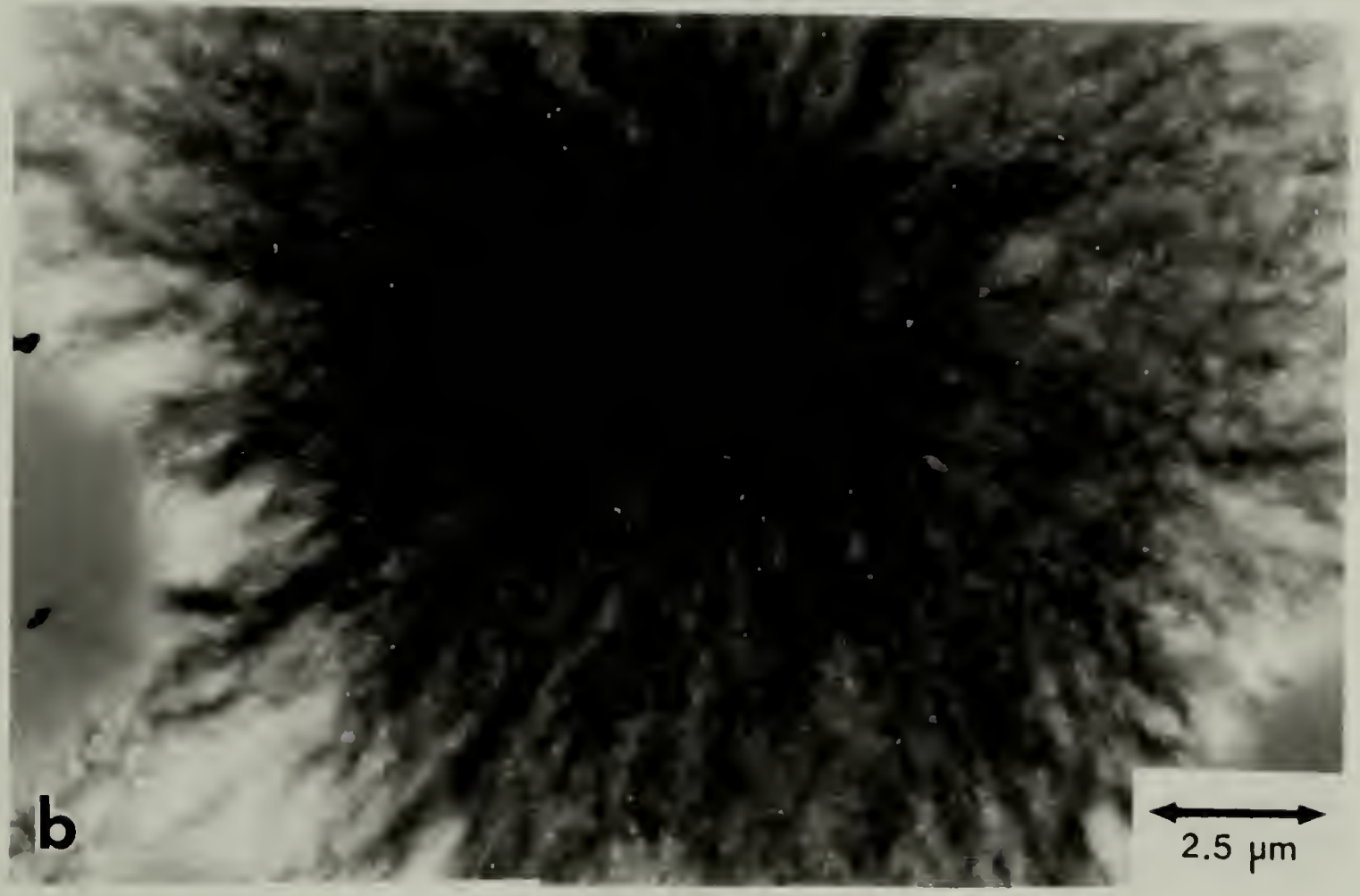

Figure 42

nearly spherical globules (which are commonly seen in the 100°C series) are present. Certainly the 175°C mold and cure temperature has not simplified the microstructure.

5.4 Wide-angle X-ray Scattering Results

Wide-angle X-ray scans of samples B-I to B-VI are shown in Figure 43. Apparently this series of samples is not as crystalline as 100°C cure series. Sample B-VI (66 percent hard segment) appears to have the highest degree of crystalline organization. Recall that for the reflection-diffraction geometry employed, most of the scattering occurs in the top 0.1 mm of the sample (i.e. the skin). Optical micrographs (see Figures 35a to 35c) show the skin layer of sample B-VI indeed has the highest crystalline organization.

5.5 Mechanical Properties

The mechanical properties of this series of samples range from a soft rubber at low hard segment content to a very tough thermoplastic at high hard segment content (see Figure 44). Modulus increases with increasing hard segment content while ultimate elongation decreases (see Table 11). Toughness reaches a plateau of about 1.6×10^9 Joules/m^3 at 32 percent hard segment and stays roughly

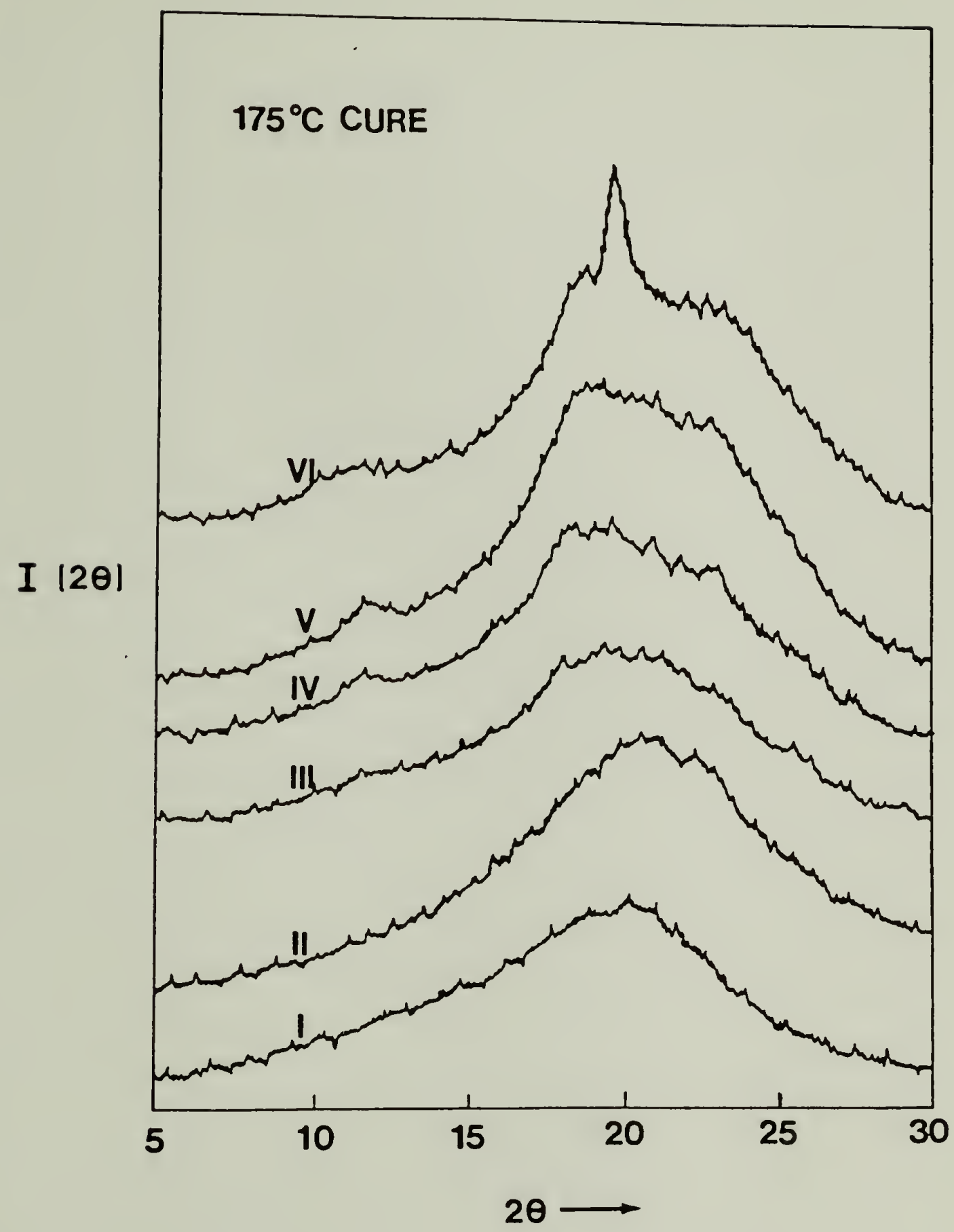

Figure 43. Wide-angle X-ray scans of samples B-I to B-VI; sample B-VI shows the sharpest reflections.

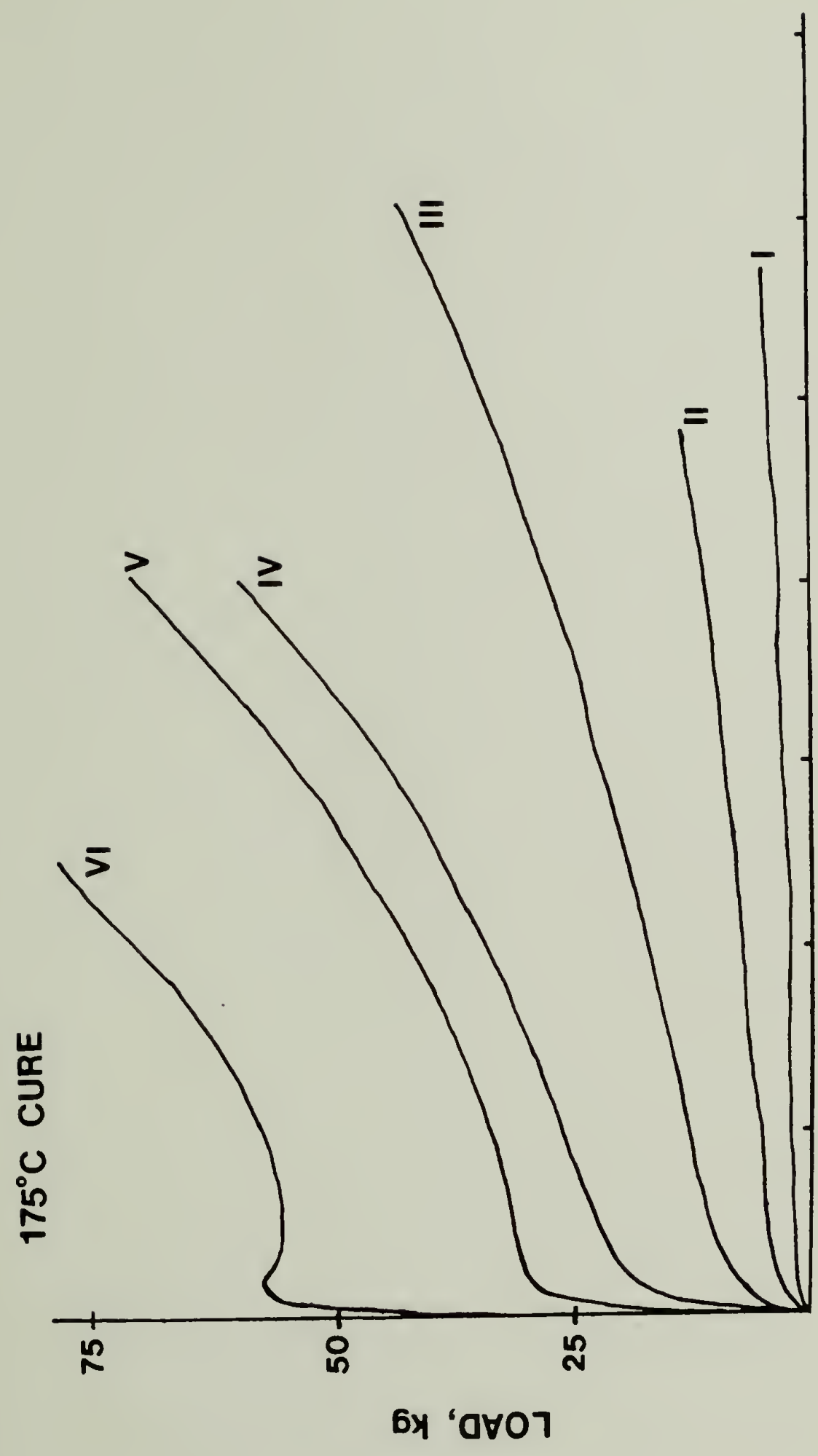

Figure 44. Load versus strain curves for samples B-I to B-VI.

TABLE 11

MECHANICAL PROPERTIES OF 175° CURE PPO-EO/MDI/BDO SAMPLES

SAMPLE DESIGNATION	WT.PERCENT SEGMENT	INITIAL MODULUS (MPa)	YIELD STRESS (MPa)	ULTIMATE ELONGATION (PERCENT)	FRACTURE STRESS (MPa)	TOUGHNESS Joules/m^3
B-I	10	0.7	----	1100	2.4	1.6×10^8
B-II	21	3.5	----	900	6.0	5.0×10^8
B-III	32	28	----	1200	21	1.6×10^9
B-IV	43	117	----	790	25	1.4×10^9
B-V	55	186	----	790	31	1.9×19^9
B-VI	66	559	26	530	37	1.9×10^9

TABLE 12

MECHANICAL PROPERTIES OF 100°C CURE PPO-EO/MDI/BDO SAMPLES

SAMPLE DESIGNATION	INITIAL MODULUS (MPa)	YIELD STRESS (MPa)	ULTIMATE ELONGATION (PERCENT)	FRACTURE STRESS (MPa)	TOUGHNESS Joules/m^3
A-I	1.4	----	700	1.7	8.3×10^7
A-II	5.5	----	800	7.8	3.3×10^8
A-III	34.4	----	1400	22	2.1×10^9
A-IV	130	----	1200	33	2.6×10^9
A-V	260	----	700	31	1.7×10^9
A-VI	520	30	400	33	1.2×10^9
A-VII	1400	44	40	38	1.6×10^8

the same with increasing hard segment content.

It is interesting to compare the mechanical properties of these samples cured at 175˚C to those cured at 100˚C (see Tables 11 and 12). The initial modulus and the modulus at 100 percent elongation show only slight differences. Fracture strength is slightly higher in the samples cured at 175˚C. Elongation at break is higher in the low hard segment content materials cured at 175˚C. The 100˚C cure materials show a maximum in ultimate elongation at intermediate hard segment content. This effect is also present in the 175˚C cure materials but, it is not as pronounced. The same trend is seen in the energy to break (toughness) for the two series. For the 100˚C cure, there is a maximum in toughness at about 40 percent hard segment content, while at 175˚C the toughness seems to reach a plateau at about 30 percent hard segment and stay roughly constant through 66 percent hard segment.

5.6 Discussion and Conclusions

The morphologies of 175˚C cure PPO-EO/MDI/BDO samples are very complicated and completely different from those of 100˚C cure samples. Apparently the high temperature cure cannot eliminate the skin/core morphology and sintlicify the interpretation of their structure-properties.

Based on the previous discussion on adiabatic temperature rise during polymerization reaction in Chapter IV, the maximum temperatures attained under adiabatic conditions for 175°C cure samples can be at least 75°C higher than those of 100°C cure samples, which means the maximum temperature rise will be well into the melting range of the crystalline hard segment phase even for samples with medium or low hard segment content. For samples B-I to B-III, the high temperature reaction might push the polymerization reaction to completion and promote further phase separation. As shown in TEM micrographs, samples B-I to B-III have a very similar phase separated globular morphology despite hard segment content. The corresponding 100°C cure samples A-I to A-III, on the other hand, show a gradual change from globular to spherulitic morphology as the hard segment content is increased.

The maximum temperature rise during curing for samples B-IV to B-VI might be so high that depolymerization, crosslinking and degradation reactions could occur. In fact, the 78 percent hard segment sample could not be prepared because the temperature rise was so high that the sample was charred. Possible crosslinking reactions might be the formation of allophanate linkage (in the case of diol chain extender), biuret linkage (diamine chain extender) and trimerized isocyanate rings.

The very complicated morphologies present in these samples may arise from the above mentioned side reactions caused by high temperature polymerization. Further systematic work will be necessary in order to understand these complicated morphologies.

C H A P T E R VI

POLYURETHANES WITH BUTENE DIOL
-AN APPROACH TO STAINING OF THE HARD SEGMENT DOMAINS

The understanding and characterization of both large scale superstructure with spherulite formation and small scale domain-crystallite ordering is of great interest in the study of polyurethane morphology. Unfortunately, the TEM investigation of small scale polymer microstructures proves to be very difficult and sometimes futile. The insufficient density contrast between phases, small crystal structure with low crystallinity, and thick specimen section make the unambiguous identification of the domain structure extremely difficult. Through the technique of selective staining of one phase, we hope to sufficiently enhance the contrast for the domain structure to be visualized via bright field TEM observation.

The polyurethane system used in this study is based on polypropylene oxide endcapped with polyethylene oxide polyol (PPO-EO), 4,4'-diphenylmethane diisocyanate (MDI), but instead of butane diol, 1,4 butene diol (BEDO) is used as the chain extender. The use of BEDO permits selective staining of the MDI/BEDO hard segment with osmium tetroxide reaction with the double bond. We anticipate the stained samples to show improved mass thickness

contrast between hard phase domains and the surrounding matrix. Since butene diol differs from butane diol by only a double bond, we expect MDI/DEDO hard segment should not differ much from MDI/BDO hard segment. The study of MDI/BEDO hard segment domain structure should be representive to that of MDI/BDO hard segment. In the following, DSC, optical microscopy, WAXS and SAXS were done to confirm that MDI/BEDO is indeed similar to that of MDI/BDO and therefore worth of study.

6.1 Differential Scanning Calorimetry Results

Figure 45 shows DSC scans of the as-reacted samples BEDO-I, BEDO-II and BEDO-III (10, 44 and 70 wt. percent hard segment). Sample BEDO-I typically shows either no transition peak (as indicated by I) or multiple transition peaks (as indicated by I') depending on the precise sampling region. The multiple transition peaks in curve I' are attributed to induced crystallization (exotherm) and re-melting (endotherm) during the DSC scan. Sample BEDO-II shows a transition peak centered at 471°K and sample BEDO-III shows much larger transition peaks centered at ~480°K and ~488°K. Since sample BEDO-II has very low crystallinity, an effort was made to improve its crystallinity by annealing. Figure 46 shows DSC results of both the as-reacted (II) and heat-treated (II') BEDO-II

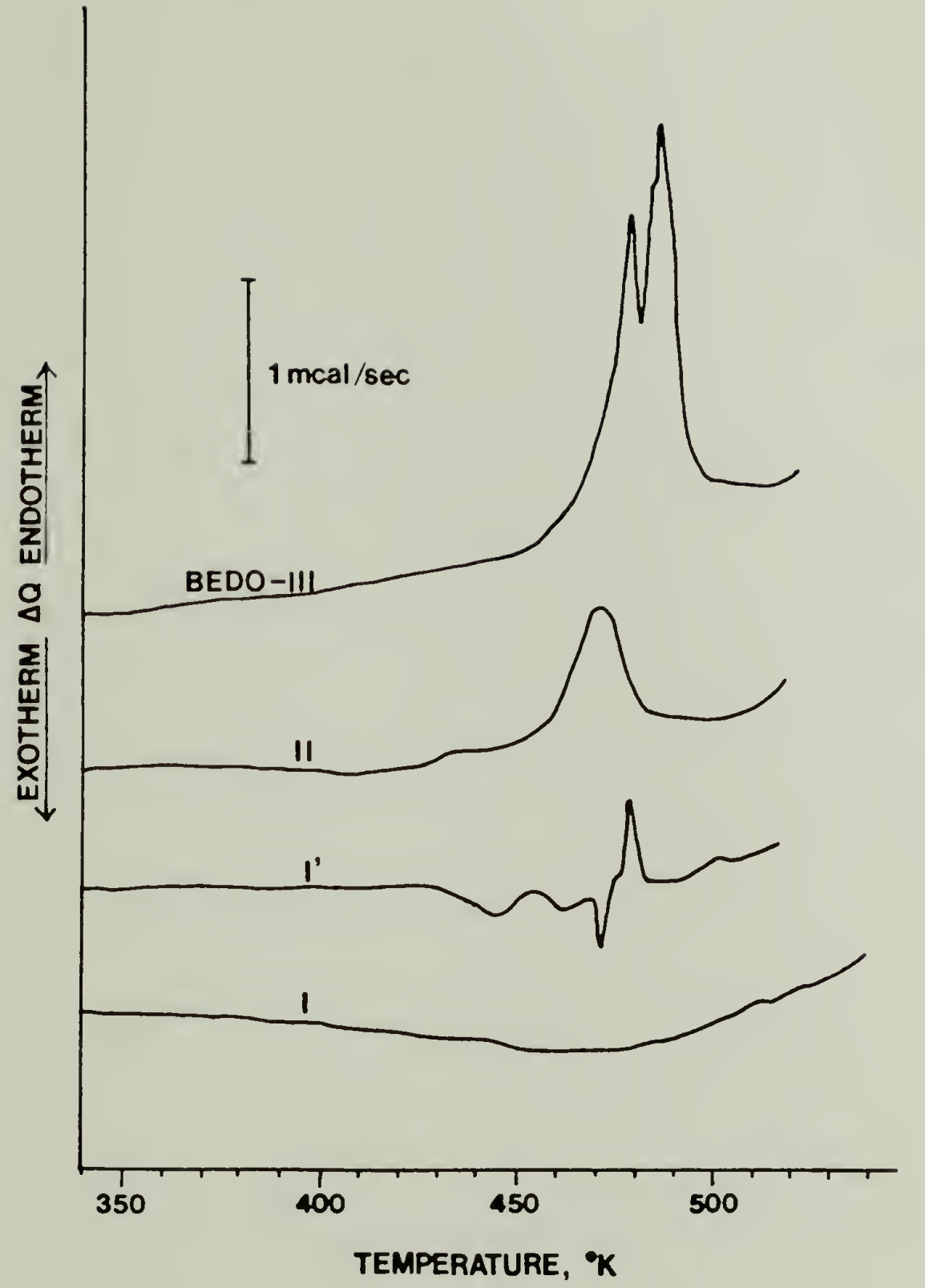

Figure 45. First run DSC scans of samples BEDO-I to BEDO-III (I and I' are two different sampling regions for sample BEDO-I).

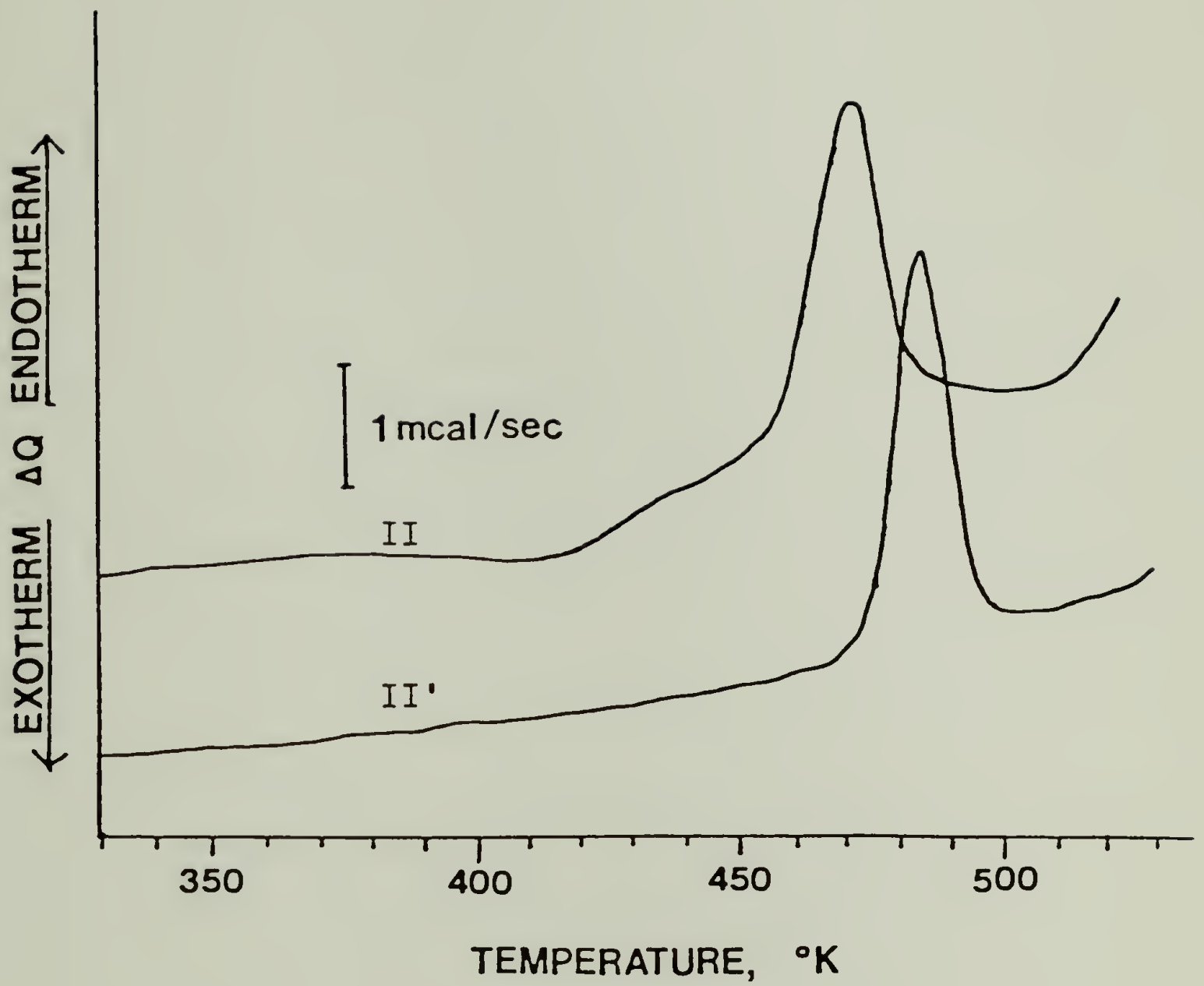

Figure 46. DSC scans of both the as-reacted (II) and annealed (II') sample BEDO-II.

sample, which was annealed at 450°K in the DSC for 3 hours and then slowly cooled at 0.31°C/min. to room temperature and rescanned. Both melting transition temperature and heat of fusion have been increased by annealing (471 vs. 386°K and 5.8 vs. 3.3 cal/g respectively). The heat of fusion of these samples are summarized in Table 13.

TABLE 13

SUMMARY OF COMPOSITION AND HEATS OF FUSION FOR AS-REACTED AND ANNEALED PPO-EO/MDI/BEDO SAMPLES

SAMPLE DESIGNATION	PPO/EO/MDI/BEDO MOLE RATIO	WT. FRACTION hard segment*	DSC (cal/g)	
			POLYMER	HARD SEGMENT*
BEDO-I	1/1.74/0.74	10.00	~0	~0
BEDO-II	1/6.18/5.18	43.75	3.3	7.5
BEDO-II'**			5.8**	13.2
BEDO-III	1/23.93/22.93	77.50	9.7	12.4

*CALCULATION OF WEIGHT FRACTION HARD SEGMENT BASED ON 1/L/M (MOLE RATIO PPO-EO/MDI/BDO) is M(250+88)/2000+L(250)+M(88)

**ANNEALED AT 450°K FOR 3 HOURS AND THEN COOLED AT 0.31°C/min. TO 400°K AND RESCAN.

6.2 Optical Microscopy Results

Figure 47 shows an optical micrograph of sample BEDO-I under crossed polarized light. A few isolated spherulites about 5 μm diameter size are scattered in the predominantly soft segment-rich matrix. These spherulites show a very well-defined Maltese cross extinction pattern. since sample BEDO-I has only 10 percent by weight hard segment content, the appearance of such well-defined spherulites is unusual and leads further support to the microemulsion polymerization ideas developed in Chapter IV. Sample BEDO-II shows two different types of extinction pattern under crossed polarizers, i.e. a well-defined Maltese cross pattern which corresponding to larger, well-formed spherulites, and speckles of birefringent area which corresponding to smaller, poorly formed spherulites/or crystallites (see Figure 48). There appear to be two different crystallization modes present in this sample. The larger, well-defined spherulites nucleate first and grow; followed later by nucleation of the smaller, poorly formed spherulites which fill the matrix. Figure 49a shows the morphology as a function of cross-section position of the as-reacted sample BEDO-III. This position dependent morphology can only be found in higher hard segment

Figure 47. Optical micrograph (crossed polarizers) of sample BEDO-I (10 percent hard segment).

Figure 48. Optical micrograph (crossed polarizers) of sample BEDO-II (43 percent hard segment).

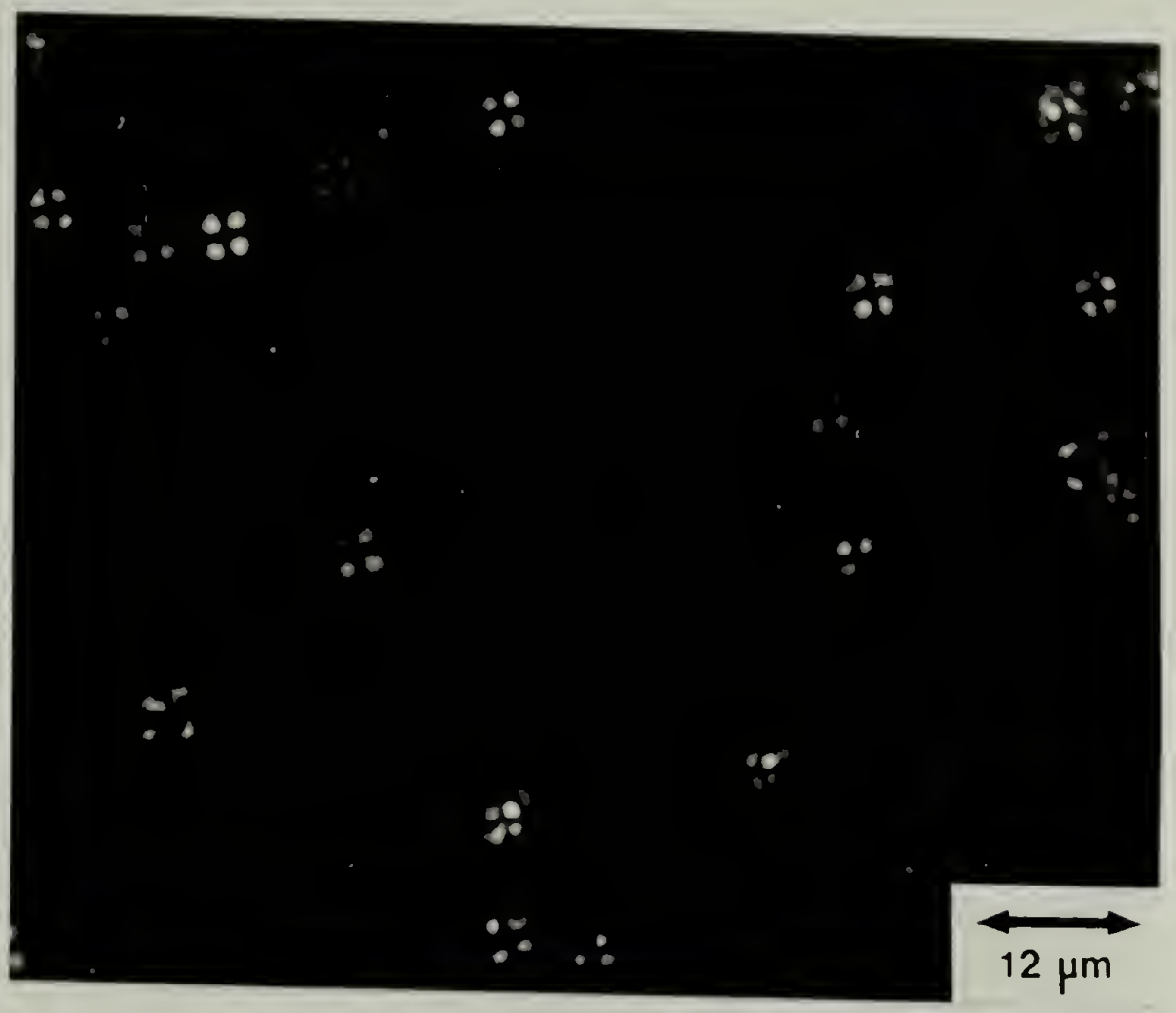

Figure 47

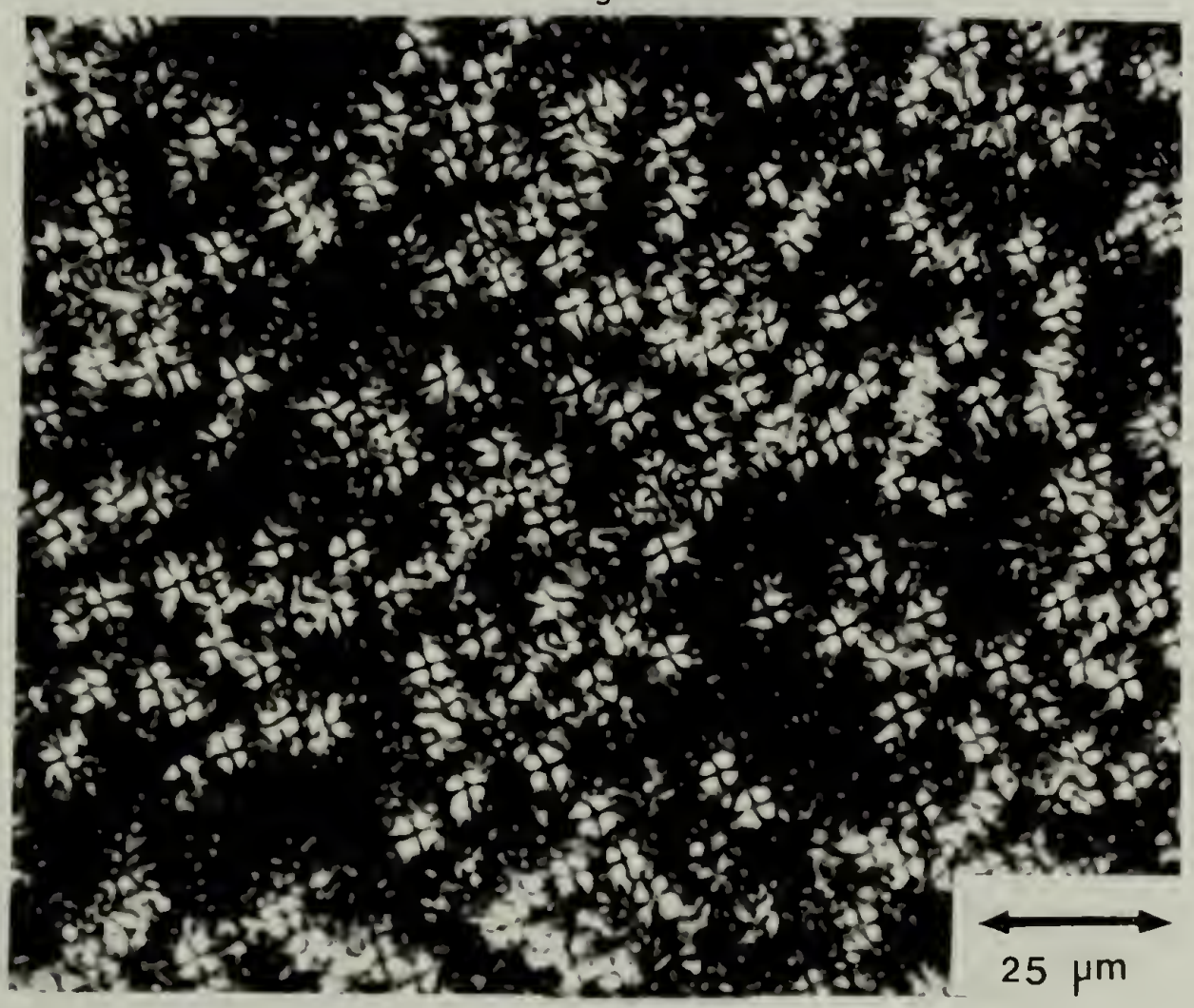

Figure 48

Figure 49. Optical micrographs (crossed polarizers) of sample BEDO-III (78 percent hard segment) showing a structure with three different layers.

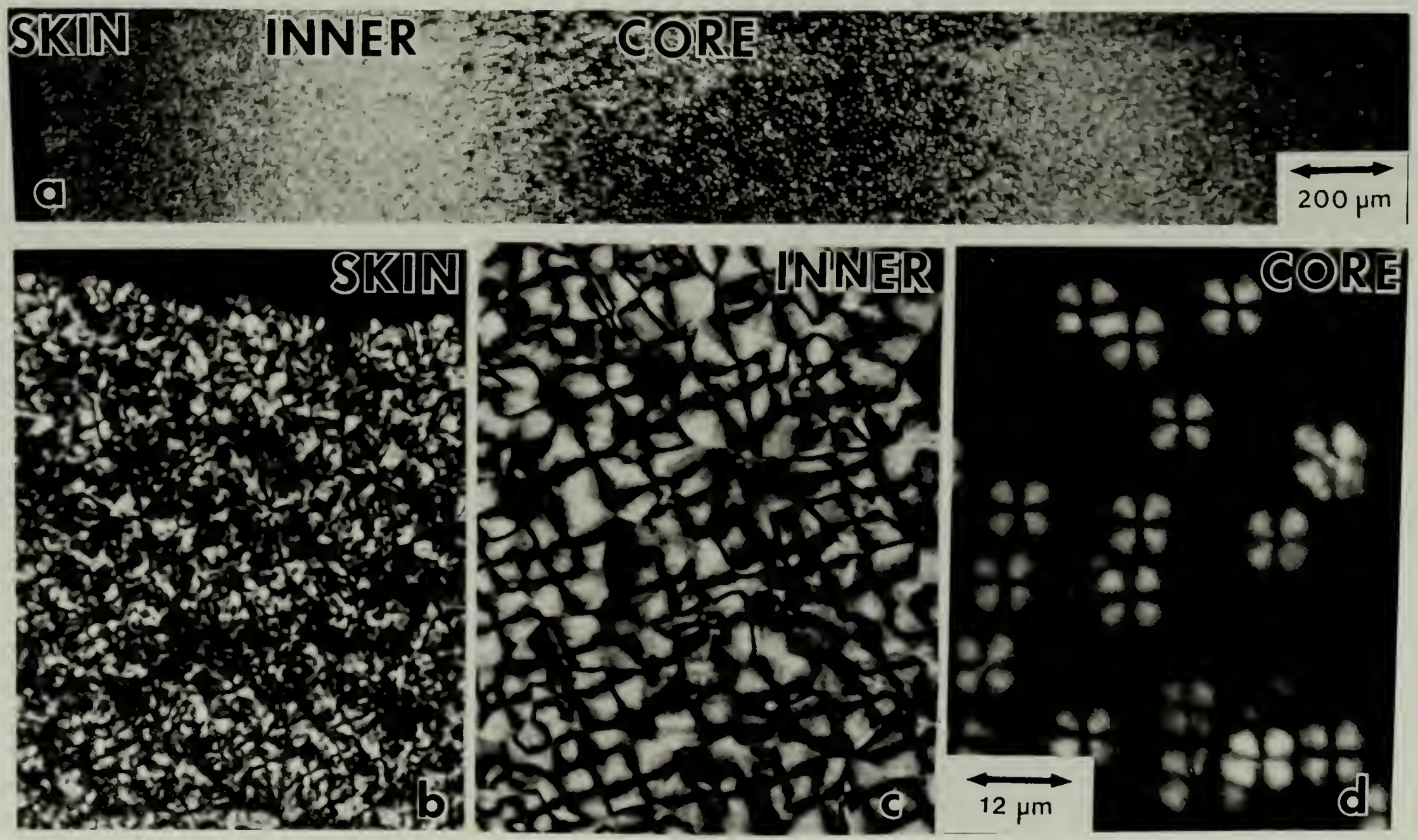

Figure 49

content samples, approximately greater than 60 percent by wt. hard segment, as mentioned in Chapter IV. There are three different morphology zones present: skin, inner and core layers in Figure 49a.

Figures 49b to 49d show the different structures of these three zones at higher magnification under crossed polarizers. The skin layer (Figure 49b) shows only a few identifiable Maltese cross patterns (well-defined highly anisotropic spherulites) present, with many irregular and smaller birefringent regions. The inner layer (Figure 49c) consists of volume filling spherulites (10-15 μm diameter), which have very strong birefringence and well-defined Maltese crosses. The core layer (Figure 49d) actually consists of two distinct sizes of spherulites. In addition to the presence of some isolated, well-defined larger spherulites (~8 μm diameter), there are also a lot of much smaller spherulites/or crystallites in the matrix as evidenced from the presence of speckles of birefringence. More details about this skin/core morphology are given in the following TEM section.

6.3 Transmission Electron Microscopy Results

Figure 50 shows a TEM micrograph of a cryo ultramicrotomed section of sample BEDO-I. It reveals sporadic occurrence of spherulitic superstructure, which is hard

Figure 50. TEM micrograph of sample BEDO-I (10 percent hard segment), note the presence of hard segment-rich spherulite.

Figure 51. TEM micrograph of sample BEDO-II (43 percent hard segment) showing non-volume filling spherulites morphology.

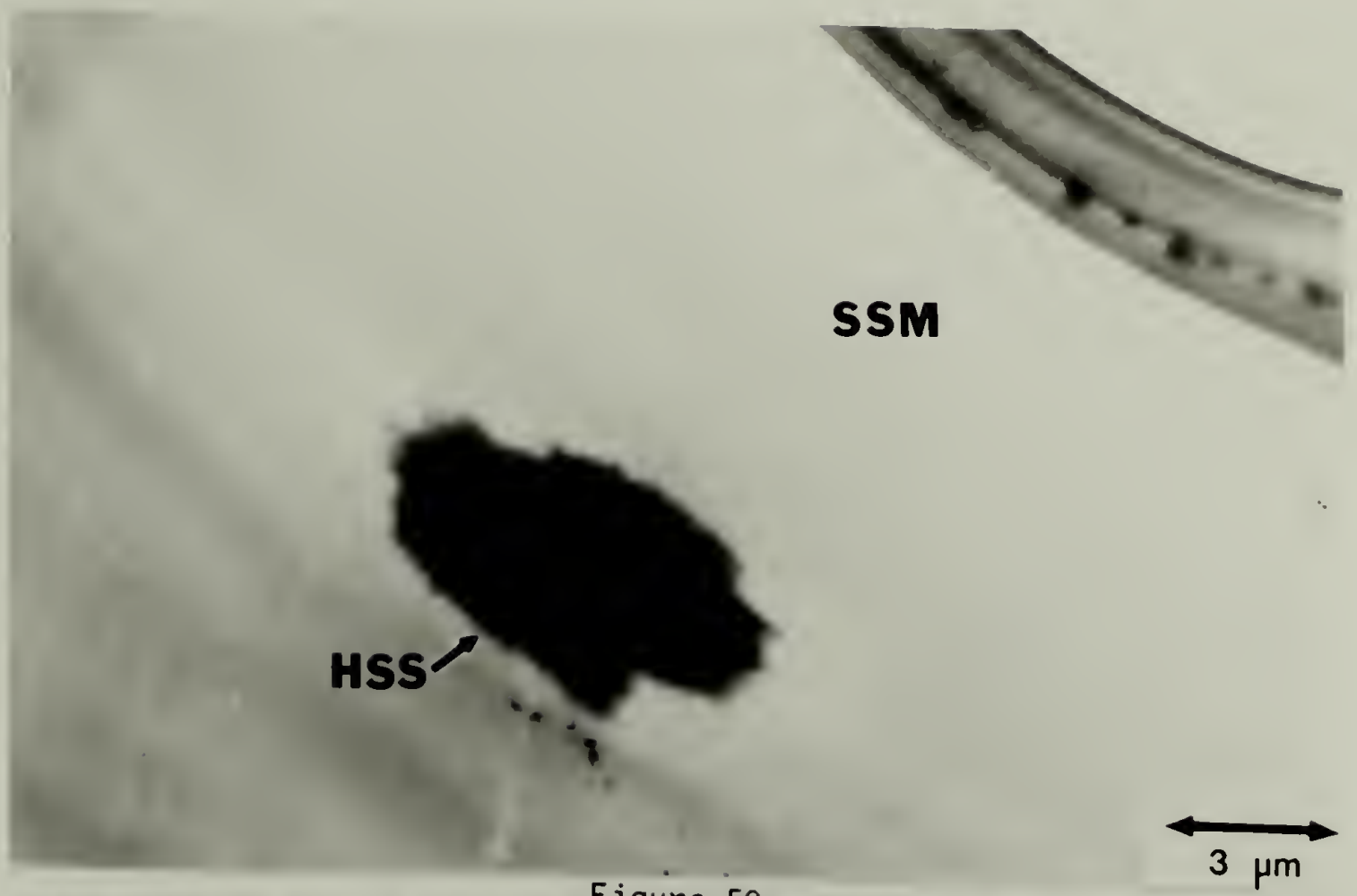

Figure 50

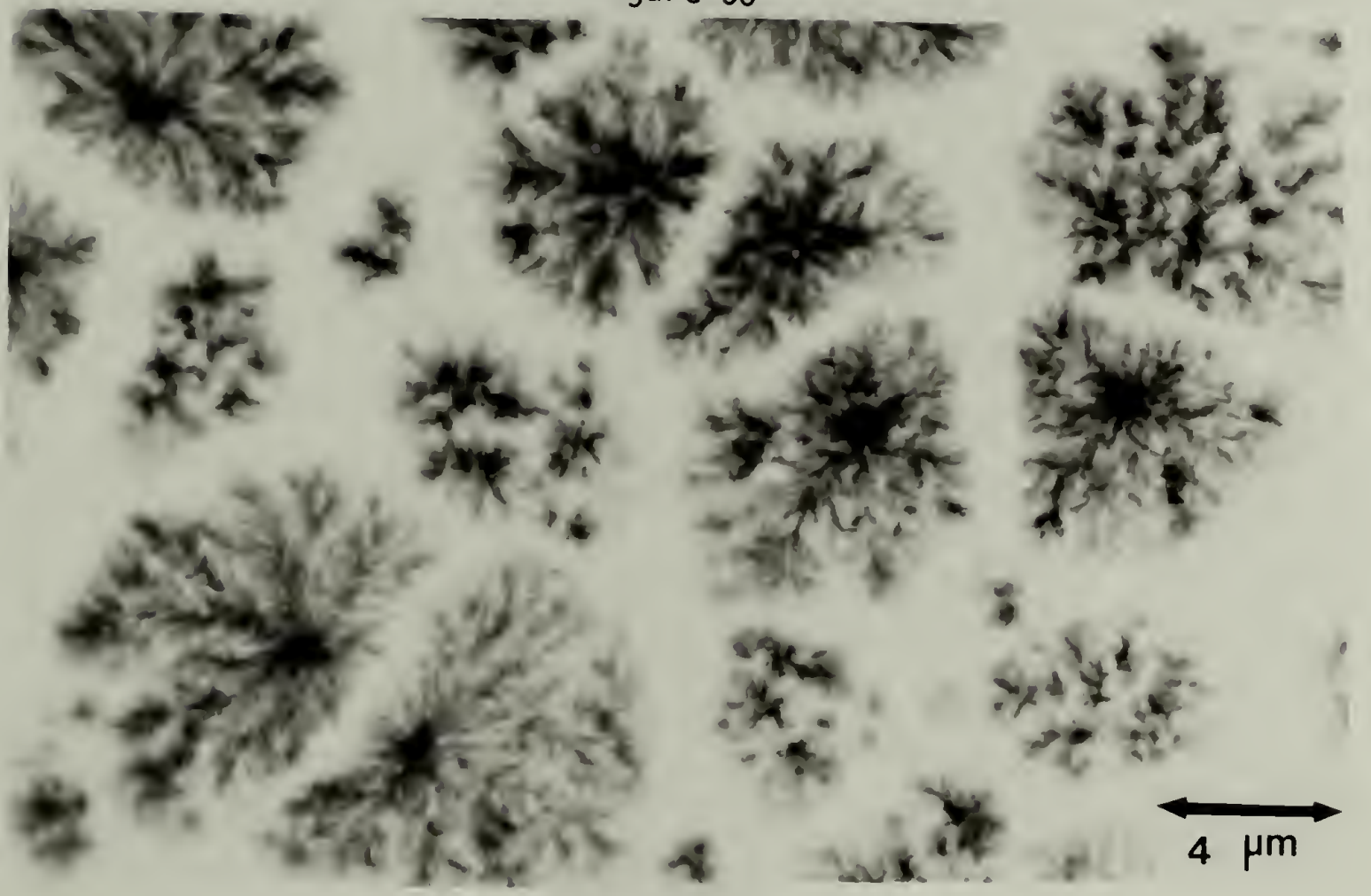

Figure 51

segment-rich, embedded in the predominantly soft segment-rich matrix. The average spherulite size is about 5 μm. From the area fraction measurements of spherulites and matrix, the volume fraction of spherulites is determined to be about 5 percent. Sample BEDO-II, as shown in Figure 51, has many spherulites ranging from 1-8 μm diameter embedded in the soft segment-rich matrix. In this case, the volume fraction of spherulites accounts for about 60 percent of total area measured, which is rather high considering the overall sample hard segment content and the low heat of fusion value. Therefore significant soft segment must be incorporated in the formation of spherulite, i.e. about 25 percent.

Figure 52 is a higher magnification micrograph of the as-reacted sample BEDO-II. The boundaries of the spherulites are rather diffuse. The morphology of the annealed sample (BEDO-II') shows no further growth of the spherulites, but the spherulites boundaries appear sharper than those of the as-reacted sample (see Figure 53) indicating better phase separation (or perfection of crystals) occurred after heat treatment.

Figures 54 and 55 show the morphology of the skin and core regions of sample BEDO-III. In the skin regions (Figure 54), there are volume filling spherulites. Besides the presence of familiar radial textured spherulites with only one identifiable nucleus (denoted by "a" in the

Figure 52. TEM micrograph of as-reacted sample BEDO-II (43 percent hard segment).

Figure 53. TEM micrograph of annealed sample BEDO-II (43 percent hard segment).

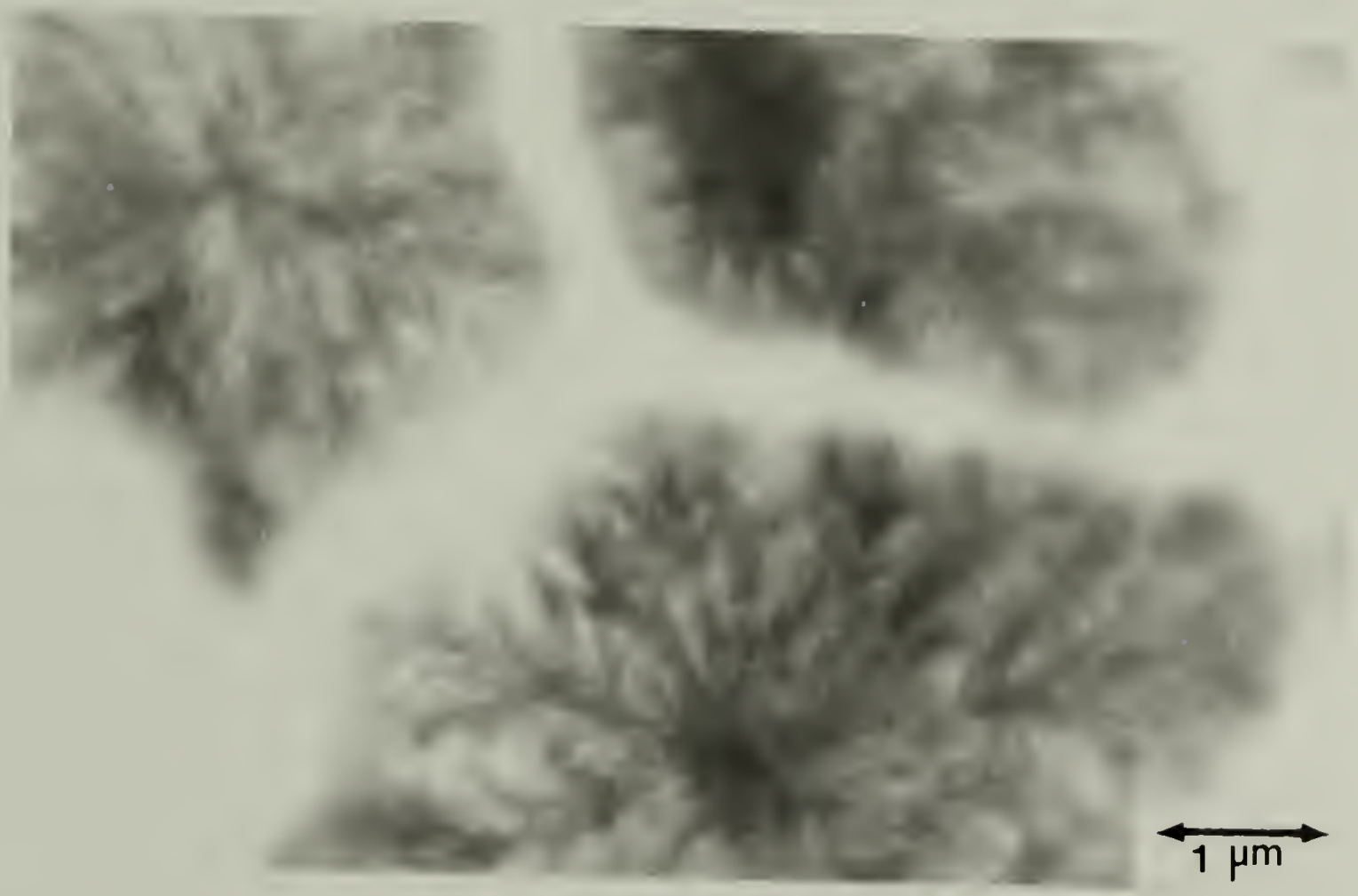

Figure 52

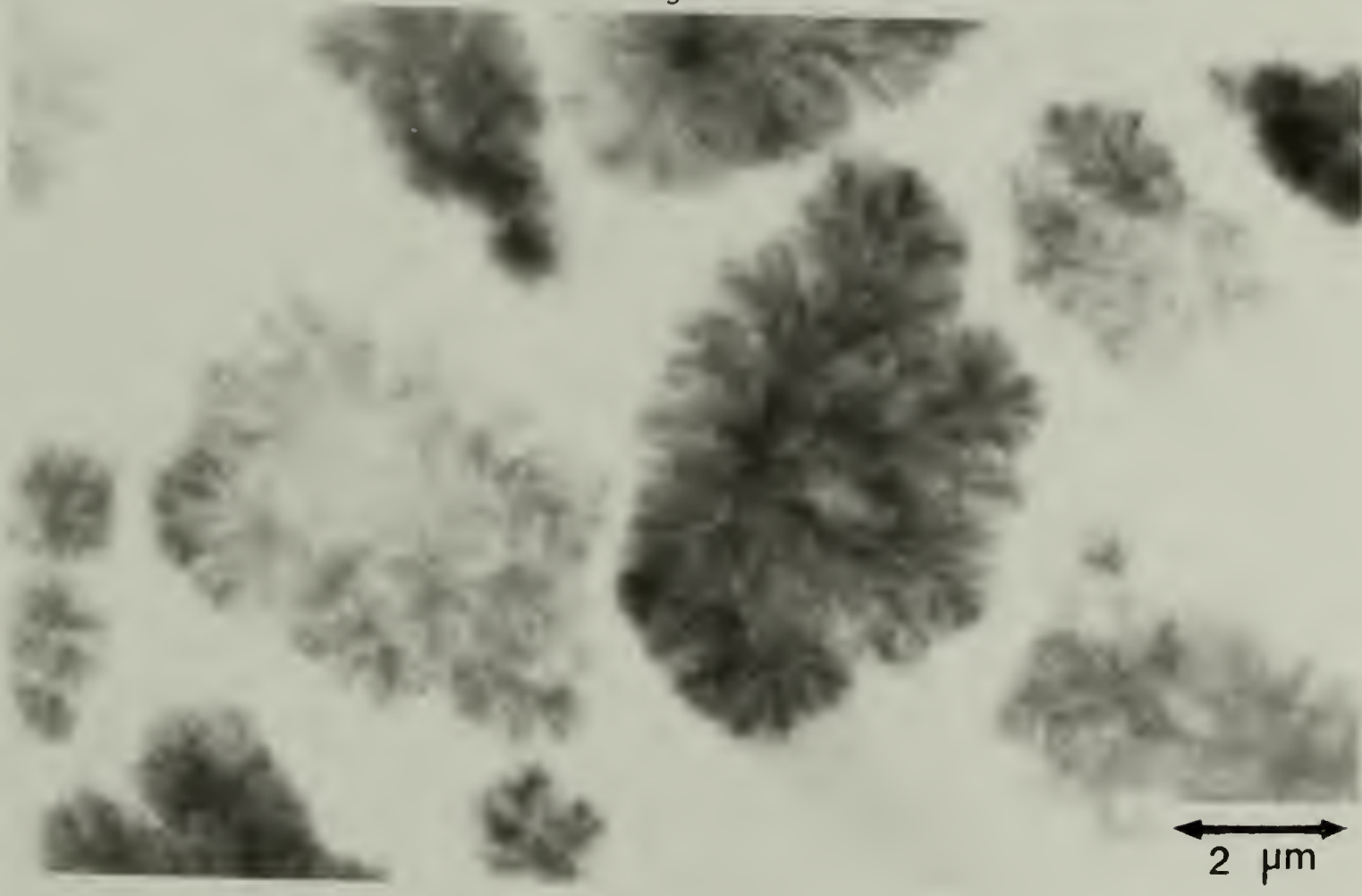

Figure 53

Figure 54. TEM micrograph of the skin regions of sample BEDO-III (78 percent hard segment) showing two different types of spherulite.

Figure 55. TEM micrograph of the core regions of sample BEDO-III (78 percent hard segment).

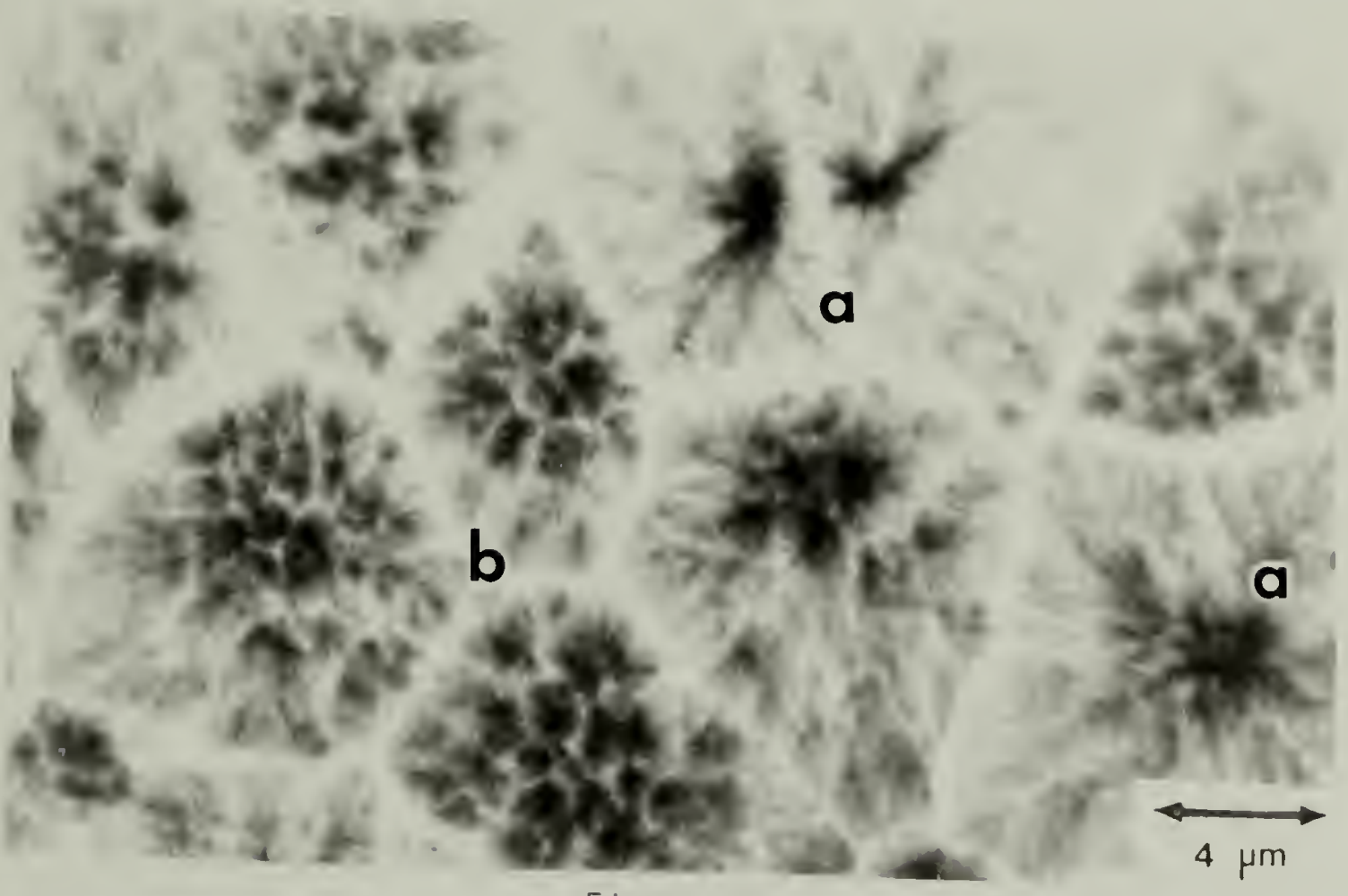

Figure 54

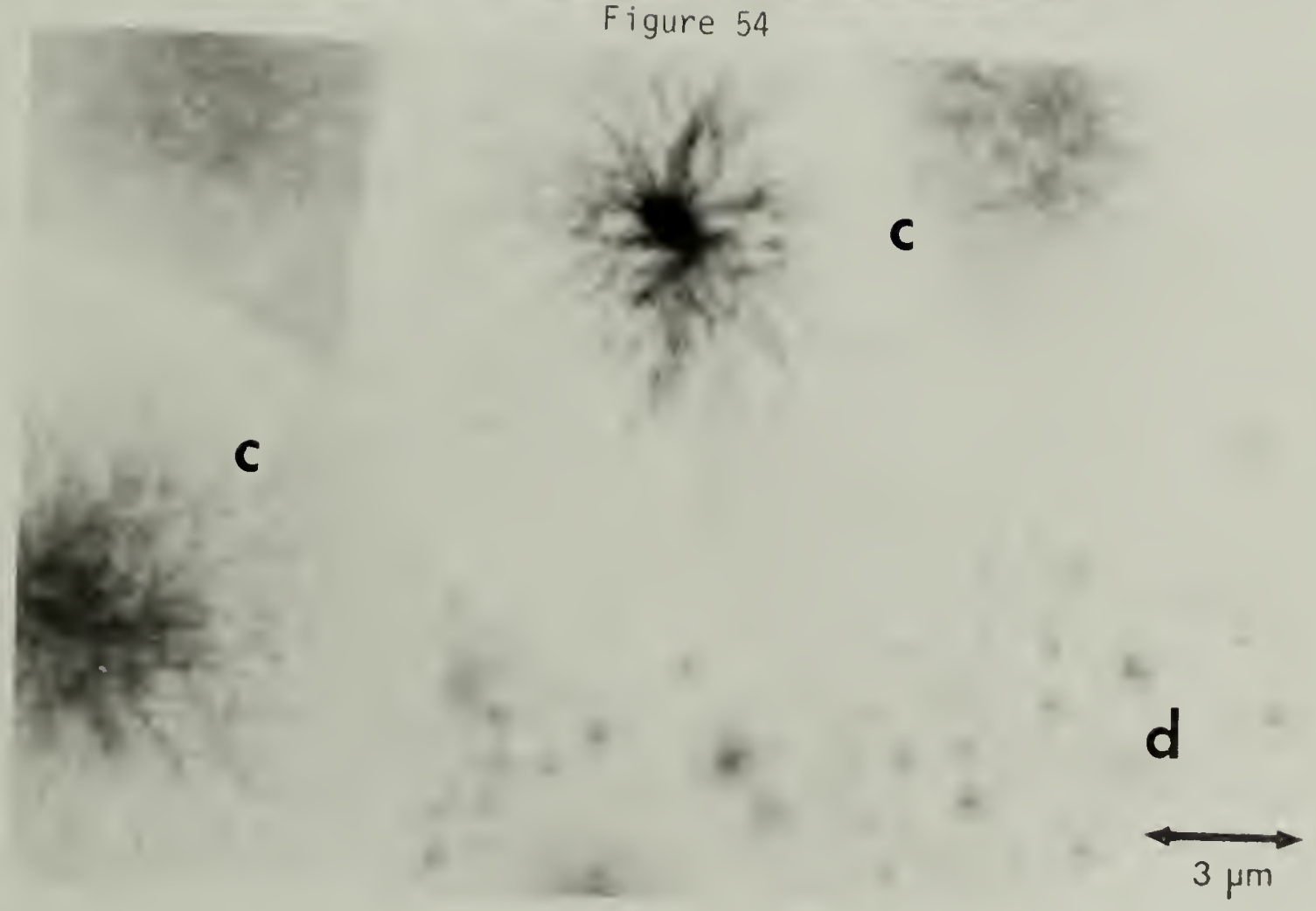

Figure 55

figure), there also exists uncommon looking "spherulite-clusters" with multiple nuclei (denoted by "b"). To the author's knowledge, this is the first report on such a multiple nuclei containing spherulite. It is unclear how these entities are formed. Under crossed polarized light, the "spherulite-clusters" do not show the distinct Maltese cross extinction patterns (see Figure 49b).

Figure 55 shows the morphology of the core regions of sample BEDO-III. Similar to the finding of the optical results shown in Figure 49d, the core regions contain volume filling spherulites of two quite different sizes - a few larger spherulites (~15 μm diameter) surrounded by many smaller spherulites (1-3 μm diameter). Both spherulite size groups are well-organized, differing only in size. There must be two different modes of nucleation-crystallization occurring in the core regions during solidification. A few spherulites nucleated first and grew, then after some time many more spherulites nucleated and quickly filled all the remaining matrix. The morphology of inner layer regions is not shown, but consists of volume filling spherulites similar to that of the core regions. It also should be noted that the spherulites boundaries in the core regions seem much more resistent to radiation damage than those of the skin regions.

6.4 Wide-angle X-ray Scattering Results

Wide-angle X-ray scattering patterns of the as-reacted samples BEDO-I, II, III and pure hard segment copolymer (MDI/BEDO, powder form, from solution polymerization) are shown in Figure 56 and their results are summarized in Table 14. Even at very low hard segment content, sample BEDO-I (10 percent by wt. hard segment) possesses a crystalline peak centered at ~7.4 Å and a very broad amorphous peak at ~4.2 Å. The 7.4 Å crystalline peak indicates that sample BEDO-I has some sort of paracrystalline order, which is consistent with the TEM results showing the presence of spherulites. Since sample A-I of the 100°C cure PPO-EO/MDI/BDO series (also 10 percent by wt. hard segment) shows neither WAXS crystalline peak nor the formation of spherulite in TEM, the MDI/BEDO hard segment is easier to crystallize than MDI/BDO hard segment in the same soft segment based polyurethanes. No evidence of soft segment crystallization is observed. The strongest lines for PEO crystals at 4.63 and 3.81 Å, as well as for isotactic PPO* crystals at 4.21 and 5.18 Å, do not appear.

---

* Our samples contain atactic PPO segment only.

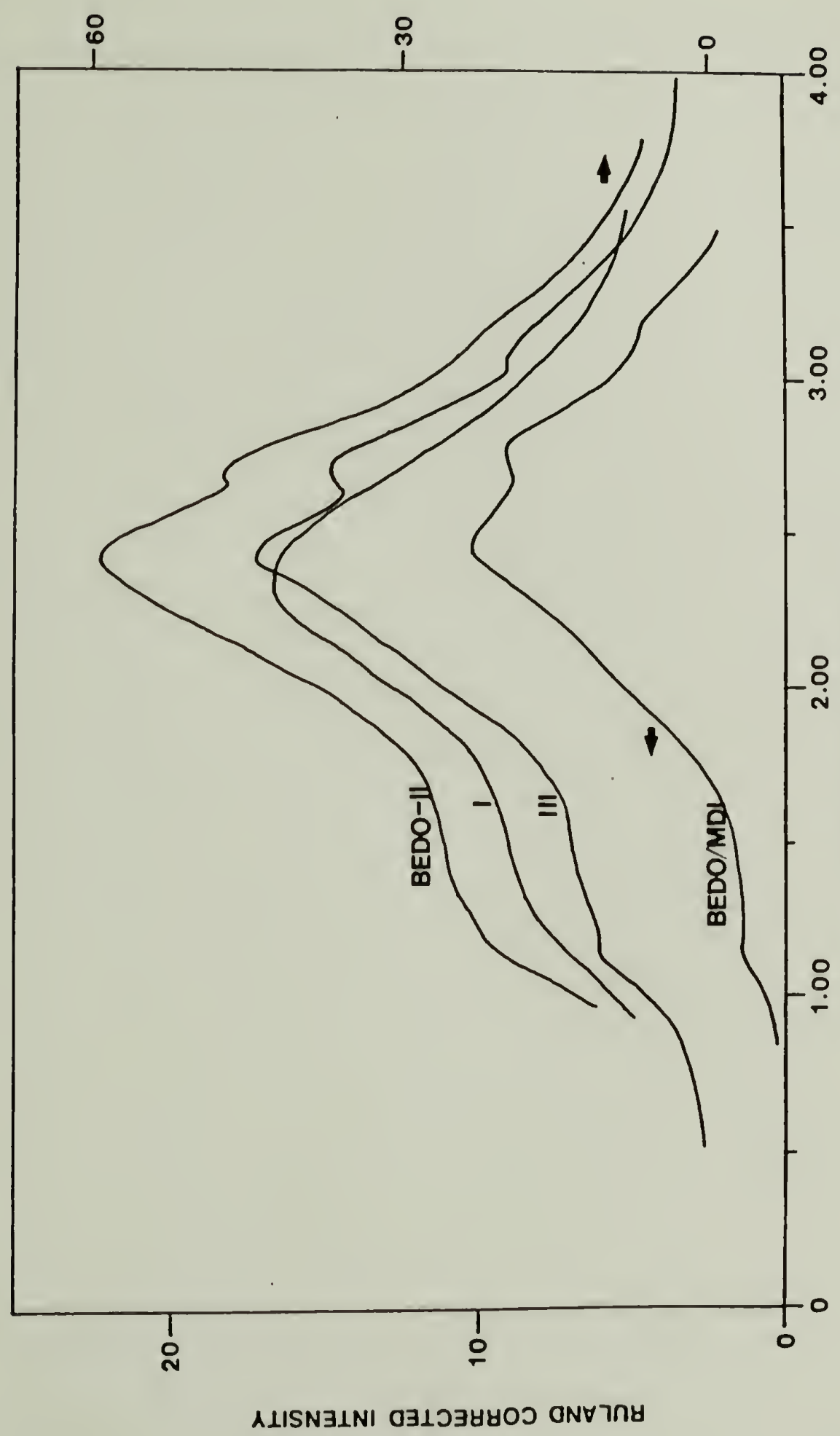

Figure 56. Wide-angle X-ray scans of samples BEDO-I to BEDO-III and pure hard segment copolymer (MDI/BEDO).

TABLE 14

WIDE-ANGLE X-RAY DIFFRACTION DATA

OF PPO-EO/MDI/BEDO SAMPLES

Sample Designation	Crystalline Peak (Å)				
BEDO-I				7.43	
BEDO-II	3.19	3.72	4.09	6.96	8.92
BEDO-III	3.30	3.70	4.13	7.14	9.02
MDI/BEDO Homopolymer	3.18	3.64	4.07		8.66

With increasing hard segment content, samples BEDO-II, BEDO-III and pure hard segment copolymer (MDI/BEDO) show more crystalline lines. The positions of the crystalline peaks as well as amorphous peak remain unchanged for these three samples (see Table 14).

6.5 Small-angle X-ray Scattering Results

The small-angle X-ray scattering patterns (without Lorentz corrections applied) of the as-reacted BEDO-I, BEDO-II and BEDO-III samples are shown in Figure 57. Sample BEDO-I shows only a very weak, broad maximum corresponding to a Bragg spacing of 260° Å. Samples

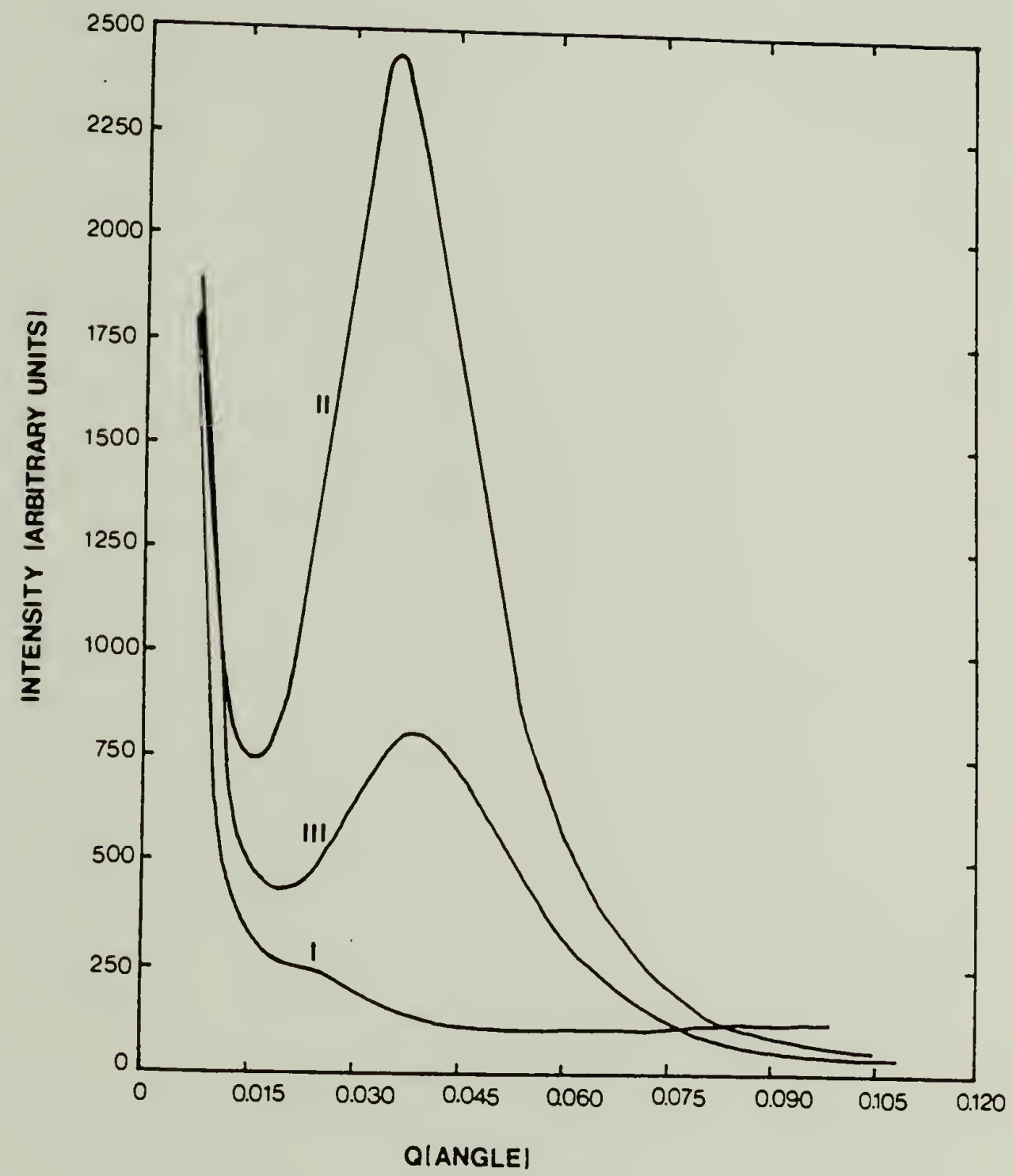

Figure 57. Pinhole SAXS scattering patterns of samples BEDO-I to BEDO-III.

BEDO-II and BEDO-III both show a well-defined peak, which corresponds to Bragg spacing of 170 and 160 Å respectively. The scattered intensity is much higher, and half width peak height is narrower in the case of sample BEDO-II than BEDO-III. It also appears that the Bragg spacing decreases as hard segment content increases. These SAXS peaks are likely due to the lamellar fibrillar structure present within the MDI/BEDO hard segment-rich spherulites.

As shown in Figures 47 and 50, there are only a few isolated spherulites present in sample BEDO-I. Moreover, TEM micrograph reveals that the lamellar fibrillar structure within these spherulites is rather poorly organized accounting for the low scattering intensity and the presence of only a very small, broad peak in SAXS pattern (note that the SAXS data acquisition time for sample BEDO-I is twice as long as that of samples BEDO-II and BEDO-III).

Sample BEDO-II has many spherulites with very well-organized lamellar fibrillar structure as seen in Figure 51. Since there are a lot of soft segments trapped between the fibrils inside the spherulite (as discussed in section 6.2), the contrast of these fibrils is better, i.e. the value of $(\rho_H-\rho_S)$ is larger. It is also evident that the product of $\phi_H.(1-\phi_H)$ is the largest for this sample. Therefore it is expected that this sample has the

strongest scattering intensity and the most well-defined SAXS peak.

Sample BEDO-III also has a well-defined SAXS peak although its scattering intensity is much weaker and the peak half width is wider than those of sample BEDO-II. Sample BEDO-III has a very complicated skin/care morphology (see Figure 49). Therefore its peak may be composed of two or more peaks due to different morphology across the sample. No attempt was tried to do the peak separation analysis and compare to the individual SAXS results of skin and core regions.

6.6 Domain Structure Characterization - TEM Results and Discussion of Cryomicrotomed Sections of OsO_4 Stained Bulk PPO-EO/MDI/BEDO Samples

One of the main goals of this thesis is to characterize domain (microphase separation) structure by direct TEM observation. It is of great interest to learn the size and shape of domain structure and see if there is any ordering and connectivity between these domains.

A direct, successful visualization of small scale microstructures by TEM observation depends not only on sufficient amplitude (mass thickness or diffraction) contrast but also on obtaining a sufficiently thin sample section (thickness on the order of domain size) as well as

avoiding any alterations by electron beam irradiation damage. Since amplitude contrast in polymers is usually very low, heavy atom staining (extrinsic mass thickness contrast) and defocus microscopy (phase contrast) techniques were employed to enhance the domain contrast. The procedures of OsO_4 staining and cryomicrotoming were described earlier in section 3.2.

Figures 58a to 58c show high magnification TEM micrographs of OsO_4 stained and microtomed thin sections of sample BEDO-I, taken at near focus ($\Delta f \simeq 0$), underfocus ($\Delta f = -3.4$ μm) and overfocus ($\Delta f = +3.4$ μm) respectively at an original magnification of 20,000 X. The right hand side of the pictures has been purposely over exposed during the print making process for better contrast. The objective of taking through-focus series of pictures is to enhance the phase contrast in the defocus images, while leaving essentially only mass thickness contrast in the infocus image. In the infocus micrograph (Figure 58a) a lot of dark random OsO_4-rich regions are dispersed throughout the whole system, both in the spherulite (left hand side portion of the micrograph) and the matrix. These OsO_4-rich dark regions range from 40 to 140 Å in size. Even inside the spherulite, no obvious correlation or orientation between these dark regions is seen. In this case, the film thickness of microtomed thin section hinders observation of fine structure under 100 Å in size.

Figure 58. High magnification TEM micrographs of OsO_4 stained and microtomed thin sections of sample BEDO-I (10 percent hard segment), taken at (a) near focus ($\Delta f \simeq 0$), (b) underfocus ($\Delta f = -3.4$ μm) and (c) overfocus ($\Delta f = +3.4$ μm) respectively.

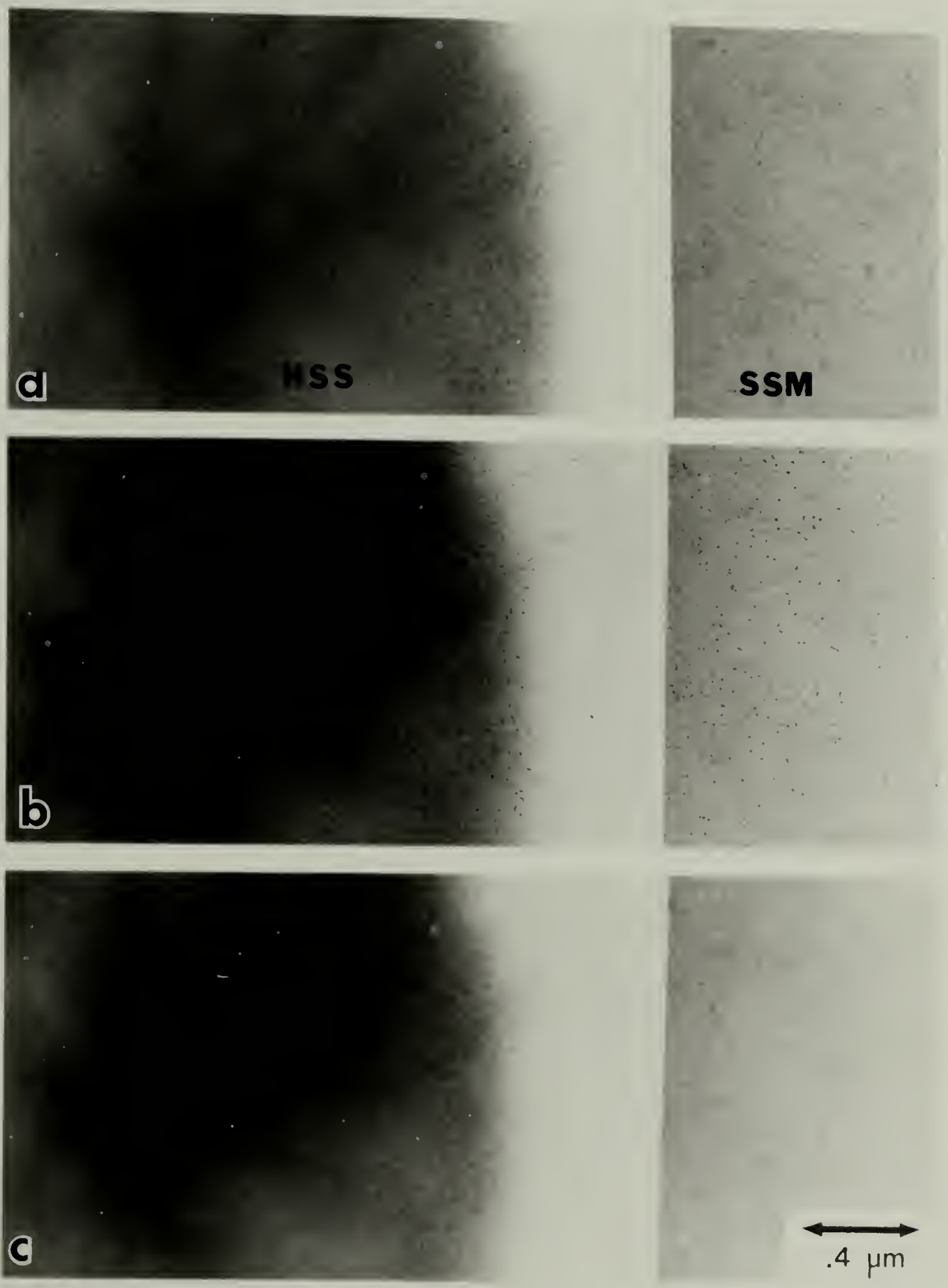

Figure 58

Figures 59a to 59e show high magnification TEM micrographs of OsO_4 stained, microtomed sample BEDO-II' (annealed sample of BEDO-II), which were taken at $\Delta f \simeq 0$, ± 3.4 μm and ± 6.8 μm respectively. The reason for using sample BEDO-II' instead of sample BEDO-II is that after annealing, sample BEDO-II' is more crystalline and phase separated than sample BEDO-II (from DSC and TEM results). The right hand side strip of the micrographs has also been purposely over exposed during printing for better contrast. This sample also shows dark OsO_4-rich regions (ranging from 40-140 Å) randomly dispersed in both spherulite and the matrix. Again, no special correlation between these OsO_4-rich dark regions is seen. These OsO_4-rich dark regions seem to be preferably present in spherulite and its periphery than in matrix suggesting that there may be more hard segment-rich molecules in the spherulite. A closer look at a very thin area (approximately 200 Å thick) around the hole (upper right region in Figure 59a where $\Delta f \simeq 0$) shows the contrast of those OsO_4-rich dark regions is not sharp and rather diffused. The contrast becomes sharper with increasing phase contrast from defocus (see Figures 59b and 59d). Note that the overfocus micrographs (Figures 59c and 59e) show reverse contrast of OsO_4-rich regions but not the spherulite's fibrillar structure. Note that at the higher defocus condition (see Figure 59d with $\Delta f \simeq -6.8$ μm), the matrix

Figures 59a, 59b and 59c. High magnification TEM micrographs of OsO_4 stained and microtomed thin sections of sample BEDO-II' (43 percent hard segment, annealed sample), taken at (a) near focus ($\Delta f \simeq 0$), (b) underfocus ($\Delta f = -3.4$ μm), and (c) overfocus ($\Delta f = +3.4$ μm) respectively.

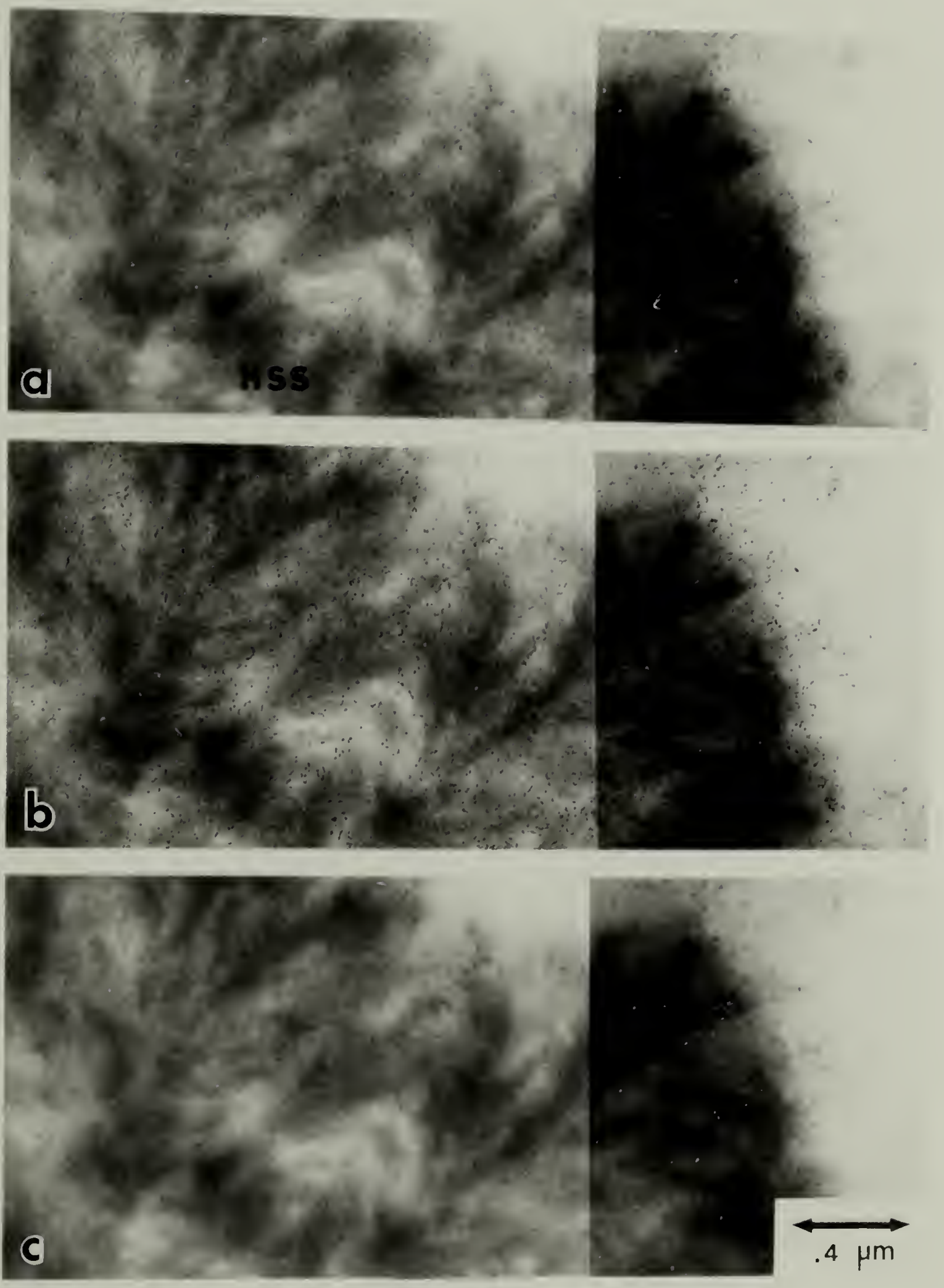

Figure 59

Figures 59d and 59e. High magnification TEM micrographs of OsO_4 stained and microtomed thin sections of sample BEDO-II' (43 percent hard segment, annealed sample), taken at (d) underfocus ($\Delta f = -6.8$ μm) and (e) overfocus ($\Delta f = +6.8$ μm) respectively.

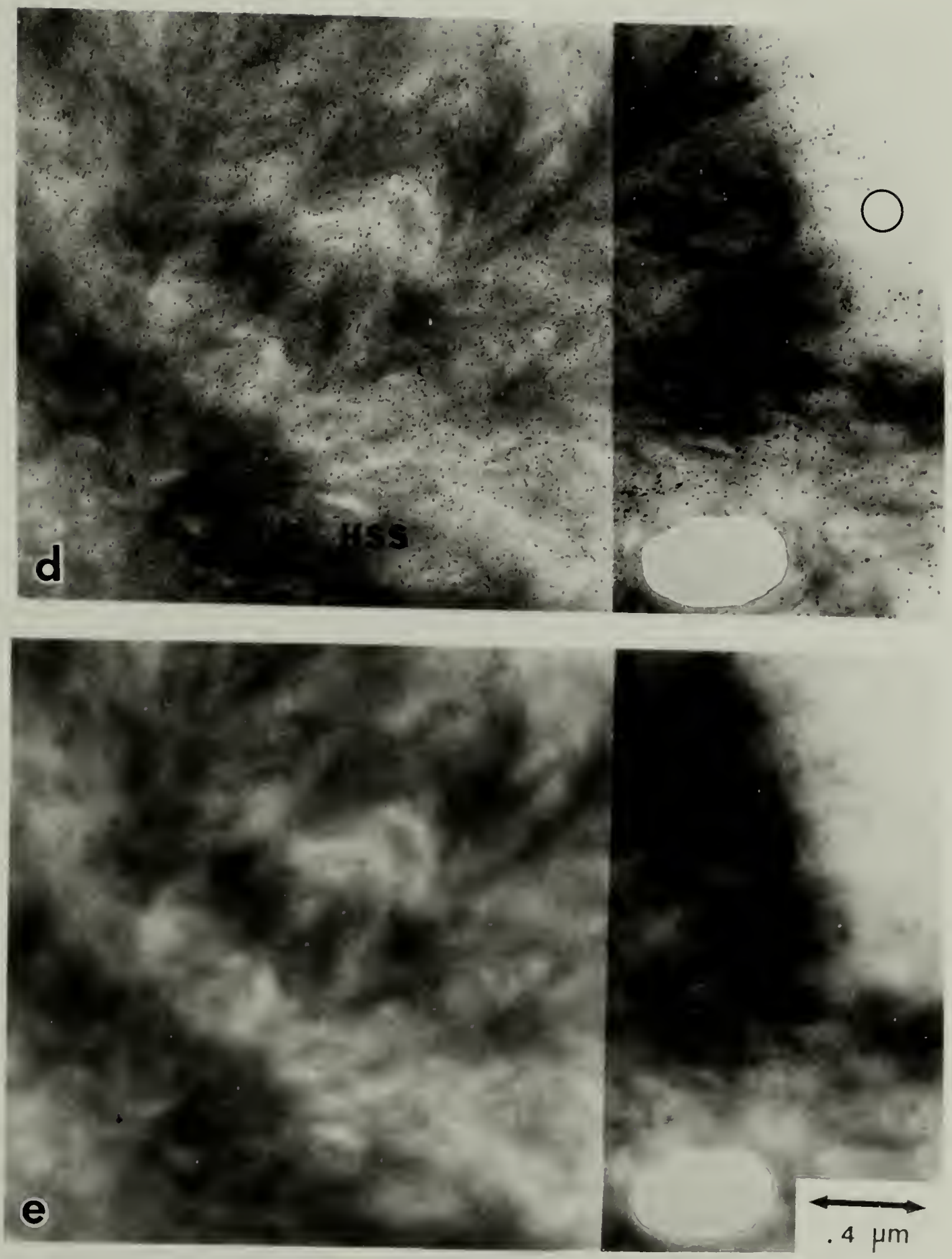

Figure 59

displays many new (phase contrast) gray regions about ~40 Å size (areas indicated by the circle).

A series of through-focus micrographs ($\Delta f \simeq 0$, ± 3.4 μm and ± 6.8 μm) of thin sections of OsO_4 stained and microtomed sample BEDO-III is shown in Figures 60a to 60e. There are clearly two different types of microstructures present in this sample, i.e. larger scale dark regions of 40-140 Å size corresponding to OsO_4-rich regions and smaller scale (phase contrast) gray regions up to 40 Å in size present in the matrix background. The OsO_4-rich dark regions are randomly distributed over the whole sample. The smaller scale gray regions seem to possess some sort of short range order (a couple of hundred Å in some cases) which is very unusual. We believe that those microstructures (either crystallite or domain entity) in these gray regions are real and not artifact because their presence won't change with through-focus as shown in the previous micrographs.

The nature of these smaller scale gray regions remains unanswered, they may be OsO_4 stained hard segment-rich domain structure or just hard segment-rich crystallites unstained by OsO_4. It is very likely that the double bond containing hard segment crystals are very impermeable to OsO_4 and cannot be stained in this case. The OsO_4 staining technique does not seem to produce satisfactory

Figure 60a. High magnification TEM micrograph of OsO_4 stained and microtomed thin sections of sample BEDO-III (78 percent hard segment), taken at near focus ($\Delta f \simeq 0$).

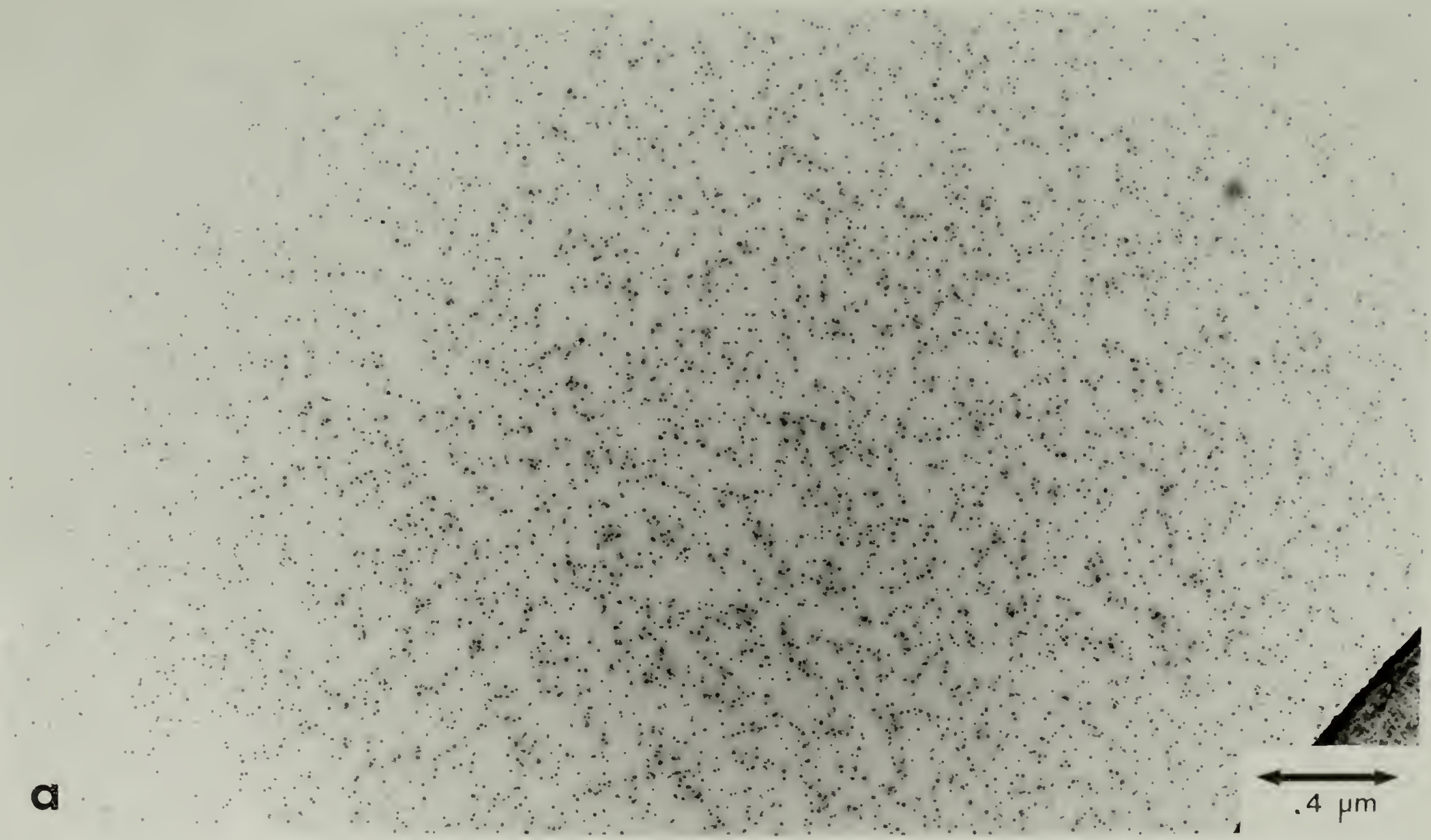

Figure 60

Figures 60b to 60e. High magnification TEM micrographs of OsO_4 stained and microtomed thin sections of sample BEDO-III (78 percent hard segment), taken at (b) underfocus (Δf = -3.4 μm), (c) overfucus (Δf = +3.4 μm), (d) underfocus (Δf= -6.8 μm) and (e) overfocus (Δf = +6.8 μm) respectively.

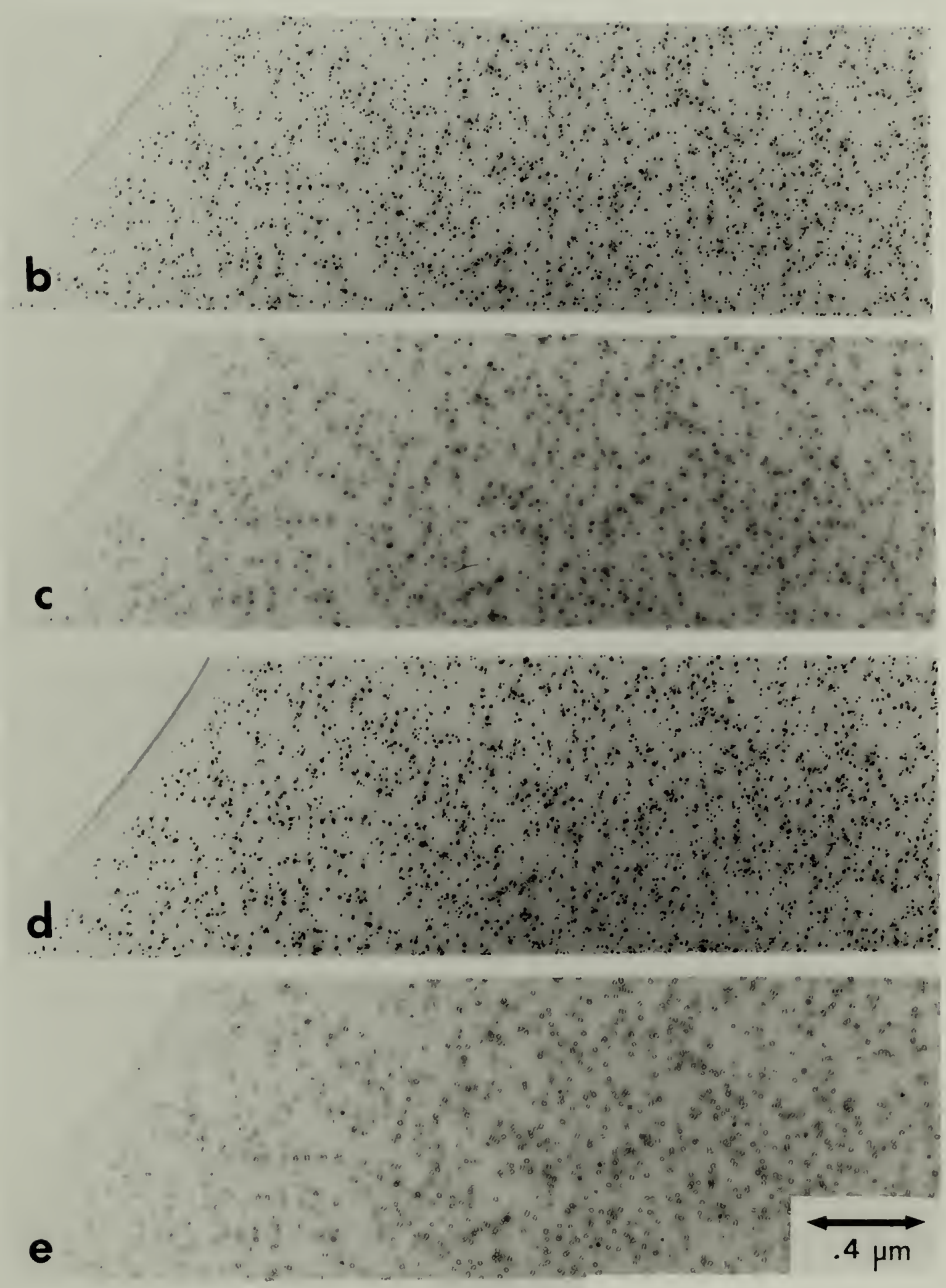

Figure 60

results and in some ways it complicates the interpretation of image analysis.

6.7 Discussion and Conclusions

The polyurethane samples used in this study were based on atactic PPO-EO soft segment and MDI/BEDO hard segment. The employment of atactic PPO-EO soft segment was to avoid soft segment crystallinity as in the case of polyester based soft segment which could complicate the interpretation of hard segment domain structure. By using an unsaturated chain extender, it was expected that the hard segment phase could be stained with OsO_4 to provide additional mass thickness (amplitude) contrast in TEM observation.

The results of direct TEM imaging of hard segment domain structure with the aid of OsO_4 staining in this study prove to be inconclusive. Although the technique of selective staining of double bonds with OsO_4 to enhance mass thickness contrast has been successfully applied to the study of phase separation in "amorphous" block copolymer systems such as polystyrene/polybutadiene and polystyrene/polyisoprene blends and diblock and triblock copolymer systems, it remains unclear whether "crystalline" hard segment domains containing double bonds

can be stained with OsO_4. As shown in the high magnification TEM micrographs of OsO_4 stained and microtomed thin sections of bulk PPO-EO/MDI/BEDO samples, the OsO_4 particles were observed to disperse randomly in both the matrix and spherulites with no obvious orientation and correlation. One possible explanation is that the crystalline hard segment domains are very resistant to OsO_4 staining so that OsO_4 molecules just diffuse into the polymer and randomly nucleate to form clusters of crystallites without preferentially staining the double bond containing hard segment domains.

In contrast to the previous study of domain streucture characterization on solution cast BEDO-II sample (44 percent by weight hard segment) by I. Fridman[68], the following differences have been found: (i) the solution cast films showed volume filling spherulites with very fine lamellar fibrillar structure while the microtomed sections of bulk sample showed non-volume filling spherulites with rather coarse and open lamellar fibrillar structure (see Figures 51 and 52), (ii) the lamellar fibrillar structure within the spherulites was observed to become much more well defined after OsO_4 staining (i.e. hard segment phase could be stained by OsO_4) in the solution cast films but not in the OsO_4 stained and microtomed bulk sample and (iii) the phenomenon of preferential OsO_4 staining of the centre of the largest

spherulites in the solution cast films was not observed in the OsO_4 stained and microtomed bulk sample. In the latter, OsO_4 particles were observed to disperse uniformly and randomly within the spherulites without any preferential staining (see Figures 53 and 59).

The different solidification and crystallization kinetics of the solution cast films and the as-reacted bulk sample may account for their morphological differences. The low degree of crystallinity of the hard segment phase in the solution cast films may be responsible for its susceptibility to OsO_4 staining. Although the preferential staining of the centre of the largest spherulites in the solution cast films was attributed to the presence of high concentration of molecules with the longest hard segment sequences, it could be an artifact introduced during the staining process. Further study is needed concerning this respect. Indeed the interpretation of domain structure with the aid of OsO_4 staining is difficult and sometimes misleading unless the intrinsic polymer morphology and OsO_4 staining mechanism are fully characterized and understood.

C H A P T E R VII

RESULTS FOR 145°C CURE PCP/MDI/BDO SERIES

This chapter is concerned with the study of polyurethane samples based on polycaprolactone diol / 4,4'-diphenylmethane diisocyanate / 1,4-butane diol from 1/2/1 to 1/6/5 (PCP/MDI/BDO) mole ratio. It is a direct extension study of my Master Thesis[88]. Both optical and electron microscopy results of cryomicrotomed sections of as-reacted samples, in contrast to the previous study of solution cast films, are presented. Also included are wide-angle and small-angle X-ray scattering results and annealing study of sample PCL-165.

7.1 Differential Scanning Calorimetry Results

Figure 61 shows first run DSC scans of the as-reacted PCP/MDI/BDO samples over the 320-520°K temperature range at a heating rate of 20°C/min. Two endothermic transition regions are observed - a very broad and weak transition near 350°K and a narrow, stronger transition below 500°K respectively.

For the as-reacted samples, the high temperature peak (circa 490°K) shifts upwards by about 10°K as the hard segment concentration increases from 13 to 43 percent.

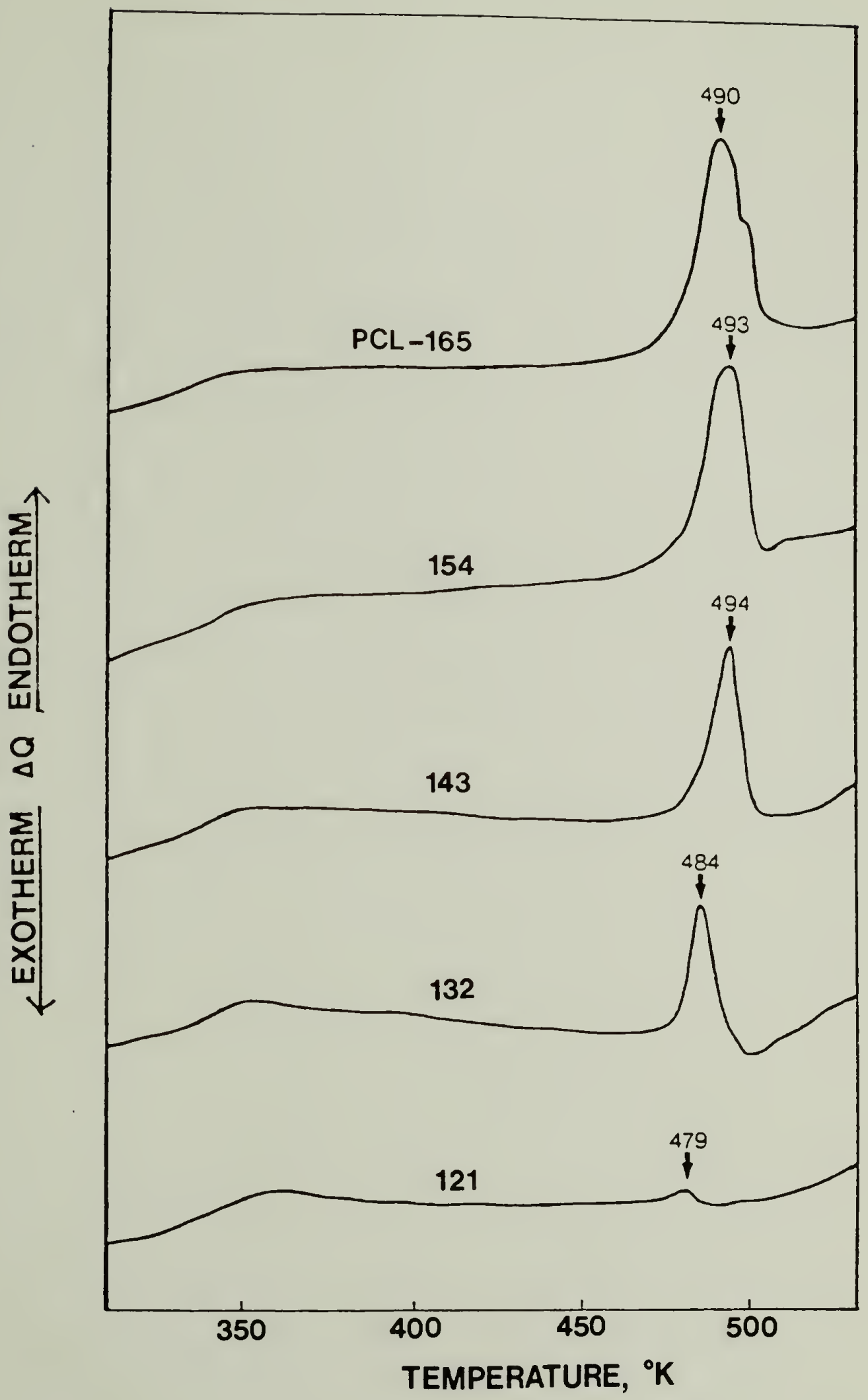

Figure 61. DSC scans of the as-reacted PCP/MDI/BDO samples over the 320-520°K temperature range.

Scans through the polycaprolactone melting range, T_m=60°C[58], indicate no significant soft segment crystallinity is present.

The heat of fusion of the high temperature transition is found to increase with increasing hard segment content for the as-reacted samples. Table 15 summarizes the DSC results for this series of samples.

Figure 62 compares DSC scans of the as-reacted and annealed PCL-165 samples. The annealed sample is made by heating the as-reacted sample at 20°C/min. from room temperature to 490°K and holding at that temperature for 1 hour and slowly cooling at 0.32°C/min. to 460°K and then holding for 3 hours in DSC. As the rescan curve shows, the peak transition temperature shifts about 13°C higher and the peak shape becomes much narrower indicating the perfection of hard segment crystallites after annealing. But interestingly, the heat of fusion (also shown in Table 15) seems to be unchanged or slightly less after annealing [annealed: 4.4 (polymer), 13.5 (hard segment) vs. as-reacted: 5.2 (polymer), 16.0 (hard segment) cal/g].

7.2 Optical Microscopy Results

The partial and crossed polarized light micrograph pairs (denoted by a and b respectively) of samples PCL-121

TABLE 15

SUMMARY OF HEATS OF FUSION OF THE HARD SEGMENT FOR THE AS-REACTED PCP/MDI/BDO SAMPLES

MOLE RATIO PCP/MDI/BDO	WT. FRACTION HARD SEGMENT	DSC (cal/g) AS-REACTED	
		POLYMER	HARD SEGMENT
1/2/1	13	0.2	14.6
1/3/2	23	1.7	14.8
1/4/3	31	2.8	14.5
1/5/4	38	4.2	15.5
1/6/5	43	5.2	16.0
1/6/5*	43	4.4*	13.5

* Sample annealed at 490°K for 1 hour and slowly cooled at 0.32°C/min. to 460°K and then held for 3 hours in DSC.

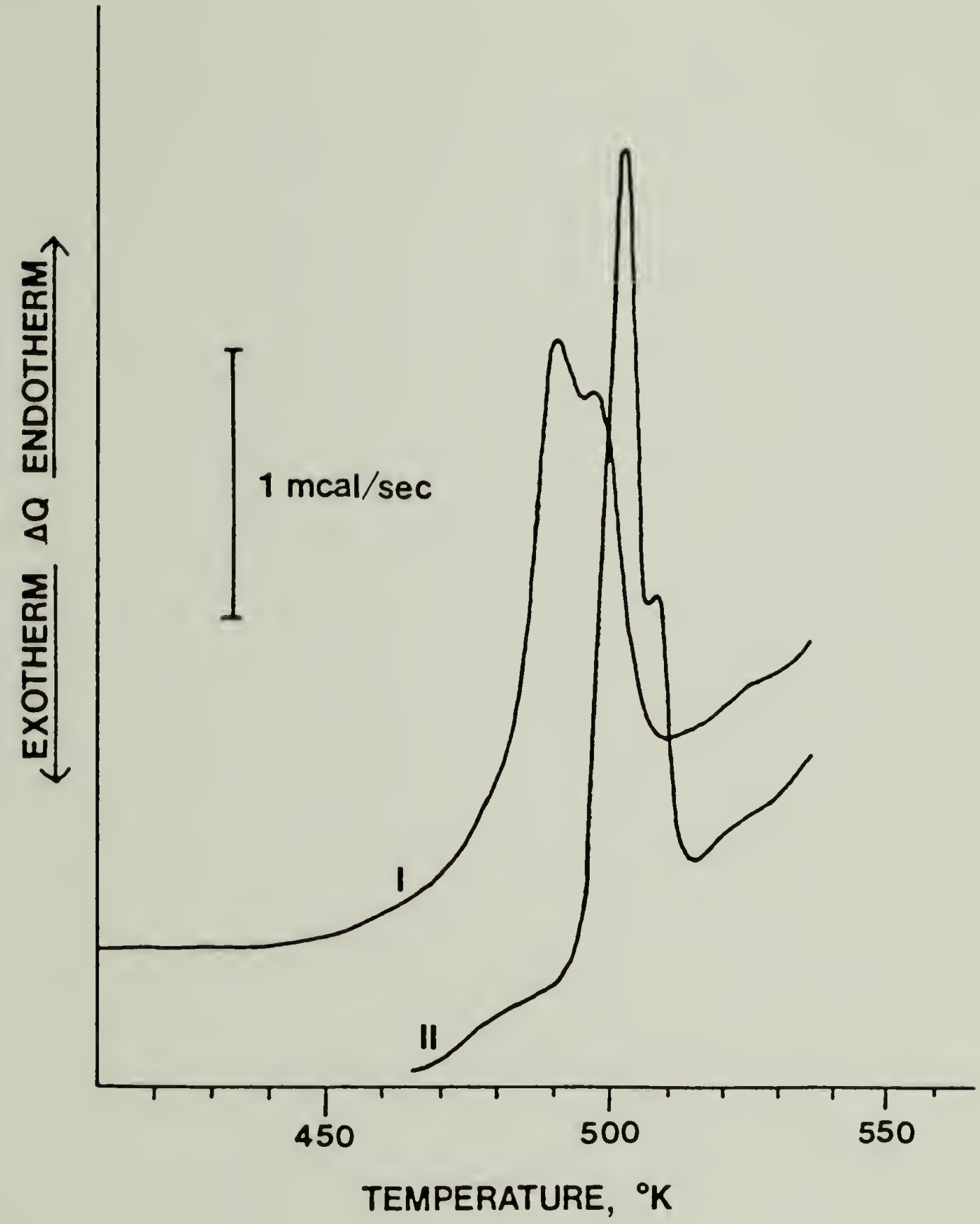

Figure 62. DSC scans of the as-reacted (I) and annealed (II) PCL-165 samples.

to PCL-165, including annealed sample PCL-165, are shown in Figures 63 to 68. Sample PCL-121 is found to consist of both spherulitic superstructure (10-20 μm size) and smaller, poorly formed arrays of crystallites (1-5 μm) (see Figure 63a). Under crossed polarizers (Figure 63b), these small crystallites show only speckles of birefringence while the spherulites show both very strong (also very radial oriented) and faint birefringence areas. The familiar Maltess cross extinction pattern is not seen. Later TEM results will try to explain why these spherulites have different extinction patterns.

Besides the presence of non-volume filling spherulites, sample PCL-132 shows many of micron sized globules (HSG, hard segment-rich globule, as indicated by arrows in Figure 64a) present in the matrix. These globules are optically isotropic and cannot be seen under crossed polarized light (see Figure 64b). Figures 65a and 65b show that sample PCL-143 has almost volume filling spherulites with only a few globules present. In sample PCL-154, there are lots of hard segment-rich globules present as seen in Figure 66a. It is also noted that the extinction patterns of this sample show weaker birefringence in the centre and stronger birefringence in the periphery of spherulites (see Figure 66b). These same features can be more clearly seen in Figure 67b of sample PCL-165. Interesting enough, sample PCL-165 shows the

Figure 63. Optical micrographs of sample PCL-121 (13 percent hard segment): (a) uncrossed polarizers; (b) crossed polarizers.

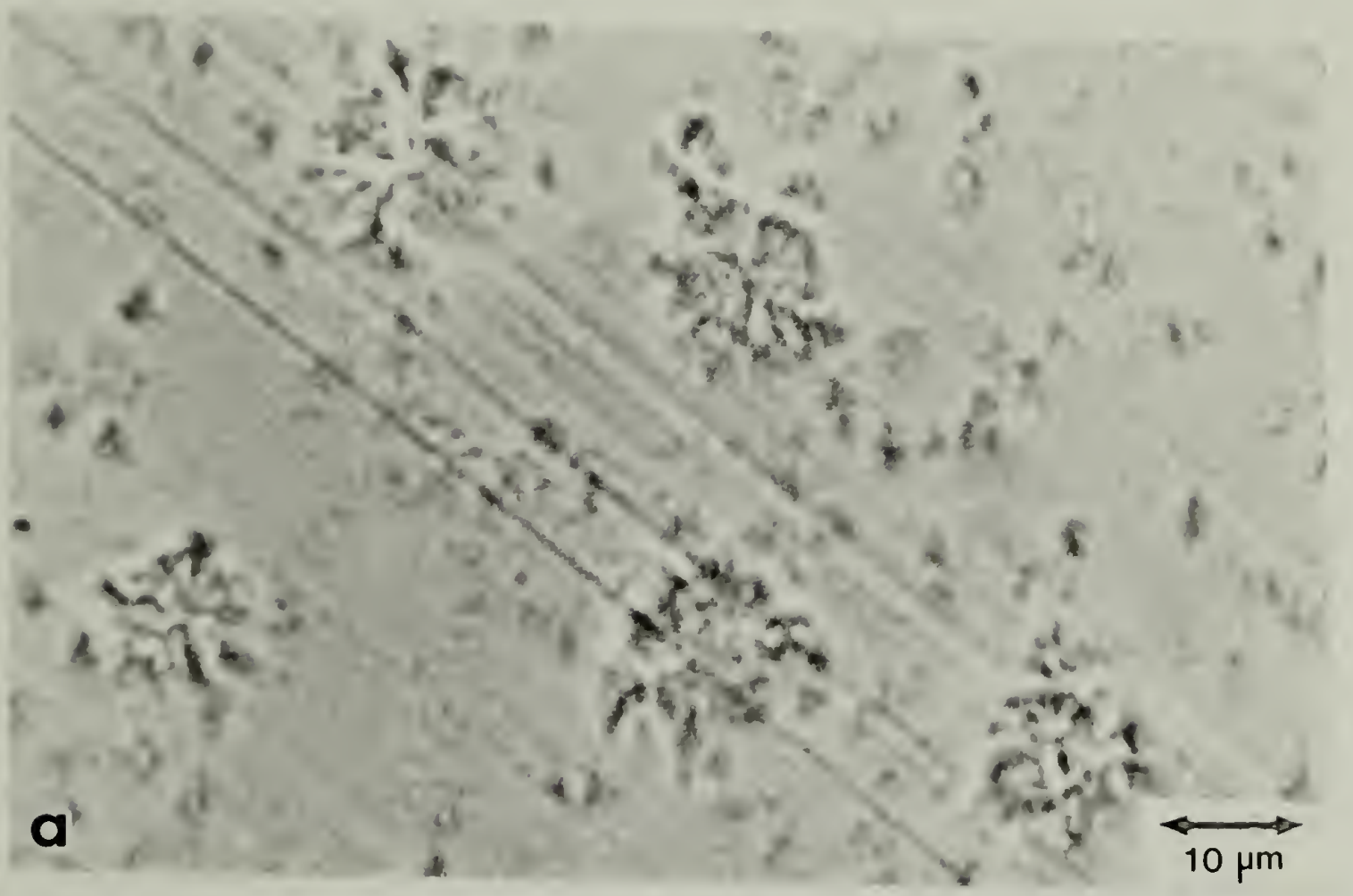

Figure 63

Figure 64. Optical micrographs of sample PCL-132 (23 percent hard segment): (a) uncrossed polarizers; (b) crossed polarizers.

Figure 64

Figure 65. Optical micrographs of sample PCL-143 (31 percent hard segment): (a) uncrossed polarizers; (b) crossed polarizers.

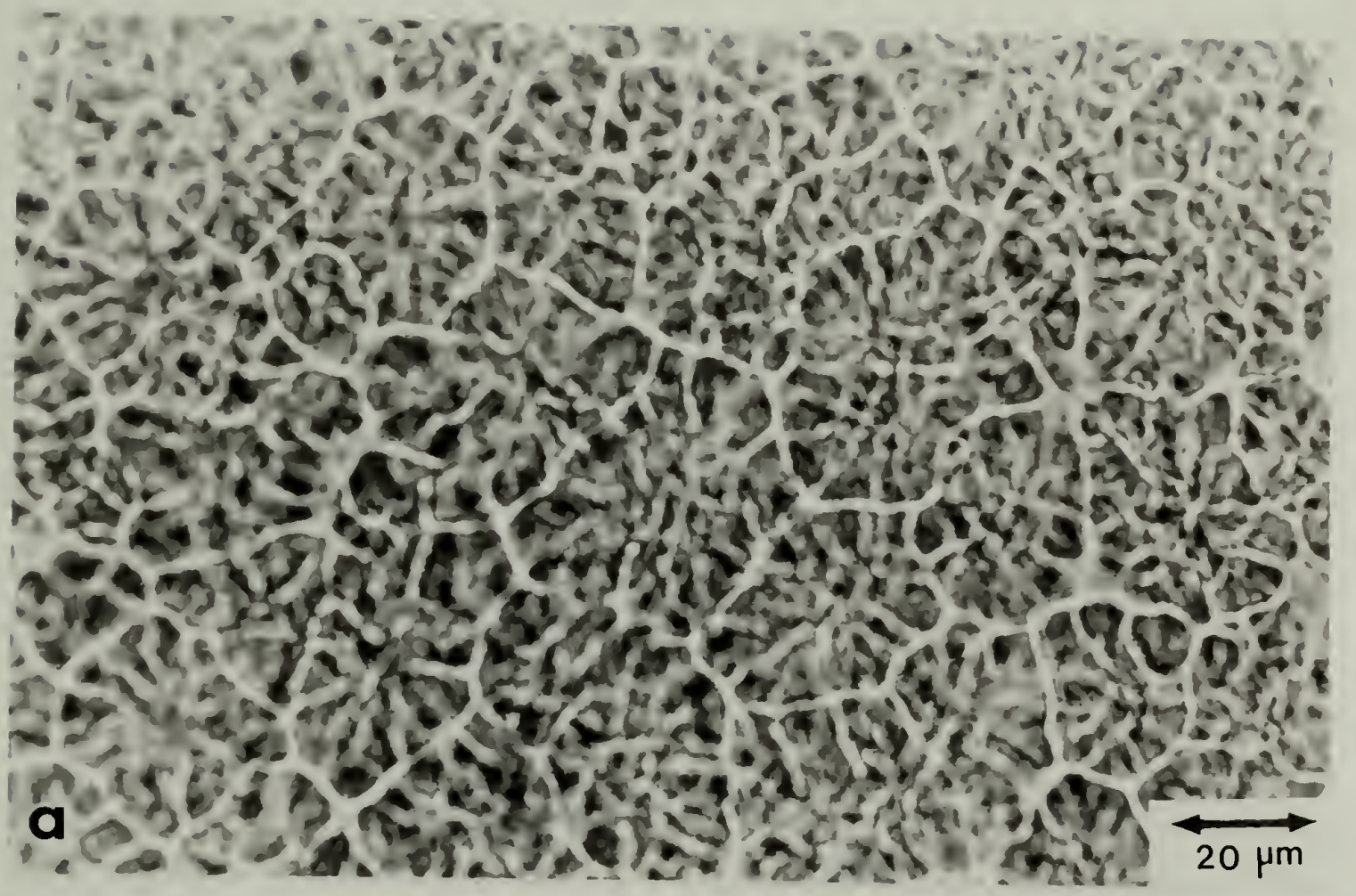

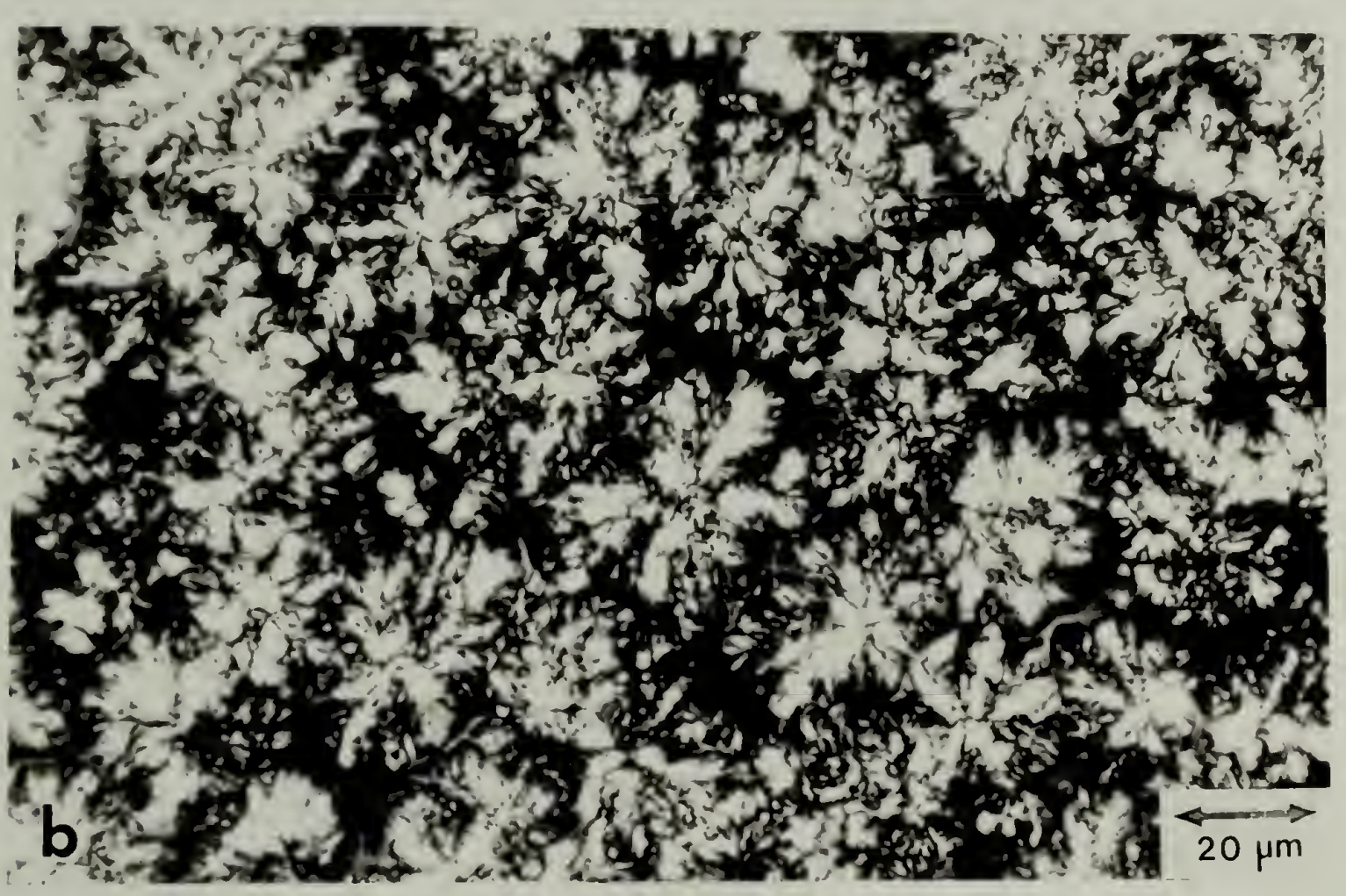

Figure 65

Figure 66. Optical micrographs of sample PCL-154 (38 percent hard segment): (a) uncrossed polarizers; (b) crossed polarizers.

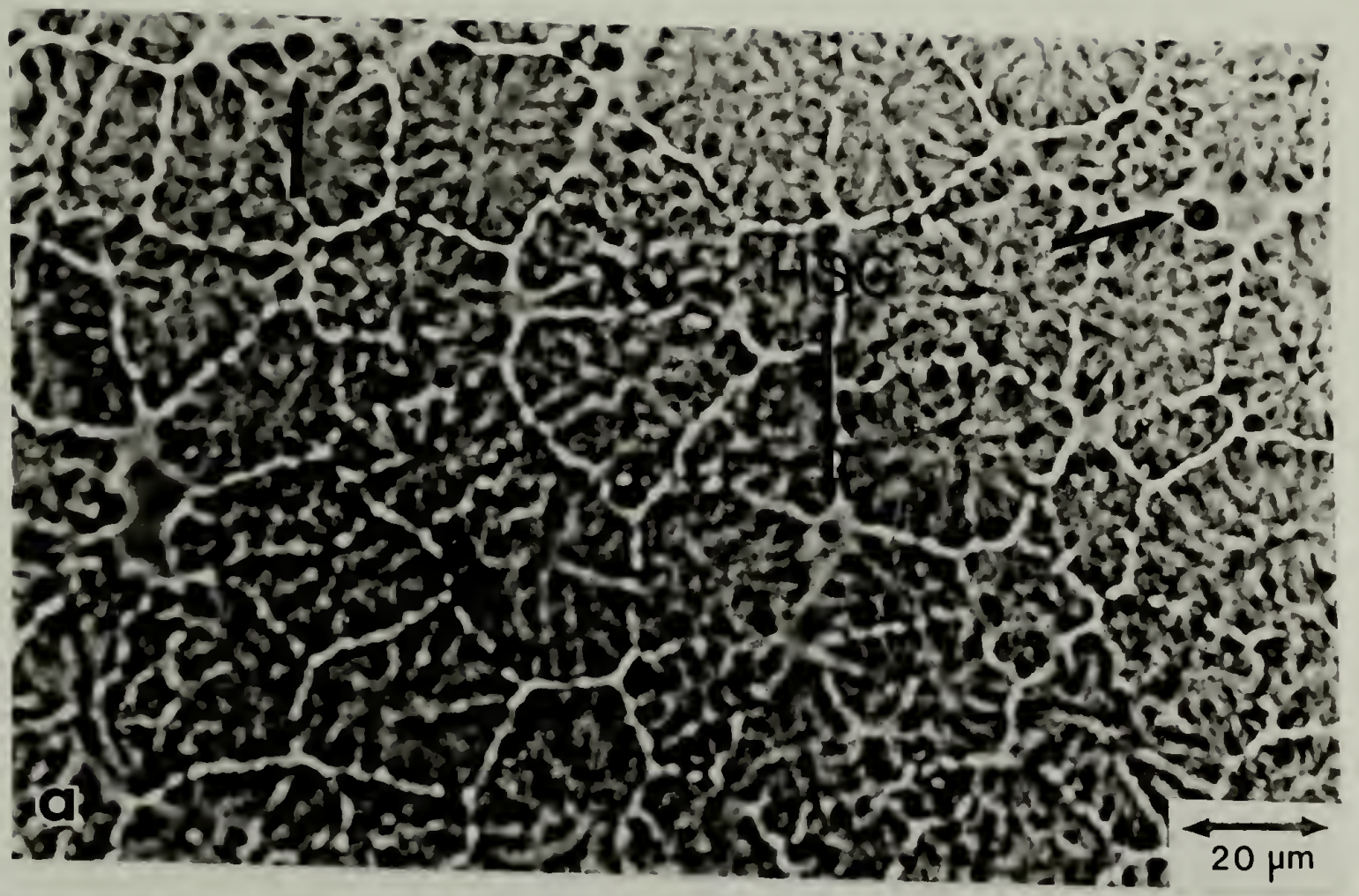

Figure 66

Figure 67. Optical micrographs of sample PCL-165 (43 percent hard segment): (a) uncrossed polarizers; (b) crossed polarizers.

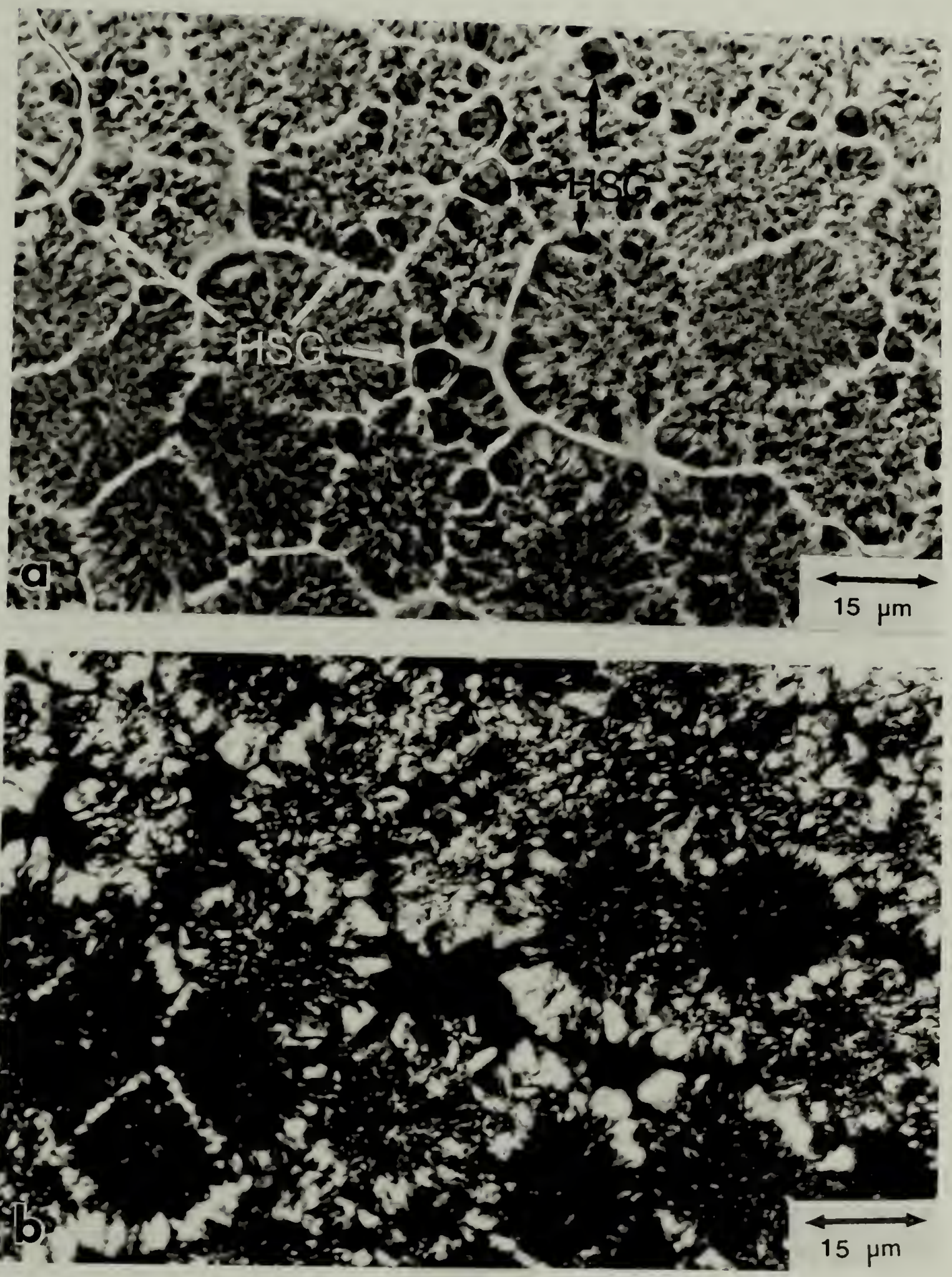

Figure 67

Figure 68. Optical micrographs of annealed sample PCL-165 (43 percent hard segment): (a) uncrossed polarizers; (b) crossed polarizers.

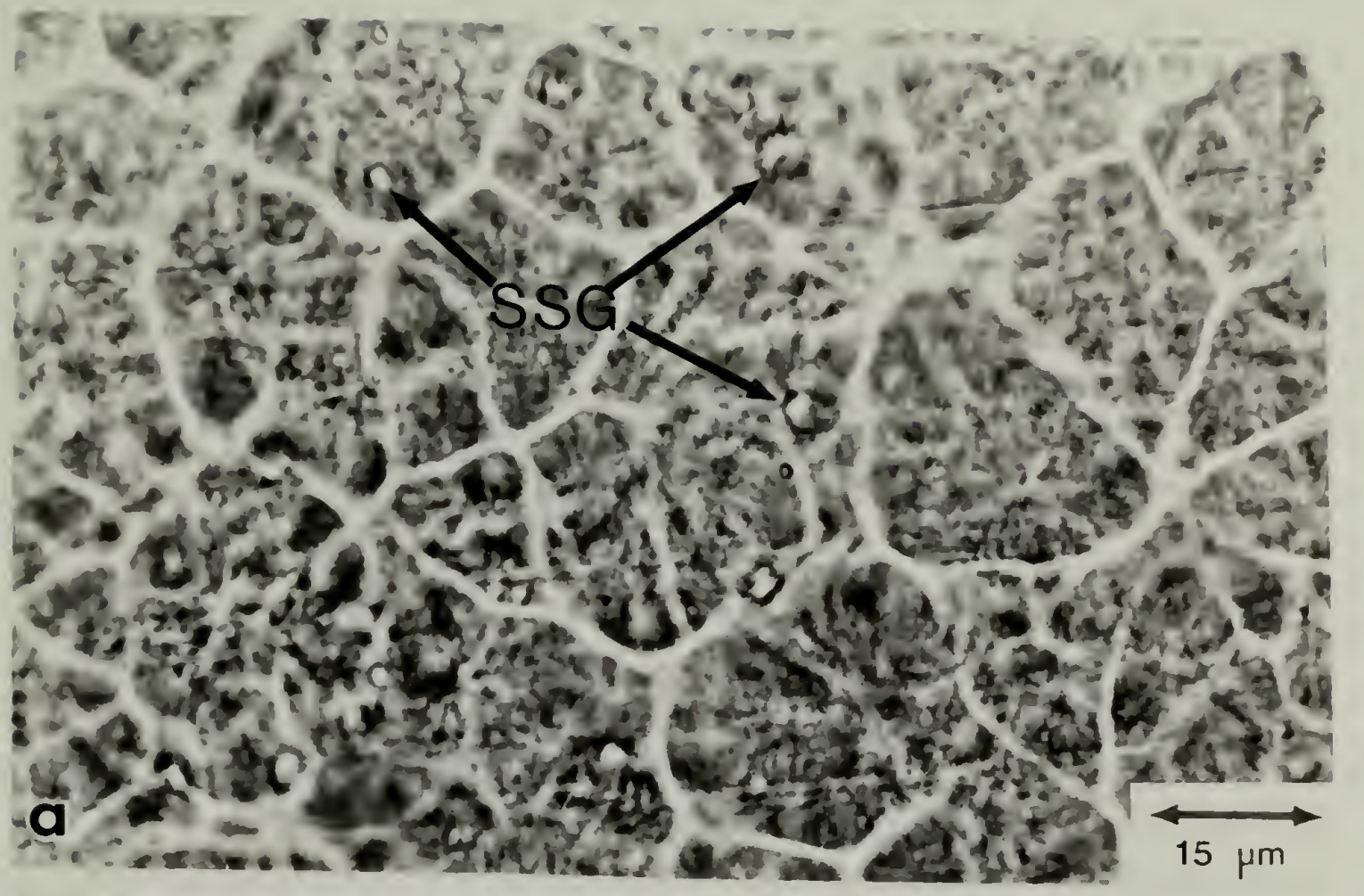

Figure 68

highest concentration of globules present in the matrix (see Figure 67a). The annealed PCL-165 sample (annealed as described in the DSC study) shows pronounced morphological changes in both spherulite and globule structures (see Figures 68a and 68b). The interior of globules reverses its contrast after annealing (see Figure 68a). In order to differentiate the hard segment-rich globule (HSG) in the as-reacted sample from the annealed sample, we call it a soft segment-rich globule (SSG). The change in structure of spherulite itself is also demonstrated by the different appearance of extinction patterns as shown in Figure 68b.

7.3 Transmission Electron Microscopy Results

Figures 69a to 69d show TEM micrographs of cryo-microtomed sections of sample PCL-121, which contains 13 percent by weight hard segment (MDI/BDO). Even with only 13 percent hard segment concentration there are isolated, well-defined hard segment-rich spherulites (HSS) of 10 to 18 μm diameter embedded in predominantly soft segment-rich matrix. The shape of these spherulites is intriguing. They are composed of short, highly branched fibrils exhibiting overall spherical symmetry, with several longer (5-10 μm) and coarser fibrils (0.2-0.4 μm wide) growing

Figures 69a and 69b. TEM micrographs of sample PCL-121 (13 percent hard segment) showing hard segment-rich spherulites.

Figure 69

Figures 69c and 69d. TEM micrographs of sample PCL-121 (13 percent hard segment) showing hard segment-rich spherulites and soft segment-rich hedrites.

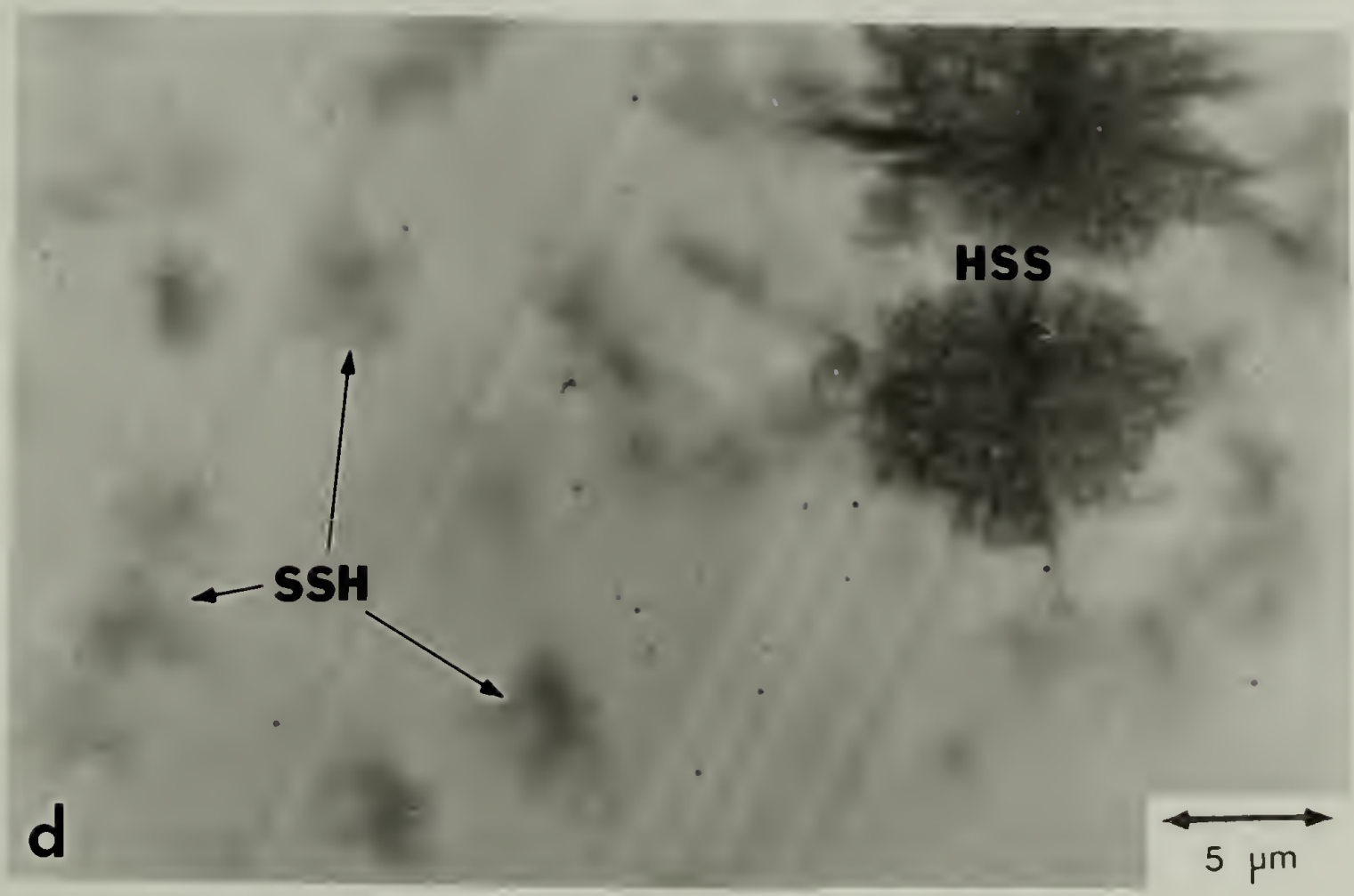

Figure 69

out into the matrix (see Figures 69a and 69b). Besides the presence of well-formed spherulites, there are also many smaller, irregular and poorly formed soft segment-rich hedrites (SSH) of 2-5 μm size in the matrix as shown in Figures 69c and 69d. Since this sample is optically translucent and with little evidence of hard or soft segment crystallinity present in the DSC traces, it is rather surprising to find that this sample contains spherulites and hedrites. From our previous study[88] on the solution cast films of sample PCL-121, we know that the soft segment (PCL, 2000 $\overline{M}n$) is capable of crystallization. The hedrites are therefore believed to be composed of crystalline soft segment (also see WAXS study).

Sample PCL-132 (see Figures 70a and 70b) shows a morphology with three different structures: hard segment-rich spherulites (HSS), soft segment-rich matrix (SSM) and structureless hard segment-rich globules (HSG). The spherulites present in sample PCL-132 are not volume filling and their sizes range from ~10 μm to ~25 μm. The fibrils on the edges of the larger spherulites appear to be more radially oriented and their length is much longer than those in the centre, which implies that during the curing further crystallization may take place and form a transcrystalline region around the spherulite. There appear to be only a few, randomly dispersed hard

Figures 70a and 70b. TEM micrographs of sample PCL-132 (23 percent hard segment) showing hard segment- rich globules and spherulites, and soft segment-rich matrix.

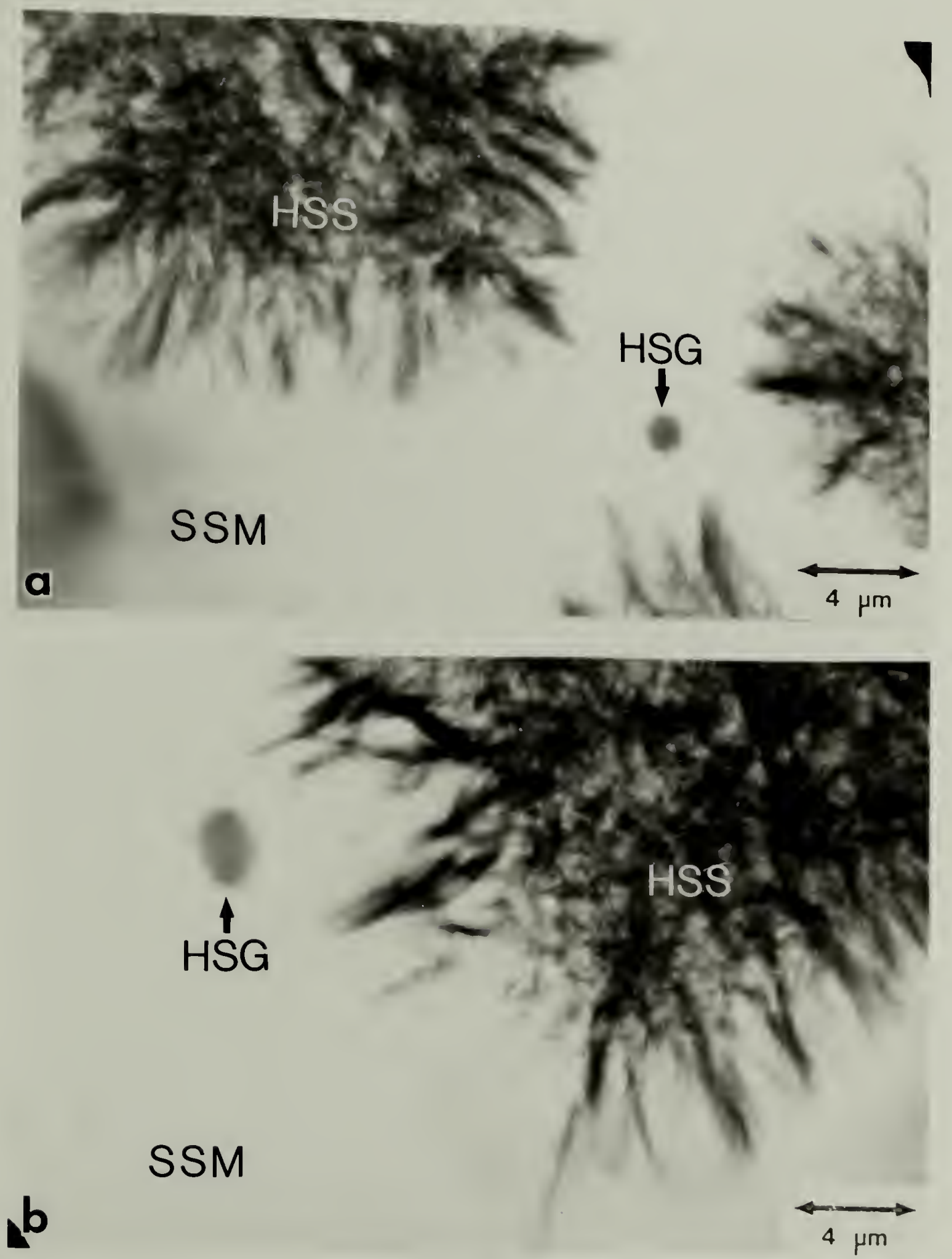

Figure 70

segment-rich globules in the matrix. These globules are featureless in both the TEM and the optical microscopy (with crossed polarizers). From the electron density contrast seen in the TEM micrographs, they must be hard segment-rich regions. The size of these globules is about 1 to 2 μm.

Figures 71a and 71b are the TEM micrographs of sample PCL-143. They show well-defined, nearly volume filling spherulites of 10-50 μm diameter. The spherulite on the left hand side of Figure 71a is composed of several very long and coarse strands which make up the spherulite skeleton, and many fine, thinner fibrils which fill in between the coarser ones. The larger strands seem to be aggregates of the thinner fibrils packing together laterally and oriented radially. The nucleus of the spherulite is comprised of a bundle of these fibrils. It is noted that in Figure 71b there are many circular areas of lighter contrast which are about 0.2 μm in size, scattered within the spherulite . These areas are probably amorphous, non-crystalline soft segment-rich regions which were partially etched away by the electron beam during observation.

The morphology of sample PCL-154 is shown in Figures 72a and 72b. There are volume filling, well-defined 20-30 μm diameter spherulites. The spherulites of Figure 72a

Figures 71a and 71b. TEM micrographs of sample PCL-143 (31 percent hard segment).

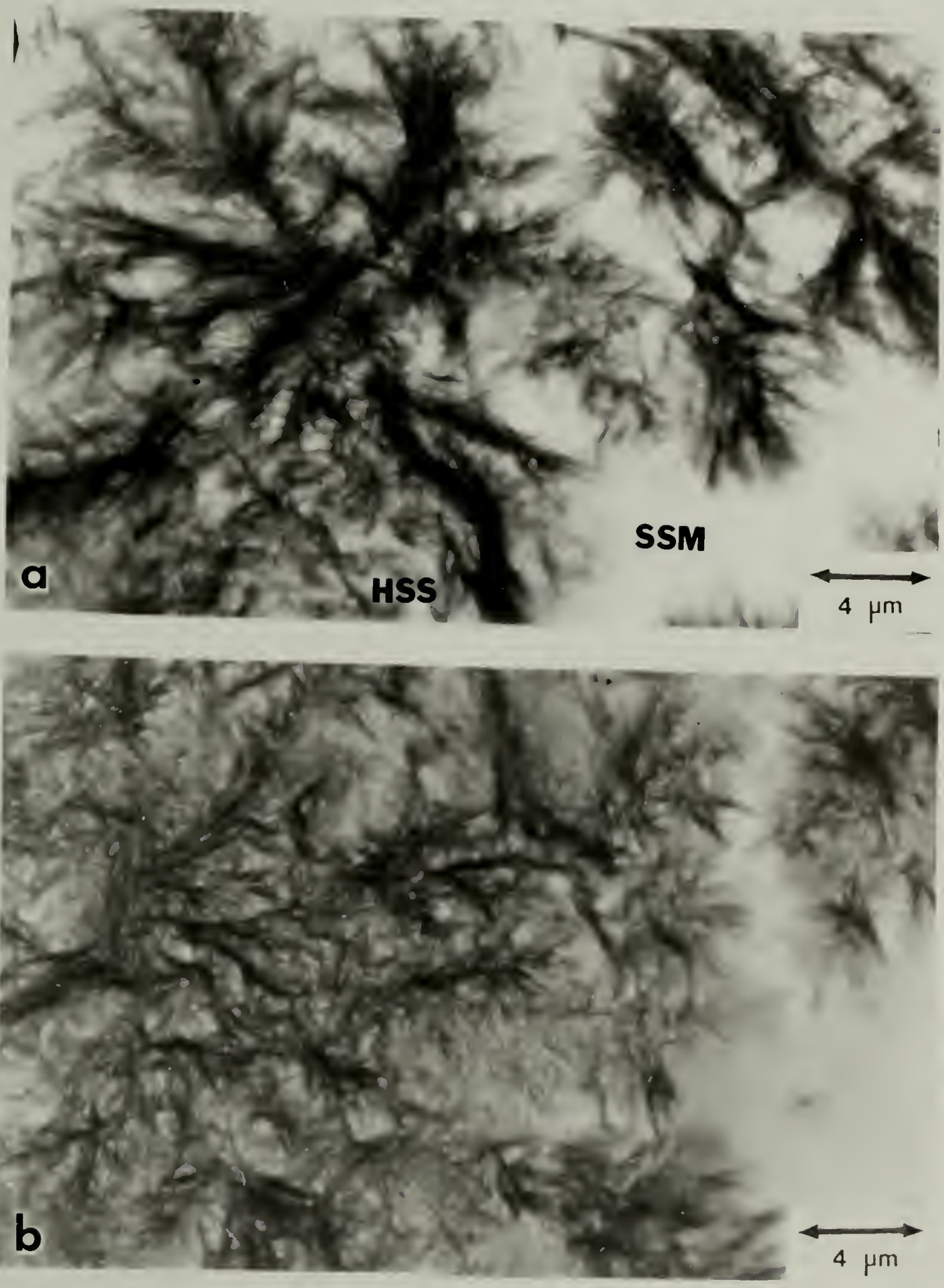

Figure 71

Figures 72a and 72b. TEM micrographs of sample PCL-154 (38 percent hard segment).

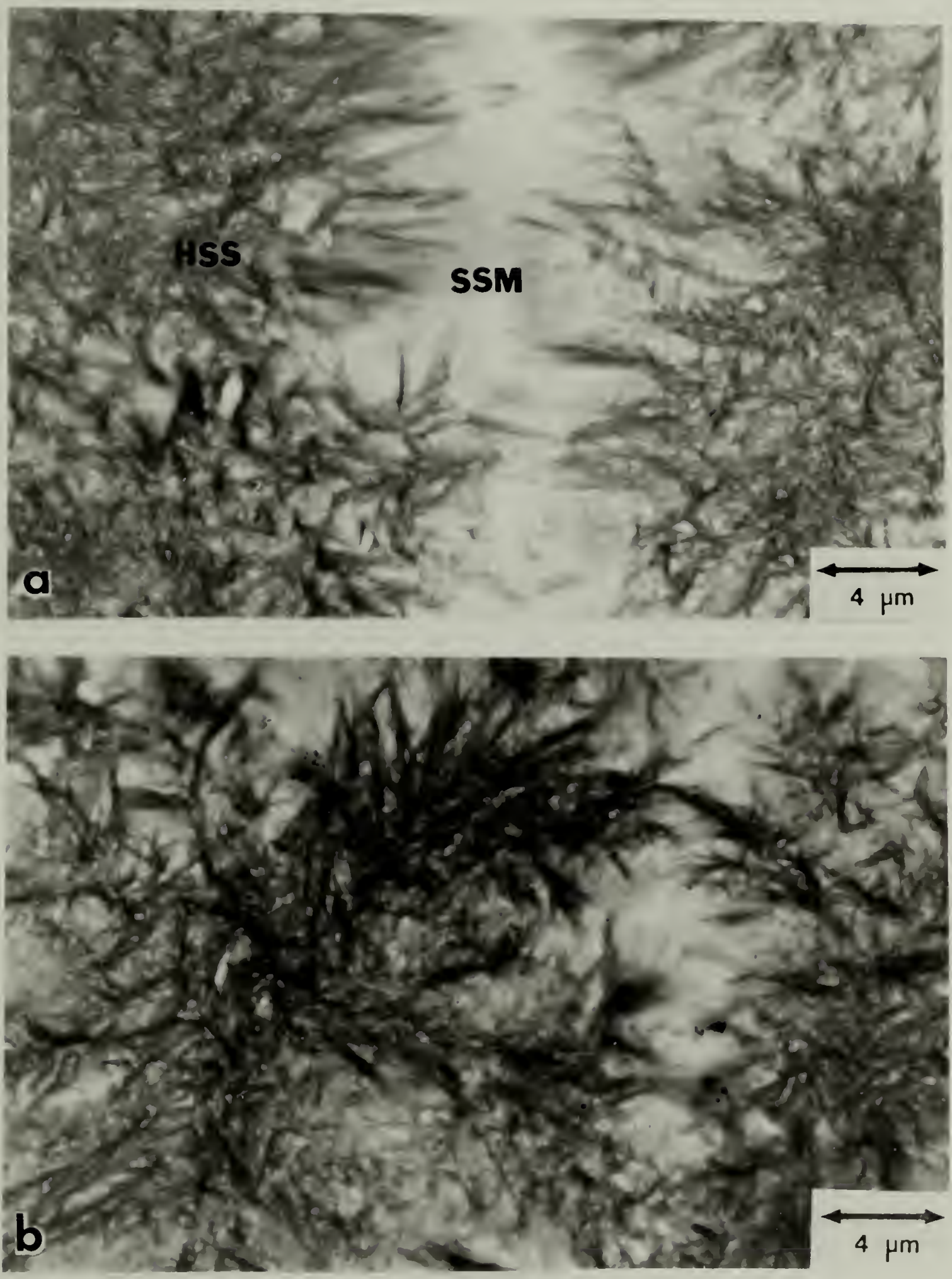

Figure 72

also show the presence of transcrystalline regions similar to those of Figures 70a and b. These transcrystalline regions were also observed in the optical micrographs (recall the more birefringent periphery). The spherulite of Figure 72b looks very similar to that of Figure 71b, except that the amorphous regions are more visible.

Figures 73a and 73b show the morphology of sample PCL-165. The overall morphology shows an interesting feature; the presence of many 1-5 μm size globules (HSG) embedded either in the outer region of spherulites (HSS) or in the matrix (SSM) between spherulites. Judging from electron density contrast, these globules should be hard segment-rich entities. There seems to be some interconnection between fibrils of spherulite and globules but in some cases fibrils seem to pass by and grow (crystallize) around the globules. Sample PCL-165 has spherulites containing very fine, short fibrils without much preferred orientation near the center region of spherulite, becoming longer and more radially oriented in the outer region of spherulite (see Figure 73a). Some spherulites have coarse, long, radial oriented fibrils throughout the whole spherulite (Figure 73b).

The effect of annealing upon the morphology of sample PCL-165 is illustrated in Figures 74a and 74b.

Figures 73a and 73b. TEM micrographs of sample PCL-165 (43 percent hard segment) showing hard segment-rich globules and spherulites, and soft segment-rich matrix.

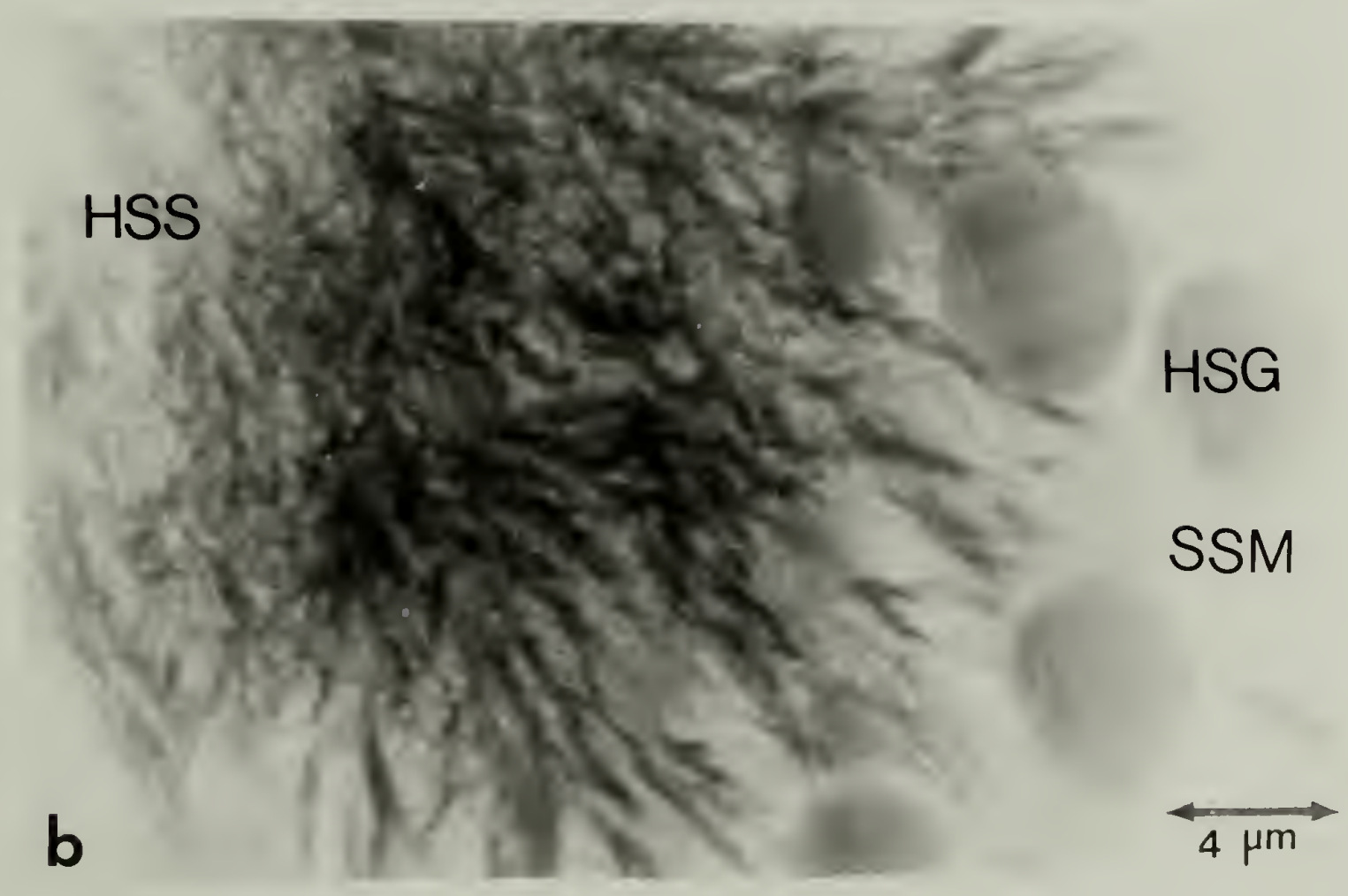

Figure 73

Figures 74a and 74b. TEM micrographs of annealed sample PCL-165 (43 percent hard segment) showing hard segment-rich spherulites and fibrils, and soft-segment rich globules and matrix.

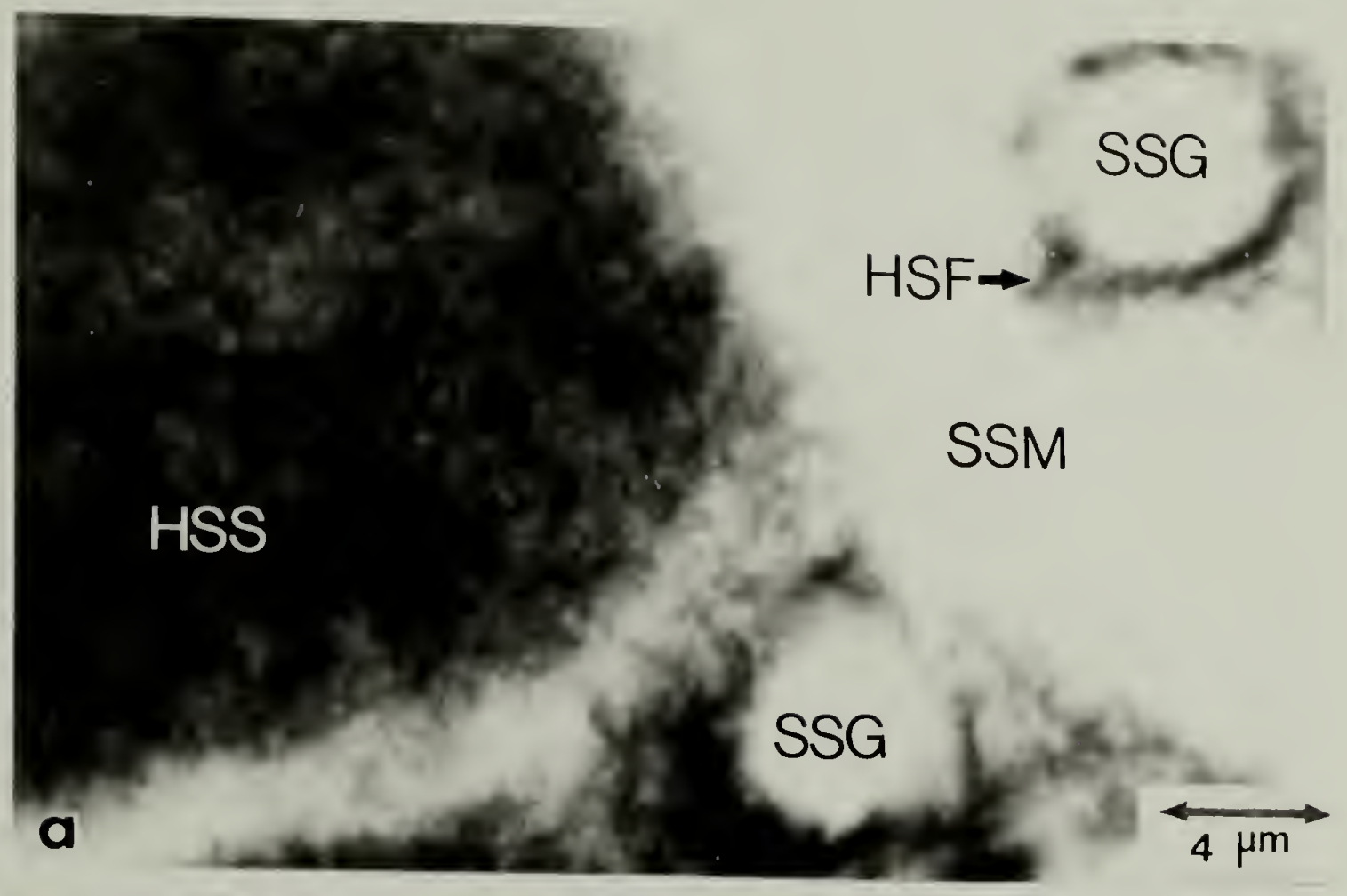

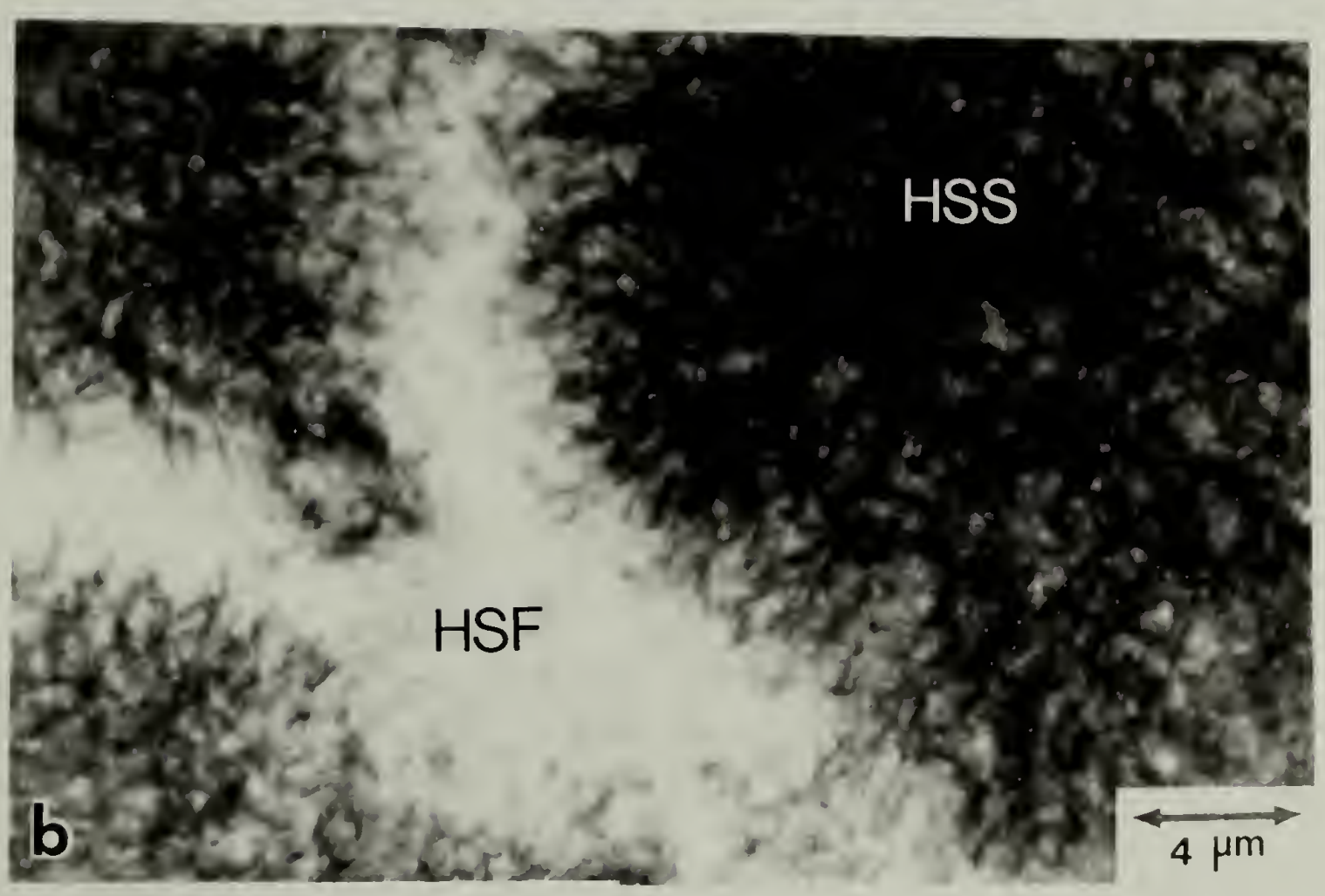

Figure 74

The annealing process is the same as described earlier in the DSC study. Figure 74a shows a dramatic change in globular morphology after annealing. The electron density contrast inside the globule is greatly reduced, nearly equals with the matrix, yet the contrast at the periphery of the globules is increased dut to the formation of a mass of short fibrils (HSF, hard segment-rich fibrils) at the periphery of the globule. Upon annealing, the hard segment-rich molecules apparently diffuse to the outside of globule, and crystallize into fibrils around the globule leaving a soft segment-rich interior.

The morphological change in spherulite itself is best shown in Figure 74b. The distinct long, coarse and more radially oriented fibrils in the outer region of spherulite in the as-reacted sample break up into shorter, and finer and more randomly oriented fibrils after annealing. After annealing, there are many new fibrils (HSF) visible in the matrix. The annealing process appears to promote further phase separation between the hard and soft segment-rich molecules as evidenced by the formation of these new fibrils. The new hard segment fibrils formed in the matrix after annealing are much finer than those in the spherulite perhaps because of the lower hard segment sequence length and the lower overall hard segment content of the matrix material.

7.4 Wide-angle X-ray Scattering Results

Wide-angle X-ray scattering patterns of the as-reacted PCP/MDI/BDO based polyurethane samples are shown in Figure 75 and the results are summarized in Table 16. For the sake of comparison, wide-angle X-ray diffraction data of pure hard segment, MDI/BDO copolymer and pure soft segment, poly-ε-caprolactone homopolymer (PCL) are included in Table 17.

Evidence of soft segment crystallinity is seen in sample PCL-121, which shows sharp 4.17 and 3.78 Å reflections corresponding to the PCL homopolymer 4.14 and 3.74 Å reflections. The rest of the samples show no evidence of soft segment crystallinity. The presence of soft segment crystallinity in sample PCL-121 is likely related to the long soft segment sequences in the random block copolymer. Hard segment crystallinity, detectable in samples of 23 percent hard segment content and higher, is more pronounced with increasing hard segment. The hard segment ~8.5 and ~4.6 Å reflections (as indicated in Figure 75) can be used as a convenient way to qualitatively follow the amount of hard segment crystallinity.

Since both the soft and hard segments are capable of crystallization, this system can contain at least three phases.

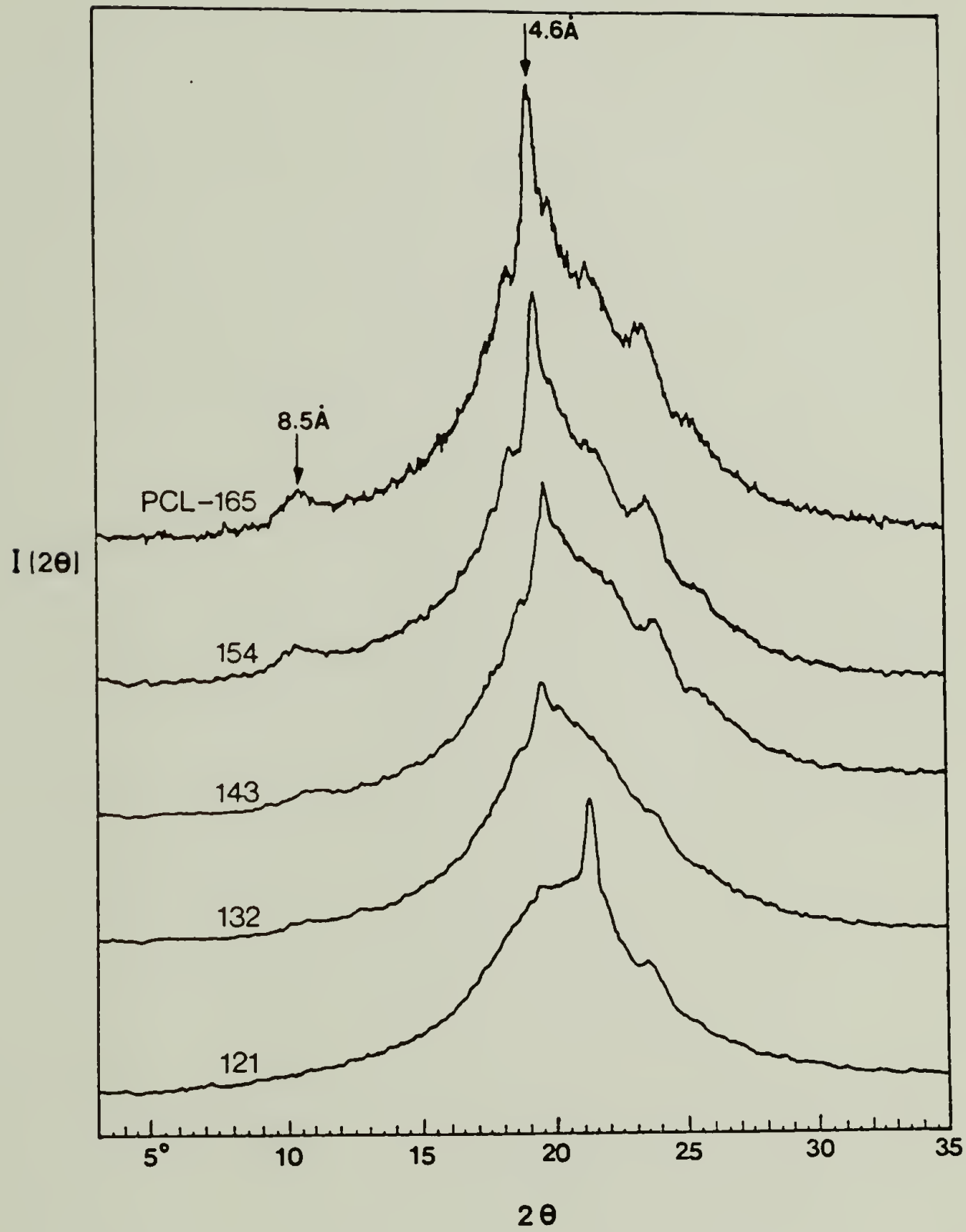

Figure 75. Wide-angle X-ray scans of the as-reacted PCP/MDI/BDO samples.

TABLE 16

WIDE-ANGLE X-RAY DIFFRACTION DATA OF PCP/MDI/BDO SAMPLES

Sample Designation	PCL-165	PCL-154	PCL-143	PCL-132	PCL-121
Crystalline peaks (Å)	8.45	8.58	8.39	8.66	
	4.83	4.85	4.74	4.75	
	4.62	4.60	4.53	4.55	4.52
	4.46	4.46	4.41	4.40	
	4.15	4.19	4.23	4.27	4.17
	4.09	4.13	4.11	4.16	
	3.78	3.78	3.73	3.77	3.78
	3.53	3.50	3.52	3.50	

TABLE 17

WIDE-ANGLE X-RAY DIFFRACTION DATA OF MDI/BDO COPOLYMER AND POLY-ε-CAPROLACTONE HOMOPOLYMER

Sample Designation	Most Crystalline peaks (Å)
MDI/BDO copolymer	3.77 4.09 4.58
Poly-ε-caprolactone homopolymer	4.144 3.735 2.227

7.5 Small-angle X-ray Scattering Results

The results of small-angle X-ray scattering of the as-reacted bulk samples (without Lorentz corrections) are shown in Figure 76 and the Bragg spacing measurements are summarized in Table 18. It is noted that even sample PCL-121, which contains 13 percent by weight hard segment, shows a broad Bragg maximum corresponding to a d-spacing about 190 Å. The long spacings for the rest of the samples are all about the same (i.e. 210 Å) despite their different hard segment contents. One approach is to assume that these low-angle spacings represent the

TABLE 18

SMALL-ANGLE X-RAY BRAGG SPACING FOR AS-REACTED PCP/MDI/BDO SAMPLES

Sample Designation	Small-angle Bragg Spacing, Å
PCL-121	190
PCL-132	210
PCL-143	210
PCL-154	210
PCL-165	210

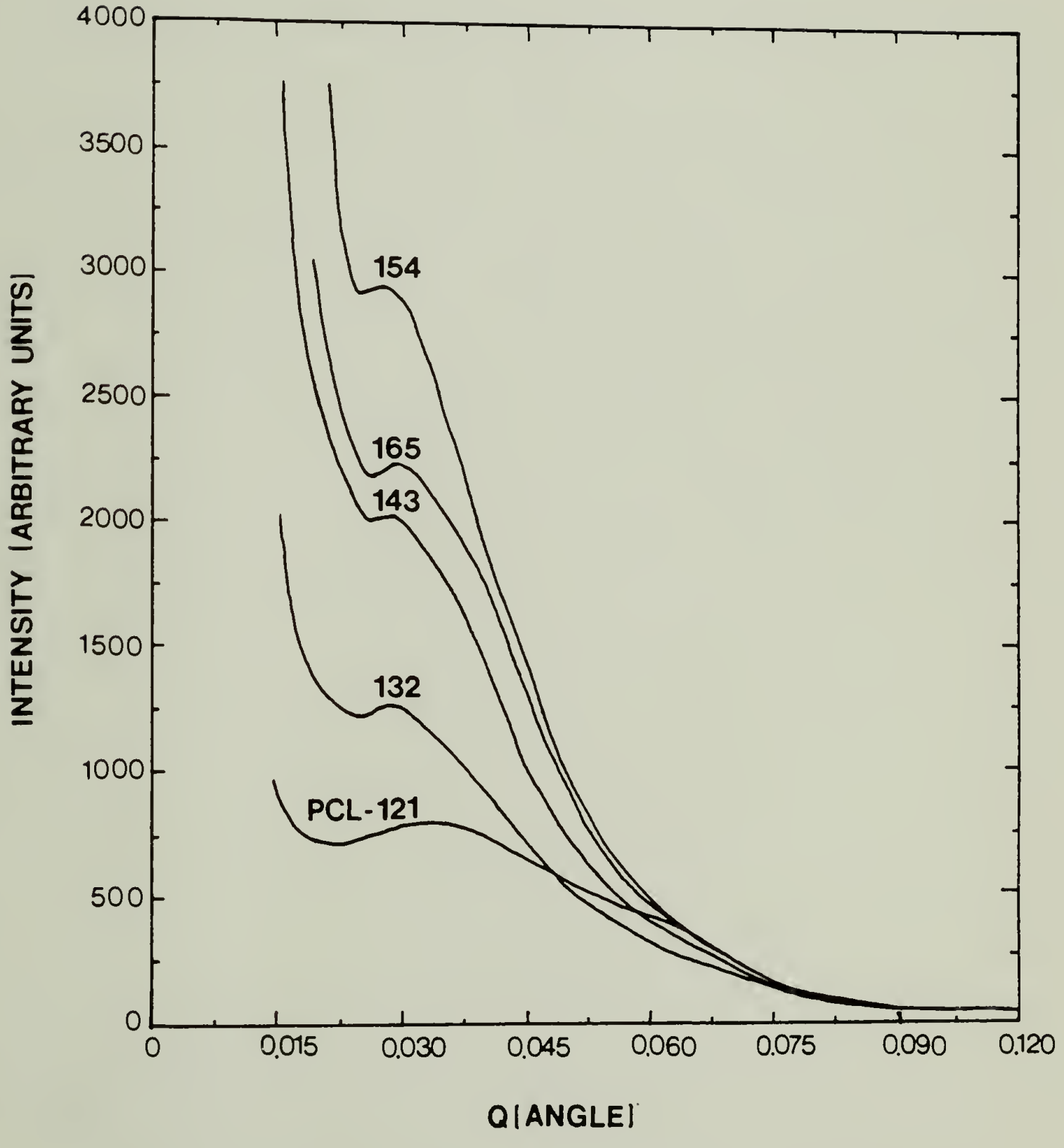

Figure 76. Pinhole SAXS scattering patterns of as-reacted of PCP/MDI/BDO samples.

center-to-center distance of lamellar stacks of hard segment units which are separated by an intervening soft segment phase. If the average domain thickness increases with average hard segment length and the amorphous region thickness is independent of composition then one expects an increases in hard segment domain thickness and thus the long spacing, which is not observed. Several possibilities could account for the observed insensitivity of long period to hard segment content.

Schneider et al.[40] reported that their polyether and polyester (2000 molecular weight) based polyurethanes also showed no or little change in SAXS peak spacing (L ≈ 182 - 210 Å without Lorentz corrections) with different hard segment content (range from 10 percent to 40 percent MDI by weight). Interestingly, their TEM results also revealed the presence of spherulitic superstructure. Therefore the SAXS maxima may arise from the lamellar fibrillar structure associated with spherulitic superstructure and not from the so-called microdomain structure.

The SAXS scattering intensity increases with hard segment concentration with the exception that sample PCL-154 has a higher intensity than PCL-165. If we consider only a two-phase system, then from SAXS theory we

have

$$I(S) \sim \phi\,(1-\phi)(\Delta\rho)^2\,\frac{\sin^2 N\pi S}{\sin^2 \pi S}$$

and $$Q = \int I(S)S^2 ds = \phi(1-\phi)(\Delta\rho)^2$$

where I is scattering intensity

$$S = \frac{4\pi}{\lambda}\sin\frac{\theta}{2}$$

θ : scattering angle

ϕ : volume fraction crystalline phase

$(\Delta\rho)^2$: mean square electron density fluctuation within the sample

Q : small angle invariant (total integrated intensity)

$\frac{\sin^2 N\pi S}{\sin^2 \pi S}$: coherent scattering factor for lamellar stacks

N : number of lamellae in a stack

The volume fraction product $\phi(1-\phi)$ of PCL-165 is slightly larger than that of PCL-154 (.245 vs. .236). If we assume that $(\Delta\rho)^2$ is about the same for both samples, because the scattering intensity of PCL-154 is larger than that of PCL-165, we can argue that the

coherent scattering term, $(\frac{\sin^2 N\pi S}{\sin^2 \pi S})$, of PCL-154 is larger than that of PCL-165. Which implies that sample PCL-154 has better ordered phase than sample PCL-165. Our TEM results also show that the spherulites become more volume filling (less matrix present) with increasing hard

segment content up to sample PCL-154. Although sample PCL-165 has the highest hard segment content, it becomes less volume filling and has more globules and matrix present. If SAXS maximum is due to the lamellar fibrillar structure, it is reasonable to predict the scattering intensity of sample PCL-154 will be higher than PCL-165, which is exactly our SAXS finding.

7.6 Discussion and Conclusions

TEM micrographs of cryomicrotomed sections of samples PCL-121 to PCL-165 show complete different morphologies from those of previously studied solvent (DMF) cast samples[88]. In solvent cast study, no globular morphology was observed in any of these samples and no spherulitic superstructure was observed in sample PCL-121. Solvent cast samples PCL-132 to PCL-165 showed volume filling spherulites morphology with spherulite size decreased markly with decreasing hard segment content. In addition, the lamellar fibrillar structure within spherulites in the solvent cast samples appeared to be much finer than that of microtomed bulk samples. It is obvious that although solvent cast film technique provides an easy and convenient way of preparing TEM specimen, it erases and alters the as-reacted polymer morphology which bears direct relation to its processing history.

Microscopy of cryomicrotomed sections proves to be the most valuable technique available to characterize the undistorted as-reacted polymer morphology.

Comparison between 10 percent by weight hard segment (MDI/BDO) polyester (sample PCL-121) and polyether (sample A-I) soft segment based polyurethanes shows both samples have a phase separated morphology with the former has hedritic and spherulitic structures while the latter has a globular structure. WAXS and microscopic results show polyester soft segment ($\overline{M}n$ = 2000) is capable of crystallization and hedrites/spherulites formation. Polyether soft segment, on the other hand, is less polar and noncrystalline and can hardly incorporate with hard segment to form a spherulitic structure. In this sense polyester soft segment is more compatible with hard segment than polyether soft segment.

In the annealing study of sample PCL-165, DSC results show the perfection of hard segment crystallites after annealing as evidenced from the shifting of peak melting temperature to higher temperature and the narrowing of transition peak width. The annealing process also promotes further phase separation between the hard and soft segment-rich molecules as shown in TEM micrographs with new hard segment fibrils formed in the matrix and at the periphery of the globules. The change of globules morphology after annealing also provides a direct proof

that polymer molecules can diffuse even microns in distance upon annealing.

SAXS results show all samples except PCL-121 have about the same Bragg spacing of 210 Å despite their different hard segment contents. Sample PCL-121 has a different spacing of 190 Å. These SAXS maxima are believed to arise from the lamellar fibrillar structure (LFS) associated with spherulitic superstructure and not from the microdomain structure. TEM micrographs show all samples except PCL-121 have a very similar spherulitic superstructure morphology. Therefore it is not surprising to find these samples have about the same Bragg spacing although their scattering intensities vary.

The unique morphology of sample PCL-121 showing the presence of both hedritic and spherulitic structures may account for the difference of its SAXS diffraction maximum.

In comparison, the SAXS results of PCP/MDI/BDO based samples are simpler and easier to interpret than those of PPO-EO/MDI/BDO based samples since the former have very similar and uniform structures while the latter have very complicated and heterogeneous structures as shown from TEM micrographs.

C H A P T E R VIII

SUMMARY AND CONCLUSIONS / POSSIBLE FUTURE WORK

8.1 Summary and Conclusions

In the course of this study a significant effort was made to understand how processing, morphology and properties are interrelated, so that we can predict physical, particularly mechanical properties of the sample with known morphology and make the best performance polymer product by optimizing processing variables. The key to reaching this goal is through morphological characterization of the as-reacted sample and relation to the processing history. The understanding of the virgin morphology by means of TEM study of cryomicrotomed thin sections of the bulk sample is by far the most sensitive and valuable characterization technique because the original morphology which is linked to the processing history can be preserved and studied.

We have shown that polyurethane random block copolymer can have many possible structures depending on chemical composition, formulation and thermal history. These structures include hard segment-rich globules (HSG), fibrils (HSF), spherulites (α, β-HSS), hard segment-rich matrix (HSM), micro paracrystallite hard segment domains

(MPC), and soft segment-rich hedrite (SSH), pocket regions (SSP), globules (SSG) and matrix (SSM). In addition, the sample can have pronounced skin/core morphology at high hard segment concentration due to the high exothermic heat of polymerization. The universal findings of globules and skin/core morphology in virtually all the sample types examined lead us to conclude what is usually thought to be homogeneous and isothermal batch reaction is really non-homogeneous and nonisothermal reaction. The former is caused by poor mixing or incompatibility of the reacting components, plus further phase separation during the polymerization and solidification (molecular weight, hydrogen-bonding or crystallization effect). The latter is due to high exothermic reaction nature of polyurethane and poor heat conductivity of polymer. These two factors greatly affect the polymerization kinetics and subsequently the final morphology. The deviation from the ideally random (most probable) distribution of molecular weight and hard segment block length can be significant in this case. Therefore the important part of the reaction, during which the micron and the hundred angstrom scale morphology is determined, is the first few minutes (seconds for RIM formulations) before the solidification of the mixture. The complex, simultaneously occurring (macro) phase separation-polymerization-(micro) phase separation-crystallization processes will vary according to sample composition,

position in the mold and the detailed temperature history.

Figure 77 shows schematic representations of the various structures with different dimensions present in the 100° cure PPO-EO/MDI/BDO based polyurethane samples. It clearly illustrates how heterogeneous and complicated the morphology can be depending on compositions and thermal history.

The mechanical properties of polyurethanes can be tailored by using various kinds of components and compositions. In particular, in order for the sample to have the quality of high elongation and toughness, it is necessary for the sample to have both soft segment-rich matrix and hard segment-rich spherulites morphology (e.g. samples A-III and A-IV as shown in Figures 19, 20 and 24). The effect of heterogeneous skin/core morphology on the tensile properties of the sample was also clearly illustrated in Figure 25 where the core region was shown to undergo ductile deformation while the skin region crack and break prematurely through spherulite boundaries. The presence of uniform structure within the sample is greatly desired for better mechanical properties.

Figure 77. Schematic representations of the various structures with different dimensions present in the 100°C cure PPO-EO/MDI/BDO based polyurethane samples:
(a) micro paracrystallite (MPC) structure (10s-100 Å in size),
(b) hard segment-rich fibrillar (HSF) structure (100s Å in width),
(c) hard segment-rich globule (HSG) structure and spherulites (α- and β-HSS) structure (μms in size), and
(d) hard segment-rich matrix (HSM) and skin/core morphology (mm in dimension).

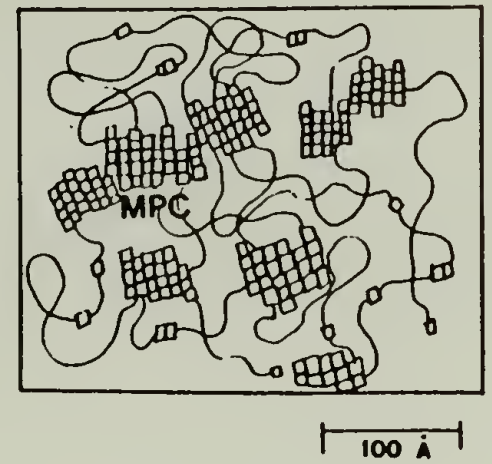
MPC
100 Å

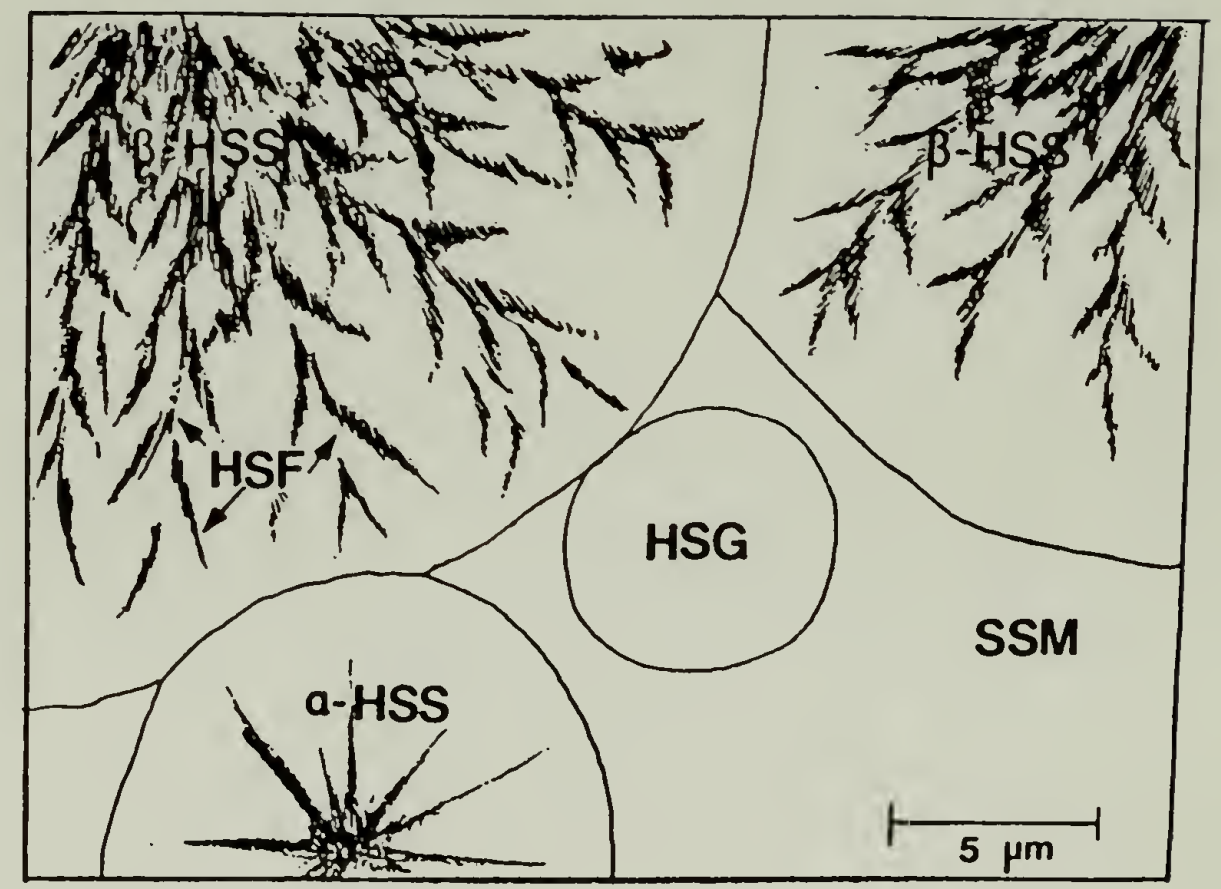
β-HSS
β-HSS
HSF
HSG
SSM
α-HSS
5 μm

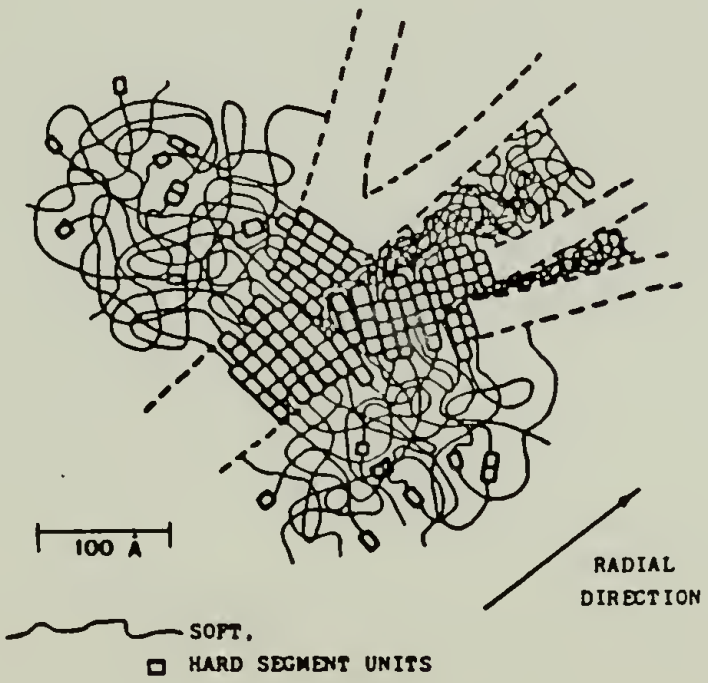
100 Å
RADIAL
DIRECTION
SOFT.
HARD SEGMENT UNITS

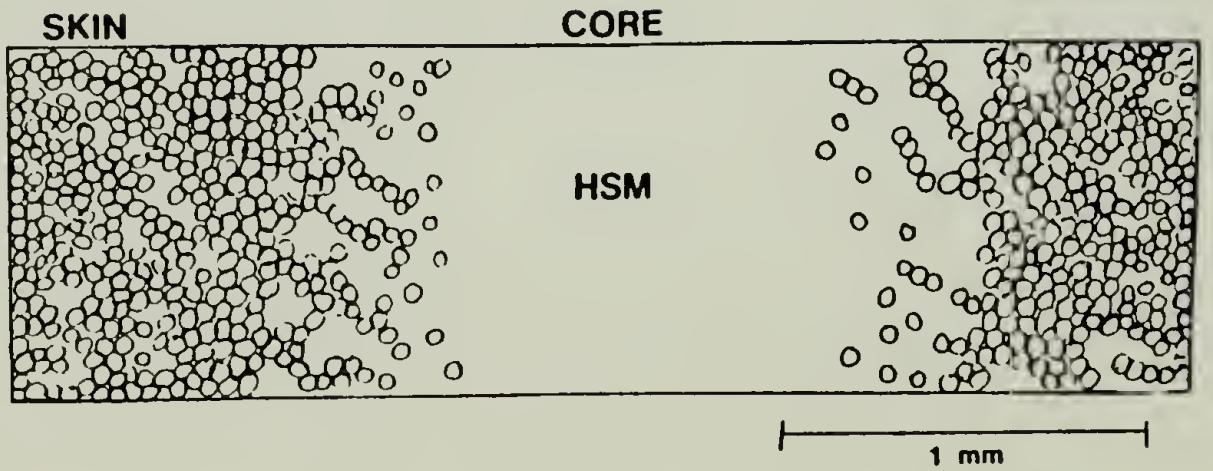
SKIN
CORE
HSM
1 mm

8.2 Possible Future Work

All polyurethane systems we have studied are not so well-defined in the sense that they are random block copolymer with very broad distribution in both molecular weight and hard segment block length sequence. In order to gain an unambiguous understanding of processing and morphology dependent properties, a better designed study is of course needed. I would like to propose the following ideas for future study:

The preparation of polyurethane model compounds with specific hard segment block length sequence and molecular weight distribution is recommended in order to better characterize morphology and structure-properties relationship. The model compounds can then be used to determine the hard segment crystal structure, its heat of fusion and minimum hard segment block size needed for crystallization or phase separation to occur. The characterization of different phase separated morphologies such as globules, spherulites and micro paracrystallite domains as a function of hard segment block length is also a great interest to us.

The effect of macrophase separation on the polymerization kinetics and the resultant polymer morphology and properties should be studied. The macrophase separation during bulk or RIM polymerization may arise from (i) the

incompatibility of the reacting components, (ii) poor or nonstoichiometric mixing and (iii) the precipitation of polymer molecules formed from the remaining reaction matrix, which may result in incomplete reaction and structural inhomogeneities in the sample. The last argument is especially true in the case of highly catalyzed RIM polymerization where reaction can be diffusion limited and terminated prematurely[89].

Due to the high exothermic heat of reaction and macrophase separation problems in the bulk polymerization process, the expected isothermal reaction from well-mixed components can hardly be obtained. It is suggested that solution polymerization method should be tried to determine if the real homogeneous and isothermal reaction condition can be achieved. The comparison of molecular weight, molecular weight distribution and morphology between the solution and bulk polymerized samples should be made.

It is recommended that the morphology and mechanical properties of other polyurethane systems such as crosslinked and RIM polyurethanes be also characterized and compared. In RIM polyurethanes, the study of the effect of fillers and post cure on the structure-properties of the sample is also of great interest to us.

For the characterization of microphase structure in the polymeric materials, SAXS is a powerful technique and

is widely used in the measurement of interdomain spacings, domain boundary diffuseness and the degree of microphase separation. The analysis of SAXS pattern is usually based on an ideal two-phase system, the applicability of similar analysis to the very complicated multi-phase polyurethane system (e.g. 100° C cure PPO-EO/MDI/BDO polyurethane system) is clearly inadequate. The analysis and interpretation of SAXS results certainly deserves a very careful examination. Indeed, it is a very challenging research topic in the future.

REFERENCES

1. J.A. Koutsky, N.V. Hein, and S.L. Cooper, J. Poly. Sci. (Letters), 8, 353 (1970). "Some Results on Electron Microscope Investigations of Polyether-Urethane and Polyester-Urethane Block Copolymers".

2. N.S. Schneider, C.R. Desper, J.L. Illinger, A.O. King, and D. Barr, J. Macro. Sci., B11, 527 (1975). "Structural studies of Crystalline MDI-Based Polyurethanes".

3. S.L. Cooper and A.V. Tobolsky, J. Appl. Poly. Sci., 10, 1873 (1966). "Properties of Linear Elastomeric Polyurethanes".

4. D. S. Huh and S. L. Cooper, Polymer Engr. and Sci., 11, 369 (1971). "Dynamic Mechanical Properties of Polyurethane Block Polymers".

5. K. Onder, R.H. Peters, and L. C. Spark, Polymer, 18, 155 (1977). "Crystallization Phenomena in Some Polyesterurethanes".

6. L.L. Harrell, Jr., Macromolecules, 2, 607 (1969). "Segmented Polyurethanes: Properties as a Function of Segment Size and Distribution".

7. G.L. Wilkes and J.A. Emerson, J. Appl. Physics, 47, 4261 (1976). "Time Dependence of Small Angle X-Ray Measurement on Segmented Polyurethanes Following Thermal Treatment".

8. G.L. Wilkes, S. Bagrodia, W. Humphries, and R. Wildnauer, J. Poly. Sci. (Letters), 13, 321 (1975). "The Time Dependence of the Thermal and Mechanical Properties of Segmented Urethanes Following Thermal Treatment".

9. S.B. Clough and N.S. Schneider, J. Macro. Sci., B2, 553 (1968). "Structural Studies on Urethane Elastomers".

10. H.K. Frensdorff, Macromol., 4:4, 369 (1971). "Block-Frequency Distribution of Copolymers".

11. L.H. Peebles, Jr., Macromol., 9, 58 (1976). "Hard Block Length Distribution in Segmented Block Copolymer".

12. R.J. Cella, J. Poly. Sci., Symposium No. 42, 727 (1973). "Morphology of Segmented Polyester Thermoplastic Elastomers".

13. S.L. Aggarwal, Polymer, 17, 938 (1976). "Structure and Properties of Block Polymers and Multiphase Polymer Systems: An Overview of Present Status and Future Potential".

14. A. Noshay and J.E. McGrath, Academic Press, N.Y., 365-392 (1977). "Block Copolymers Overview and Critical Survey--H. Polyurethane".

15. D.C. Allport and A.A. Mohajer, Block Copolymers (D.C. Allport and W.H. Janes Eds.), 443, John Miley a Sons, "Property-Structure Relationships in Polyurethane Block Copolymers".

16. D.M. Rice and R.J.G. Dominguez, Polymer Eng. and Science, 20, 1192 (1980). "Reaction Injection Molding (RIM) Elastomers Having Superior High Temperature Performance".

17. J. Lindt, Plastics World, 40-57 (1979). "Tomorrow's Gold Rush--RIM Urethanes".

18. J. Sneller, Modern Plastics, 5, 38 (1980). "Where RIM gets its New Momentum".

19. E. Broyer and C. W. Macosko, Polymer Engineering and Science, 18, No. 5, 382-387 (1978). "Curing and Heat Transfer in Polyurethane Reaction Molding".

20. M. Tirrell, L. J. Lee and C. W. Macosko, ACS SYMPOSIUM SERIES, No. 104, Polymerization Reactors and Processes, J. N. Henderson and T. C. Bouton, Editors. 1979. "Conversion and Composition Profiles in Polyurethane Reaction Molding".

21. J.M. Castro and C.W. Macosko, Soc. Plast. Eng. Tech. Papers, 38, 434 (1980). "Kinetics and Rheology of Typical Polyurethane Reaction Injection Molding Systems".

22. I. D. Fridman and E. L. Thomas, L. J. Lee and C.W. Macosko, Polymer, 21, 393-402 (1980). "Morphological Characterization of Reaction Injection Molded (RIM) Polyester Based Polyurethanes".

23. C.E. Wilkes and C.S. Yusek, J. Macro. Sci., B7, 157 (1973). "Investigations of Domain Structure in Urethane Elastomers by X-Ray and Thermal Methods".

24. R.W. Seymour and S.L. Cooper, Macromol., 6, 48 (1973). "Thermal Analysis of Polyurethane Block Copolymers".

25. N.S. Schneider and C.S. Paik Sung, Polymer Engr. and Sci., 17:2, 73 (1977). "Transition Behavior and Phase Segregation in TDI Polyurethanes".

26. M.F. Froix and J.M. Pochan, J. Poly. Sci., 14, 1047 (1976). "Phase Structure in a Polyurethane above Soft Segment Tg via Calorimetric and NMR Techniques".

27. G.L. Wilkes and R. Wildnauer, J. Appl. Phys., 46, 4148 (1975). "Kinetic Behavior of the Thermal and Mechanical Properties of Segmented Urethanes".

28. G.W. Miller and J.H. Saunders, J. Appl. Polymer Sci., 13, 1277 (1969). "The Thermal Analyses of Polymers. II. Thermomechanical Analyses of Segmented Polyurethane Elastomers".

29. W.J. MacKnight, M. Yang, and T. Kajiyama, Polymer Prep., 9:1, 860 (1968). "Differential Scanning Calorimetry of Polyurethanes".

30. R.J. Zdrahala, R.M. Gerkin, S.L. Hager and F.E. Critchfield, J. of Applied Polymer Science, 24, 2041-2050 (1979). "Polyether--Based Thermoplastic Polyurethanes. I. Effect of the Hard-Segment Content".

31. T.R. Hesketh, J.W.C. Van Bogart and S.L. Cooper, Polymer Engineering and Science, 20, No. 3, 190-197 (1980). "Differential Scanning Calorimetry Analysis of Morphological Changes in Segmented Elastomers".

32. R. Bonart, J. Macro. Sci., B2, 115 (1968). "X-Ray Investigations Concerning the Physical Structure of Cross-linking in Segmented Urethane Elastomers".

33. R. Bonart, L. Morbitzer, and E.H. Muller, J. Macro. Sci., B9, 447 (1974). "X-Ray Investigations Concerning the Physical Structure of Crosslinking in Urethane Elastomers. III. Common Structure Principles for Extensions with Aliphatic Diamines and Diols".

34. R. Bonart, L. Morbitzer, and G. Hentze, J. Macro. Sci., B3, 337 (1969). "X-Ray Investigations Concerning the Physical Structure of Crosslinking in Urethane Elastomers. II. Butanediol as Chain Extender".

35. I. Kimura, H. Ishihara, K. Saito, and H. Ono, Rpts. Prog. Polymer Phys. Japan, 13, 205 (1970). "Property and Structure of Segmented Polyurethane. III. X-Ray Study on Orientation of Hard Segment".

36. R.R. Lagasse, J. Appl. Poly. Sci., 21, 2489 (1977). "Domain Structure and Time Dependent Properties of a Crosslinked Urethane Elastomer".

37. S.L. Samuels and G.L. Wilkes, J. Polym. Sci. Symposium, No. 43, 149 (1973). "The Rheo-Optical and Mechanical Behavior of a Systematic Series of Hard-Soft Segmented Urethanes".

38. I. Kimura, H. Ishihara, and H. Ono, Macromol., 7, 355 (1974). "Morphology and Deformation Mechanism of Segmented Poly (urethane ureas) in Relation to Spherulitic Crystalline Textures".

39. R.R. Lagasse and K.B. Wischmann, ACS Organic Coatings and Plastics Preprints., 37, 501 (1977). "Castable Thermoplastic Urethane Elastomers. II. Structure Property Correlation".

40. S.B. Clough, N.S. Schneider, and A.O. King, J. Macro. Sci., B2, 641 (1968). "Small Angle X-Ray Scattering from Polyurethane Elastomers".

41. Zohar Ophir, J. of Polymer Science: Polymer Physics Edition, 18, 1469-1480 (1980). "SAXS Analysis of a Linear Polyether and a Linear Polyether Urethane--Interfacial Thickness Determination".

42. C.S. Paik Sung, C.B. Hu and C.S. Wu, Macromolecules, 13, 111-116 (1980). "Properties of Segmented Poly (urethaneureas) Based on 2,4-Toluene Diisocyanate. 1. Thermal Transitions, X-Ray Studies, and Comparison with Segmented Poly (urethanes)".

43. S.L. Samuels and G.L. Wilkes, Polymer Letters, 9, 761 (1971). "Anisotropic Superstructure in Segmented Polyurethanes as Measured by Photographic Light Scattering".

44. G.M. Estes, R.W. Seymour, and S.L. Cooper, Macro., 4, 452 (1971). "Infrared Studies of Segmented Polyurethane Elastomer. II. Infrared Dichroism".

45. C.S. Paik Sung, T.W. Smith and N.H. Sung, Macromolecules, 13, 117-121 (1980). "Properties of Segmented Polyether Poly (urethaneureas) Based on 2,4-Toluene Diisocyanate. 2. Infrared and Mechanical Studies".

46. W.J. MacKnight and M. Yang, J. Polymer Sci.: Symposium, No. 42, 817-832 (1973). "Property--Structure Relationships in Polyurethanes: Infrared Studies".

47. G.A. Senich and W.J. MacKnight, Macromolecules, 13, 106-110 (1980). "Fourier Transform Infrared Thermal Analysis of a Segmented Polyurethane".

48. R.A. Assink, J. Poly. Sci., 15, 59 (1977). "The Study of Domain Structure in Polyurethanes by NMR".

49. G.L. Wilkes, S.L. Samuels, and R. Crystal, J. Macro. Sci., B10, 203 (1974). "Scanning and Transmission Electron Microscopy Studies on a Model Series of Spherulitic Segmented Polyurethanes".

50. I. Kimura, H. Ishihara, K. Saito, K. Tamaki, and H. Ono, Rpts. Prog. Polymer Phys. Japan, 13, 209 (1970). "Property and Structure of Segmented Polyurethane. IV. Aggregation Structure of Hard Segments".

51. I. Kimura, H. Ishihara, and H. Ono, Macromol. Prepr., 1, 525 (1971). "Morphology and Deformation Mechanism of Segmented Polyurethanes in Relation to Spherulite Crystalline Texture".

52. C.G. Seefried, Jr., J.V. Koleske, and F.E. Critchfield J. Appl. Poly. Sci., 19, 2493 (1975). "Thermoplastic Urethane Elastomers. I. Effects of Soft Segment Variations".

53. C.G. Seefried, Jr., J.V. Koleske, F.E. Critchfield, and J.L. Dodd, Polymer Engr. and Sci., 15, 646 (1975). "Thermoplastic Urethane Elastomers. IV. Effects of Cycloaliphatic Chain Extender on Dynamical Mechanical Properties".

54. C.G. Seefried, Jr., J.V. Koleske, and F.E. Critchfield J. Appl. Poly. Sci., 19, 2503 (1975). "Thermoplastic Urethane Elastomers. II. Effects of Variations in Hard Segment Concentration".

55. F.E. Critchfield, J.V. Koleske, G. Magnus, and J.L. Dodd, J. Elastoplastics, 4, 22 (1972). "Effect of Short Chain Diol on Properties of Polycaprolactone Based Polyurethanes".

56. C.G. Seefried, Jr., J.V. Koleske, and F.E. Critchfield Polymer Engr. and Sci., 16, 771 (1976). "Thermoplastic Urethane Elastomers. V. Compatible and Incompatible Blends with Various Polymers".

57. J.V. Koleske and R.D. Lundberg, J. Polymer Sci., Part A-2, 7, 795 (1969). "Lactone Polymers. I. Glass Transition Temperature of Poly-ε-Caprolactone by Means of Compatible Polymer Mixtures".

58. J.V. Koleske and R.D. Lundberg, J. Polymer Sci., Part A-2, 10, 323 (1972). "Lactone Polymers. IV. Glass Transition Temperature of Monomeric Lactones and Their Polymers".

59. C.G. Seefried, Jr., J.V. Koleske, and F.E. Critchfield J. Polymer Sci., Part A-2, 14, 2011 (1976). "Lactone Polymers. VIII. Dynamic Mechanical Properties of ε-Caprolactone Copolymers".

60. G.W. Miller, and J. H. Saunders, J. Poly. Sci., A1, 1923 (1970). "Thermal Analysis of Polymers. III. Influence of Isocyanate Structure on the Molecular Interactions in Segmented Polyurethanes".

61. S.L. Cooper, R.W. Seymour, and J.C. West, in Encyclopedia of Polymer Science, Suppl., 1, 521 (1976). "Polymerthane Block Polymers".

62. R. Bonart, Die Angewandte Makromoleculare Chemie, 58/59, 259 (1977). "Segmented Polyurethane".

63. J. Blackwell and M.R. Nagarajan, Polymer, 22, 202 (1981). "Conformational Analysis of Poly (MDI-Butanediol) Hard Segment in Polyurethane Elastomers".

64. J. Blackwell, M.R. Nagarajan and T.B. Hoitink, Polymer, 22, 1534 (1981). "Structure of Polyurethane Elastomers. X-ray Diffraction and Conformational Analysis of MDI-Propandiol and MDI-Ethylene Glycol Hard Segments".

65. J. Blackwell and K.H. Gardner, Polymer, 20, 13 (1979). "Structure of the Hard Segments in Polyurethane Elastomers".

66. J. Hocker and L. Born, J. of Polymer Science: Polymer Letters Edition, 17, 723-730 (1979). "The Structure of Two Modifications of the MDI-Bismethylurethane as a Model Substance for Hard Segments in Polyurethane Elastomers".

67. A.L. Chang and E.L. Thomas, Advances in Chemistry Series, No. 176, 31. Multiphase Polymers (S.L. Cooper and G.M. Estes, Editors), "Morphological Studies of PCP/MDI/BDO Based Segmented Polyurethanes".

68. I. D. Fridman and E. L. Thomas, Polymer, 21, 388 (1980). "Morphology of Crystalline Polyurethane Hard Segment Domains and Spherulites".

69. E.L. Thomas and E.J. Roche, Polymer, 20, 1413 (1979). "Critical Evaluation of Electron Microscope Evidence for Order in Glassy Polymers".

70. E.J. Roche and E.L. Thomas, Polymer, 22, 333 (1981). "Defocus Electron Microscopy of Multiphase Polymers: Use and Misuse".

71. G. Porod, Kolloid Z., 124, 83 (1951). "Die Rontgenklein-winkelstreuung von Dichtgepackten Kolloiden System I. Teil".

72. P. Debye and A.M. Bueche, J. Appl. Phys., 20, 518 (1949). "Scattering by an Inhomogeneous Solid".

73. O. Kratky, Pure and Appl. Chem., 12, 483 (1966). "Possibilities of X-Ray Small Angle Analysis in the Investigation of Dissolved and Solid High Polymer Substances".

74. J.A. Manson and L.H. Sperling, Plenum Press, 153, (1976). "Polymer Blends and Composites".

75. J. Ferguson and N. Ahmad, Europ. Polym. J., 13, 865 (1977). "Chemical Structure and Physical Properties in Polyester Based Segmented Polyurethanes - II. Tensile Properties".

76. G. Lunardon, Y. Sumida and O. Vogl, Die Ange. Makromol Chemie, 87, 1 (1980). "Effects of Molecular Weight and Molecular Weight Distribution of Polyester Bsed Soft Segments on the Physical Properties of Linear Polyurethane Elastomers".

77. R.W. Seymour, J.R. Overton and L.S. Corley, Macromolecules, 8, 331 (1975). "Morphological Characterization of Polyester-Based Elastoplastics".

78. I.D. Fridman, Master's Thesis, University of Massachusetts, (September 1979). "Morphological Characterization of Reaction Injection Molded (RIM) Polyurethanes".

79. J.M. Castro and C.W. Macosko, AIChE J., 28, 250 (1982). "Studies of Mold Filling and Curing in the Reaction Injection Molding Process".

80. J.M. Castro, F. Lopez-Serrano, R.E. Camargo, M. Tirrell and C.W. Macosko, J. of Appl. Polym. Sci., 26, 2067 (1981). "Onset of Phase Separation in Segmented Urethane Polymerization".

81. J.M. Castro and C.W. Macosko, AIChE J., 28, 250 (1982). "Studies of Mold Filling and Curing in the Reaction Injection Molding Process".

82. E.C. Steinle, F.E. Critchfield, J.M. Castro and C.W. Macosko, J. of Appl. Polym. Sci., 25, 2317 (1980). "Kinetics and Conversion Monitoring in a RIM Thermoplastic Polyurethane System".

83. J.M. Castro, S.D. Lipshitz and C.W. Macosko, AIChE J., 28, 973 (1982). "Laminar Tube Flow with a Thermosetting Polymerization".

84. S.C. Misra, J.A. Manson and L.H. Sperling, ACS Symposium Series, 114, 157 (1979).

85. J. Mijovic and J.A. Koutsky, Polymer, 20, 1095 (1979). "Correlation Between Nodular Morphology and Fracture Properties of Cured Epoxy Resins".

86. R.E. Cuthrell, J. Appl. Polym. Sci., 11, 949 (1967). "Macrostructure and Environment-Influenced Surface Layer in Epoxy Polymers".

87. L.J. Lee and C.W. Macosko, Soc. Plast. Eng. Tech. Papers, 24, 151 (1978). "Design and Characterization of a Small Reaction Injection Molding Machine".

88. A.L. Chang, Master's Thesis, University of Minnesota, (December 1978). "Morphological Studies of PCP/MDI/BDO Based Segmented Polyurethanes".

89. E.B. Richter and C.W. Macosko, Polym. Eng. and Sci., 18, 1012 (1978). "Kinetics of Fast (RIM) Urethane Polymerization".

APPENDIX

UNION CARBIDE HAND CAST PROCEDURE FOR URETHANE ELASTOMERS

MOLDS

Glass plates, 1 pc 7 1/2" x 12", 1 pc 9" x 12".

Teflon spacer, 1/2" wide with the desired thickness, to fit the outer edge of the mold.

Hysol mold release

Spring clamps

FLASKS

500 ml 4-necked round-bottom flask equipped with mechanical stirrer, vacuum inlet and thermometer. A heating mantle may be used to warm the polyol blend.

PROCEDURE

1. Mix polyol, chain extender and catalyst at the desired ratios in the reaction flask.
2. Attach the flask to a vacuum pump and degas with stirring for 20 minutes.
3. While the polyol blend is degassing, also degas the isocyanate to be used.
4. Break the vacuum on the isocyanate container and weigh the required amount into a small beaker

(use the wet tare method to insure best accuracy).

5. Stop the stirrer on the polyol blend flask and break the vacuum.
6. Add the required amount of isocyanate, reapply the vacuum, start the stirrer and stir vigorously under vacuum for at least 15 seconds.
7. Break the vacuum and rapidly pour the liquid system between the glass plates which were previously coated with Hysol. Note: it is best to clamp the mold such that the gap at the top if 1/2" to facilitate pouring.
8. Clamp the mold securely around its perimeter using the spring clamps and place the entire assembly in the oven.

GENERAL

a. Most MDI based polymers are run using 0.01 to 0.03 pt Sn dibutyl dilaurate catalyst per 100 pt polyol blend. This actually gives gel times of 30 seconds. At this level of catalyst, the polymer is typically allowed to cure overnight at 100°C.

b. A total charge weight of 190 g is required to fill the molds described above when the spacer thickness is 125 mils.

c. Prior to casting the polyol may be heated. This, of course, increases the rate of the reaction. Temperature should be monitored.

d. Similarly, the molds can be preheated prior to casting. A pyrometer is used to determine actual mold temperature.